

(ur) DIMENSIONS

The Journal of Undergraduate Research in Natural Sciences and Mathematics

California State University, Fullerton

Volume 13 Spring 2011

Marks of a CSUF Graduate from the College of Natural Sciences and Mathematics

Graduates From The College Of Natural Sciences And Mathematics

Understand the basic concepts and principles of science and mathematics.

Are experienced in working collectively and collaboratively to solve problems.

Communicate both orally and in writing with clarity, precision and confidence.

Are adept at using computers to do word processing, prepare spreadsheets and graphs, and use presentation software.

Possess skills in information retrieval using library resources and the Internet.

have extensive laboratory/workshop/field experience where they are utilize the scientific method to ask questions, formulate hypotheses, design experiments, conduct experiments, and analyze data.

Appreciate diverse cultures as a result of working side by side with many people in collaborative efforts in the classroom, laboratory and on research projects.

In many instances have had the opportunity to work individually with faculty in conducting research and independent projects. in addition to the attributes of all NSM students, these students generate original data and contribute to the research knowledge base.

Have had the opportunity to work with very modern, sophisticated equipment including advanced computer hardware and software.

Dimensions:

The Journal of Undergraduate Research in Natural Sciences and Mathematics is an official publication of California State University, Fullerton. Dimensions is published annually by CSUF, 800 N. St. College BLVD., Fullerton, CA 92834. Copyright ©2011 CSUF. except as otherwise provided, Dimensions grants permission for material in this publication to be copied for use by non-profit educational institutions for scholarly or instructional purposes only, provided that 1) copies are distributed at or below cost, 2) the author and Dimensions are identified, and 3) proper notice of the copyright appears on each copy. if the author retains the copyright, permission to copy must be attained directly from the author.

About the Cover:

Man's tenacious hunger for exploration of the unknown fostered the need to develop new tools... tools for measuring, listening, calculating, and seeing the un-seeable. Tools that are as brilliant as the secrets they may uncover.

This journal is a testament to these users of tools.

Stainless steel symbolizes the brilliant resolve of these explorers seeking form amid the chaos, a study of trial and error, failure and success. Increasing the corpus of human knowledge through scientific research.

Acknowledgements

Executive Editor

Amber Shah

Editors

Ernesto Casillas, Biology
Julie Yang, Chemistry/Biochemistry
Erin Driver, Geology
Mikhail Popov, Mathematics

Advisor

Dr. Rochelle Woods, Assistant Dean
for Student Affairs

Graphic Design

Carolyn Luu, Layout Editor
Brian Bouskill, Cover Designer

Graphic Design Advisor

Arnold Holland, Associate Professor

College of the Arts

Dr. Joseph H. Arnold, Jr., Dean
Andi Sims, Assistant Dean for Student Affairs

College of Natural Sciences and Mathematics

Dr. Robert A. Koch, Acting Dean

Dr. Mark Filowitz, Associate Dean

Dr. Kathryn Dickson, Acting Chair Department
of Biological Science

Dr. Christopher Meyer, Chair Department
of Chemistry/Biochemistry

Dr. David Bowman, Chair Department of
Geological Sciences

Dr. Paul De Land, Chair Department of
Mathematics

Dr. James M. Feagin, Chair Department
of Physics

Special Thanks To

President Milton A. Gordon
and Dean Robert A. Koch
for their support and dedication to Dimensions.

Articles

Geology

8

Designing a Test of the Assumption of Neutrality
within the Late Cretaceous Holz Shale, Santa Ana
Mountains, California

By: **Michelle Gevedon**

13

Incised River Meanders in western and
northwestern Thailand: Implications for the
late Cenozoic regional tectonics of
northwestern Indochina

By: **Angela Perez**

18

Mineralogy And Petrography Of The
Polymetamorphic Kings Sequence, Lake Kaweah
Pendant, West-Central Sierra Nevada Batholith, Ca.

By: **Crystal A. Castellanos**

19

The Effect of Barriers on Slip Partitioning in an
Upward Branching Fault System

By: **Jennifer Tarnowski, David Bowman, and David Oglesby**

20

Partitioned exhumation and thrust faulting in
northern Prince William Sound, south-central
Alaska constrained by apatite (U-Th)/He dating

By: **Michael Prior**

Chemistry/Biochemistry

28

Measuring levels of PM10 pollution in the Chiang
Mai basin in Northern Thailand

By: **Steven Schill**

Biological Sciences

32

Effects of Artificial Moonlight
on the Foraging Behavior of Desert Rodents

By: **Bryan White**

36

Effects of Prairie Dogs
on the Diet of Thirteen-lined Ground Squirrels
(*Spermophilus tridecemlineatus*)

By: **Denise Soto**

40

The Effects of Age and Sexual Experience
on the Mating Success of the Male House Cricket
Acheta domesticus

By: **Eric S. Peralta**

45

Physiological differences of two desert shrubs
across differently-aged substrates
in the Mojave Desert

By: **Karolis Raudys**

49

Effects of Cactus Removal on Grassland Rodents

By: **Leslie Herington**

54

Localization And Identification Of Protein Kinase C
Subtypes Ascidian Sperm Activation

By: **Rolando Ruiz**

63

Influence Of Anthropogenic Noise On Song
Structure In *Calypte* Hummingbirds

By: **Sarah English**

Mathematics

71

Remarks on De Sitter Spacetime: Geometry
in the Theory of Relativity

By: Peter Ho

82

Economical Generating Sets
for the Symmetric and Alternating Groups
Consisting of Cycles of a Fixed Length

By: Josh Maglione

97

Rindler Temperature Result
and Distributional Modes

By: Joshua Strong

107

The Sayre-Reitsma Direct Proof
of the Steiner-Lehmus Theorem

By: Jonathan Sayre and Jeremy Reitsma

114

Statistical Modeling of the Fat Fraction in
Magnetic Resonance Imaging (MRI)

By: Anne M. Calder, Eden A. Ellis, Li-Hsuan Huang,
and Kevin Park

124

A Comparative Study of Divergence Metrics
in the Analysis of Neuronal Data

By: Mikhail Y. Popov, David Rock, and Victor Ying

Biographies

138

Designing a Test of the Assumption of Neutrality within the Late Cretaceous Holz Shale, Santa Ana Mountains, California

Michelle Gevedon
Advisor: Dr. Nicole Bonuso

Department of Geological Sciences, California State University, Fullerton, CA, USA

Abstract

Recent theory suggests that biodiversity is controlled predominantly by species abundance based on two assumptions: first, that species are interchangeable, or neutral, and second, that the number of individuals increases linearly with area (Hubbell, 2001). Hubbell's Unified Neutral Theory of Biodiversity (UNTB) is controversial because it contradicts traditional ideas that competition and specialization are the main influences on speciation. UNTB provides many testable theoretical models that have been applied to modern habitat, but are untested in the fossil record. The Holz Shale of Silverado Canyon, Irvine, California provides an ideal site to test for the existence of the linear relationship required for neutrality because well-preserved and abundant fossils are exposed in a complete section. Faunal specimens were sampled laterally; two sample sets from two communities, for a total of four samples were collected from areas of increasing size. Each fossil was counted and identified to the genus level. Linear change in abundance patterns between samples was examined using the 2-Way t-Statistic. The correlating sample sets from each bedding plane were compared to test for statistical significance between the two populations. The results show a positive correlation and liner relationship between area and abundance. Future tests of the assumption of neutrality should use the methods designed in this study, and must identify potentially neutral species. Using the Paleobiology Database, data regarding the ecologies of collected fauna was collected to isolate potentially neutral species. Based on this research, future tests of the assumption of neutrality can determine the neutrality of species in fossilized communities.

Introduction

During the Late Cretaceous, approximately 83 mya, the coastal margin of California was dominated by Cordilleran-style tectonics fueled by the subduction of the Farallon plate. Such active tectonics and arc magmatism result in the influx of nutrients via large cations shedding into the flanking forearc basins, allowing communities of marine fauna to flourish. Forearc basins provide ideal locations for paleoecological studies due to their rapid sedimentation rates, vast faunal abundance,

and wide-spread preservation; such a forearc basin environment and community is preserved in Silverado Canyon of the Santa Ana Mountains (SAMs) within Irvine Ranch National Natural Landmark (IRNNL) in Irvine, California (Figure 1) (Cooper and Sawlon, 2006).

Of the forearc sediments found in the SAMs, the Holz Shale Member of the Ladd Formation is the most fossiliferous and represents a shallow marine shelf to a shallow continental slope environment, the most ideal habitat for benthic marine invertebrates. Here the diverse community contains many competing congeneric species, species belonging to a single genus, having similar life modes and trophic levels. Traditionally,

California



Figure 1: Study Location Map shows the location of the Irvine Ranch National Natural Landmark. The study area is approximately 1/16 of a mile square located directly off of Silverado Canyon Road.

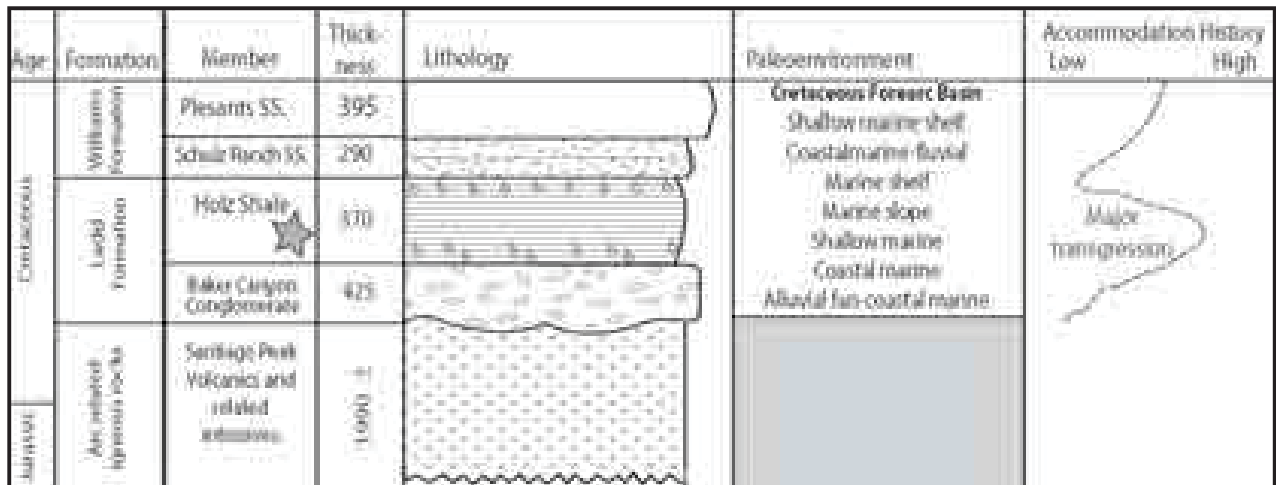


Figure #2: Santa Ana Mountains Stratigraphic Column

Stratigraphic column showing units relevant to the study. The study area located at the base of the Holz Shale Member of the Ladd Formation is marked by a star. Notice the accommodation history curve to the right indicating the sea level flux occurring during sedimentation. Such a major marine transgression has the ability to alter the paleoenvironment and is evident in lithologic changes (modified from Cooper and Sawlon, 2006).

paleoecologists and biologists have considered the dominant mechanisms or driving forces for speciation to be: specialization for optimal exploitation of resources and inhabitation of niches, the ability to utilize new resources, and inter-species competition, all of which apply to the Holz Shale communities (Sundberg and Cooper, 1978; Sundberg, 1980, 1982, 1993).

Modern ecological theory, however, specifically the Unified Neutral Theory of Biodiversity (UNTB) (Hubbell, 2001) asserts that organisms of the same community belonging to the same trophic level do not compete, even if they rely on the same resources. Instead, UNTB regards organisms in a community as neutral or interchangeable, and implies that species abundance is a driving force of speciation. The mathematical models supporting the UNTB have been applied and proven successful in many ecological settings, but have yet to be tested in the fossil record (Hubbell, 2001). If it is possible to determine how biodiversity has responded to changes in habitable space in the past, it may eventually be possible to predict how biodiversity will respond to future crises in area caused by anthropogenic activities such as urbanization and deforestation.

In order to determine whether the UNTB applies to the fossil record, we must test the basic assumption of neutrality. Neutrality within the UNTB is based on the prediction that as area increases, the abundance of organisms found within that area will increase accordingly. Our hypothesis states that a linear relationship exists between genera abundance and area. By developing a method to test this hypothesis we can ultimately

test for the predicted pattern of neutrality; recognizing such patterns within the fossil record is important because it provides the ability to test speciation processes on an evolutionary time scale rather than a modern, shorter time scale.

Geologic Setting

The IRNNL was established in part to continue the preservation of the formations found within the SAMs, arguably the most complete preserved example of the Late Cretaceous arc and forearc complex in North America (Cooper and Sawlon, 2006), with the Ladd formation representing the true Cretaceous forearc basin. The Ladd Formation is comprised of the Baker Canyon Conglomerate followed conformably by Holz Shale. The Baker Canyon Conglomerate has an internal facies grading from a semi-terrestrial fan in the east to a shallow marine fan delta (Sundberg, 1980, 1982, 1993). The unit is made of rounded to semi-rounded igneous and volcanic clasts likely derived from the Santiago Peak Volcanics and the Southern California Batholith representing the arc itself, with occasional channel cuts and fills, and preserved bars and swales typical of an alluvial fan. By tracking fossil presence in the various units of the forearc, it is possible to monitor bathyal depths; the Baker Canyon Conglomerate is made of sediments from a shallow and high energy marine coastal environment, whereas the Holz Shale member represents a deeper, lower energy environment conducive to sustaining the life and preservation of benthic marine invertebrates (Cooper and Sundberg, 1978; Cooper and Sawlon, 2006).

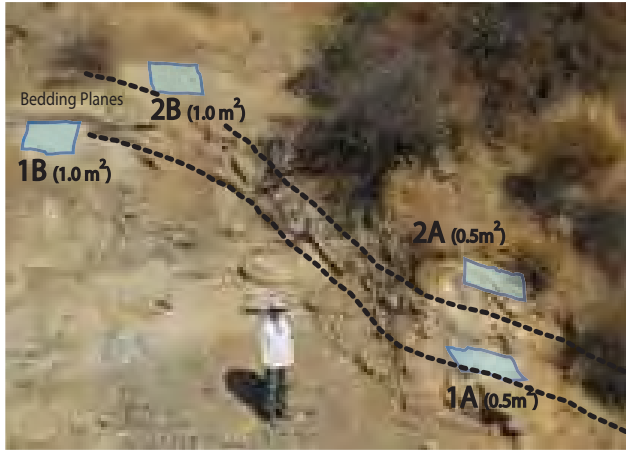


Figure #3: Sampling Scheme

Figure showing the sampling site divided into areas 1A and 2A each of 0.5m² and corresponding to areas 2A and 2B, each of 1.0m², respectively. Area 1A is 9.5 meters from area 2A along the same bedding plane, while area 1B is 10.1 meters from area 2B along the same bedding plane.

The Holz Shale in general is dark gray mudstone with lesser siltstone. The upper and middle Holz Shale is a dark gray-green with sparse mega fossils that indicate an environment farther off shore; the lower Holz Shale is siltier, lighter in color, with extremely abundant invertebrate marine fauna; the middle Holz Shale represents the deepest marine environment of the forearc. These changes in bathyal depths are the result of the eustatic sea level transgression of the Turonian (Figure 2) (Sundberg 1980; Cooper and Sawlon, 2006). Environmental change is evident in the petrology, with finer sands and silts composing the middle Holz, and also by the reappearance of fossils when depths again reach those of a shallow marine shelf. These changes are supported by foraminifera data (Cooper and Sawlon, 2006). Environment dependent lithological differences are important to this study because the quantity of the samples necessary can only be supplied from locations with extremely abundant specimens for collection. Based on the known lithological changes within the Holz Shale, sample locations can only be selected from the upper and lower strata of the member.

Structurally, the SAMs are a part of a geographically extensive monocline exposed as long, laterally extensive beds generally striking northwest and dipping 40° southwest (Cooper and Sundberg, 1978; Sundberg, 1982). These laterally extensive outcrops make it possible to follow single bedding planes for several meters allowing lateral sampling of fossil beds for testing species area relationships.

Methods

In order to accurately investigate the presence of a linear relationship between genera abundance and area for assessment of the assumption of neutrality, the samples collected must belong to the same community. A lateral sampling scheme, collecting samples from a single bedding plane, insures that each sample set has been collected from a single community. Two samples, one of 0.5m² and one of 1.0 m², were collected along each of the two bedding planes (for a total of four samples.) Areas 1A and 1B are 0.5m², and correspond to areas 2A and 2B, 1.0 m² respectively (Figure 3).

It is important to limit the distance between sample sites of the same bedding plane, even if the bedding plane is easily detectable for many meters. In order to avoid habitat patchiness which would result in sampling error, corresponding sites of increasing area should be within close proximity to one another, and some continuity of the community between sites must be established. Sample sets 1 and 2 are 10.1m and 9.5m apart respectively. Likewise, to avoid sampling error resulting from taphonomic (postmortem) transport, sample sites should be located within well established paleocommunities, as opposed to fossiliferous layers accumulated via means of turbidite, sediment gravity flow or other mechanisms. The communities within the Holz Shale have well been established by Sundberg and Cooper (1978) and Sundberg (1980, 1981, 1982, 1993).

All identifiable specimens from each area were counted; specimens were identified in the field and in the laboratory solely by the author to ensure consistent taxonomic identification. Identifications were made to the genus level via comparison with previously identified specimen from Silverado Canyon belonging to the Sundberg Fossil Collection housed at California State University Fullerton, and with plates from Popenoe (1937 and 1940) and Packard (1916 and 1922). For the purpose of the preliminary study, identifications will be made to the genus level because it can be presumed that genera and species populate a community in a similar fashion. If it could be determined that a relationship between area and abundance is evident at the genus level, a more detailed and extensive study may be done at the species level.

Holz Shale Rank Abundance

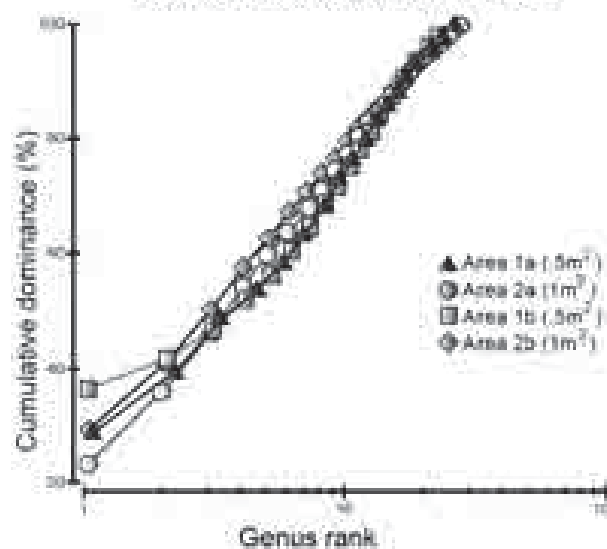


Figure #4: Holz Shale Genera Rank Abundance Curve

When comparing the Rank Abundance curves for each individual sampling areas it is clear that the behaviors of each area's abundance are the same. The genera abundance for each area resembles a linear function, confirming the hypothesis that area and abundance increase in a linear manner.

Figure #5: Potentially neutral species table
 Species belonging to the listed genera generally possess the same life modes and ecology categories.

After identification, a rank abundance curve was generated by plotting the identified genera from each sampling area by that area's cumulative dominance. Statistical similarity of the two sample sets was determined by calculating the Two-Way t-Statistic. Data regarding the paleoecological settings and life modes of specimens were collected via the Paleobiology Database (www.paleodb.org).

Results And Interpretations

With the exception of one genus of Echinodermata (*Hemaster*), two genera of Scaphopoda (*Baculites* and *Dentalium*) and 10 individual samples of bryozoans, the vast majority of specimen collected were gastropods and bivalves. The sum of identifiable specimen from the four sample sites is 710 with sample 1A had a count of 87 specimens, 2A had a count of 270 specimens, 1B had a count of 96 specimens and 2B had a count of 257 specimens. The most abundant genera are the bivalves *Syncyclonema*, *Glycymeris*, and *Parallelodon*.

The rank abundance curve generated by PRIMER (Figure 4) shows a positive correlation and linear relationship between the abundances of genera from each sample site. This indicates that as area increases the abundances of present genera also increase in a linear fashion, supporting the project's hypothesis. In order to show that the relationships between the sample sites are statistically similar, the calculated Two-Way t-Statistic resulted in a p-value of 0.047 indicating positive similarity. This result suggests that the relationship between samples within sites 1 and 2 are more similar to themselves than between the other two sites. The next step in testing the assumption of neutrality is to isolate species that may potentially be considered neutral or interchangeable. In order to be considered potentially neutral, the species must exploit similar resources for nutrients, sunlight, and space. Therefore, potentially neutral species must belong to the same trophic level and employ the same life modes. Based on the paleoecological data collected from the Paleobiology Database, of the 21 collected genera, approximately 62% are epifaunal, living on top of the substrate, 33% of the genera are infaunal, living buried or partially buried in the substrate and

approximately 5% of the genera are nektonic, swimming freely. As an example, of the identified epifauna, 11 genera or 85% are suspensions feeders; congeneric species of these 11 genera are candidates of potential neutrality in future studies. Figure 5 shows the paleoecological data collected for the genera sampled, and highlights genera whose species may be considered neutral.

Discussion And Conclusion

Based on the study's positive results determining the most basic element of the assumption of neutrality, it is reasonable to conduct a more comprehensive study using the sampling scheme and methods devised by this project. Future tests of the assumption of neutrality within UNTB should meet sampling criteria established through this study. As the result of the establishment of a linear relationship between genera abundance and area, future studies should take the effort of locating a sample site with preservation quality allowing for identification to the species level. Identification of fauna to the species level will allow for a test of the concept of species neutrality within the UNTB. To do so, these studies should isolate and compare species belonging to the same genera in the manner shown in Figure 5. Additionally, future sites chosen should select a location large enough to collect three lateral samples per bed, instead of the two lateral samples collected by this study. Having additional sample sites will more accurately show the area versus species abundance relationship, and while statistics will still be a helpful tool in determining the similarity of the populations, more exact interpretations can be made from the raw data.

Acknowledgments

I would like to express my appreciation to Dr. Nicole Bonuso for sending this project my way, and for always providing insightful guidance when I am frustrated and confused; and to Michael Prior for his many hours of field assistance on several relentlessly sunny days.

References

- Cooper, J.D. and Sawlon, M.G., 2006. Evaluation of the Irvine Ranch Land Reserve Potential National Natural Landmark of Orange County for its representation of Continental Margin Geologic History of the South Pacific Border Province, p. 86-121.
- Cooper, J.D. and Sundberg F.A., 1978, Late Cretaceous Environments, Northern Santa Ana Mountains, Southern California, p. 535-546.
- Hubbell, S. P., 2001, A Unified Theory of Biodiversity and Biogeography; Princeton University Press, Princeton.
- Packard, E. L., 1916. Faunal studies in the Cretaceous of the Santa Ana Mountains of Southern California, University of California Publishing Bulletin, Department of Geological Sciences, v. 9, p.379-402.
- Packard, E. L., 1922, New Species from the Cretaceous of the Santa Ana Mountains, California, University of California Publishing Bulletin, Department of Geological Sciences, v. 13, p.413-462.
- Popenoe, W.P., 1937, Upper Cretaceous Mollusca from Southern California. Journal of Paleontology, V.11-5, p.379-402.
- Popenoe, W.P., 1942, Upper Cretaceous Formations and Faunas of Southern California, Bulletin of the American Association of Petroleum Geologists, v. 26-2, p.1 62-178.
- Sundberg, F.A. 1980, Late Cretaceous Paleoecology of the Holz Shale, Orange County, California. Journal of Paleontology, v. 54-4, p. 840-857.
- Sundberg, F.A. 1981, Cretaceous Lithophaga (Mollusca: Bivalvia) from the West Coast of North America. Journal of Paleontology, v. 55-4, p. 901-902.
- Sundberg, F.A. 1982, Late Cretaceous Paleoenvironments and Paleoecology of the Santa Ana Mountains, Orange County, California, p. 59-67.
- Sundberg, F.A. 1993, Coniacian and Santonian (Upper Cretaceous) Paleontology and Paleoenvironments of the Santa Ana Mountains, in Dunn G. and McDougall, K., eds. Mesozoic Paleogeography of the Western United States-II Pacific Section SEPM, Book 71, p. 187-196.

Incised River Meanders in western and northwestern Thailand: Implications for the late Cenozoic regional tectonics of northwestern Indochina

Department of Geological Sciences, California State University, Fullerton, CA, USA

Angela Perez
Advisor: Dr. Brady Rhodes

Abstract

Incised meanders form only rarely when a sinuous stream develops upon a low-gradient floodplain and then subsequently incises its bed into the underlying bedrock without readjusting its channel, resulting in a sinuous river lying within a canyon (Rogers, 2002). In Thailand, little is known about the distribution and characteristics of incised meanders. Incised meanders may help researchers understand the region's late-Tertiary tectonic history, which currently contains gaps in knowledge between the late Miocene to the early Pliocene due to lack of sedimentary rocks and datable events (Morley, 2002). Huai Mae Sa, Huai Mae Ya and Mae Nam Khong are streams with incised meanders that were studied in northern Thailand to test the hypothesis that uplift, followed by erosion, created the dense drainage networks and rugged terrain seen today. Results show that changes in sinuosity and gradient, with no accompanying changes in bedrock, suggests relic streams have been rejuvenated through migration of knick points caused by a change in local base level. The streams examined here have profiles that fit our idea of how knick points contribute to the incision. The data suggests that the sinuosity of the streams is not caused by landslides or differences in bedrock erosional resistance. I suggest that the geomorphology of these incised meanders may fill a gap in our knowledge of Thailand's late Cenozoic tectonic history and that these relic older streams formed during a late Miocene to Pliocene tectonic quiescence and were rejuvenated during Pliocene to Holocene time.

Introduction

Northern Thailand lies in northwestern Indochina, southeast of the Himalayan Mountains. Beginning ~40 my ago, the Himalayan Mountains began to rise as the Indian plate started to collide with mainland Asia; this on-going collision caused the Indochina region to move to the Southeast and rotate clockwise from the Himalayan Mountains along several strike-slip faults. During this time, east-west extension resulted in the opening of intra-continental rift basins in northern Thailand (Morley, 2002). These basins are elongated on a north-south trend and vary in size (Rhodes, 2005). Basins in this area were formed over folded Paleozoic and Mesozoic rocks and were reoriented by faulting during

the Oligocene to early mid-Miocene (Morley, 2001). Numerous faults cut northern Thailand, slicing both the Pre-Tertiary rocks and Tertiary basins. The pre-basin structural grain and younger faults and basins contribute to Thailand's distinctive physiography (Rhodes, 2004). One enigmatic feature of Thailand's physiography is the existence of incised meandering streams.



Figure 1: Map of Thailand with respect to the Himalayan Mountain Ranges. Thailand is southeast of the ranges and has been greatly affected by India's collision with mainland Asia (maps.google.com).

Meandering streams that have eroded their channels downward, cutting deep into the underlying bedrock, are known as incised meanders. Typically an incised meandering stream is low gradient, sinuous, and has a deep incision into a resistant (normally bedrock) base (Rogers, 2002). Alluvial erosion coupled with tectonics is the main cause of incised meanders. Incision may be caused by regional uplift coupled with little to no tilting, forcing the stream to cut down in order to readjust to a new, lower local base level. The

amount of incision into the underlying bedrock is controlled mostly by the degree of base level change, resulting in steepened gradients, and therefore increased stream power (Limarino, 2001). As the base level lowers, the gradient becomes steeper and the stream power increases allowing the river to incise toward base level. Studies on these rivers have shown a steady-state relationship between uplift and erosion due to slope and stream velocity changes (Aswathy, 2008).

However, heterogeneous bedrock may be a confounding factor, forcing the stream to take the path of least resistance. This may cause the stream to meander through the less resistant bedrock forming a sinuous path. Understanding the existing bedrock type underlying a river is imperative when assessing the cause of its sinuous channel. Deflections in the pathway of the stream caused by such things as active strike-slip faults, landslides and man-made obstructions might also cause a sinuous pattern (Rhodes, 2004).



Figure 2: Shaded relief map of Thailand. Many of the smaller streams that drain the mountains west and north of Chiang Mai have segments with incised meanders. These are located in the Pai Drainage Basin, as shown on the map, and will be the focus of the project (maps.google.com).

Spectacular examples of incised meanders occur mostly in desert areas, such as the Colorado Plateau in the Southwestern U.S. (Harden, 1990) and the Pannagon River in India (Aswathy, 2008). Both rivers show similar incision as the meanders that have been described in Western Thailand (Rhodes, 2004); however, they are not in a tropical setting covered by vegetation which makes their incision more visible. Reconnaissance analysis of LandSat images located several examples of incised meanders occurring in tributaries of the Pai River, northwest of Chiang Mai, in Northwestern Thailand (Figure 1).

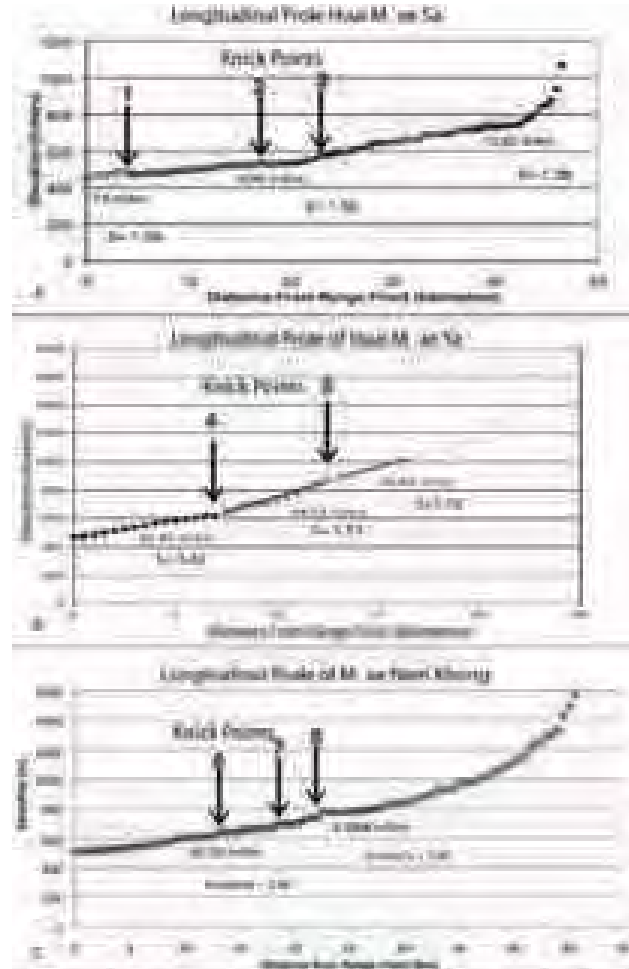


Figure 3(A-C): Longitudinal Profiles of stated river. Here we found points along the graph that were higher than would be suspected. These points are termed knick points and occur when there is a negative change in base level and rivers become rejuvenated. In some instances, the gradient levels change which in turn changes the sinuosity of the rivers.

Little is known about the distribution and characteristics of incised meanders in northern Thailand. The existence of the meandering channels may have significant implications for late Tertiary tectonic history of this area. A gap in knowledge between the late Miocene to the early Pliocene (late Tertiary) in northern and western Thailand exists due to the lack of late-Tertiary sedimentary rocks in the area (Morley, 2002). Incised meanders, if they formed during this time period, may help in the understanding of the region's late-Tertiary history.

The goal of this study is to analyze the relationship between incised meanders of northern and western Thailand and the record of regional uplift in Pliocene to Holocene time (less than 5 Ma). The study will also illuminate the developmental process of meandering stream formation, rejuvenation of relic meandering streams and formation of incision. The relationship and distribution of these developmental processes will further enable an increased understanding of regional tectonics. Results from this project may lift constraints on our understanding of the regions tectonic response to the ongoing Himalayan collision.

Model Demonstrating Knick Point Formation and Activity

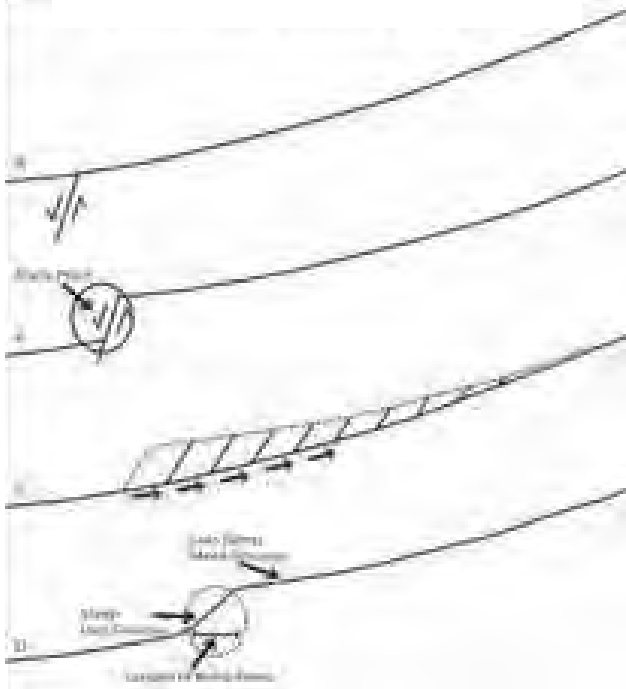


Figure 4: Longitudinal models of incised meanders containing knick points. Sketch A is a depiction of a meandering stream before displacement occurs. Sketch B displays the effects of uplift and creation of a knick point on a stream profile. Once displacement occurs, the knick point continues to cut back into the river creating an incision as shown in Sketch C. Each of the rivers explored contain a profile that now resembles Sketch D. Here we see the knick point has created a steep, less sinuous stretch in front of it and a less steep, more sinuous reach behind it.

Methods

Using satellite imagery, the locations of the incised meanders on Google Earth base maps were used to calculate stream gradient, and sinuosity. Stream gradient is the downstream slope measured by dividing the river length by the elevation drop, thereby producing a longitudinal profile. The elevation data were collected directly

from Google Earth by hovering the mouse over the stream channel. The accuracy of the elevations was verified from an overlain scan of a 1:50,000 scale topographic map. Plotting elevation data for every half-kilometer provides a detailed look at the stream's profile. Due to the imprecision of elevation data in Google Earth the profiles are not perfectly smooth, however they still provide sufficient information to be able to draw some significant conclusions.

Sinuosity was calculated by dividing channel length by valley length as measured on the 1:50,000 scale topographic maps. The channel length is the distance of the river measured down the centerline of the channel. The valley length is the distance down the centerline of the valley through which the river meanders. A straight channel will have the same length as its valley and therefore a sinuosity of 1. Streams with a sinuosity >1.5 are considered sinuous (Harden 1990). In order to evaluate the relationship between channel sinuosity and underlying geology, a map of the stream channels was digitally overlain on a geologic map (Hess, 1979). Selected streams were visited in the field in order to qualitatively verify that the streams had bedrock channels, and to verify the underlying rock type.

Simplified Geology of the Pai Drainage Basin



Figure 5: The incised meandering streams illustrated here will be the main focus for this project. Mae Man Khong, Huai Mae Sa and Huai Mae Ya are believed to have been influenced by surrounding tectonic activity. Their position of the knick points noted in Figure 2(A-C) are displayed here.

Results/Discussion

The longitudinal profiles of Huai Mae Sa, Huai Mae Ya and Mae Nam Khong were examined and each contain key areas in which there is an abrupt change in their gradient (Figures 3A-C). These changes are what I have interpreted to be knick points. When the base level of a stream changes due to uplift or a drop it causes the river to incise in order to maintain the same base level, resulting in a knick point (Figure 4). When the lower reaches of a meandering stream crosses an active fault, a knick point is formed in the channel at the fault. The knick point erodes headward up the channel. As this migration continues, the channel increases its gradient downstream of the knick point, destroying meanders whereas the channel upstream of the knick point remains unchanged (Humphrey, 2000). Figure 4 is a basic model demonstrating a normal fault crossing a stream and causing a local base-level drop. The area downstream of the knick point is rejuvenated and tends to be less sinuous as the channel adjusts to the new base level. The change in sinuosity and gradient, with no obvious changes in the underlying rock-type across the knick point suggests the knick point is caused by rejuvenation, not a contrast in erosional resistance. The knick points are shown on the geologic map of Figure 5.

Huai Mae Sa, located as the southeastern tributary of the Pai River (Figure 5) starts with an elevation of 450 m at the intersection of the river's flood plain and the Pai river and steadily climbs at a 7.6 m/km gradient. A knick point occurs 4 km from the base of the river stretching about 2 km with a 10 m drop in elevation. A second knick point, which doesn't exactly fit our model, occurs at 17 km and extends only .5 km with a 7 m decline in elevation. A third knick point occurs at 24.5 m from the base that stretches about .5 km with a 9 m drop in elevation. The overall sinuosity for this river is 1.31, however, if you divide up the river's sinuosity its reach of the river downstream of the first knick point is 1.39 and jumps up to 1.55 and then drops back down to 1.38 after the final knick point. At Huai Mae Sa we found changes in the bedrock geology from quaternary alluvium to granitic basement rocks, however, at the knick points of the river the bedrock is only composed of granite.

Huai Mae Ya, located on the eastern side of the Pai River in Figure 5, has its source at 1657 m. Two locations on the profile have a significant abrupt increase elevation that I interpret to be knick points. The first knick point is 7km from the base of the river consists of a 94 m drop in elevation with a 2km length. The second knick point at 13 km from the base has a 79 m drop over 1.5km. A high gradient of 35.07 m/km and a low sinuosity of 1.21 were calculated for the stream as a whole. When dividing the stream up at each knick point, the flood plain has a gradient of 23.40 m/km and a sinuosity of 1.42 followed by a 44.53m/km gradient and 1.13 sinuosity after the first knick point. This section doesn't fit our model, however, the stretch after the second knick point has a sinuosity of 1.16 and a gradient of 38.85 m/km, which is significantly lower than the preceding one and fits our basic model. Bedrock geology at Huai Mae Ya is granitic at the knick point and throughout the entire length of the stream.

Mae Nam Khong, located on the northwestern portion of the Pai drainage basin map (Figure 5), is composed of mostly sandstone and shale. The length of the river is 45.5 km from its source at 1569 m to where it emerges from the Western Ranges at 510 m elevation. It steadily climbs at a gradient of 10.751 m/km with its first knick point at 13.5 km from its intersection with the Pai River. This knick point consists of an 8 m drop over .5 km. The second knick point occurs at 19 km above the intersection, and has a 11 m drop over .5 km. The third knick point, at 22.5 km above the intersection has a drop of 18, over 1.5 km. At the third knick point, the gradient drops significantly from 10.751 to 6.245 and sinuosity increases from 1.39 to 2.0.



Figure 6(A-B): In field photographs taken of large granitic outcrops located within the river channels. The top photograph depicts the sinuous nature of the rivers as well.

These data reveal that Huai Mae Ya and Huai Mae Sa are sinuous rivers which cut through granitic basement rocks (Figure 6 A-B). Bedrock geology at Huai Mae Ya is granitic in composition, at the knick point and throughout the length of the river. The bedrock geology at Huai Mae Sa, shifts from quaternary unconsolidated alluvium to granitic basement rocks at its floodplain and several places in the river; however, at the knick points of the Huai Mae Sa river, the bedrock was composed only of granite. At Mae Nam Khong, the bedrock was composed of mostly sandstone and shale. At each knick point, the bedrock geology remains the same while the sinuosity and gradient levels change. The Huai Mae Ya and Huai Mae Sa rivers contain granitic bedrock which is a much more resistant as compared to Mae Nam Khong's shale/sandstone bedrock. This fact gives substantial evidence for the rejuvenation of preserved streams because the Huai Mae Ya, and Huai Mae Sa rivers have significant sinuosity and gradient change while maintaining the same bedrock composition.

Conclusion

Based on the data discussed above, I make the following conclusions: All three stream contain incised meanders that were created through uplift and erosion during Pliocene to Holocene time. All of these streams have a knick point that match our proposed model for the rejuvenation of relic streams (Figure 4). Here, the migration of knick points is the mechanism for the incision of these rivers. The location of the knick points is unrelated to changes in the underlying bedrock.

Results from this project may prove useful to researchers when selecting sites for future projects in order further increase our knowledge about this gap in rock history. Future work should include further investigation involving different portions of these and other rivers in western and northern Thailand to further substantiate the idea that meandering streams are remnants of older streams that were revived in the uplift of Pliocene to Holocene time.

Acknowledgements

Fieldwork for this research was supported by the Instructionally Related Activities Fund of the CSUF Associated Students via the Environmental Science research in Thailand Program administered by Dr. Richard Deming. Additional funding was received from a Faculty-Student research grant administered by the CSUF Vice President for Academic Affairs. I would like to thank my research advisor Dr. Brady Rhodes, as well as all the faculty members of the Chiang Mai University involved in aiding the completion of this project.

References

- Aswathy, M. , Vijith, H. , & Satheesh, R. (2008). Factors influencing the sinuosity of pannagon river, kottayam, kerala, india: An assessment using remote sensing and gis. *Environmental Monitoring & Assessment*, 138(1-3), 173-180.
- Harden, Deborah. (1990) Controlling Factors in the Distribution and Development of Incised Meanders in the Central Colorado Plateau. *GSA Bulletin*, 102(1) 233-242.
- Hess, A. & Koch, K.E. 1979. Geologic Map of Northern Thailand, Chiang Dao Sheet. Federal Institute for Geosciences and Natural Resources, Germany, 1:250 000.
- Humphrey, N., & Konrad, S. (2000). River incision or diversion in response to bedrock uplift. *Geology [Boulder]*, 28(1), 43-46.
- Limarino, C. , Tripaldi, A. , Re, G. , Net, L. , Marenni, S. , et al. (2001). Tectonic control on the evolution of the fluvial systems of the vinchina formation (miocene), northwestern argentina. *Journal of South American Earth Sciences*, 14(7), 751-762.
- Morley, C. , Woganan, N. , Sankumarn, N. , Hoon, T. , Alief, A. , et al. (2001). Late oligocene-recent stress evolution in rift basins of northern and central thailand; implications for escape tectonics. *Tectonophysics*, 334(2), 115-150.
- Morley, C. (2002). A tectonic model for the tertiary evolution of strike-slip faults and rift basins in se asia. *Tectonophysics*, 347(4), 189-215
- Rhodes, B. P., Charusri, P., Kosuwan, S., Lamjuan, A. (2004), Tertiary Evolution of the Three Pagodas Fault, Western Thailand: in, Wannakao, L., Youngme, W., Srisk, K., and Lertsirivorkul, R., editors, Proceedings of the International Conference on Geology, Geotechnology and Mineral Resources of Indochina, Khon Kaen University, Thailand, p. 498 -505.
- Rhodes, B., Conejo, R., Benchawan, T., Titus, S., Lawson, R., et al. (2005) Palaeocurrents and provenance of the Mae Rim Formation, Northern Thailand: implications for tectonic evolution of the Chiang Mai basin. *Journal of the Geological Society London*. 162(1), 51-63.
- Rogers, R. , Karason, H. , Vander Hilst, R. , et al. (2002) Epeirogenic uplift above a detached slab on northern Central America. *Geological Society of America*. 30(11), 1031-1034.

Mineralogy And Petrography Of The Polymetamorphic Kings Sequence, Lake Kaweah Pendant, West-Central Sierra Nevada Batholith, Ca.

Crystal A. Castellanos
Advisor: Dr. Diane Clemens-Knott

Department of Geological Sciences, California State University, Fullerton, CA, USA

Abstract

The Lake Kaweah pendant, located ~40 km northeast of Visalia, CA in the western Sierra Nevada foothills, is composed predominantly of the Kings Sequence, a Late Triassic to Middle Jurassic marine metasedimentary to calcsilicate unit. Protoliths of the Kings Sequence were deposited in a submarine fan system containing craton-derived sand, silicic volcaniclastic units, silicic tuff, and ash-flow tuff, all interbedded with mudstone, carbonate, and marl (Saleeby et al., 1978). Few petrologic studies of the Kings Sequence have been undertaken, presumably due to its complex metamorphic and deformational history. The goal of the current study is to produce a detailed mineralogic description of the Kings Sequence exposed in the northernmost part of the Lake Kaweah pendant. Preliminary petrographic analysis, coupled with scanning electron microscopy, suggests that mineral assemblages were equilibrated in the greenschist facies then partially re-equilibrated in the hornblende-hornfels facies. The Late Jurassic history of the Kings Sequence was undoubtedly complex, including deformation events associated with convergent margin tectonics as well as metamorphism during construction of a superimposed Late Jurassic arc. The roots of this arc are preserved in the Mill Creek Complex that is represented in the Lake Kaweah pendant by a 163 ± 1.5 Ma quartz diorite pluton surrounded by a tungsten skarn. By ~139 Ma, this portion of the Kings Sequence was exposed at the surface, where it formed the depositional basement for the non-marine Goldstein Peak formation. Both the Kings Sequence and Goldstein Peak formation units were metamorphosed together in the hornblende-hornfels facies during the Early Cretaceous intrusion of the tonalitic to granitic plutons that surround the Lake Kaweah pendant (locally $\sim 115 \pm 5$ Ma).



Author holding a piece of green olivine tremolite picotite-bearing hornfels. The high nickel and chromium contents of this rock identify it as a metamorphosed piece of the Earth's mantle.

The Effect of Barriers on Slip Partitioning in an Upward Branching Fault System

Department of Geological Sciences, California State University, Fullerton, CA, USA

Jennifer Tarnowski
Advisor: Dr. David Oglesby and Dr. David Bowman

Abstract

The finite element method and slip-weakening friction are employed to investigate dynamic rupture propagation on a branched fault system. The system consists of an oblique-normal fault at depth connected to vertical and dipping fault branches ~5km from the surface. The branches accommodate predominately strike-slip and dip-slip motion, respectively. When rupture is nucleated on the fault at depth, dynamic unclamping favors rupture propagation to the vertical fault, with no rupture on the dipping fault. However, when a zone of doubled normal stress, referred to as a "barrier," is located on the vertical fault, rupture is delayed on the vertical fault, causing shear stress to increase and normal stress to decrease along the corresponding area of the dipping fault. Consequently, the dynamic nature of the stresses facilitates slip on both segments. There is a correlation between barrier area and the ease with which an earthquake at depth propagates to both upper branches, suggesting a critical patch size for nucleation on the dipping fault. Due to the fault geometry, the relationship between barrier area and slip magnitude is non-linear. Increasing the slip-weakening distance by a factor of $\sqrt{2}$ necessitates the use of a critical barrier area that is increased by a factor of ~2, which is consistent with the critical patch size relationship (Day, 1982). Further numerical models show that the behavior above is relatively general, and does not require finely-tuned stress and frictional parameters.

Partitioned exhumation and thrust faulting in northern Prince William Sound, south-central Alaska constrained by apatite (U-Th)/He dating

Michael Prior
Advisor: Dr. Phillip A. Armstrong

Department of Geological Sciences, California State University, Fullerton, CA, USA

Abstract

The southern margin of Alaska is an accretionary complex that is being deformed and exhumed in response to shallow subduction of the Yakutat microplate. Widespread deformation of the accretionary prism associated with subduction may be focused within the western Chugach Mountains and northern Prince William Sound (CM-PWS), and accommodated on small-scale faults. Fault locations in northern PWS are poorly constrained by traditional methods as they cut monotonous greywacke and are untraceable beneath glaciers and fiords. Apatite (U-Th)/He ages [AHe] are used to constrain the exhumation history across College and Harriman Fiords and determine background exhumation rates using a 1000 meter elevation transect on Mt Muir. AHe ages across Harriman Fiord and southern College Fiord show little variance, but ages across northern College Fiord are 3.8 and 5.2 Ma on the south and north sides, respectively. This age difference corresponds to a differential exhumation rate of ~190 m/Ma faster on the south side of northern College Fiord, but uniform exhumation along the southern section and Harriman Fiord. The transect displays a zigzag pattern of younger samples above older ones, suggesting two thrust faults displaced rocks with similar thermal histories since ~5 Mya. Faults are north-verging, trend northeast and result in two offsets with displacements of ~375 meters. Faults are observed along the elevation transect suggesting many small thrusts are common within larger deformed blocks. Increased exhumation ~5Mya and thrust faults are likely due to continued subduction of the Yakutat microplate causing widespread deformation throughout the CM and PWS.

Introduction

The southern Alaskan margin represents a long-lived convergent boundary that has recorded a complex history of terrane accretion and subduction throughout the Mesozoic and into the Cenozoic. Currently Alaska is one of the only places in the world where an allochthonous terrane is being actively subducted at a shallow angle beneath a continental margin. Shallow, or flat slab, subduction occurs at ~10% of all subduction zones and develops due to complex interactions between the mantle and slab rheology and the properties

of the overriding plate (van Hunen et al., 2002). The shallow subduction of the Yakutat microplate at approximately 6° causes widespread deformation throughout southern Alaska and represents a unique opportunity to study these processes in an active setting.

In southern Alaska, deformation is focused in the Chugach Mountains close to the collision zone where oblique convergence results in dextral faulting in eastern PWS and compressional regimes in western PWS (Bol and Gibbons, 1992) (Figure 1). Subsidiary faulting is observable over a wide range of scales and has accompanied deformation along major structural boundaries. The amount of deformation accommodated on subsidiary faults within the Chugach Mountains and northern Prince William Sound is largely unknown, which may influence how this actively deforming orogen is developing in response to compressive stress. Determining the relationship between these structures, and the history of displacement along them, is a crucial question in Alaskan tectonics.

Previous studies have focused on major structural boundaries such as the Border Ranges fault zone (Little and Naeser, 1989), Contact fault (Enkelmann et al., 2008; Bol and Gibbons, 1992), and the areas outside of the Alaskan syntaxis (Buscher et al., 2008), but little has been done to assess subsidiary faulting within the CM and PWS and the part they play in accommodating strain associated with shallow subduction. While major structures have obvious importance, a complete picture of shallow subduction needs to account for extensive subsidiary faulting that may accommodate large amounts of distributed strain. Several questions related to the history of subsidiary faults may be answered by collecting a suite of samples for thermochronometric analysis. By utilizing the low closure temperature of the apatite helium system (~70 °C) (Wolf et al., 1996) the locations of inferred faults, timing and amount of recent exhumation accommodated along them, and interaction with larger structures may be addressed. Determining if small-scale faults play an important role in the exhumation of the Chugach Mountains and northern PWS will help create a more complete picture of orogenic development along continental margins undergoing active shallow subduction.

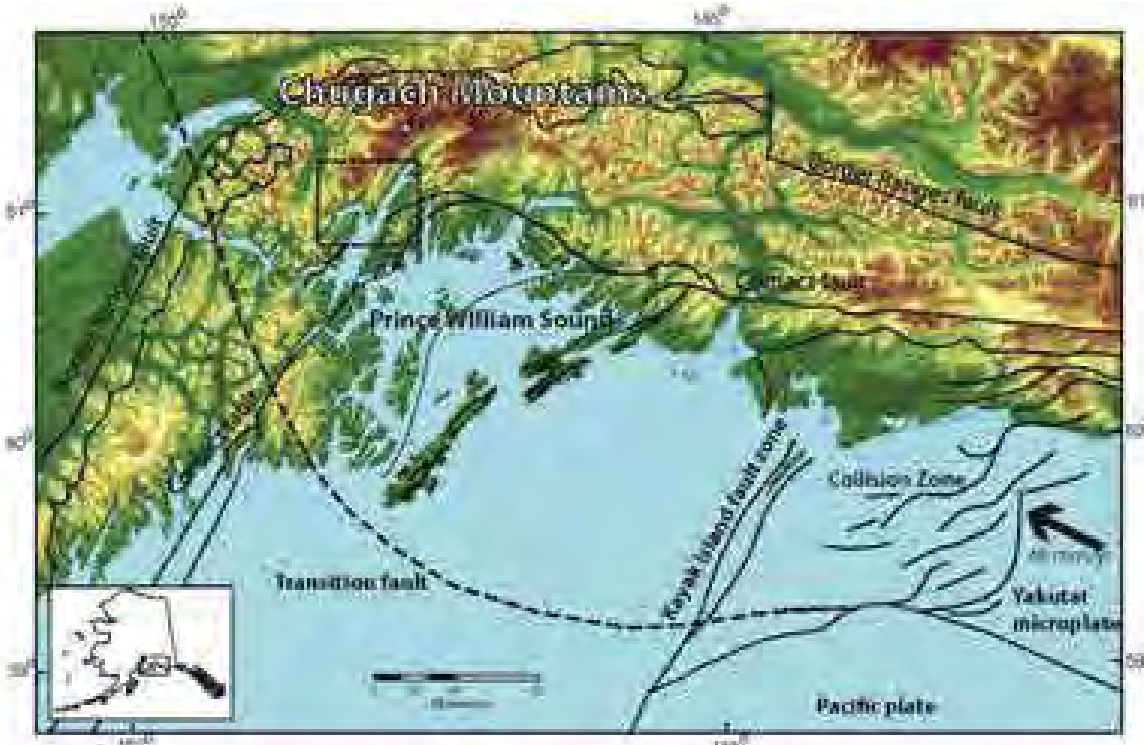


Figure 1: The Chugach Mountains and Prince William Sound are located along the south-central coast of Alaska (shown on inset map), where high relief and precipitation resulted in extensive Cenozoic glaciation. The rugged topography developed under the influence of shallow subduction of the Yakutat microplate, which causes widespread deformation throughout southern Alaska. Extensive faulting within PWS is inferred by the geomorphic expression of fjords and glaciers that follow the structural grain of major faults like the Contact fault and Border Ranges fault. Exhumation along subsidiary faults is poorly constrained due to the scarcity of marker units and the monotonous lithology. Mt Marcus Baker is shown by the triangle and the dashed box shows the location of Figure 2.

Geologic Setting

The Chugach Mountains are located at approximately 61 N°/147° W at the center of the southern Alaska syntaxis where elevation rises abruptly from sea level in western Prince William Sound to 4,016 meters at Mt. Marcus Baker, only twenty kilometers away. The dramatic topography of southern Alaska has formed from a combination of energetic plate interactions deforming and uplifting rock, and extensive Cenozoic glaciation dissecting this topography into rugged peaks and valleys (Péwé, 1975). Exhumation and deformation in the western Chugach Mountains (CM) and northern Prince William Sound (PWS) is caused by shallow subduction of the buoyant Yakutat microplate beneath a series of allochthonous terranes that have been accreted to the North American continent in the last 230 million years (Plafker et al., 1994). The Wrangellia Composite terrane is bound to the north by the Denali fault and to the south by the Border Ranges fault zone (BRFZ), and has acted as the accretionary surface for the Southern Composite terrane

that consists of the Cretaceous Chugach terrane and the Paleocene Prince William terrane (Plafker et al., 1994). The Valdez Group sandstone of the Chugach terrane is the predominant lithology exposed in Prince William Sound where it forms resistant outcrops and high relief within the sampling area. The Yakutat microplate is located east of the dextral Fairweather Fault and west of the Kayak Island Fault Zone (Plafker et al., 1989). To the south the Transition Fault separates the Yakutat microplate from the Pacific Plate (Plafker et al., 1989). Geophysical studies by Christeson et al., (2010) indicate that the Yakutat has crustal thicknesses 24-27 km, whereas normal oceanic crust of the Pacific Plate is 5.0-5.5 km. The nearly vertical Transition Fault juxtaposes basalts of the Yakutat and those of the Pacific Plate that are 15-30 Ma younger. This dramatic difference in age and thickness suggests that the Yakutat originated as an oceanic plateau, possibly near a spreading center, and was subsequently translated north on strike-slip faults (Christeson et al., 2010).

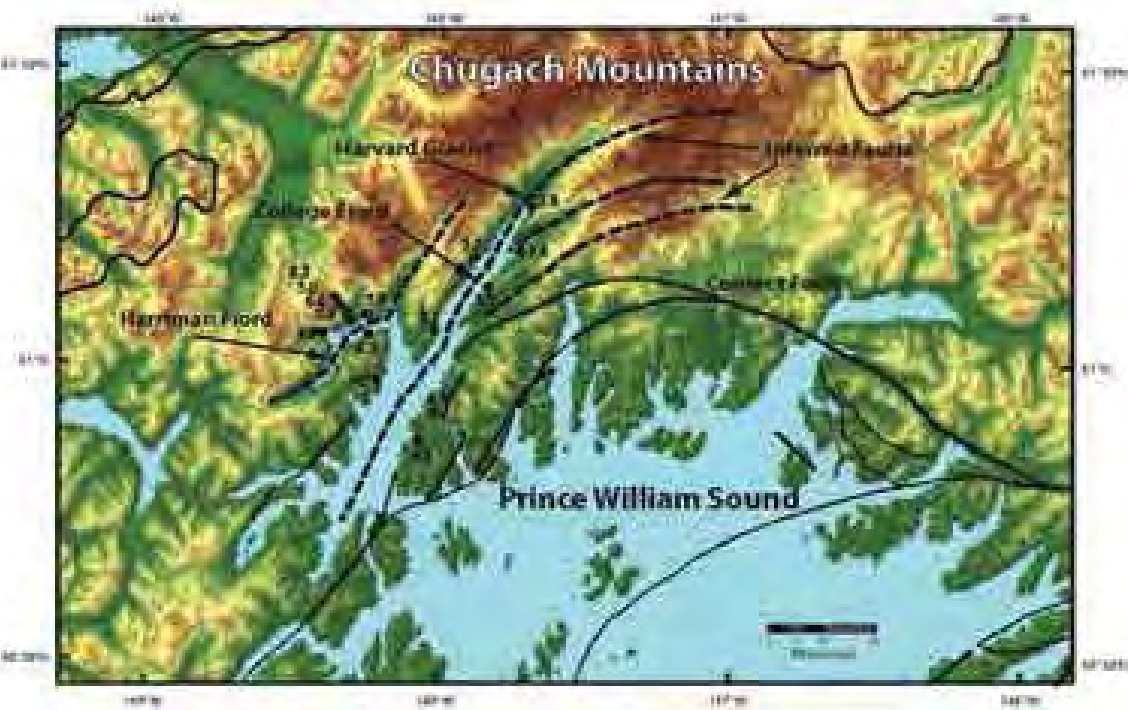


Figure 2: Map showing locations of AHe samples and inferred faults within College and Harriman Fiords. Sample locations cover the area across inferred faults (dashed lines) within College and Harriman Fiords and include an elevation transect along Mt. Muir. Apatite (U-Th)/He dating was conducted on ten samples and ages were compared across the trend of faults to determine if differential exhumation is accommodated along these subsidiary structures. AHe ages (shown on the map in Ma) generally decrease northward towards the core of the Chugach Mountains, and display little difference across Harriman Fjord and southern College Fjord.

Yakutat microplate subduction began during the Late Oligocene (~25 Ma), and subducts at ~ 6° beneath the North American Plate (Eberhart-Phillips et al., 2006). The subducted portion of the Yakutat microplate extends as far north as the Denali fault, causing widespread deformation within central Alaska and as far inland as the Canadian Cordillera (Haeussler, 2008; Mazzotti and Hyndman, 2002). Currently the Yakutat microplate is also being underplated beneath southern Alaska and accounts for large influxes of rock into the accretionary prism, which are potentially balanced by localized exhumation within the CM-PWS region (Bol and Gibbons, 1992). Contractual strain in northern PWS, due to orthogonal convergence, is expressed by reverse faults and parallel folding that occurs south of the Border Ranges fault. South verging asymmetrical folding is also abundant due to underplating of accreted material south of the Border Ranges fault (Bol and Gibbons, 1992).

Inferred Faults

The presence of inferred faults within northern PWS is based on the geomorphic expression of College and Harriman fiords and the current trend of large tidewater glaciers such as Harvard, Yale, Barry, and Harriman Glaciers, which suggests that faults have acted as a structural control on Cenozoic glaciation within the region (Figure 2). Trend of the fiords follows the structural grain of the Contact and Border Ranges faults, which trend N40E but bend nearly 90° clockwise in the syntactical region of the Chugach Mountains. The combined effects of oroclinial folding and oblique subduction of the Yakutat microplate resulted in the extreme relief of the western Chugach Mountains. Orographic effects during uplift of the CM caused extensive glaciation (Pewe, 1975), which allowed mountain, valley, and tidewater glaciers to shape the topography into rugged peaks cut by steep valleys and fiords. Together these observations are consistent with faults controlling the trend of glaciers, and being potential structures that could accommodate exhumation.

Mt. Muir Elevation Transect

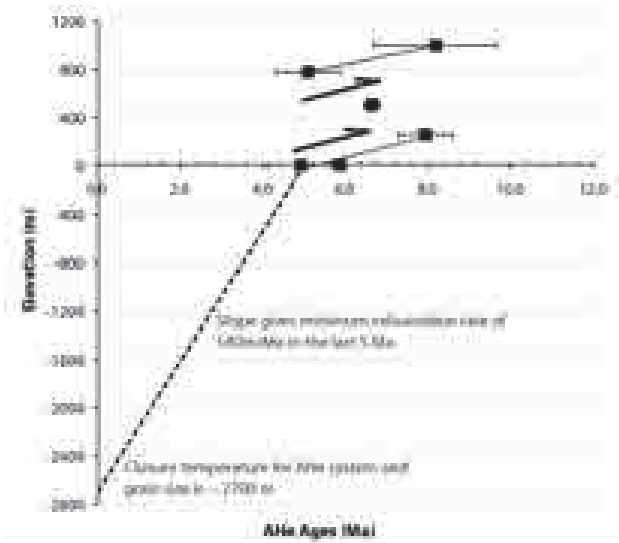


Figure 3: Apatite helium age versus elevation plot for Mt. Muir transect. Note the zigzag pattern of ages and the similarity of the increasing gradients between the lower three samples and the upper two samples. The similarity of these gradients suggests these age sets were at similar depths and temperatures prior to thrusting (shown in bold arrows). The dashed line shows the minimum slope (exhumation rate) by connecting the youngest age with predicted closure temperature depth (2700 m).

Methods

(U-Th)/He Thermochronometry using Apatite

(U-Th)/He dating is based on the retention of α particles (${}^4\text{He}$) produced by the decay of ${}^{238}\text{U}$, ${}^{235}\text{U}$, ${}^{232}\text{Th}$, and ${}^{147}\text{Sm}$. The amount of helium retained is directly related to the time spent below the closure temperature, allowing the system to act as a chronometer. At geologic timescales radiogenic helium completely diffuses from the crystal structure of apatite above $\sim 70^\circ \text{C}$ and is completely retained below $\sim 40^\circ \text{C}$ (Ehlers and Farley, 2002). Helium is partially retained between these temperatures. The transition from partial to complete retention is not a specific temperature because the time spent in the partial retention zone (PRZ) influences the retentivity. However, at relatively rapid cooling rates the concept of a closure temperature can be applied (Reiners and Brandon, 2006). Assuming a monotonic cooling rate of $10^\circ \text{C}/\text{Myr}$, the closure temperature for AHe dating is $\sim 70^\circ \text{C}$ (Wolf et al., 1996), which allows interpretation of shallow crustal processes. The closure temperature is also a function of the grain size because the apatite crystal itself is the diffusion domain (Farley, 2000). If an average surface temperature of 0°C and an average geothermal gradient of $\sim 23^\circ \text{C}$ from the Cook Inlet Basin (Magoon, 1986) are assumed, then cooling paths can be constrained to a depth of 2.7 km. At this depth AHe ages are

effectively zero, because at geologic time scales all radiogenic helium is diffused as fast as it is produced. By coupling a specific depth with a zero age, (U-Th)/He dating can be applied to calculate rates of exhumation based on the produced AHe ages. The average grain width of samples collected corresponds to a half-prism dimension of $44.5 \mu\text{m}$, which assuming a cooling rate of $10^\circ \text{C}/\text{Myr}$, corresponds to a closure temperature of $\sim 62^\circ \text{C}$ (Farley, 2000).

Apatite grains used in analysis need to be euhedral, and free of high U and Th inclusions such as zircon and monazite (Ehlers and Farley 2002). Zircon is not dissolved by nitric acid (HNO_3) and therefore the helium contributed by inclusions will not have parent isotopes that are measured, resulting in erroneously old ages. Due to kinetic energy, α particles (${}^4\text{He}$) can travel up to $20 \mu\text{m}$ within a crystal lattice and will be ejected if they are near crystal edges. Ejected α particles result in erroneously young ages as a portion of the U and Th concentrations measured will be daughterless isotopes. To account for ejected alpha particles, raw AHe ages are corrected with an α -correction factor (F_α) (Farley, 1996). F_α is a function of the crystal width and the ideal geometry, which closely approximates the euhedral hexagonal prism (Ehlers and Farley, 2002). The geometry of extensively fragmented or rounded grains does not allow for a simple correction factor (Ehlers and Farley, 2002), therefore selection of euhedral grains is preferred. The quality of apatite yielded is dictated by the lithology available for sampling; the number of acceptable grains is limited in clastic sediments due to rounding and fragmentation, while igneous samples contain more euhedral grains.

The helium concentration of each apatite grain is measured by heating the samples with a Q-switched Nd-YAG laser to completely diffuse all radiogenic helium. Diffused helium is purified, a ${}^3\text{He}$ spike is introduced, and the ${}^4\text{He}/{}^3\text{He}$ ratio is measured in the mass spectrometer. ${}^{238}\text{U}$, ${}^{235}\text{U}$, ${}^{232}\text{Th}$, and ${}^{147}\text{Sm}$ concentrations are determined by dissolving each grain in HNO_3 and running the solution through an inductively coupled plasma mass spectrometer (IC-PMS). Using known decay constants for ${}^{238}\text{U}$, ${}^{235}\text{U}$ and ${}^{232}\text{Th}$ and the ratio of ${}^{238}\text{U} / {}^{235}\text{U}$, initial concentrations can be found and used to calculate the time by solving the following equation for (t) (Wolf et al., 1996).

$${}^4\text{He} = [8 \times {}^{238}\text{U} (e^{\lambda {}^{238}t} - 1)] + [7 \times {}^{238}\text{U} / 137.88 (e^{\lambda {}^{235}t} - 1)] + [6 \times {}^{232}\text{Th} (e^{\lambda {}^{232}t} - 1)]$$

$$137.88 = \text{present day ratio of } {}^{238}\text{U} / {}^{235}\text{U}$$

λ = decay constants*

t = helium age

${}^4\text{He}$, ${}^{238}\text{U}$, ${}^{235}\text{U}$ = measured concentrations of isotopes

*Constants account for number of α particles produced in each decay series

Results

AHe Ages

Grain ages were averaged to produce ten sample ages that range from 3.8–8.2 Ma, with an average age of 5.3 Ma for samples collected at sea level. Five samples previously collected by Arkle et al., (2010) are included in the mapped sample locations. The youngest AHe age of the new samples is 3.8 Ma from at the terminus of Harvard Glacier, which is also the northernmost sample and closest to the core of the Chugach Mountains. The highest elevation transect sample has the oldest age of 8.2 Ma, whereas the oldest sea level sample has an age of 6.4 Ma.

AHe ages on the SE side of College Fiord decrease from ~4.8 Ma northward toward the core of the CM to 3.7-3.8 Ma (Figure 2). Ages on the west side of College Fiord are older at 5.1-5.2 Ma and show relatively little northward change. The largest difference in AHe ages perpendicular to the trend of College and Harriman Fiords is observed in the northern reach of College Fiord where ages are ~3.8 and 5.2 Ma on the southeast and northwest sides respectively. Along southern College Fiord, AHe ages are essentially the same, with ages of 4.7 Ma and 4.8 Ma on the southeast side and 4.7 Ma on the northwest side. Across Harriman Fiord, the AHe ages display little variation; the closest samples have ages of 4.9 and 5.9 Ma on the northern side and 6.3, 5.1, and 4.7 Ma on the southern side.

Six samples were collected from the northwest side of Harriman Fiord on Mt. Muir to determine background exhumation rates in northern PWS. Four high-elevation samples (253, 503, 778, and 1000 m) and two sea level samples from opposite sides of the transect trend were collected (Figure 2). The age-elevation plot (Figure 3) shows the lowest elevation (0 m) samples with ages of 4.9-5.9 Ma. Ages increase to 7.9 Ma at 253 m, but decreases further up section to 6.5 Ma at 503 m and 5.1 at 750 m. Above 750 m AHe age increases to 8.2 Ma at 1000 m. This zigzag pattern is not the normal pattern expected from an elevation transect; normally AHe ages become progressively older at higher elevations. The two highest and the three lowest elevation samples define two parallel age profiles (Figure 3). Error bars do not overlap between samples in a single age profile, but do show a similar range in each profile. This suggests the AHe ages are not scatter, and may be due to fault activity.

Interpretations

Exhumation Rate and Timing

Calculations of exhumation rates are based on the AHe ages, assuming an average surface temperature of 0° C and a closure temperature of 62° C. These temperatures correspond to depth of ~2.7 km using a geothermal gradient of 23 °C/km from the Cook Inlet Basin (Magoon, 1986). Exhumation rates are assumed to have persisted from 5 Ma since the Transition Fault became locked (Eberhart-Phillips et al., 2006). Beginning as early as 5 Mya a period of exhumation at a minimum rate of 540 m/Myr is required to project the age profile to the closure depth (Figure 3). Based on the age profile slopes, exhumation rates prior to 5 Ma are 90 m/Myr and 72 m/Myr for the lowest and highest segments, respectively. Thrusting postdates this initial period of slower exhumation and is younger than the displaced age profiles that include ages of ~5 Ma. A previously slower exhumation rate, which increased in the last 5 Mya, is consistent with continued contractional strain related to subduction and the interpretation that focused exhumation shifted northward towards the core of the Chugach Mountains.

Fault Throw Across College Fiord

The Contact fault has reverse displacement within western PWS where the fault trend is orthogonal to motion of the Yakutat microplate (Bol and Gibbons, 1992). AHe ages are younger by a factor of two on the northwest side of the Contact fault relative to the southeast side. Reverse displacement and distinctly younger AHe ages are expected to be present along faults in College and Harriman Fiords based on their proximity to the Contact fault and their similar trend. The northern section of College Fiord exhibits the largest difference in AHe ages, with ages on the northwest and southeast sides of 5.2 and 3.8 Ma, respectively. This age difference corresponds to a 190-m/Myr difference in exhumation rate. Assuming differential exhumation began 5

Mya, a throw of ~955 m (south side up) is computed across northern College Fiord. The southern College Fiord and Harriman Fiord have essentially no difference in age and therefore no difference in exhumation rate and magnitude. These throw calculations suggest a complex history of movement along inferred faults within northern Prince William Sound. The northern section of College Fiord is closest to the hypothesized locus of exhumation at the core of the Chugach Mountains (Arkle et al., 2010), which may influence exhumation along this section and produce the asymmetrical pattern

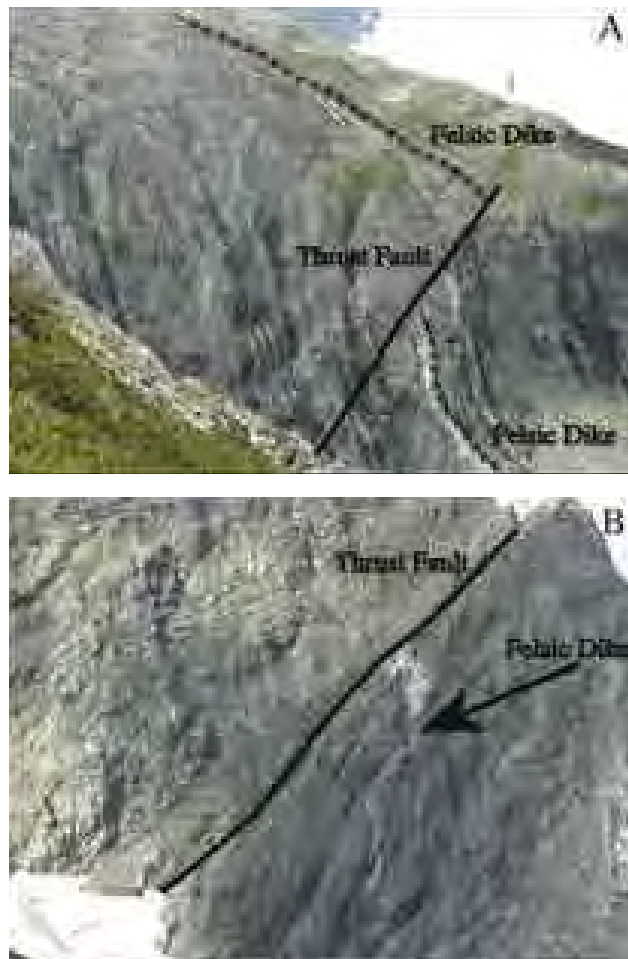


Figure 4: Field photos showing faults offsetting light-colored felsic dikes. These thrusts dip south and are roughly parallel to bedding within the Valdez Group sandstone. Photo A shows an offset dike that continues up the slope above the fault. The dike in Photo B is cut by a fault and has no visible continuation. The abundance of these faults indicates that strain is widely distributed in PWS along many smaller structures. Photos by Peter Haussler.

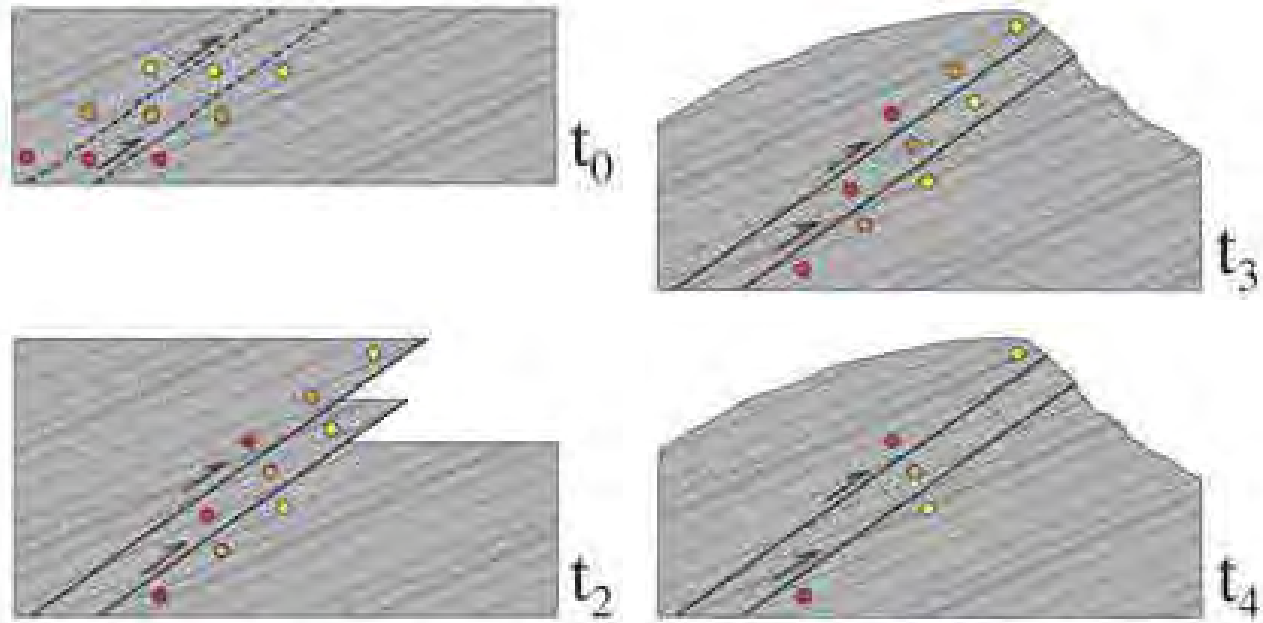


Figure 5: Schematic cross sections showing interpretation of how thrust faults offset and stack packages of rock with younger AHe ages on top of rocks with older AHe ages. Progressive deformation of the accretionary prism is shown in time slices beginning at t_0 when rocks are undeformed above the closure temperature. The rocks are offset by an initial thrust at t_1 , followed by a second fault at t_2 . At t_3 a simplified topography is shown with the current fault geometry. Different shapes represent samples with different cooling ages and outlined shapes at t_3 designate uncollected samples.

of AHe ages. The northward decrease in AHe ages on the southeast side of College Fiord and the lack of AHe age change on the northwest side suggests that differential rock uplift may be partitioned along a potential fault in College Fiord; the southeast side of College Fiord may have been uplifted and exhumed more rapidly along its northern reach than along its southern reach.

Thrust Faulting

The decrease in AHe age with elevation increase is opposite of the expected pattern and suggests that ages are displaced from their original positions. The zigzag pattern of AHe ages in the elevation profile suggests that at least two thrust faults displaced samples with similar ages on top of one another, resulting in younger ages at higher elevations (Figure 3). Error bars do not overlap and make it unlikely that age scatter produces the observed pattern. The similarity in exhumation rates given by two age-elevation profiles suggests that these samples experienced a similar thermal history and subsequently were displaced

by thrusting. Haeussler et al., (2008) document a similar pattern of cooling ages in the Tordillo Mountains ~ 230 km northwest in the Alaska Range, which they attribute to thrust faults. Previously unidentified thrust faults were observed on the Mt. Muir elevation transect. These south-dipping thrusts displace light-colored felsic dikes that serve as marker units (Figure 4). The Valdez Sandstone consists of monotonous sequences of greywacke and slaty argillite that dip roughly parallel to the faults, which makes identification of faults difficult in the absence of marker units. A model using two north-verging thrust faults was employed to explain the zigzag pattern of elevation transect ages (Figure 5). In this model the first fault offsets the higher elevation age profile and the second fault slips in-sequence to displace the 503 m sample above the low elevation profile. After age profiles are displaced on top of each other the rock is sampled, and AHe ages produce the zigzag pattern observed in the elevation transect (Figure 3). Based on the age distribution, offset on the faults is ~375 m, which may be accomplished with relatively small displacements due to the steeply dipping faults shown in Figure 4.

Discussion

Detailed sampling within the CM-PWS has provided a more complete picture of how the accretionary wedge has been deformed by shallow subduction in the late Cenozoic. Determination of the subsidiary faults contribution to strain accommodation and related uplift/exhumation within the Chugach Mountain helps constrain the style of deformation in the area. For the last ~5 Ma, exhumation has been greatest at the core of the Chugach (Arkle et al., 2010) and primarily focused between the major structural boundaries. The results demonstrate that deformation and exhumation within the Chugach Mountains and northern Prince William Sound is broadly distributed on subsidiary faults between these major structures. Most large-magnitude differential exhumation appears to occur across major faults such as the Contact fault (Arkle et al., 2010); however smaller thrust faults may control the trend of glaciers and fiords. The difference in AHe age along the northeast trend of College Fiord may reflect the gradual migration of rapid exhumation towards the core of the Chugach Mountains and away from Harriman and southern College Fiord.

Thrust faulting on Mt. Muir, expressed in the age-elevation relationships, is an example of the complex regime of faulting and deformation within the accretionary prism. Based on the age-elevation relationships of the Mt Muir transect, it is possible that thrust faults have displaced rocks with similar cooling histories after a period of slow exhumation. Since 5 Ma, exhumation related to overall rock uplift increased and thrusting displaced the age profiles. An increased rate of exhumation in the last 5 Ma combined with thrust faulting indicates there has been a substantial increase in strain related to the shallow subduction of the Yakutat microplate. This strain has been distributed across many small-scale faults, which enhanced uplift/exhumation toward the core of the CM, but between the major bounding structures. By using low temperature thermochronology it is possible to identify structures that are poorly constrained by other observational methods. Characterizing different contractional and exhumation regimes along small-scale faults in the Chugach Mountains and northern Prince William Sound reflects how continued Yakutat microplate collision and subduction has shaped southern Alaska.

Acknowledgements

I would like to thank Phil Armstrong for the amazing opportunity to conduct research in Alaska and for his constant support and guidance throughout my geologic education; Jenny Arkle for ever-present lab assistance and valuable geologic discussions; Jade Brush and Peter Haeussler for making sampling possible and thoroughly enjoyable.

References

- Arkle, J.C., Armstrong, P.A., Haeussler, P.J., 2010, Focused exhumation in the southern Alaska syntaxis: Thermo 2010, 12th International Conference on Thermochronology, p. 224.
- Bol, A.J. and Gibbons, H., 1992, Tectonic implications of out-of-sequence faults in an accretionary prism, Prince William Sound, Alaska: *Tectonics* v. 11, p. 1288-1300.
- Buscher, J.T., Berger, A.V., and Spotila, J.A., 2008, Exhumation in the Chugach-Kenai Mountain Belt above the Aleutian Subduction Zone, southern Alaska: in Freymueller, J.T., Haeussler, P.J., Wesson, R.L., and Ekström, G. (eds.), *Active tectonics and seismic potential of Alaska*, American Geophysical Union Monograph Series 179, p. 151-166
- Christeson, G.L., Gulick, S., van Avendonk, H., Worthington, L.L., Reece, R.S., and Pavlis, T.L., 2010, The Yakutat terrane: Dramatic change in crustal thickness across the Transition fault, Alaska: *Geology*, v. 38, p. 895-898.
- Eberhart-Phillips, D., Christensen, D.H., Brocher, T.M., Hansen, R., Ruppert, N.A., Haeussler, P.J., and Abers, G.A., 2006, Imaging the transition from Aleutian subduction to Yakutat collision in central Alaska, with local earthquakes and active source data: *Journal of Geophysical Research*, v. 111, p. 1-31.
- Ehlers, T.A., and Farley, K.A., 2002, Apatite (U-Th)/He thermochronometry: Methods and applications to problems in tectonic and surface processes: *Earth and Planetary Science Letters* v. 206, p. 1-14.
- Enkelmann, E., Zeitler, P.K., Pavlis, T.L., Garver, J.I., and Ridgeway, K.D., 2009, Intense localized rock uplift and erosion in the St. Elias orogen of Alaska: *Nature Geoscience Letters*.
- Farley, K.A., Wolf, R.A., and Silver, L.T., 1996, The effects of long alpha-stopping distances on (U-Th)/He ages: *Geochimica et Cosmochimica Acta*, v. 60, p. 4223-4229.
- Farley, K.A., 2000, Helium diffusion from apatite: General behavior as illustrated by Durango fluorapatite: *Journal of Geophysical Research*, v. 105, p. 2903-2914.
- Haeussler, P.J., 2008, An overview of the neotectonics of interior Alaska: Far-field deformation from the Yakutat microplate collision: in Freymueller, J.T., Haeussler, P.J., Wesson, R.L., and Ekström, G. (eds.), *Active tectonics and seismic potential of Alaska*, American Geophysical Union Monograph Series 179, p. 83-108.
- Haeussler, P.J., O'Sullivan, P., Berger, A.L., and Spotila, J.A., 2008, Neogene exhumation of the Tordillo Mountains, Alaska, and correlations with Denali (Mt. McKinley): in Freymueller, J.T., Haeussler, P.J., Wesson, R.L., and Ekström, G. (eds.), *Active tectonics and seismic potential of Alaska*, American Geophysical Union Monograph Series 179, p. 269-285.
- Little, T.A., and Naeser, C.W., 1989, Tertiary Tectonics of the Border Ranges Fault System, Chugach Mountains, Alaska: deformation and uplift in a forearc setting: *Journal of Geophysical Research* v. 94, p. 4333-4359.
- Magoon, L.B., 1986, Present-day geothermal gradient, geologic studies of the lower Cook Inlet Cost No. 1 Well, Alaska outer continental shelf, U.S. Geological Survey, Bulletin, 1596, p. 41-46.
- Mazzotti, S., and Hyndman, R.D., 2002, Yakutat collision and strain transfer across the northern Canadian Cordillera: *Geology*, v. 30, p. 495-498.
- Péwé, T.L., 1975, Quaternary geology of Alaska, U.S. Geological Survey, Professional Paper, 835, 139 p.
- Plafker, G., Nokleberg, W.J., and Lull, J.S., 1989, Bedrock geology and tectonic evolution of the Wrangellia, Peninsular, and Chugach Terranes along the Trans-Alaskan Crustal Transect in the Chugach Mountains and southern Copper River Basin, Alaska: *Journal of Geophysical Research*, v. 94, p. 4255-4295.
- Plafker, G., Moore, J.C., and Winkler, G.R., 1994, Geology of the Southern Alaska margin, in Plafker, G., and Berg, H.C., eds., *The Geology of Alaska*: Boulder, Colorado, Geological Society of America, *The Geology of North America*, v. G-1.
- Reiners, P.W., and Brandon, M.T., 2006, Using thermochronology to understand orogenic erosion: *Annual Review of Earth and Planetary Science* v. 34, p. 419-466.
- van Hunen, J., van den Berg, A.P., and Vlaar, N.J., 2002, On the role of subducting oceanic plateaus in the development of shallow flat subduction: *Tectonophysics*, v. 352, p. 317-333.
- Wolf, R.A., Farley, K.A., and Silver, L.T., 1996, Helium diffusion and low-temperature thermochronometry of apatite: *Geochimica et Cosmochimica Acta* v. 60, p. 4231-4240.
- Wolf, R.A., Farley, K.A., and Kass, D.M., 1998, Modeling the temperature sensitivity of the apatite (U-Th)/He thermochronometer: *Chemical Geology*, v. 148, p. 105-114

Measuring levels of PM10 pollution in the Chiang Mai basin in Northern Thailand

Steven Schill
Advisor: Dr. Narongpan Chunram

Department of Chemistry and Biochemistry, California State University, Fullerton, CA, USA

Abstract

In this study, field measurements of atmospheric PM10 (10-micron Particulate Matter) concentrations in the Chiang Mai basin in Northern Thailand are analyzed. While the importance of pollution regulation has been gaining attention in the Chiang Mai basin, legislation to regulate PM10 levels has been difficult to promote and enact due to the general acceptance of field burning as a viable and profitable method to prepare for the planting of new crops. Additionally, the lack of vehicular inspection regulation contributes to increased levels of combustion-related pollutants. The importance of PM10 is described relative to environmental and health-related impacts, and data are analyzed to show pollution levels since 1999. Maximum measured levels of PM10 pollution consistently reach 200 - 300 $\mu\text{g}/\text{m}^3$ during seasonal field burning in the month of March of each year, approximately double the maximum value established by the US Environmental Protection Agency National Ambient Air Quality Standards.

Introduction

The city of Chiang Mai, Thailand, has consistently exhibited high levels of atmospheric pollution for many years. One of the most prevalent pollutants in the Chiang Mai area is particulate matter less than ten microns in diameter, PM10 (Chongprasith, 2011). Sources of PM10 include a variety of combustion activities such as nearby field burning and urban fuel emissions (Hassett-Sipple, 2008). Field burning is a common activity in the Chiang Mai Province (Changwat) since a large portion of land is dedicated to farming and agriculture. The topography of Chiang Mai Province is such that particulate matter from surrounding areas falls into the basin containing the central city of Chiang Mai and these particles become trapped for extended periods of time. The problems associated with field burning have gained some attention by local government agencies which have recently passed legislation to reduce PM10 emissions. However, enacting and promoting this legislation remains a difficult task due to the traditional acceptance of field burning in Northern Thailand. There is also a lack of regulation on vehicular

emissions in Thailand, which contributes a great deal to the atmospheric pollution in the densely populated central city. Scooters, motorcycles, and larger vehicles are not subject to inspection by any standards and, as a result, fuel emissions contain large amounts of pollutants. High PM10 concentrations have both environmental implications for the global climate and health-related implications for local residents.

The environmental implications for high concentrations of PM10 are largely associated with the activity and reactivity of aerosol particulates in the atmosphere. An aerosol is any small solid or liquid particle suspended in air, ranging in size from several microns (10^{-6} meters) to more than 100 microns in diameter; some aerosol particles can remain in the atmosphere for over a year (Hinds, 1999). Aerosols can have both direct and indirect effects on the global climate. The direct effect on climate change refers to the ability of aerosol particles to affect the radiative balance within the atmosphere as a result of composition, size and phase. The indirect effect of atmospheric aerosol refers to the ability of aerosol particles to facilitate cloud formation, thereby acting as cloud condensation nuclei (CCN). How clouds affect the radiative balance depends on the cloud lifetime and the chemical properties of the CCN, which govern the water uptake tendencies of a given cloud (Imhoff, 2009). Furthermore, aerosols can undergo chemical reactions in the atmosphere which alter the water uptake properties of the particles. Aerosol reactivity also contributes to the indirect effect of cloud formation processes, and is also adversely affected by phase transitions of these particles in the atmosphere (Finlayson-Pitts, 2003). For these reasons it is of great importance to study levels of particulate pollution in the atmosphere, such as the levels of PM10 pollution in Chiang Mai, Thailand.

The health-related implications of high concentrations of PM10 are largely associated with the size of PM10 aerosol. Previous studies have shown that long-term exposure to atmospheric particulate matter can lead to the development of chronic cardiopulmonary injury and increased mortality (Pope, 2002). Additionally, exposure to particulate matter

results in the formation of reactive oxygen species (ROS) and subsequent cellular oxidative stress. These ROS species can induce programmed cell death, known as apoptosis, and damage cellular DNA (Upadhyay, 2003). It is important to note that the definition of PM10 includes all particles less than or equal to ten microns in diameter. Particles less than 2.5 microns in diameter, otherwise known as PM2.5, are known to be of greater health risk due to their tendency for deeper alveolar deposition within the human lung (Ferin, 1992). These smaller particles can damage lung tissue and lead to the development of lethal disease. Although there are separate regulation limits for PM10 and PM2.5, it is still important to monitor PM10 concentrations because those measurements can also contain PM2.5.

Experimental

Data presented in this study were collected at three sampling locations in the city of Chiang Mai, Thailand, referred to as "Chiang Mai," "Chiangmai," and "Uparaj College." At each location was collected one data point per day sampling multiple components of atmospheric interest including PM10 as well as sulfur dioxide, nitrogen dioxide, carbon monoxide, and ozone. This study presents data for PM10 concentrations for an extended period of time (1999-2011). The author, S. Schill, participated in the 2011 portion of the project as part of the Environmental Science Research in Thailand program. All data is available on the internet via the website for the Thailand Pollution Control Department (PCD) at <<http://pcd.go.th/indexEng.cfm>>.

Results and Discussion

As previously mentioned, a large source of PM10 in Chiang Mai, Thailand is the field burning from local agricultural areas. Farmers burn the fields when they are ready to switch their crops, as this eliminates old plant material and the resulting ash will facilitate new growth. Figure 1 shows evidence of field burning in a local village approximately ten kilometers north of the city of Chiang Mai in a district known as Mae Rim.



Figure 1: Evidence of field burning of a rice paddy in the Mae Rim district, approximately 10 km north of the city of Chiang Mai, Thailand.

The Provincial Government has recently passed legislature to fine residents for burning the fields, but this legislature is extremely difficult to enforce, as field burning has been widely accepted throughout the community for many decades. Current efforts are underway by local university faculty to educate the community on the dangers of air pollution, but science education is extremely limited in most communities in Northern Thailand. Additionally, fuel emissions from vehicles not subject to inspection by any standards contribute a great deal to PM10 concentrations in the atmosphere. The field burning activities and fuel emissions are two of the largest contributors to increased pollution in Chiang Mai, and the evidence of this pollution can be seen in a mountain-top view of Chiang Mai Airport which shows reduced visibility as a result of aerosol particulate matter (fig. 2) on January 6, 2011, at the beginning of the field burning period.



Figure 2: Chiang Mai city view from the temple at Doi Suthep, approximately 20 km east of Chiang Mai. Elevation is approximately one kilometer, and reduced visibility is due to high levels of atmospheric pollution.

Field burning is performed annually, and is most common in the month of March as the seasonal change facilitates the growth of new crops. Data collected at three sampling locations in the Chiang Mai basin show the seasonal increase in PM10 concentration as a function of date (fig 3).

From data collected at the Chiang Mai location that increased concentrations of PM10 in the month of March of each consecutive year are observed. The highest measured PM10 concentration occurred in May 1999, and is significantly higher than any other measured value. This is likely caused by out-of-control wildfires which occurred during that time. Expanded data for the monitoring site at Changmai during the 2008-2011 period are presented in Figure 4. It is also important to note the measured values of PM10 concentration at times where field burning is taking place. These peak values are in the range of $200 - 300 \mu\text{g}/\text{m}^3$, which is significantly higher than the upper regulation limit of $150 \mu\text{g}/\text{m}^3$ established by the 2006 revision of the Clean Air Act (CAA) National Ambient Air Quality Standards of the United States Environmental Protection Agency (EPA). Comparisons are made to the United States EPA due to the stringent regulation in the US, which has been motivated by recent research in an effort to improve air quality and health.

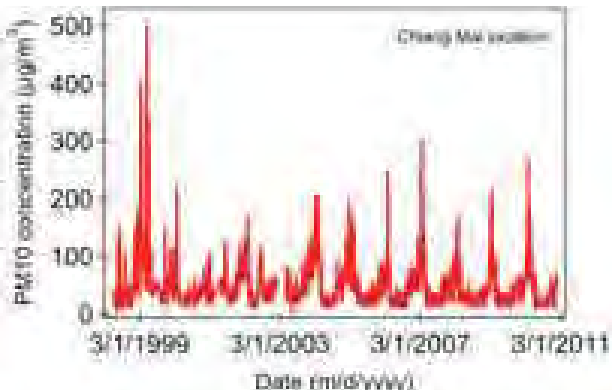


Figure 3: Concentration of PM10 as a function of date; data collected at Chiang Mai location.

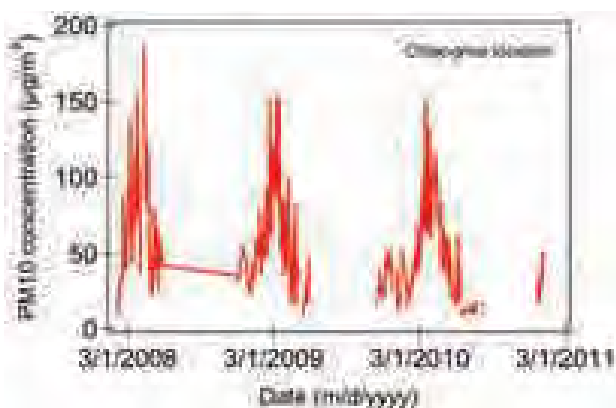


Figure 4: Concentration of PM10 as a function of date; data collected at Chiangmai location.

Once again, there is clear distinction that the peak concentrations of PM10 occur in the month of March each year. While maximum measured PM10 concentrations at are slightly lower at the Chiang Mai location than those measured at other sampling locations, they are still at the maximum value established by the US EPA National Ambient Air Quality Standards. Additionally, the definition of PM10 includes all particles less than ten microns in diameter. This includes PM2.5 particles which are known to significantly increase health risks via inhalation. While data at the Chiang Mai location may seem within the EPA National Ambient Air Quality Standards, it is important to note that the PM2.5 concentrations here are likely much higher than the established upper limit of 35 $\mu\text{g}/\text{m}^3$ for acceptable air quality as a result of field burning and fuel emissions. (The 200-300 $\mu\text{g}/\text{m}^3$ level is for MAXIMUM levels allowed.)

Data collected at the Uparaj College location also indicates increased PM10 concentration in March of each year (fig. 5). The highest measured PM10 concentration occurred in March 2007, and is significantly higher than the EPA National Ambient Air Quality Standards. Peak values are once again on the order of 200 - 300 $\mu\text{g}/\text{m}^3$, consistent

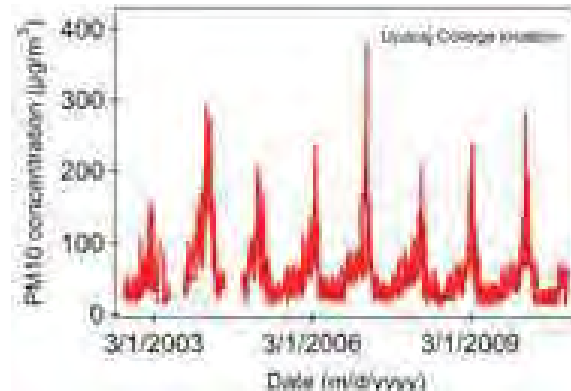


Figure 5: Concentration of PM10 as a function of date; data collected at Uparaj College location.

with the measurements from the Chang Mai sampling locations. The data from Chiang Mai, Chiangmai, and Uparaj College, call for better regulation of PM10 emissions to prevent undesirable environmental and health related consequences of increased pollution.

Conclusion

Increased concentrations of PM10 in the atmosphere have adverse implications for both environmental and health-related factors. It is of great importance to measure levels of PM10 pollution to increase the understanding of the necessity for regulation of particulate matter sources. Pollution in the Chiang Mai basin in Northern Thailand analyzed in this study originate from the burning of local fields in annual preparation for new crop planting, as well as vehicular emissions from unregulated transportation sources. Previous efforts to regulate PM10 levels have proven ineffective so it is important to continue to monitor pollution levels so that new regulations can be developed to ensure reduction of atmospheric pollutants.

Acknowledgements

This study was made possible by the CSUF Associated Students, Inc./Instructionally Related Activities support of Environmental Science Research in Thailand (ESRT) Program at California State University, Fullerton (Schill) and Chiang Mai Rajabhat University, Thailand (Chunram). Special acknowledgement is also extended to Dr. Richard Deming (California State University, Fullerton) for coordination of the ESRT Program.

References

- Chongprasith et. al. (2011). Pollution Control Department (Bangkok, Thailand). <http://pcd.go.th/indexEng.cfm>
- Ferin et. al. (1992). Am. J. Respir. Cell Mol. Biol. 6, 535
- Finlayson-Pitts, B.J. (2003). Chem. Rev. 103, 4801-4822.
- Hassett-Sipple et. al. (2008). Environmental Protection Agency (United States of America). <http://www.epa.gov>
- Hinds, William C. (1999). Aerosol Technology: Properties, Behavior, and Measurements of Airborne Particles. John Wiley & Sons, Inc.
- Imhoff, Marc. (2009). National Aeronautics and Space Administration (United States of America). <http://terra.nasa.gov/FactSheets/Aerosols/#top>
- Pope et. al. (2002). JAMA. 287, 9
- Upadhyay et. al. (2003). Am J Respir Cell Mol Biol. 29,180

Effects of Artificial Moonlight on the Foraging Behavior of Mojave Desert Rodents

Bryan White
Advisor: Dr. Paul Stapp

Department of Biological Science, College of Natural Science and Mathematics, California State University, Fullerton, CA, USA

Abstract

Desert rodent communities are extremely diverse, which has prompted researchers to ask how so many species can coexist on similar, limited resources. Differences in foraging preferences associated with predator avoidance may contribute to coexistence. I determined how the foraging behavior of Mojave Desert rodents, especially pocket mice (*Chaetodipus*), were influenced by the increase in perceived predation risk associated with moonlight, which I simulated using artificial illumination. Millet (6.00 g) was mixed into trays filled with 2 L of pre-sifted sand. Seed trays were placed at stations located at different distances (2-82 m) from Coleman dual-fuel camping lanterns, and in either open or shrub microhabitats, so that rodents could choose to forage from resource patches with different levels of perceived risk. I also live-trapped rodents to identify likely foragers near the lanterns, and to determine the diversity and abundance of rodents in the area. Background illumination levels were recorded with using a Lux meter. I predicted that the amount of seeds removed would be highest at seed trays farthest from lanterns and under shrubs, and lowest at stations closest to lanterns and in open microhabitats. Surprisingly, I found no effect of distance, microhabitat, or illumination level on the amount of seeds removed by rodents. However, the amount of seed removed differed among study locations. Future studies should be conducted on larger, more homogeneous study areas to test our hypotheses.

Introduction

Desert rodents are intriguing animals because of their ability to survive in extremely harsh climates where resources are limited. Desert rodent communities are extremely diverse, which has prompted researchers to ask how so many species can coexist on the same resources, seeds (Brown 1988). In the Mojave Desert, for example, six different genera (*Ammospermophilus*, *Chaetodipus*, *Dipodomys*, *Neotoma*, *Onychomys*, *Perognathus*, *Peromyscus*), representing three rodent families (Heteromyidae, Muridae, Sciuridae) can all be captured in roughly the same area (Stevens et al. 2009). Most explanations suggest that animals reduce competition via resource partitioning, but differences in predator avoidance abilities may also contribute to coexistence (Kotler 1984).

It is widely accepted that desert rodents differ in their microhabitat preferences, and that these preferences reflect differences in the ability of rodents to detect and avoid predators, including owls, mammalian carnivores, and snakes. For example, quadrupedal rodents such as pocket mice (*Chaetodipus*, *Perognathus*), tend to forage in the cover of large shrubs, whereas bipedal rodents such as kangaroo rats (*Dipodomys*) are often found in open microhabitats between shrubs (Kotler 1984). Kangaroo rats are adapted to forage in open microhabitats in which there is little cover from visual predators (Thompson 1982; Kotler 1984). These adaptations include hopping locomotion, the ability to hear very low frequency sounds (1-3 kHz), and dorsally located eyes that should aid in spotting predators (Thompson 1982; Kotler 1984). Predation rates on rodents by owls are higher both in open microhabitats and (in a separate experiment) during periods of full moon, when levels of illumination might make movements more conspicuous (Kotler 1988). In contrast, pocket mice lack these morphological specializations, but presumably can move more efficiently beneath the denser shrub canopy (Thompson 1982). Interestingly, owls and rattlesnakes, the two most important rodent predators in the Mojave Desert, may have different effects on microhabitat use by rodents. Owls directly affect the perception of risk by desert rodents (Kotler 1988), which is higher in open microhabitats (Brown et al. 1988). The presence of rattlesnakes, which tend to hide near shrubs to wait for prey and to avoid being eaten themselves, decreased foraging of kangaroo rats in shrub microhabitats, although only during summer, when snakes are active (Bouskila 1995).

The response of rodents to predation risk has traditionally been measured in 2 ways: analysis of microhabitat characteristics at locations where rodents are captured, and foraging experiments to estimate differences in seed removal rates associated with different microhabitats. Optimal foraging theory states that animals will forage in an area until the costs of continued foraging, including perceived predation risk, outweigh the benefits (Morris 1997). The giving-up density (GUD) the density of seeds remaining in an artificial seed patch after a foraging bout, reflects this quitting harvest rate, and

thus provides an index of an animal's perceived risk and foraging costs associated with particular microhabitats (Brown et al. 1988). Both methods have been used to study how moonlight intensity affects rodent activity. Kotler (1984) found that increased illumination, simulated by camping lanterns, decreased captures in open microhabitats for some species and shifted habitat use for others in the Great Basin. Others have reported that bright moonlight reduces overall rodent activity aboveground (Brown et al. 1988).

I modified Kotler's (1984) approach to investigate the possible effects of artificial illumination on foraging behavior of rodents in shrub and open microhabitats in the Mojave Desert. Rather than studying shifts in captures in different microhabitats, I measured seed removal rates in artificial seed trays placed at different distances from an artificial light source, a gas-powered Coleman lantern. I also quantified variation in light levels at varying distances from the lantern and in the open and beneath shrubs to understand better how actual light levels differ between these microhabitats. I predicted that seed removal rates would be lower (and GUDs higher) in trays close to the lanterns, where illumination was greatest, than at trays where there was only natural light. I also expected that rodents would remove relatively more seeds from trays beneath shrubs than in open microhabitats, especially near the lanterns, where the difference in illumination would be greatest.

Methods

My study site was conducted approximately 5 km NW of the Desert Studies Center, Zzyzx, California, during the months of June and July 2010. The site was a broadly sloping bajada at the base of an alluvial fan. Vegetation consisted mostly of creosote bush (*Larrea tridentata*), burrobush (*Ambrosia dumosa*) and desert holly (*Atriplex hymenelytra*), with scattered forbs and grasses. The substrate was a mixture of medium-size to small rocks and gravel, with some sandy washes. Shrub microhabitats were considered to be any shrub that appeared large enough to provide adequate canopy cover over a seed tray. Open microhabitats were locations that were at least 1 m from shrubs.

To determine which rodent species were present at my site and foraging in seed trays, I set large Sherman live traps on the night prior to foraging trials. Traps were baited with commercial bird seed that had been microwaved for 5 min to prevent germination. During June, 30 traps were placed at same locations as the seed trays. During July, trapping was done in a 7 x 7 grid (49 traps separated by 10 m) in the area where seed trays were placed.

Artificial seed trays were houseplant saucers (6 cm deep and 32.5 cm in diameter) buried so that edges were flush with the ground. When set, each tray contained 6.00 g of millet mixed in 2 L of pre-sifted, fine sand. In June, I placed trays 2, 12 and 22 m points along 2 parallel lines extending out from a central Coleman (Dual Fuel) camping lantern. This was repeated 3 times at 50-m intervals, for a total of 30 trays. In July, I placed 32 trays from (2 m to 72 m at 10 m increments) in four different directions extending out from two centrally-placed lanterns. Two lanterns were used in the second design in an attempt to increase illumination levels. At a given location, seed trays were randomly assigned to be either in a shrub or open microhabitat. One additional tray was covered with hardware cloth to prevent foraging and was used as a control to quantify changes in weight of seeds due to moisture overnight (Stapp and Lindquist 2007).

Trays were set out at dusk. I allowed rodents to forage in seed trays for approximately 4 h. The remaining seeds and sand were collected from trays and taken back to the Desert Studies Center lab, where the sand was sifted to remove seeds. The

seed was cleared of debris and weighed using a precision scale to estimate the amount of seeds removed. Seed trays were considered to have been foraged if the amount of seed removed differed by >2% of control trays from that night.

At the beginning of each foraging trial, I measured light intensity using an Extech 401036 light meter. Illumination was measured by placing the light meter on the seed tray so that the light receptor faced straight up. This measured the ambient light in the area, as opposed to the relative intensity that a rodent may perceive being emitted from a light source (either the moon and stars or lantern). I assumed that rodents look to their immediate surroundings, rather than some distant light source, to decide the relative risk of the potential foraging patches. Trials were conducted under similar background moon conditions (waxing gibbous).

All statistical analyses were conducted in Microsoft Excel (2007) Data Analysis Toolpack and Minitab 15 (Minitab Inc. 2007).

Results

Based on a total trapping effort of 64-trap-nights over the 2 trapping sessions, pocket mice *Chaetodipus* (17 individuals of 2 species, *C. penicillatus*, *C. formosus*, that were not be distinguished) were the most abundant rodents, followed by Merriam's kangaroo rat (*D. merriami*, 6 individuals) and the desert woodrat (*Neotoma*, 1 individual). I therefore assumed that most trays were visited by pocket mice.

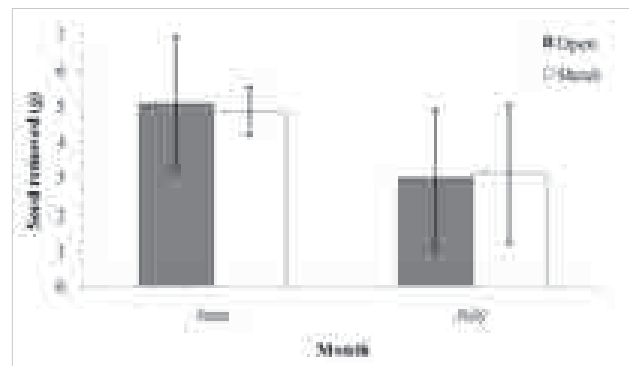


Figure 1: Amount of seed removed by rodents (g) from lanterns in open and shrub microhabitats in the Mojave Desert during foraging experiments in June and July 2010. Error bars represent 95% confidence intervals.

A total of 62 seed trays were set out during the 2 trials. During the June trials, 3 of 30 trays (1 shrub, 2 open, 1 spilled) were considered to have not been foraged, whereas in July, more than 2/3 (22/32) of the trays were not foraged (10 shrub, 12 open, 1 spilled). Only results from seed trays that were considered foraged were included in the analysis. Combining across all distances and trials, there was no significant difference in the amount of seeds removed in shrub and open microhabitats during June or July (Fig. 1; $P > 0.05$). Combining both trials, the amount of seed removed was not related to distance to the lanterns in either open (Fig. 2; $R^2 = 0.007$, $P = 0.745$, $DF = 15$) or shrub (Fig. 2; $R^2 = 0.15$, $P = 0.0936$, $DF = 18$) microhabitats.

Illumination levels were highest in seeds trays near the lanterns, but declined considerably by 12 m from the lanterns (Fig. 3). Shrub and open trays were exposed to similar light levels.

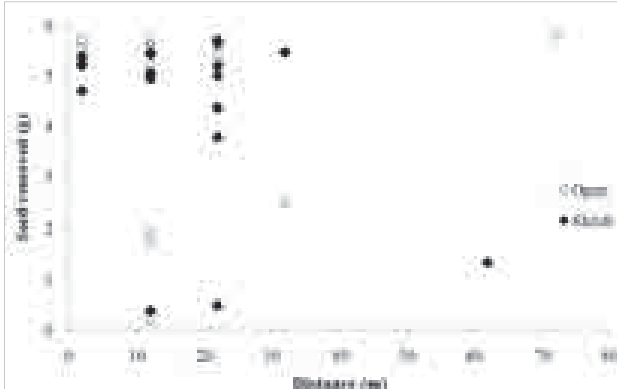


Figure 2: Amount (g) of seeds removed by rodents at different distances (m) from lanterns in open and shrub microhabitats in the Mojave Desert in June and July 2010 trials combined. Trays contained 6 g of seeds at the start of the trials and were set out for approximately 4 h.

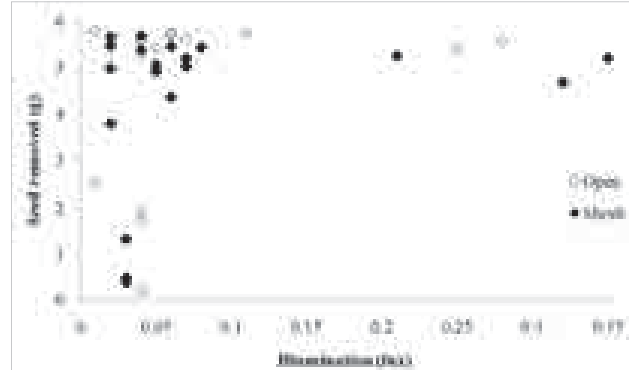


Figure 4: Seed removed (g) at different illumination levels (lux) as measured by an Extech light meter in both open and shrub microhabitats in the Mojave Desert during foraging experiments in June and July 2010. The seed removed (g) axis represents the amount of seed removed during one foraging experiment. The illumination (lux) axis represents the amount of ambient light at a given seed tray.

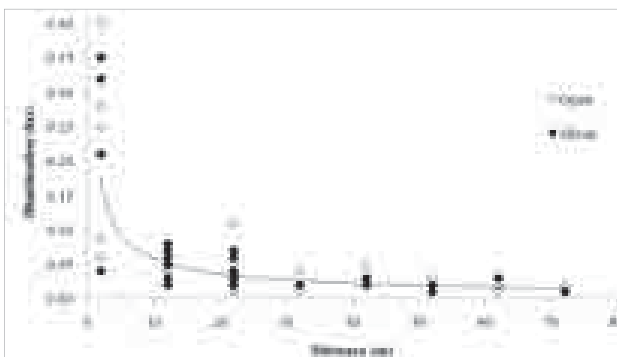


Figure 3: Illumination level (lux) at different distances (m) from the lanterns, as measured by an Extech light meter in the Mojave Desert in June and July 2010. The illumination (lux) axis represents the amount of ambient light at a given seed tray. Lines are shown only to represent the trend, but not indicate a statistically significant relationship.

Surprisingly, illumination did not influence seed removal rate in the way that I predicted. At all levels of illumination and in both shrub and open microhabitats, rodents consumed most of the seeds in the trays (Fig. 4). In fact, the amount of seeds removed was lowest and most variable at the lowest light intensities.

Discussion

I found no evidence to support my hypothesis that rodents would spend more time foraging in darker, shrub microhabitats, where risk of predation would presumably be lower. This was particularly surprising because pocket mice were the most common rodents I captured at my study sites and probably were responsible for most of the foraging in seed trays. Pocket mice are quadrupedal and generally prefer the cover

of shrubs (Kotler 1988), and therefore would be expected to be sensitive to predation risk. My results differ from those of Kotler (1984), who found, based on live-trapping, that rodents, including quadrupedal species, increased their use of shrub microhabitats in the presence of artificial illumination. However, Kotler (1984) also found that seed enrichments increased the use of the open microhabitat by kangaroo rats. This suggests that, in my study, while pocket mice may have focused their foraging efforts on removing seeds from under shrubs, kangaroo rats may have been opportunistically foraging in brighter areas, and due to its larger body size and bipedal locomotion, consistently removed large amounts of seeds from those trays.

The fact that rodents ate nearly all the seeds in seed trays at all distances from the lanterns and irrespective of illumination levels suggests that the bright light associated with the lanterns did not deter them from foraging. In fact, rodents removed the smallest amounts of seed in trays at the darkest light levels, including some beneath shrubs (Fig. 4). This suggests that factors other than illumination and microhabitat influenced foraging behavior at these low light levels. It also suggests that rodents can find a large amount of dispersed seed (6 g) in a relatively short time. It is possible that multiple rodents visited a given tray, but I was not able to determine the number of rodents using each tray.

If I were to repeat this study, I would increase the number of replicate seed trays and use the same experimental design throughout. I also would keep a record of whether there are tracks in trays as an index of foraging. Another way to improve my experimental design would be to video record seed trays to know how many animals and of which species visited a seed tray during a foraging bout.

Acknowledgements

I thank Dr. Bill Hoese, Dr. Darren Sandquist, Dr. William Presch, the Stapp Lab, Rob Fulton, Jason Wallace, Norma Charest, Pamela Lopez, SCERP, and the Desert Studies Center staff. Financial support was provided by the National Science Foundation through SCERP, the Judith Presch Desert Research Scholarship and the Department of Biological Science at CSUF.

References

- Bouskila, A. (1995). Interactions between predation risk and competition: A field study of kangaroo rats and snakes. *Ecology*, 76(1), 165-178.
- Brown, J. S., Kotler, B. P., Smith, R. J., & Wirthz, W. O., II. (1988). The effects of owl predation on the foraging behavior of heteromyid rodents. *Oecologia*, 76(3), 408-415.
- Kotler, B. P. (1984). Risk of predation and the structure of desert rodent communities. *Ecology*, 65(3), 689-701.
- Kotler, B. P. (1988). Environmental heterogeneity and the coexistence of desert rodents. *Annual Review of Ecology and Systematics*, 19, 281-307.
- Morris, D. W. (1997). Optimally foraging deer mice in prairie mosaics: A test of habitat theory and absence of landscape effects. *Oikos*, 80(1), 31-42.
- Stevens, R. D., & Tello, J. S. (2009). Micro- and macrohabitat associations in mojave desert rodent communities. *Journal of Mammalogy*, 90(2), 388-403.
- Stapp, P., & Lindquist, M (2007). Roadside foraging by kangaroo rats in a grazed short-grass prairie landscape. *Western North American Naturalist*, 67(3), 368-377.
- Thompson, S. D. (1982). Microhabitat utilization and foraging behavior of bipedal and quadrupedal heteromyid rodents. *Ecology*, 63(5), 1303-1312.
- Thompson, S. D. (1982). Structure and species composition of desert heteromyid rodent species assemblages: Effects of a simple habitat manipulation. *Ecology*, 63(5), 1313-1321.

Effects of Prairie Dogs on the Diet of Thirteen-lined Ground Squirrels (*Spermophilus tridecemlineatus*)

Denise Soto
Advisor: Dr. Paul Stapp

Department of Biological Science, College of Natural Science and Mathematics, California State University, Fullerton, CA, USA

Abstract

In northern Colorado, thirteen-lined ground squirrels (*Spermophilus tridecemlineatus*) are more abundant in grasslands without black-tailed prairie dogs (*Cynomys ludovicianus*) than in active prairie dog colonies. The intensive habitat modifications associated with colonies may reduce the quality and abundance of food resources, which might help explain why these omnivorous ground squirrels are less abundant in areas with prairie dogs. I used stable carbon (C) and nitrogen (N) isotope analysis to characterize the trophic relationships among plants and animals on and off of prairie dog colonies. I hypothesized that the carbon (C) stable isotopic ratios of ground squirrels would be lower, and nitrogen (N) ratios higher, off of colonies, indicating that squirrels consume greater amounts of food that include nutrition-rich insects derived from cool-season, C₃ plants. Tissue samples were collected from ground squirrels on active colonies and in grassland areas without prairie dogs ("off colony") between May and August in 2004 and 2005. In 2010, arthropods were captured on and off colonies and plant samples were collected off colonies to represent the most abundant food items for squirrels on shortgrass steppe. Although stable N analysis suggested that ground squirrels ate a similar mixture of plant and animal matter on and off colonies in both years, there was a significant decrease in δ¹³C value of squirrel tissues in 2005 off colony, suggesting an increase in consumption of C₃ plant derived foods. In contrast, arthropods from colonies in 2010 had significantly lower δ¹³C values than those collected off colony, suggesting that they took advantage of C₃ forbs associated with prairie dog disturbances. Both on and off colony, δ¹⁵N values increased in a predictable fashion with trophic position, with predatory spiders and omnivorous ground squirrels having the highest δ¹⁵N and herbivorous grasshoppers having the lowest. Stable isotope analysis proved to be a useful approach to characterize the trophic relationships among plants and consumers in shortgrass steppe, and determine the potential effects of prairie dogs on thirteen-lined ground squirrels.

Introduction

In the shortgrass steppe of northern Colorado, the grazing and burrowing activities of black-tailed prairie dogs (*Cynomys ludovicianus*) significantly alters grasslands in ways that benefit some species while harming others (Stapp 1998, Stapp 2007). Prairie dogs alter plant species composition

(Agnew et al. 1986, Whicker and Detling 1988), creating relatively mosaic plant community structures in their colonies (Whicker and Detling 1988). Prairie dogs also significantly reduce the amount of aboveground plant biomass (Whicker and Detling 1988) and plant cover, which increases bare ground and decreases plant height (Aldana and Stapp 2007). In general, compared to prairie dog colonies, areas of shortgrass steppe without prairie dogs have a mixture of warm-season and cool-season plants, and more vegetation overall (Stapp 1998).

Thirteen-lined ground squirrels (*Spermophilus tridecemlineatus*) are small, diurnal, ground-dwelling squirrels that inhabit the grasslands of the central Great Plains (Streubel and Fitzgerald 1978). In northern Colorado, ground squirrels emerge from hibernation in the middle of March and are active until early August (Flake 1971). During this period, they must regain the weight lost during their fast, mate, and reproduce (Streubel and Fitzgerald 1978). Thirteen-lined ground squirrels are omnivorous, with a diet that consists of arthropods, insects, seeds, and flower heads (Flake 1973).

Thirteen-lined ground squirrels are the most common and widespread mammals in shortgrass steppe (Stapp et al. 2008). However, ground squirrels are most abundant in grassland areas where prairie dogs are absent (Agnew et al. 1986, Stapp 2007). The reduction in both the amount and variety of food resources associated with colonies may help explain why ground squirrels are less abundant in areas with prairie dogs. However, the effect of prairie dogs is not clear. Both species are diurnal and semi-fossorial, and prairie dogs may directly compete with or be antagonistic towards ground squirrels, or affect them indirectly, by modifying habitat or food availability (Aldana and Stapp 2007).

Stable isotope analysis allows researchers to identify the food items that have been incorporated into an organism's tissues, allowing them to determine consumer diet (Stapp et al. 1999). Inferences about diet can be made based on the relative amounts of heavier isotopes in organisms (DeNiro and Epstein 1978, 1981). Fecal analysis is biased against detecting foods that are completely digestible, while stomach content analysis usually requires killing the animal (Herrera et al. 2002). Carbon (¹³C/¹²C) and nitrogen (¹⁵N/¹⁴N) are the most commonly used isotopic ratios for identifying diet sources (Stapp 2002). A consumer's δ¹³C value, calculated by expressing the C isotopic ratio relative to a standard, is

Sample (Family; n)	Carbon $\delta^{13}\text{C}$ (‰)				Nitrogen $\delta^{15}\text{N}$ (‰)			
	On colony	95% CI	Off colony	95% CI	On colony	95% CI	Off colony	95% CI
Thirteen-lined ground squirrels								
2004 (20)	-19.38	0.89	-19.54	0.75	7.08	1.12	7.52	0.41
2005 (10)	-18.23	1.14	-22.34	1.93*	8.70	0.60	7.63	0.25
Combined (30)	-19.00	0.74	-20.47	1.04	7.62	0.82	7.56	1.33
Arthropods								
Predatory spiders (Lycosidae; 3)	-18.90	1.33	-16.07	1.30*	8.74	1.16	8.52	2.03
Predatory beetles (Carabidae; 3)	-23.10	2.22	-19.69	1.51	6.05	0.76	8.31	0.26*
Detritivorous beetles (Tenebrionidae; 3)	-21.22	0.75	-22.33	0.86	7.13	2.14	4.40	1.34
Crickets (Gryllidae; 3)	-23.71	0.26	-20.91	2.85	4.81	0.11	5.71	0.44*
Generalist grasshoppers (Acrididae; 3)	-23.54	1.18	-22.27	2.10	4.05	2.64	1.45	2.53
Specialist grasshoppers (Acrididae; 3)	-17.53	1.68	-14.75	0.49*	2.94	2.01	2.49	1.39
All arthropods combined (18)	-21.74	1.25	-19.75	1.57	6.68	1.01	6.74	1.16
Plants								
C_3 plants (3)	-	-	-26.84	1.53	-	-	2.71	1.99
C_4/CAM plants (4)	-	-	-14.50	1.69	-	-	4.20	0.97

Table 1: Means and 95% CI of carbon and nitrogen isotopic ratios of ground squirrels and arthropods on and off prairie dog colonies and of plants collected off colony. Bold-face values with an asterisk are significantly different based on the lack of overlap between 95% CI.

similar to that of its diet (DeNiro and Epstein 1981, Stapp et al. 1999). Therefore, the source of energy for thirteen-lined ground squirrels can be determined by comparing the $\delta^{13}\text{C}$ values of squirrel tissue to those of potential food items, such as plants and insects. For example, plants with C_3 (20.0‰ to -35.0‰), C_4 (-7.0‰ to -15.0‰) and CAM (-10.0‰ to -22.0‰) photosynthesis have different C isotope ratios (Ehleringer et al. 1986); the tissues of insects feeding on these plants would be similarly depleted or enriched. Likewise, the $\delta^{15}\text{N}$ value typically increases by 3-5‰ with each stepwise increase in trophic level (Schoeninger, DeNiro and Tauber 1983). Therefore, $\delta^{15}\text{N}$ provides information on diet source and trophic position and can be used to determine if an animal is an herbivore, omnivore or carnivore.

To better understand how the presence of prairie dogs affects ground squirrels, I used stable isotope analysis to characterize the trophic relationships among plants, insects, and squirrels on and off prairie dog colonies in northern Colorado. Specifically, I hypothesized that $\delta^{13}\text{C}$ values of ground squirrels would be lower and $\delta^{15}\text{N}$ values higher off of colonies, indicating that squirrels consume a greater variety of foods, including protein-rich insects derived from cool-season, C_3 plants.

Methods

My study area was the Pawnee National Grasslands, located 40 km north of Greeley, CO, USA. The climate is semiarid and vegetation is classified as shortgrass steppe, which is dominated by perennial, warm-season grasses such as buffalograss (*Buchloe dactyloides*) and blue grama (*Bouteloua gracilis*) (Lauenroth and Milchunas 1991). From May to September of 2004 and 2005, ground squirrels were live trapped on and off prairie dog colonies. Animals were weighed, identified by sex, age, and reproductive status, and marked with an aluminum ear tag. A sample of ear tissue was humanely collected, placed in 75% ethanol, and then stored at -80°C. Research on live animals was approved by the Institutional Animal Care and Use Committee at California State University Fullerton and was performed following the guidelines of the American Society of Mammalogists (Gannon et al. 2007).

Terrestrial macroarthropods, representing the most common arthropod families, were captured on and off prairie dog colonies in 2010 using pitfall traps and by hand, and stored in 75% ethanol. Plant samples, representing the most common species found on the study area, were collected in 2010 on areas without prairie dogs. Tissues of 5 individual plants were combined to represent a given plant species. Squirrel, arthropod and plant samples were dried at 68°C. Samples were then homogenized using a mortar and pestle. Approximately 3 mg of ground plant tissue and 1 mg of ground animal tissue were loaded into individual tin capsules for isotope analysis.

The C and N isotope ratios of each sample were determined using an elemental analyzer interfaced to a continuous-flow isotope-ratio mass spectrometer at the University of California Davis Stable Isotope Facility (Davis, CA). Standards were PeeDee Belemnite for C and atmospheric nitrogen for N. Overlap between 95% confidence intervals and t-tests were used to compare means, with $\alpha = 0.05$ to determine if results were statistically significant.

Results

Stable isotope ratios suggested that ground squirrels are omnivorous, eating a mixture of plants and insects derived from C_3 or C_4/CAM plants. There was no significant difference in $\delta^{13}\text{C}$ of squirrel tissues on and off colonies in 2004 (Table 1); however, in 2005, $\delta^{13}\text{C}$ of squirrel tissues off colonies were significantly depleted compared to those from on colonies, suggesting that a greater proportion of the diet of squirrels off colonies were derived from C_3 plants. There were no significant differences in $\delta^{15}\text{N}$ between squirrel tissues collected on and off colonies in either year, suggesting that squirrels maintained the same omnivorous diet regardless of the presence of prairie dogs.

Unlike ground squirrels, $\delta^{13}\text{C}$ values of arthropods collected on prairie-dog colonies tended to be depleted in $\delta^{13}\text{C}$, suggesting consumption of more C_3 -derived material (Table 1). Collectively, $\delta^{13}\text{C}$ values of arthropods collected on colonies were significantly depleted compared to those from off-colony areas (paired t-test, $t = 2.91$, d.f. = 5, $P = 0.033$). $\delta^{13}\text{C}$ values of wolf spiders (Lycosidae) and specialist

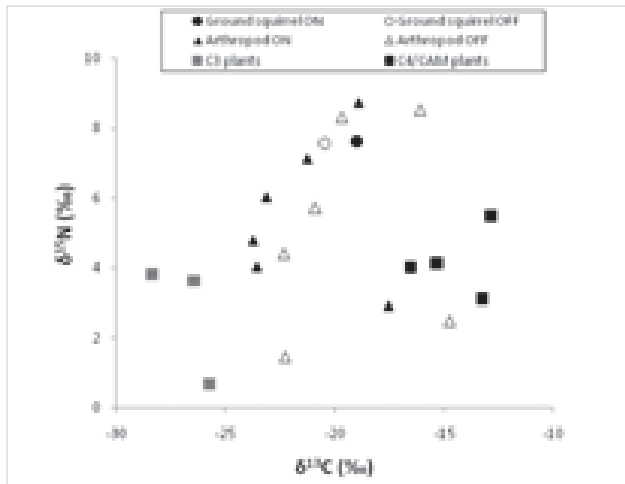


Figure 1: Stable C and N isotopic ratios of thirteen-lined ground squirrels and terrestrial arthropods collected on and off black-tailed prairie dog colonies in northern Colorado. Plants were collected off colonies. Values are means ($n = 3-12$), with error bars omitted for clarity (see Table 1).

grasshoppers (Acrididae) collected on colonies were significantly lower than those from off-colony areas (Table 1). Similarly, arthropod tissues collected on colonies tended to be enriched relative to those off colony, as reflected in their higher $\delta^{15}\text{N}$ values (Table 1). However, results for $\delta^{15}\text{N}$ were more variable than those for $\delta^{13}\text{C}$, and, considered collectively, $\delta^{15}\text{N}$ values did not differ significantly between colony and off-colony sites (paired t-test, $t = -0.161$, d.f. = 2, $P = 0.886$). However, $\delta^{15}\text{N}$ values of predatory ground beetles (Carabidae) and detritivorous field crickets (Gryllidae) were significantly higher off colonies than on colonies (Table 1).

Visual inspection of a biplot of mean $\delta^{13}\text{C}$ and $\delta^{15}\text{N}$ for all taxa revealed that most consumer species consume a diet of a mixture of C_3 and C_4/CAM plants, as well as the consistent shift in $\delta^{13}\text{C}$ values of arthropods toward C_3 -derived foods on colonies (Fig. 1). Fig. 1 also shows the predicted increase in $\delta^{15}\text{N}$ with increasing trophic level: predatory species (spiders, beetles) and ground squirrels tended to have the highest $\delta^{15}\text{N}$ values, whereas herbivorous grasshoppers had the lowest values and scavenging detritivores had intermediate values (see Table 1).

Discussion

Stable isotope analysis suggested that the source of C in the diet of thirteen-lined ground squirrels differed between prairie dog colonies and grassland areas without prairie dogs, at least in 2005. Compared to 2004, diets of ground squirrels on and off colony diverged more in 2005, with $\delta^{13}\text{C}$ values on-colony becoming

more enriched, suggesting consumption of C_4/CAM -derived resources, and those off-colony becoming more depleted, suggesting consumption of more material from C_3 plants. Rainfall in winter and spring of 2005 (304 mm) was much higher than in the previous year (154 mm; SGS-LTER weather data), which could increase the production of cool-season C_3 plants and associated insects, especially in off-colony areas. Consequently, my hypothesis that the diet of ground squirrels off prairie dog colonies would be composed from plants and arthropods with a lower C isotopic ratio was partially supported. However, the $\delta^{15}\text{N}$ values of squirrels were similar on and off colonies, indicating that the squirrels ate similar mixtures of plant and animal matter.

In contrast to the ground squirrels, there was a consistent increase in the use of C_3 plants by arthropods on prairie dog colonies compared to grasslands without prairie dogs. Warne et al. (2010) reported that C_3 plants are of higher nutritional value to arthropods than C_4 plants. Although vegetative cover is lower overall on colonies than off, C_3 plants such as forbs and invasive weeds are still common on areas around prairie dog mounds and disturbances (Stapp 2007), which could provide food for insects. Although squirrel tissues and arthropod tissues were collected during different years, if I assume that isotopic ratios of arthropods from 2004-05 were similar to those from 2010, then it does not appear that squirrels consumed many arthropods on prairie dog colonies, at least of the potential prey species I studied.

The pattern of $\delta^{15}\text{N}$ values (Fig. 1) showed the expected trophic relationships within food webs on and off prairie dog colonies. Wolf spiders, which were expected to be exclusively predatory, had the highest $\delta^{15}\text{N}$ values. Ground squirrels also had enriched $\delta^{15}\text{N}$ values, underscoring their omnivorous habits, which may also include vertebrate prey such as bird eggs and chicks (With 1994), which I did not sample. In contrast, grasshoppers, which eat primarily grasses or forbs had low $\delta^{15}\text{N}$ values that were similar to those of prairie dogs (3.55‰; Stapp and Salkeld 2009). There was no evidence, however, of a difference in the length or complexity of food webs on and off prairie dog colonies.

One limitation of stable isotope analysis is that it usually cannot provide the type of species-level diet information that could be obtained from fecal or stomach content analyses. Nevertheless, I was able to use this approach to compare the broad diets of ground squirrels and arthropods on and off prairie dog colonies, without sacrificing individual squirrels or the need to learn microhistological techniques. Future studies could include these more detailed methods to estimate the specific items in these consumers' diets and should also aim to collect representative samples from the same on and off colony sites during the same years to facilitate comparisons.

Acknowledgements

I thank Mark Lindquist, Kevin Meierbachtol and SGS-LTER field crews for collecting plant and insect tissues. Dan Salkeld and the Stapp plague-project field crews collected squirrel tissues. My research was supported by a Faculty-Student Research and Creative Activities Grant from the CSUF Faculty Development Center and the Department of Biological Sciences

References

- Agnew, W., Uresk, D.W., & Hansen, R. M. 1986. Flora and fauna associated with prairie dog colonies and adjacent ungrazed mixed-grass prairie in Western South Dakota. *Journal of Range Management*. 39: 135-139.
- Aldana, J. & Stapp, P. 2007. Effects of prairie dogs on above ground activity of thirteen-lined ground squirrels (*Spermophilus tridecemlineatus*). Dimensions: The Journal of Under Graduate Research in Natural Science and Mathematics, California State University, Fullerton. 9: 7-12.
- Dawson, T.E., Mambelli, S., Plamboeck, H.A., Templer, P.H., & Tu, K.P. 2002. *Stable isotopes and plant ecological research*. Pp.512-523 in, Stable Isotope in plant ecology, Volume 33.
- DeNiro, M. J., & Epstein, S. 1981. Influence of diet on the distribution of nitrogen isotopes in animals. *Geochimica Cosmochim. Acta*. 45: 341-351.
- DeNiro, M. J., & Epstein, S. 1978. Influence of diet on the distribution of carbon isotopes in animals. *Geochimica Cosmochim. Acta*. 42: 495-506.
- Ehleringer, J.R., Rundel, P.W., & Nagy, K.A. 1986. Stable isotope in physiological ecology and food web research. *TREE*. 1: 42-45.
- Flake, D. L. 1973. Food habitats of four species of rodents on a short-grass prairie in Colorado. *Journal of Mammalogy*. 54: 636-647.
- Gannon, W.L., Sikes, R.S., & THE ANIMAL CARE AND USE COMMITTEE OF THE AMERICAN SOCIETY OF MAMMALOGIST. 2007. Guidelines for the capture, handling, and care of mammals as approved by the American Society of Mammalogist. *Journal of Mammalogy*. 88: 809-823.
- Herrera, G. L., Gutierrez, E., Hobson, K.E., Altube, B., Diaz V. & Sanchez-Cordero, V. 2002. Sources of assimilated protein in five species of New World frugivorous bats. *Oecologia*. 133: 280-287.
- Lauenroth, W. K. and Milchunas, D. G. 1991. *Short-grass steppe*. Pp. 183-226 in, Natural grasslands: introduction and Western Hemisphere. Ecosystems of the World. Elsevier, New York.
- Schoeninger, M. J., DeNiro, C. J. & Tauber, H. 1983. Stable nitrogen isotope ratios of bone collagen reflect marine and terrestrial components of prehistoric human diet. *Science*. 220: 1381-1383.
- Stapp, P. 1998. A reevaluation of the role of prairie dogs in Great Plains grasslands. *Conservation Biology*. 12: 1253-1259.
- Stapp, P. 2002. Stable isotopes reveal evidence of predation by ship rats on seabirds on the Shiant Islands, Scotland. *Journal of Applied Ecology*. 39: 831-840.
- Stapp, P. 2007. Rodent communities in active and inactive colonies of black-tailed prairie dogs in shortgrass steppe. *Journal of Mammalogy*. 88: 241-249.
- Stapp, P., M.D. Lindquist and B. Van Horne. 2008. Ecology of mammals of the shortgrass steppe. Pages 132-180 in W.K. Lauenroth and I.C. Burke, editors. *Ecology of the shortgrass steppe: A long-term perspective*. Oxford University Press.
- Stapp, P., Polis, G. A., & Sanchez Pinero, F. 1999. Stable isotopes reveal strong marine and El Niño effects on island food webs. *Nature*. 401: 467-469.
- Streubel, D. P. & Fitzgerald, J. P. 1978. *Spermophilus tridecemlineatus*. *Mammalian Species*. 103: 1-5.
- Warne, W.R., Pershall, D.A., & Wolf, B.O. 2010. Linking precipitation and C3-C4 plant production to resource dynamics in higher trophic-level consumers. *Ecology*. 91: 1628-1638.
- Whicker, A. D. & Detling, J. K. 1988. Ecological consequences of prairie dog disturbances. *Bioscience*. 38: 778-785.
- With, K.A. 1994. The hazards of nesting near shrubs for a grassland bird, the McCown's Longspur. *Condor*. 96: 1009-1019.

The Effects of Age and Sexual Experience on the Mating Success of the Male House Cricket *Acheta domesticus*

Eric S. Peralta
Advisor: Dr. Sean E. Walker

Department of Biological Science, College of Natural Science and Mathematics, California State University, Fullerton, CA, USA

Abstract

Age and sexual experience are factors that have rarely been studied in insects. House cricket (*Acheta domesticus*) males have been studied extensively in regards to what type of acoustic signals females choose. However, acoustic signals are long-distance and are only part of the process of mate choice. During courtship, when the male is close to the female, numerous other factors could influence male success. We examined how male age and sexual experience impact mating success. We hypothesized that older males will have higher mating success than younger males and that sexually experienced males will have higher mating success than males with no experience. In the first experiment, virgin males of different ages were paired with virgin females. In the second experiment, males with varying degrees of sexual experience were paired with virgin females. Prior to this experiment, sexually mature males were placed in one of two conditions for 48 hours with 2 virgin females or no female partners. After this period, the males were isolated for 48 hours before being presented with a virgin female for observation. In each experiment, we measured the number of successful matings, number of attempted matings, and female latency to mating. Our results indicate that females make more attempts to mate with and have shorter latency to mating times with older males. Sexual experience appears to have no effect on female preference.

Introduction

Male crickets use acoustic signals (Phonotaxis) to attract females and initiate mating (Walker, 1957; Alexander, 1961; Crankshaw, 1979; Stout and McGhee, 1988; Wagner and Reiser, 2000). Additionally, larger male size may increase female preference (Gray 1997). Phonotaxis has been well studied

(Andersson, 1994) and because of its significance in female mate attraction, it is sometimes assumed that it is the only factor in male mating success. In house crickets, *Acheta domesticus*, having an attractive song does not always result in successful mating (Gray, 1997) and increased reproductive success for older male crickets has been seen in the field (Zuk and Simmons, 1997). Older male field crickets, *Gryllus veletis* and *Gryllus pennsylvanicus*, were found to attract more females than younger field crickets did in both simulated and natural field conditions (Zuk, 1987; Zuk 1988). Sexual selection suggests that older age can indicate good genes and therefore increase a male's reproductive success. Thus, it is possible that male age may be an important factor that influences female mate choice other than phonotaxis.

While little is known about the role that age plays in male mating success, even less is known about male sexual experience. Female age and sexual experience and their effects on mating have been studied to a higher degree. Female sexual experience in the fish, *Poecilia reticulata*, has been shown to cause no change in female preference (Kodric-Brown and Nicoletto, 2001). Additionally, it has been shown to decrease female preference for males in flies, *Anastrepha suspensa*, (Sivinski, 1984). Some studies have not been able to completely disentangle female age and sexual experience from each other (field crickets: Prosser et al. 1997). In *A. domesticus*, both female age and sexual experience have recently been found to influence mate choice (Mautz and Sakaluk, 2008). However, cricket male sexual experience has yet to be tested in regards to mating success. This study was carried out to determine the roles of age and sexual experience on male mating success in the house cricket, *Acheta domesticus*.

Methods

Crickets were reared from laboratory stock or obtained from Fluker Farms and maintained in our laboratory at CSUF. The laboratory stock was originally obtained from Fluker Farms. They were kept in 84 L containers at 18-24°C on a 12:12 light:dark cycle. Crickets were provided with egg cartons, moistened substrate, and cat food and water *ad libitum*. Males and females were removed from culture upon adult eclosion to ensure virginity. Crickets were then isolated into individual 15 cm x 15 cm x 5 cm containers and given cat food and water *ad libitum*.

Trials conducted examining the impact of age consisted of one virgin male and one virgin female and those conducted looking at the effects of experience had one presumably sexually experienced male and one virgin female. Each pair was observed for one hour or until successful mating occurred. Trials would end earlier if there was no acoustic signaling by the male after 30 minutes or no courtship song after 45 minutes.

Age

Males remained in their individual containers until they reached 1, 2, 3, 4, or 5 weeks post adult molt or age groups 1, 2, 3, 4, and 5 from hereon after. Twenty males were used per age group. Males were used in experiments on the day they turned each specific age or up to two days after. Females were aged between 8 and 16 days post adult molt. Trials were run between 12:00 pm and 9:00 pm between 21.3°C and 28.3°C with a mean temperature of 23.2°C.

Females were put into a 1-L container and allowed to acclimate for five minutes. After this period, a male was placed into the container while in a small vial, allowing him to see the female but not allowing him to come into contact with her. He was allowed to acclimate for three minutes. After this period, the male was released into the container with the female and observations began. The number of matings per age group, the number of trials with mating attempts per age group, and time until mating was measured. All trials were video recorded for later observations.

Sexual Experience

Males used in this experiment were all 2 weeks post-adult molt. Females were aged between 8 and 16 days post adult molt. When males reached the appropriate age, they were placed into one of two treatments: experience and no experience. Twenty males were used per age group. Males in the experience treatment were placed into a 1-L container with two virgin females for 48 hours during which time the male would acquire sexual experience. After this period, the male was again isolated into a 15 cm x 15 cm x 5 cm container with cat food and water *ad libitum* for 48 hours. After this 48 hour isolation, males were paired with a virgin female and observations began. Males in the no experience treatment underwent the same procedure but instead of being placed with two virgin females, they were placed by themselves. Trials were run between 5:00 pm and 9:30 pm between 22.3°C and 24.0°C with a mean temperature of 23.0°C. The number of matings per experience group, the number of trials with mating attempts per experience group, and time until mating was measured.

Results

Age

No significant relationship was found between the number of matings per age group (Figure 1). Age groups 1-4 each had 2 matings occur while age group 5 had 4 matings. There was a significant difference between age and the number of trials that had mating attempts per age group (Figure 2). Age group 1 had the fewest mating attempts with 2 while age group 5 had 9.

Total Number of Matings for Each Age Group

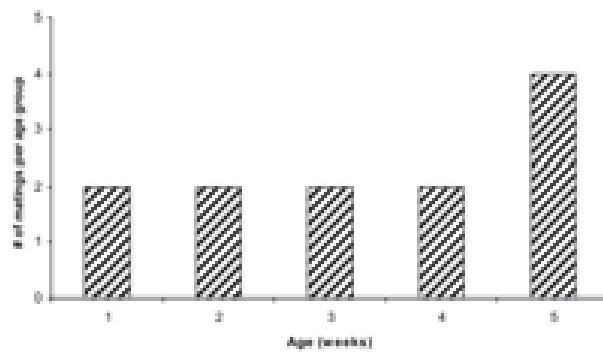


Figure 1: Total number of matings per age group. No significant relationship between the number of matings per age group was found (Logistic Regression, $\chi^2=1.15$, $P=0.2846$).

Mating Attempts by each Age Group

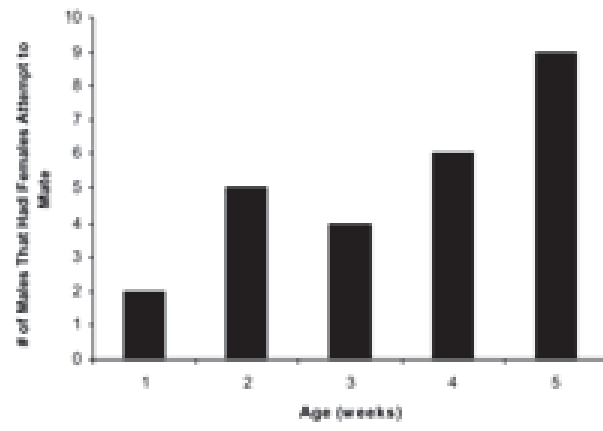


Figure 2: The number of trials that had attempted matings per age group. A significant relationship was found between trials with attempted matings and age (Logistic Regression, $\chi^2=5.52$, $P=0.0188$).

The time until mating significantly decreased as age increased (Figure 3). Males in age groups 1-3 took anywhere from about 2-50 minutes to successfully mate. Excluding one 3-week old male that mated in under 3 minutes, the males in age groups 1-3 took from 10-50 minutes to successfully mate. Males in age groups 4-5 all took under 6 minutes.

Sexual Experience

Males with and without sexual experience were similar in number of matings per age group and number of trials with mating attempts (Figures 4, 5). The number of matings per age group for experienced and inexperienced males was 5 and 6, respectively. The number of trials with mating attempts for experienced and inexperienced males were 7 and 8, respectively. Additionally, there appears to be no significant difference between sexually experienced and inexperienced males in time until mating (Figure 6).

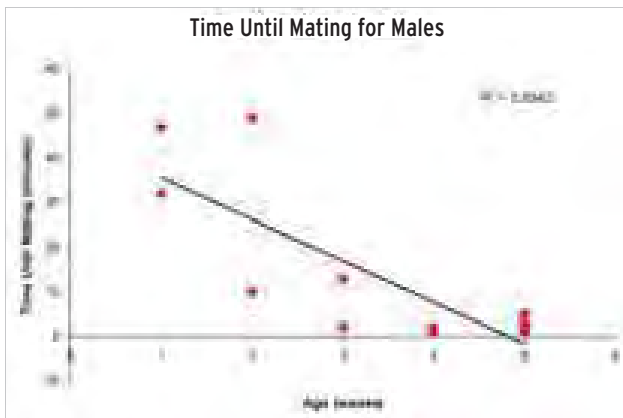


Figure 3: The time until each successful mating per age group. A significant relationship between age and time until mating for individuals that mated (Linear Regression, $t(9)=-4.87, P=0.0009$)

Discussion

Male age appears to influence female preference. Although the number of matings per age group was not significantly different from each other, older age groups showed a higher number of attempted matings and shorter latency to mating. This is consistent with the results from other field crickets (Zuk, 1987; Zuk 1988; Zuk and Simmons, 1997). However, as opposed to just showing preference for age as in Zuk (1987, 1988), this study shows actual courtship and mating interactions between males and females. Age groups 4 and 5 were the most successful in regards to number of attempted matings and latency until mating. These results agree with the sexual selection hypothesis that older males may indicate higher genetic quality.

An important factor in successful mating is the use of phonotaxis during courtship. Although this study did not examine calling or courtship song, its influence should not be omitted. The field cricket, *Gryllus campestris*, has been found to change their calling song to a more attractive song as they age (Jacot

Number of Trial With Mating Attempts per Experience Group

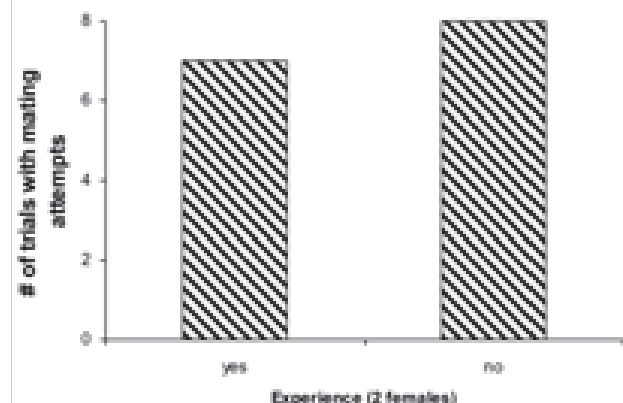


Figure 4: The number of matings per experience group.

Number of Matings per Experience Group

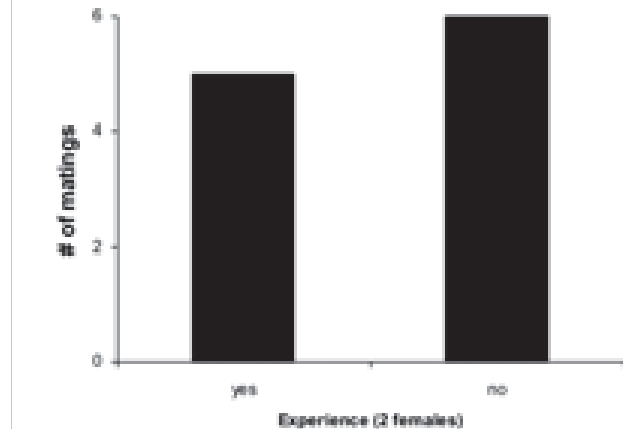


Figure 5: The number of trials with mating attempts per experience group.

et al., 2007). However, in *A. domesticus*, females become less selective for song as they age (Walikonis et al., 1991; Gray, 1999) which may indicate that males do not change their song. Since the age of all of the females used in this experiment was controlled for, their preference for song should not vary and they should base their decisions on additional criteria, in this case, age. The greater number of successful matings and shorter latency to mating for older males in this experiment support the importance of age in female mate choice.

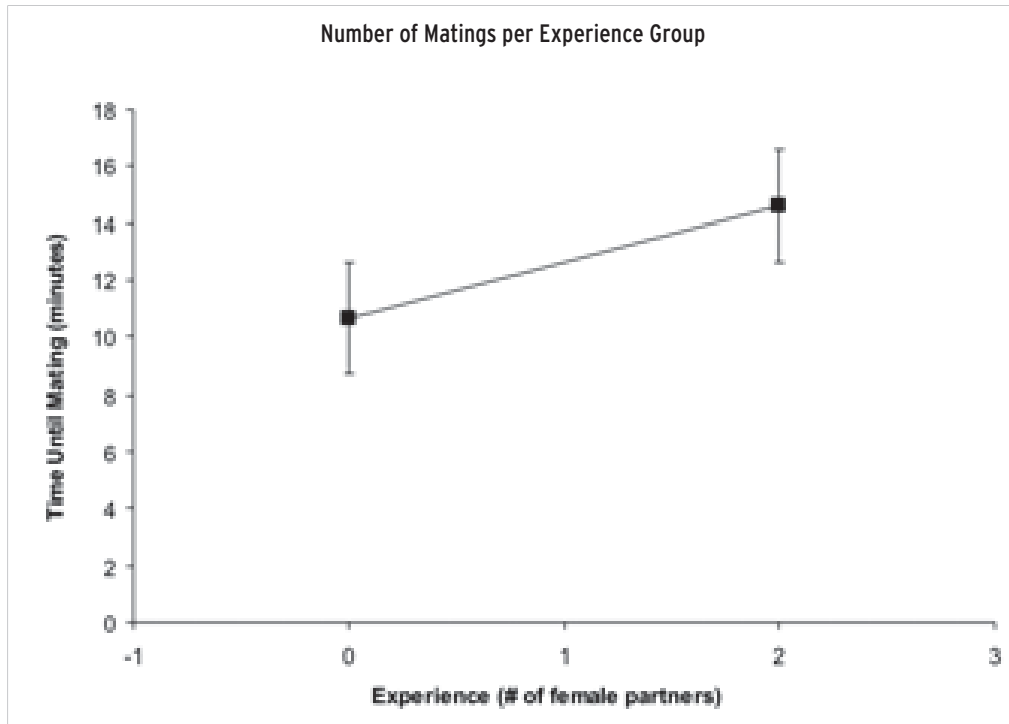


Figure 6: Time until mating for sexually experienced and non-experienced males. (T-test, $P=0.6666$; 0 Experience ($n=6$), 2 Experience ($n=5$))

Sexual experience does not appear to change female preference or male success. The number of matings per experience group, number of mating attempts, and latency to mating were similar and showed no significant difference between experience groups. This is consistent with the studies by Kodric-Brown and Nicoletto (2001) and Sivinski (1984). Mautz and Sakaluk (2008) found that female mate choice can be influenced by the age and experience of the females but these factors had been controlled in the experiment. The females were all of the same age and experience.

The males in the experience experiment were two weeks old when they began their isolation with two females. By the time they were finished and ready to be observed with a virgin female, they were 3 weeks old. Based on the data from the age experiment, these males would not be the very attractive. While gaining experience with two females for 48 hours, it is possible that some of the males may not have even mated at all. In fact, during this 48 hour period, only a few females were observed with a spermatophore attached to them. Still, they were observed calling and courting continually and would have gained some experience interacting with females. Since the females were young and selective and had been isolated since adult eclosion, their decisions about mating with the

experienced males should not be based on previous mating experience. If mating with experienced males was beneficial to the female or her offspring, higher mating success for experienced males should have been observed despite the young age.

There are many extrinsic factors that influence female mate choice. These include predation risk (Hedrick and Dill, 1993), parasite load (Zuk, 1988), and temperature (Kindle et al., 2009). The absence of predators and parasites in this experiment helps to support the effects of either male age or sexual experience as the critical factors that influencing mate choice. We did have low frequency of mating in all treatments. The mean temperatures for the age and sexual experience trials were 23.2°C and 23.0°C, respectively. Kindle et al. (2009) found that the highest female mating frequency in *A. domesticus* and *Gryllodes sigillatus* occurred at 32°C. Although not the objective of this study, it is possible that temperature interacts with male age or experience and manipulations done at higher temperatures could result in stronger or weaker effects than seen here.

Acknowledgements

Thank you to the lab of Dr. Sean Walker and NSF-DBI-UMEB #060292.

References

- Alexander, R. D. 1961. Aggressiveness, territoriality, and sexual behavior in field crickets (Orthoptera:Gryllidae). *Behaviour*, 17, 130-223
- Andersson, M. 1994. Sexual Selection. Princeton, New Jersey: Princeton University Press.
- Crankshaw, O.S. 1979. Female choice in relation to calling and courtship songs in *Acheta domesticus*. *Animal Behaviour*, 27, 1274-1275
- Gray, D.A. 1997. Female house crickets, *Acheta domesticus*, prefer the chirps of large males. *Animal Behaviour*, 54, 1553-1562
- Gray, D.A. 1999. Intrinsic factors affecting female choice in house crickets: time cost, female age, nutritional condition, body size, and size-relative reproductive investment. *Journal of Insect Behavior*, 12, 691-700
- Hedrick, A.V., and L.M. Dill. 1993. Mate choice by female crickets is influenced by predation risk. *Animal Behaviour*, 46, 193-196
- Jacot, A., H. Scheuber, and M.W.G. Brinkhof. 2007. The effect of age on sexually selected acoustic display. *Ethology*, 113, 615-620
- Kindle, T.K., K.M. Johnson, T.M. Ivy, C.B. Weddle, and S.K. Sakaluk. 2009. Female mating frequency increases with temperature in two cricket species, *Gryllodes sigillatus* and *Acheta domesticus* (Orthoptera: Gryllidae). *Canadian Journal of Zoology*, 84, 1345-1350
- Kodric-Brown, A., and P.F. Nicoletto. 2001. Age and experience affect female choice in the guppy (*Poecilia reticulata*). *The American Naturalist*, 157, 316-323
- Mautz, B.S., and S.K. Sakaluk. 2008. The effects of age and previous mating experience on pre- and post-copulatory mate choice in female house crickets (*Acheta domesticus* L.). *Journal of Insect Behavior*,
- Prosser, M.R., A.M. Murray, and W.H. Cade. 1997. The influence of female age on phonotaxis during single and multiple song presentations in the field cricket, *Gryllus integer* (Orthoptera: Gryllidae). *Journal of Insect Behavior*, 10, 437-449
- Savinksi, J. 1984. Effect of sexual experience on male mating success in a lek forming tephritid *Anastrepha suspensa* (Loew). *Florida Entomologist*, 67, 126-130
- Stout, J.F., and R. McGhee. 1988. Attractiveness of the male *Acheta domesticus* calling song to females. II. The relative importance of syllable period, intensity, and chirp rate. *Journal of Comparative Physiology*, 164, 277-287
- Wagner, W.E., and M.G. Reiser. 2000. The importance of calling song and courtship song in female mate choice in the variable field cricket. *Animal Behaviour*, 59, 1219-1226
- Walikonis, R., D. Schoun, D. Zacharias, J. Henley., P. Coburn, and J. Stout. 1991. Attractiveness of the male *Acheta domesticus* calling song to females. III. The relation of age-correlated changes in syllable period recognition and phonotactic threshold to juvenile III biosynthesis. *Journal of Comparative Physiology*, 169, 751-764
- Walker, T.J. 1957. Specificity in the response of female tree crickets (Orthoptera: Gryllidae: Oecanthinae) to calling songs of the males. *Annals of the Entomological Society of America*, 50, 626-636
- Zuk, M. 1987. Variability in attractiveness of male field crickets (Orthoptera: Gryllidae) to females. *Animal Behaviour*, 35, 1240-1248
- Zuk, M. 1988. Parasite load, body size, and age of wild-caught male field crickets (Orthoptera: Gryllidae): effects on sexual selection. *Evolution*, 42, 969-976
- Zuk, M., & L.W. Simmons. 1997. Reproductive strategies the crickets (Orthoptera: Gryllidae). *Mating Strategies in Insects and Arachnids* : 89-109

Physiological differences of two desert shrubs across differently-aged substrates in the Mojave Desert

Department of Biological Science, College of Natural Science and Mathematics, California State University, Fullerton, CA, USA

Karolis Raudys
Advisor: Dr. Darren Sandquist

Parameter	Y1	Y2	II	II
Substrate age (years)*	1-200	3k-16k	40k-110k	140k-300k
Substrate type*	Active wash Fluvial clay/silt	Eolian silt	Argillitic horizon	Vesicular horizon
Dominant vegetation*	<i>H. salsola</i> <i>L. tridentata</i> <i>A. dumosa</i>	<i>L. tridentata</i> <i>A. dumosa</i>	<i>T. schidigera</i> <i>L. tridentata</i> <i>A. dumosa</i>	<i>T. schidigera</i> <i>L. tridentata</i> <i>A. dumosa</i>

*Based on classification in Miller et al. 2009 (k = thousand)

Table 1: Description of study sites under investigation.

Abstract

Desert environments are not often considered to be diverse ecosystems with marked differences in the productivity of the inhabiting biota. However, detailed investigations of the underlying physiology of desert plants suggest that this perception is overly simplified. In this study, we explored variation of productivity over small spatial scales using two dominant Mojave Desert shrubs (*Larrea tridentata* and *Ambrosia dumosa*) across four differently-aged substrates. We examined leaf-level physiological diversity over smaller spatial scales than previous studies, and predicted that plants on intermediate aged substrates (3,000 to 16,000 years) would show the best physiological performance due to these soils having the most favorable resource conditions. Although there were clear differences in plant performance between closely-neighboring substrates that spanned the 300,000 year chronosequence, we found that plants on intermediate-aged substrates actually had the lowest individual performance. This result may be explained by the influence of substrate on other factors, such as plant abundance and competition, but nonetheless demonstrates that diversity of productivity is present on small spatial scales and coupled with substrate heterogeneity in this desert system.

Introduction

Deserts represent one of the most challenging and environmentally stressful habitats on the planet, however, many plant species have successfully adapted to these harsh ecosystems. In the Mojave Desert of North America two shrub species, *Larrea tridentata* and *Ambrosia dumosa*, are particularly successful, seeming to expand endlessly across the desert horizon, even into other neighboring North American deserts. Although these expanses appear to cover similar looking ranges of substrate, small-scale differences can be seen after a closer and more attentive assessment. Such structural subtleties can have an effect on the success of the plants occupying them (Hamerlynck et al. 2002).

While previous studies have investigated plant performance differences across separate desert communities and large-scale topographic features (Hamerlynck et al. 2000), our aim was to examine potential differences at a much smaller spatial scale as mediated by diversity in substrate ages (Table 1).

Identifying variation in physiological properties across these substrates will allow us to gain a greater understanding of how the age and physical features of different substrates can affect overall plant performance. We predict that indicators

of plant performance and water status, such as specific leaf area, water potential, stomatal conductance, and photosynthetic rate, would all be greatest for plants growing on the Y2 substrate because of greater abundance of nutrients and greater water retention (Hamerlynck et al. 2000). Performance is predicted to decrease on Y1 and I1 substrates, and be lowest on I2 substrates because of decreased water retention capabilities of the substrates and less abundant nutrients.

Materials and Methods

The field site was located in the Mojave *National Preserve* along the Kelso-Cima road. The landscape here is a vast bajada composed of various aged substrates inter-spersed by washes and dominated by *L. tridentata* and *A. dumosa* plants. Specific study sites were located upslope from the Kelso-Cima road and the adjacent railroad so as to avoid disturbance caused by these anthropogenic features.

Using the ArcPad version of an Arc-GIS computer program (ESRI, Redlands, CA) we created polygons from the boundaries of various aged substrates based on a map published by Miller (2009). Polygons were grouped into four substrate age categories (in years): Y1: 1-200, Y2: 3,000-16,000, I1: 40,000-110,000, and I2: 140,000-300,000. Then, four polygons were selected for each substrate type to be sampled. These constitute our replicate plots for analyses. Plots belonging to the same age categories were seldom in close proximity to one another in order to have a wider representation of the whole study site. Within each plot studied, five plants each of the two dominant species (*L. tridentata* and *A. dumosa*) were selected for sampling and marked with an orange ribbon and pin flag for consistent identification.

Data collection took place during the first four days of April, 2009. Each day, one plot of each substrate age was sampled. The data collection process was virtually identical each sampling day. It began at approximately 2:30 am with measurement of pre-dawn water potential using a pressure chamber (PMS Instruments, Albany, OR) for three plants of each species in each plot. Pre-dawn water potential represents a plant's highest water status in a given day. At approximately 12:00 pm we measured stomatal conductance, which indicates a plant's water status and flux, on five

Substrate	SLA (youngest)	A_{max} ($\mu\text{mol m}^{-2} \text{s}^{-1}$)	Pre-dawn Ψ (MPa)	Midday Ψ (MPa)	g_{stom} ($\text{mm}^2 \text{ s}^{-1}$)					
	Lat	Amdu	Lat	Amdu	Lat					
Y1	4.88 (0.33)	6.39 (0.29)	-0.13 (-0.09)	-0.26 (-0.06)	-0.79 (-0.09)	-1.09 (-0.12)	114.91 (14.86)	208.76 (24.64)		
Y2	4.67 (0.12)	5.87 (0.09)	-0.09 (-0.06)	-0.19 (-0.06)	-0.89 (-0.12)	-1.29 (-0.16)	74.22 (11.54)	103.00 (10.45)		
I1	4.98 (0.19)	6.58 (0.21)	12.73 (8.12)	29.68 (19.16)	-2.76 (-0.26)	-1.81 (-0.99)	-4.28 (-0.19)	-2.88 (0.27)	98.79 (14.44)	141.94 (16.52)
I2	3.41 (0.20)	6.32 (0.09)	15.29 (11.62)	29.64 (19.31)	-2.26 (-0.16)	-1.63 (-0.20)	-3.89 (-0.13)	-2.60 (0.19)	99.31 (6.37)	141.82 (19.66)

Note: SLA = specific leaf area; A_{max} = net photosynthesis; Ψ = water potential; g_{stom} = stomatal conductance.

Table 2: Mean values ($\pm 1 \text{ SE}$) for carbon and water use traits of *Larrea tridentata* (Latr) and *Ambrosia dumosa* (Amdu) across a substrate age gradient (youngest to oldest = Y1 to I2; see Table 1).

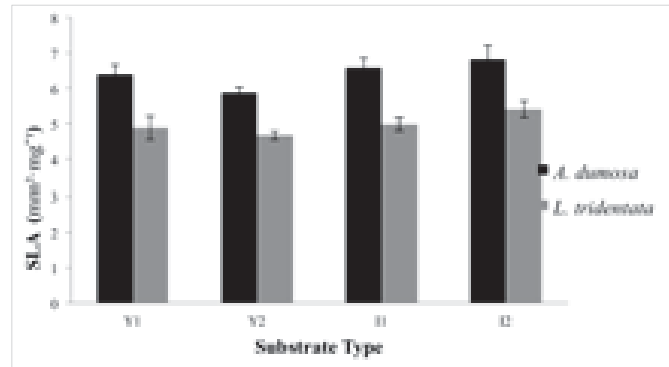


Figure 1: Mean ($\pm 1 \text{ SE}$) specific leaf area of *Ambrosia dumosa* and *Larrea tridentata* across the four substrate age types.

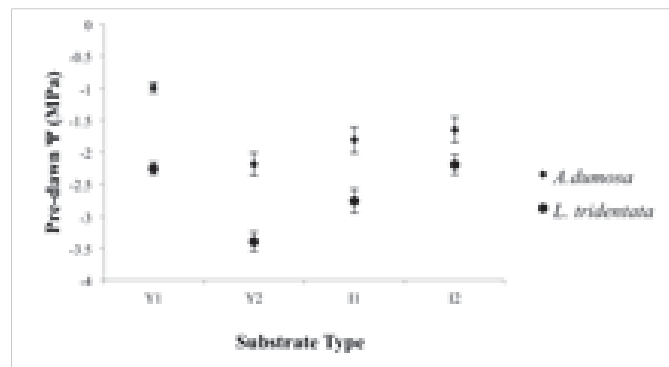


Figure 2: Mean ($\pm 1 \text{ SE}$) pre-dawn water potentials of *Ambrosia dumosa* and *Larrea tridentata* across the four substrate age types.

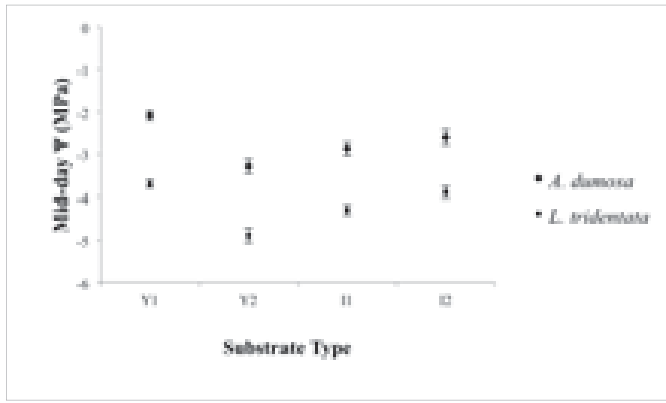


Figure 3: Mean (± 1 SE) mid-day water potentials of *Ambrosia dumosa* and *Larrea tridentata* across the four substrate age types.

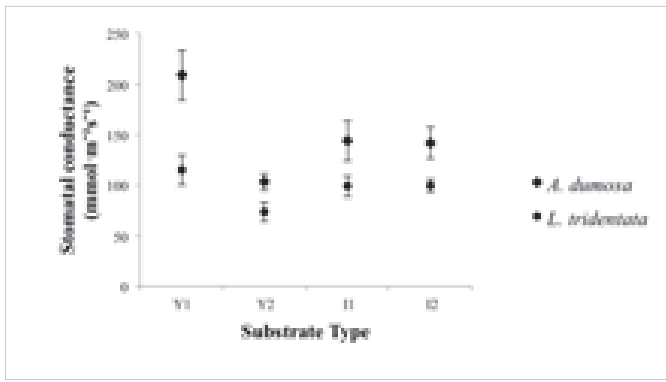


Figure 4: Mean (± 1 SE) stomatal conductance of *Ambrosia dumosa* and *Larrea tridentata* across the four substrate age types.

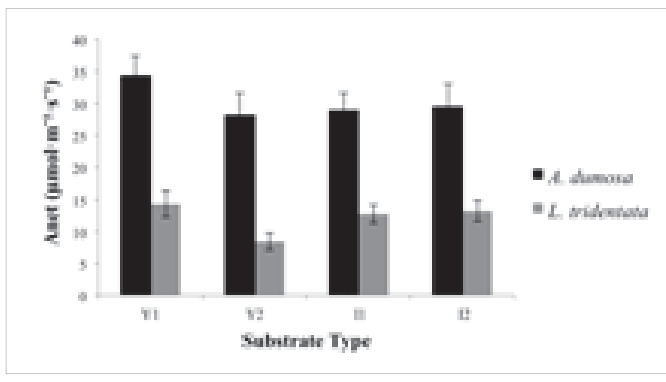


Figure 5: Mean (± 1 SE) photosynthetic rates of *Ambrosia dumosa* and *Larrea tridentata* across the four substrate age types.

plants of each species and photosynthetic rates on three plants of each species using a steady state diffusion porometer (Decagon Devices, Pullman, WA) and a LiCor 6400 portable photosynthesis system (LI-COR, Lincoln, NE), respectively. In the process of collecting this data, leaf and stem samples were also collected from the same five plants. Measurements of mid-day water status for the day, started at approximately 2:00 pm and used the same plants as those in the pre-dawn collection period. The same procedures were followed for four consecutive days so that each substrate type had four representative plots.

In the lab, the mass and area of the leaf samples were measured and used to determine specific leaf area (mass/area:SLA) of each plant. SLA is an indicator of plant allocation and carbon gain.

Results and Discussion

In contrast to our predictions, all indicators of physiological performance were poorest for plants of the Y2 substrate, and this was true for both *L. tridentata* and *A. dumosa* (Table 2, Figures 1-5). Surprisingly, plants on the youngest substrates, Y1, showed the highest values for performance. This was unexpected because the lack of soil development in Y1 substrates precludes high nutrient accumulation or water retention. The older substrates, I1 and I2, showed intermediate values compared to Y1 and Y2.

The unexpectedly poor performance of plants on the Y2 substrate suggests the possible influence of other factors that affect plant physiological performance, such as competition and variability within the substrate type. Indeed, plant density and cover were visually greater on the Y2 substrates than on others (per observation), which may cause greater competition in spite of more abundance in nutrient and water resources here. Furthermore, plants are largely absent from the most active washes of Y1 substrates, creating localized areas with virtually no competition and abundant water, albeit low nutrient availability. These confounding factors will be further considered during the continuation of our study; however, our present results do indicate a clear difference in plant physiological performance across a small, desert landscape with what otherwise appears as total spatial homogeneity.

Acknowledgements

I would like to thank Dr. Sandquist for his guidance and support throughout this whole process. I would also like to express gratitude to all current and former lab members who have helped complete this project: Miguel, April, Matthew, Dorian, Joe, and Vickie.

References

- Hamerlynck, E.P., McAuliffe, J.R., McDonald, E.V., and S.D. Smith. (2002) Ecological responses of two Mojave desert shrubs to soil horizon development and soil water dynamics. *Ecology*, 83: 768-779.
- Hamerlynck, E.P., McAuliffe, J.R., and S.D. Smith. (2000) Effects of surface and sub-surface soil horizons on the seasonal performance of *Larrea tridentata* (creosotebush). *Functional Ecology*, 14: 596-606.
- Miller, D.M., Bedford, D.R., Hughson, D.L., McDonald, E.V., Robinson, S.E., and K.M. Schmidt. (2009) Mapping Mojave Desert ecosystem properties with surficial geology. *The Mojave Desert: Ecosystem Process and Sustainability*, 225-251.
- Schwinning, S., Sandquist, D.R., Miller, D.M., Bedford, D.R., Phillips, S.L., and J. Belnap. (2011) The influence of stream channels on distributions of *Larrea tridentata* and *Ambrosia dumosa* in the Mojave Desert, CA, USA: patterns, mechanisms and effects of stream redistribution. *Ecohydrology*, 1: 12-25.
- Wright, I.J., Reich, P.B., and M. Westoby. (2001) Strategy shifts in leaf physiology, structure and nutrient content between species of high- and low-rainfall and high- and low-nutrient habitats. *Functional Ecology*, 15: 423-434.

Effects of Cactus Removal on Grassland Rodents

Department of Biological Science, College of Natural Science and Mathematics, California State University, Fullerton, CA, USA

Leslie Herington
Advisor: Dr. Paul Stapp

Abstract

Prickly-pear cactus (*Opuntia polyacantha*) is often considered a pest by livestock producers in shortgrass steppe because, at high densities, it can reduce the amount of forage available to cattle. Removal of cactus by herbicide has been proposed as a method to increase forage production, but the consequences of cactus removal for other native plants and animals have not been determined. In June 2009, herbicide (Tordon 22k) was aerially sprayed on a privately owned 160-ha pasture adjacent to the Pawnee National Grasslands (PNG) in north-central Colorado. During June and July 2008–2010, small mammals were live-trapped before and after spraying at 3 sites in the treated pasture ("removal") and at 3 "control" sites in nearby untreated pastures on the PNG. One year after herbicide application, percent cover of dead and dying cactus and bare ground was significantly higher on the removal sites, while the number of cactus flowers and buds was higher on the control plots. Ord's kangaroo rats (*Dipodomys ordii*), the most abundant nocturnal rodent in the area, reached comparable densities on the control and removal sites, and there was no significant difference in kangaroo rat densities between treatments after herbicide application. However, significantly fewer female kangaroo rats were in reproductive condition on removal sites than on controls, suggesting that the loss of cactus seeds, a potentially important food item for this granivore, may ultimately reduce population densities once the cactus has been entirely removed. In contrast, northern grasshopper mice (*Onychomys leucogaster*) tended to be more abundant on removal sites than on controls, perhaps in response to the increase in bare ground and insects. Additional monitoring of both plant and rodent populations may provide insight into the potential ecological consequences of cactus control.

Introduction

Livestock grazing is the predominant land use in the Central Great Plains of northern Colorado. One method of land modification to increase forage production for cattle is the removal of prickly-pear cactus (*Opuntia polyacantha*), which is unpalatable and, at high densities, can impede grazing. Prickly pear, however, provides vital vertical structure in the otherwise short vegetation and acts as grazing refuge for seeds and young plants (Robello et

al. 2002). The loss of cover for herbaceous plants and seeds has caused significant decline of plant diversity in other grasslands (Callaway et al. 2000). Seed banks associated with cactus provide a food source for granivorous rodents (Montiel and Montaña 2003). Prickly pear may also provide cover from predation and wind for small mammals and nesting cover for songbirds (Riegel 1941; Knopf 2001; Hernandez 2003).

Ord's kangaroo rats (*Dipodomys ordii*) and northern grasshopper mice (*Onychomys leucogaster*) are the most common nocturnal rodents in shortgrass steppe in northern Colorado (Stapp et al. 2008). Ord's kangaroo rat is a medium-sized kangaroo rat (52 g) that is often associated with grasslands in sandy soils (Garrison and Best 1990). It is mostly granivorous, relying on harvested and stored seeds for food (Flake 1973; Garrison and Best 1990). In contrast, northern grasshopper mice are smaller (34 g), insectivorous, and are associated with heterogeneous cover, including patches of bare ground (Harriman 1973; Stapp 1997). Both species tend to be more abundant in areas with greater vegetation structure (Stapp et al. 2008) and therefore could be negatively affected by the loss of prickly pear cactus.

In June 2009, an herbicide (picloram, sold as Tordon 22k) was aerially sprayed on a privately owned pasture near the Pawnee National Grasslands in north-central Colorado to remove cactus, with the hopes of increasing cover of dominant grasses such as blue grama (*Bouteloua gracilis*), buffalograss (*Buchloe dactyloides*), and western wheatgrass (*Agropyron smithii*). Picloram is dicot-selective, so grasses are not directly influenced by application of this herbicide; however cactus, forbs and shrubs may be affected (Tu et al. 2001).

I studied the indirect effects of cactus removal on the abundance and demography of rodents over a 3-year period. I used mark-recapture methods to estimate the density of rodents at sites where cactus was removed and nearby grassland sites where no herbicide was applied. I also measured vegetation and other habitat characteristics at removal and control sites to determine the effects of herbicide on cactus and other plants. I predicted that kangaroo rat densities would decrease in response to cactus removal, whereas grasshopper mice populations would increase.

Species	Unique Captures (M:F)		Weight (g)	
	Cactus Removal	Control	Cactus Removal	Control
Ord's Kangaroo Rat				
Spring '08	12 (3:9)	22 (13:9)	65.6 ± 0.3	62.0 ± 0.6
Summer '08	11 (6:5)	21 (12:9)	62.0 ± 2.3	64.3 ± 2.6
Spring '09	21 (12:9)	13 (5:8)	64.1 ± 2.3	66.0 ± 3.7
Summer '09	15 (11:4)	30 (16:14)	70.3 ± 1.2	67.1 ± 1.6
Spring '10	23 (17:6)	40 (18:22)	62.6 ± 0.8	64.3 ± 1.6
Summer '10	14 (9:5)	24 (14:10)	68.5 ± 2.1	73.7 ± 0.7
Northern grasshopper mouse				
Spring '08	5 (3:2)	4 (2:2)	24.9 ± 14.5	30.2 ± 2.2
Summer '08	4 (2:2)	5 (2:3)	28.8 ± 11.8	26.8 ± 4.8
Spring '09	2 (1:1)	3 (2:1)	31.0 ± 23.3	22.8 ± 4.8
Summer '09	10 (4:6)	1 (1:0)	31.7 ± 9.3	35.0 ± .
Spring '10	15 (12:3)	8 (5:3)	31.8 ± 9.3	35.0 ± 2.4
Summer '10	18 (12:6)	3 (2:1)	32.4 ± 9.4	39.7 ± .

Table 1: Total number of unique individuals, sex ratio, and mean weight (\pm SE) of Ord's kangaroo rats and northern grasshopper mice captures on 2 (2008) or 3 (2009, 2010) 0.81-ha grids on removal and control areas. Herbicide was sprayed on removal grids between June and July 2009, as indicated by dashed lines. Sites were trapped for 4 consecutive nights in each session.

Methods

My study was conducted near Briggsdale, Colorado, which is 40 km northeast of Greeley. The climate is semiarid, with a mean annual precipitation of 320 mm (USDA-ARS, Central Plains Experimental Range). The average precipitation during the time of study between 2008 – 2010 was 376 mm (USDA-ARS, Central Plains Experimental Range). The vegetation is classified as shortgrass steppe, which is dominated by two species of warm-season grass, *Bouteloua gracilis* and *Buchloë dactyloides*. Taller, cool-season grasses, half shrubs, forbs, and prickly pear are also present (Lauenroth and Burke, 2008).

Rodents were live-trapped on replicate 0.81-ha grids in the cactus removal pasture (Ball Ranch) and adjacent untreated control areas on the adjacent PNG. Grids consisted of 49 extra-long Sherman traps (H.B. Sherman Traps, Inc., Tallahassee, Florida) in a 7 by 7 array with 15-m spacing between traps. Four grids (2 removal, 2 control) were trapped in June and July 2008, with an additional pair of grids sampled during in June and July of 2009 and 2010. Herbicide was sprayed on the entire treated pasture immediately following the June 2009 trapping session.

Each grid was trapped 4 consecutive nights in each trapping session. Traps were baited using peanut butter and oats and were opened at dusk and closed at dawn to ensure only nocturnal animals were captured. All animals were given a uniquely numbered aluminum ear tag (National Band and Tag Co.) and weighed. Age, sex, and reproductive status were also noted. Sex was determined by visual inspection of external genitalia. Males were considered reproductively active if they had enlarged testes; a female was judged to be breeding condition if it had a perforate or plugged vagina, or if it had enlarged teats. Ear tissue and whisker samples were also

taken from each kangaroo rat captured in summer 2010 for stable isotope analysis of diet (results not reported here). All handling procedures and tissue collection were approved by the IACUC at California State University Fullerton, following procedures recommended by the American Society of Mammalogists (Gannon et al. 2007).

I used DENSITY (v. 3.3, Efford 2005) to estimate rodent population size using closed mark-recapture models. Density was estimated using DENSITY, with population size estimated using the algorithms from CAPTURE and effective trapping area calculated based on the mean maximum distance traveled between captures, which was used to estimate population density (Otis et al. 1978). I used the model selection criteria in DENSITY to select the best fitting model to estimate population size.

Habitat and vegetation measurements were recorded in 2010 at 10-m intervals along 3 random transects in each of the 6 grids (30 points per grid). The area of the mounds created by kangaroo rats was estimated by measuring the longest distance across the mound and multiplying it by the perpendicular measurement. Mound dimensions were only recorded for points with active mounds within 30 m of the point, and mounds was included only once in calculations of mean mound area for each grid. Percent canopy cover of bare ground, litter, cactus, and plants other than cactus were estimated in a 0.1 m² quadrat at each point. I also measured the height of the nearest grass, forb, shrub, and cactus plant at a random location associated with each transect point. I recorded percent cover of prickly pear cactus, using the color of cladodes as an index of an individual plant's condition. A green cladode was clearly alive, a yellow-green cladode

was indicative of the beginning stages of dying, yellow was nearly dead, and a gray cladode was classified as dead. The latter 3 categories were combined during analysis to form a "dead and dying cactus" cover category. I used Student's t-tests in MS Excel 2007 to compare population densities, numbers of individuals, vegetation, and habitat characteristics between removal and control sites as well as populations densities between.

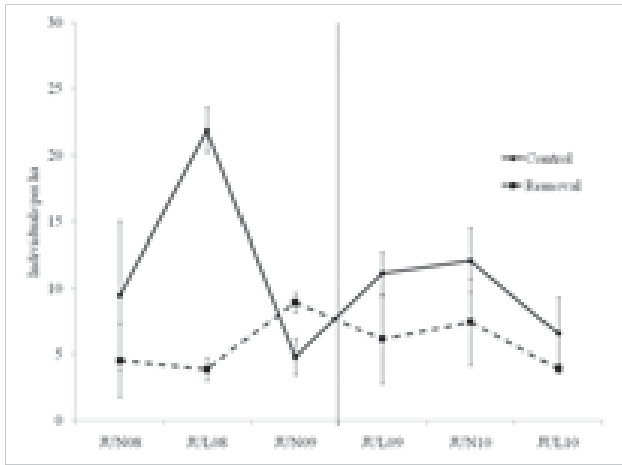


Figure 1: Estimated population densities (\pm SE) of Ord's kangaroo rat on control plots and cactus removal plots. Densities were estimated in DENSITY (Efron and Borchers, 2008) using population size estimates generated using the null model (M_0) and effective trapping area estimated by the MMDM2. The vertical dotted line represents approximate time of spraying in June 2009.

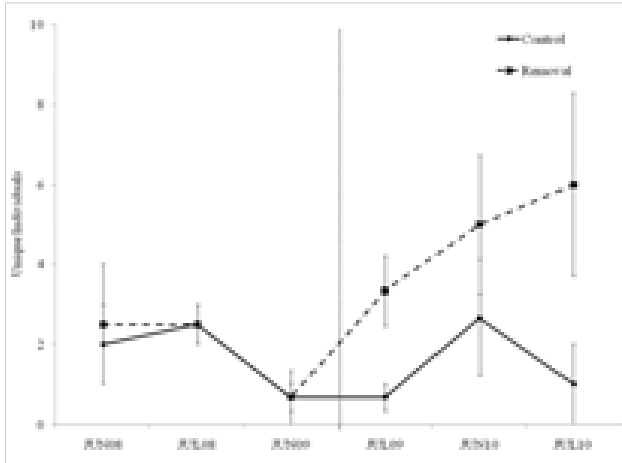


Figure 2: Mean number of individual grasshopper mice caught on control and cactus removal grids (\pm SE). The vertical dotted line represents approximate time of spraying in June 2009.

Results

Over the 6 trapping sessions between 2008 and 2010, a total of 137 unique Ord's kangaroo rats, 37 northern grasshopper mice, 2 deer mice (*Peromyscus maniculatus*), 1 plains harvest mouse (*Reithrodontomys montanus*), and 1 olive-backed pocket mouse (*Perognathus fasciatus*) were captured and released. Thirteen-lined ground squirrels (*Spermophilus tridecemlineatus*, 241 individuals) were also captured, but mostly in 2008 and 2009, when traps remained open for longer in the morning.

Collectively, more kangaroo rats were captured on the control sites than on the removal sites in 5 of the 6 trapping sessions (Table 1). On average, kangaroo rats tended to be larger (heavier) on control than removal sites in 5 of the 6 sessions. In contrast, northern grasshopper mice were more numerous on the removal sites during 4 of 6 trapping sessions, but there were no significant differences in body weight.

There were sufficient numbers of recaptures to estimate population sizes, and therefore densities, of Ord's kangaroo rats only. In most trapping sessions, the null model (M_0 ; no variation in capture probability) was selected by DENSITY as the best fitting model to estimate population size; however, other models were selected in a few other cases. Population densities of kangaroo rats varied greatly among sites within each treatment, but there were no significant differences in mean density between treatments over time (T-test; $P \geq 0.05$; Fig. 1). Conversely, the number of individual grasshopper mice captured increased after cactus removal in June 2009 and remained higher than on control sites throughout 2009 and 2010 (T-test; $P < 0.05$; Fig. 2). The proportion of female kangaroo rats in a reproductive condition varied between treatments following the removal of cactus (T-test; $P < 0.05$; Fig. 3). There was no trend in the proportion of female grasshopper mice in a reproductive condition between sites before and after treatment.

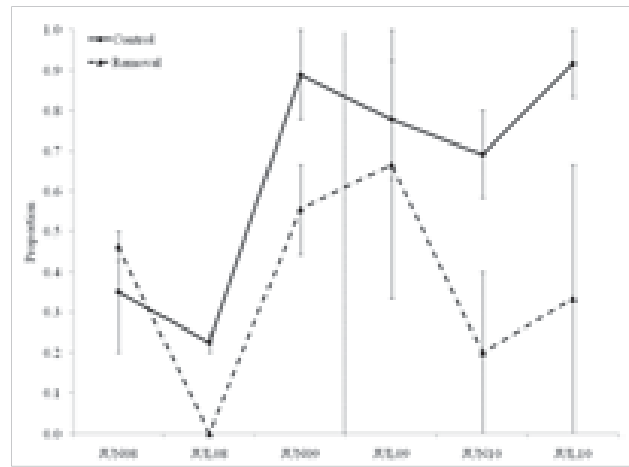


Figure 3: Mean proportion (\pm SE) of adult female Ord's kangaroo rats in reproductive condition on control and cactus removal grids. The vertical dotted line represents approximate time of spraying in June 2009.

	Cactus Removal		Control		P-value
	Mean	± SE	Mean	± SE	
Proportion					
Bare ground	40.9	± 0.8	28.2	± 1.0	0.050
Plants (excluding cactus)	37.2	± 1.7	48.1	± 4.1	0.072
Litter	3.6	± 1.2	5.2	± 0.8	0.321
Cactus	16.7	± 1.0	20.2	± 2.3	0.230
Live (green) cactus	13.5	± 4.8	74.1	± 5.3	0.272
Dead/dying cactus	88.0	± 6.2	26.0	± 5.3	0.002
Cactus flowers and buds (m^{-2})	0.4	± 0.3	12.8	± 2.6	0.009
Area of kangaroo rat mounds (m^2)	37.2	± 19.0	15.0	± 5.7	0.526
Height (cm)					
Forb	19.5	± 2.2	17.8	± 1.5	0.547
Shrub	49.3	± 3.2	31.5	± 1.9	0.009
Grass	24.3	± 1.8	15.5	± 1.6	0.021
Prickly pear cactus	6.7	± 1.0	8.9	± 0.1	0.097

Table 2: Percent canopy cover of plant functional groups, density of cactus, flowers and buds, mean plant height, by functional group, and the area of kangaroo rat mounds in removal and control sites in 2010. Values are mean \pm SE ($n = 3$ sites/treatment). P-values are results of Student's t-tests to compare means between removal and control sites.

In 2010, dead and dying cactus and bare ground made up a significantly greater proportion of canopy cover on the removal sites than controls (T-test; $P < 0.05$; Table 2). Plant cover, excluding cactus, was significantly greater on control sites, and more of the cactus in control areas had buds or were flowering (T-test; $P < 0.05$). Shrubs and grasses were significantly taller on the removal plots, whereas height of forbs and prickly pear did not differ. The area of kangaroo rat mounds was significantly greater on the removal sites.

Discussion

Contrary to my prediction, population densities of Ord's kangaroo rats did not decrease in response to cactus removal (Fig.1), suggesting that the abundance of this species was not negatively affected by herbicide spraying, at least not by 2010. There was, however, a significant decrease in the proportion of female kangaroo rats in the reproductive condition on removal sites relative to controls. Kangaroo rats are relatively long-lived and store seeds, and it is possible that their numbers were not yet been affected by the loss of seed production by cactus, at least not 1 year after spraying. The decrease in breeding activity may indicate that food resources have decreased, which might result in a population decline in the future. Stable carbon and nitrogen isotope analysis of the kangaroo rat tissues I collected may reveal a shift in the diet of kangaroo rats away from cactus seeds.

As expected, herbicide application resulted in a decrease in cover of live cactus and an increase in cover of litter, i.e. dead cactus, and in the amount of bare ground (Table 2). Compared to control sites, there was very little evidence of cactus reproduction (buds or flowers) on the removal sites.

Much dead and dying cactus remained, which may still provide vegetation structure, as well as a residual source of seeds. It may take up to 3 years for the cactus to be completely eliminated from the removal pastures (Tu et al., 2001). The difference in plant height between removal and control plots more likely reflected the fact that removal plots were not grazed in spring and summer 2010, rather than any effect of the herbicide.

The increase in bare ground on removal sites might help explain the increase in northern grasshopper mice on these sites relative to the controls. Grasshopper mice tend to prefer areas with large amounts of bare ground, including mounds of kangaroo rats, pocket gophers and prairie dogs (Stapp 1997; Stapp et al. 2008). The amount of arthropod prey might also have increased in response to cactus removal, although I did not measure changes in insect abundance. Prickly-pear cactus is important in shortgrass steppe because it disrupts the competitive effects of blue grama and buffalo grass over other plants (Rebolledo et al. 2002). Cactus also provides a spiny refuge that both collects organic matter and protects seedlings from grazing. The removal of cactus therefore would be expected to increase the homogeneity of vegetation in pastures in favor of the competitive dominants. Although this may increase forage for livestock, it might also lead to a decrease in vegetation structure and diversity, with effects on other plant and animal species. Researchers therefore should continue to study changes in the abundance of small mammals, and possibly insects, in response to cactus removal to understand the long-term consequences. However, because of the cost of herbicide application, it is not likely to be widely used except in situations where cactus cover is extremely high on private lands.

Acknowledgements

We thank Mark Lindquist, Sean Hauser, Casey Cardinal, Kevin Meierbachtol and the SGS-LTER field crew for assistance in the field, the Stapp lab for assistance and support in the lab, and the Ball family for allowing us to work on their property. Sallie Sprague and Nicole Kaplan provided logistical support. My project was supported by a Research Experience for Undergraduates supplement from NSF to the SGS-LTER project (DEB-0823405), a Faculty-Student Research and Creative Activities Grant from the CSUF Faculty Development Center, and the Department of Biological Sciences at CSUF.

References

- Callaway, R., Kikvidze, Z., and Kikodze, D. (2000) Facilitation by unpalatable weeds may conserve diversity in overgrazed meadows in the Caucasus Mountains. *Oikos* 89:275-282.
- Efford, M.G., Warburton, B., Coleman, M.C., and Barker, R.J. (2005). A field test of two methods for density estimation. *Wildlife Society Bulletin* 33: 731-738.
- Efford, M.G., and Boprchers, D.L. (2008). Spatially explicit maximum likelihood methods for capture-recapture studies. *Biometrics* 64: 377-386.
- Flake, L. (1973). Food habits of four species of rodents on a shortgrass prairies in Colorado. *Journal of Mammalogy* 54:636-647.
- Gannon, W.L., et al. (2007). Guidelines of the American Society of Mammalogists for the use of wild mammals in research. *Journal of Mammalogy* 88: 809-823.
- Garrison, T.E., and Best, T.L. (1990) *Dipodomys ordii*. Mammalian Species 353:1-10.
- Harriman, A.E. (1973). Self selection of diet in northern grasshopper mice (*Onychomys leucogaster*). *American Midland Naturalist* 90:97-106.
- Hernandez, F., Henke, S.E., Silvy, N.J. Rollins, D. (2003). The use of prickly pear cactus as nesting cover by northern bobwhites. *Journal of Wildlife Management* 67:417-423.
- Knopf, F.L. (1996). Mountain Plover (*Charadrius montanus*). The Birds of North America, No. 211. The Academy of Natural Sciences and the American Ornithologists Union, Washington D.C.
- Montiel, S., and C. Montaña. (2003). Seed bank dynamics of the desert cactus *Opuntia rafetra* in two habitats from the Chihuahuan desert. *Plant Ecology* 166:241-248.
- Riegel, A. (1941). Some coactions of rabbits and rodents with cactus. *Transactions of the Kansas Academy of Science* 44:96-103.
- Robello, S., Milchunas, D.G., Noy-Meir, I., and Chapman, P.L. (2002) The role of a spiny plant refuge in structuring grazed shortgrass steppe plant communities. *Oikos* 98:53-64.
- Stapp, P. (1997). Habitat selection by an insectivorous rodent: patterns and mechanisms across multiple scales. *Journal of Mammalogy* 78:1128-1143.
- Stapp, P., Van Horne, B., and Lindquist, M.D. (2008). *Ecology of mammals of the shortgrass steppe*. Pp. 132-180. *Ecology of Shortgrass Steppe: A Long-term Perspective*. W.K. Lauenroth and I.C. Burke, eds. Oxford University Press, New York.
- Tu, M., Hurd, C., and Randall, J.M. (2001). *Picloram*. Pp. 7i: 1-9 in Weed Control Methods Handbook. The Nature Conservancy. Arlington, VA.

Localization And Identification Of Protein Kinase C Subtypes Ascidian Sperm Activation

Rolando Ruiz
Advisor: Dr. Robert A. Koch

Department of Biological Science, College of Natural Science and Mathematics, California State University, Fullerton, CA, USA

Abstract

In *Ascidia ceratodes*, sperm activation is characterized by a morphological change known as mitochondrial translocation. This event is an actin:myosin-driven process and is dependent on internal calcium ion (Ca^{2+}_i) release by the endoplasmic reticulum (ER). Ca^{2+}_i activates protein kinase C (PKC), which facilitates signal transduction leading to mitochondrial translocation (MTL). Based on previous studies, we proposed that in activated sperm cells, the elevation of Ca^{2+} concentration from ER stores stimulates PKC to relocate from mitochondrion-associated sites to the plasma membrane where it triggers a pathway leading to Ca^{2+} entry and myosin activation. It is known that myosin powers MTL. We also hypothesized that PKC δ subtype is present in ascidian sperm. To test these hypotheses, cytosolic-, and mitochondrial-rich fractions were prepared and checked for purity using succinate dehydrogenase (SDH) and lactate dehydrogenase (LDH) enzymatic assays. PKC activity was tested in the two fractions with a PKC assay kit. Various PKC pseudosubstrates were used as inhibitors to identify the PKC subtype. SDH activity was >85% in mitochondrial fractions and LDH activity was >85% in cytosolic fractions. Nearly 100% of PKC activity was associated with cytosolic fractions in both activated and unactivated sperm cells. PKC δ and PKC β , were both present in ascidian sperm cells. We concluded that PKC is not associated with the mitochondrion and both conventional and novel PKC are present in ascidian sperm.

Introduction

Fertilization is the process by which two haploid cells merge to form a diploid zygote. In ascidians, sperm activation is one of the earliest processes that occurs during fertilization and prepares the sperm for penetration of the egg's protective layers. The sperm of the sea squirt, *Ascidia ceratodes*, is a good model

for studying sperm activation because it is characterized by a signature event known as mitochondrial translocation (MTL), whose several steps can easily be observed *in vitro* (Garrett, Goel, Yasui, & Koch, 1999). MTL requires binding of the sperm to glycoproteins on egg follicles cells via sperm adhesion proteins on the plasma membrane overlying the mitochondrion (C. Lambert, 1982). Simultaneously, a signaling cascade initiates the rounding of the mitochondrion and its movement from the base of the head towards the tail by an actin:myosin-dependent process required for cell movement, an action that drives the head of the sperm toward the egg plasma membrane (C. Lambert & Lambert, 1984). The MTL process can be triggered through binding with the egg, egg water (Garrett, et al., 1999), low-sodium sea water, chloride-free sea water, high pH seawater (C. C. Lambert & Epel, 1979), mas7 (Butler, et al., 1999), or the integrin-binding monoclonal antibody, 12G10 (Soratorio & Koch, 2002).

In ascidian sperm, calcium ion concentrations increase when the cells are activated by high pH or low-sodium seawater (C. C. Lambert & Lambert, 1981). Calcium ion concentration can also increase from external calcium entering the cells via calcium channels. Following *in vitro* activation, internal calcium release and external calcium entry is sufficient to cause sperm activation (Butler, et al., 1999), but *in vivo* both are required (Lotfizadeh, Allen, Ghobadi, & Koch, 2001). Protein kinase C (PKC), a calcium-dependent protein, helps facilitate signaling for MTL within the sperm cells of *A. ceratodes* (Koch, Allen, & Lotfizadeh, 2001). PKC is a serine-threonine kinase that is localized in the cytosol (Nishizuka, 1992) and re-locates to the membrane once activated by calcium ions, the phospholipid phosphatidylserine (PS), and diacylglycerol (DAG). There are 11 different isoforms, each with a regulatory and catalytic domain, which can be divided up into three groups based on structural and functional features (Tatone, et al., 2003).

PKC contain four different conserved domains: C1-C4 (Coussens, et al., 1986). The C1 domain contains DAG and phorbol ester binding sites (Burns & Bell, 1991), which is preceded by an autoinhibitory pseudosubstrate sequence that allows PKC to remain in the inactive state in the cytosol (Eichholtz, de Bont, de Widt, Liskamp, & Ploegh, 1993; Thiam, et al., 1999) (House & Kemp, 1987). Each subtype of PKC has its own specific pseudosubstrate domain. Allosteric activators, such as DAG or phorbol esters, will bind to the C1 domain and release the substrate from the autoinhibitory domain, which allows PKC to undergo a conformational change to become active (Eichholtz, et al., 1993). The C2 domain contains binding sites for PS and Ca²⁺ (Nishizuka, 1992). The C3 and C4 domains make up the ATP binding pocket and substrate binding site, respectively.

In this study, we investigate the localization and subtype of PKC in *A. ceratodes*. In many cells, PKC is known to be in the cytosol in an inactive form and after the binding of calcium to the C2 domain on PKC, it translocates to the plasma membrane or to subcellular locations, including nuclear structures, and cytoskeletal components (Keenan & Kelleher, 1998). In ascidian sperm, PKC is involved in the G-protein coupled receptor signaling pathway that leads to sperm activation (Lotfizadeh, et al., 2001). In the ascidian model, sperm cells appear to use PKC γ , and PKC γ , which becomes activated when DAG binds to the C1 domain on PKC (Lotfizadeh, et al., 2001). Upon activation, PKC is thought to phosphorylate the sodium hydrogen exchanger at the plasma membrane, which indirectly triggers external calcium to enter the cell and lead to sperm activation. Further study of localization and identification of PKC subtype may provide insights to whether it is associated with the mitochondrion during sperm activation.

Materials And Methods

Chemicals

Sodium chloride (NaCl), potassium chloride (KCl), calcium chloride dihydrate ($\text{CaCl}_2 \cdot 2\text{H}_2\text{O}$), magnesium chloride hexahydrate ($\text{MgCl}_2 \cdot 6\text{H}_2\text{O}$), magnesium sulfate heptahydrate ($\text{MgSO}_4 \cdot 7\text{H}_2\text{O}$), sodium bicarbonate (NaHCO₃), protease inhibitor cocktail, 1-Oleoyl-2-acetyl-sn-glycerol (OAG), dimethyl sulfoxide (DMSO), ethylene glycol-bis (2-aminoethylether)-N,N,N',N'-tetraacetic acid (EGTA), and ethylenediaminetetraacetic acid (EDTA) were purchased from Sigma (St. Louis, MO). Lactate dehydrogenase assay was purchased from BioAssays Systems (Hayward, CA). A MESACUP Protein Kinase Assay System was purchased from Millipore (Temecula, CA). Rhodamine conjugate-inhibitor (rim-1) was purchased from Teflabs (Austin, TX). MitoTracker Green FM was purchased from Invitrogen (Carlsbad, CA). All three PKC pseudosubstrates, PKC α - β , PKC δ , and PKC ϵ , were a gift from Driss Zoukhri, Ph.D., Tufts University, Boston, MA.

Animal Maintenance and Dissection

A. ceratodes were collected at Half Moon Bay, CA. The animals were kept on site (California State University, Fullerton) coexisting with mussels in an aquaria at 12-15° C until they were needed. The natural seawater in the tanks was constantly filtered and changed regularly. The outer tunic of the ascidians was first cut in order to remove the soft body with forceps. The sperm duct was punctured, and the gametes (dry sperm) were removed with a positive displacement pipette and stored at 4° C until used for up to three days. Sperm motility was checked prior to each MTL assay. If motility was not observed in the sperm cells, then the sample was not used.

Media

Artificial Sea Water (ASW) was prepared as follows (in mM): 492 NaCl, 9.0 KCl, 9.25 CaCl₂, 22.9 MgCl₂, 25.5 MgSO₄, and 2.02 NaHCO₃ (950-1050 mOsm) in nanopure H₂O.

Rim-1 (3mM) was dissolved in 100% DMSO and aliquoted out until use. The working concentration (300nM/1% DMSO) was diluted in ASW. MitoTracker Green FM (1mM) was dissolved in 100% DMSO to obtain a stock solution. An intermediate solution (10μM) was made in 100% DMSO before obtaining the working solution (100nM/1% DMSO) in ASW. The final concentration of DMSO must be one percent in order for the sperm cells to maintain the appropriate morphology.

Homogenization buffer was prepared with the following reagents (in mM): 20 Tris HCl (pH 7.5), 10 % glycerol, 1.0 DTT, 0.5 EDTA, 0.5 EGTA, and IX protease inhibitor cocktail as described previously (Lotfizadeh, et al., 2001).

Microscope-Slide-Based Assays

MTL measurements were performed as follows. After removal from the sperm duct, dry sperm were diluted into pH 6.8 ASW (6.8 ASW; 2 μl/ml), and an aliquot (200 μl) was dispersed onto a glass cover slip. The dead cells were allowed to sink to the bottom for one min. The same aliquot was transferred to a new glass cover slip and the cells were allowed to adhere for five min. Negative controls were treated with 6.8 ASW (200 μl), whereas positive controls were incubated in pH 9.4 ASW (9.4 ASW; 200 μl) each for 10 min. Treated sperm were incubated in an activating solution that contained OAG dissolved in ASW for 20 min. The fluid was drained and the sperm were fixed in 1% formaldehyde in ASW (15 min, room temperature), drained again, mounted in 50% glycerol in ASW, sealed with fingernail polish, and analyzed by phase contrast microscopy.

In each experiment, 100 sperm cells per cover slip (three cover slips per microscope slide) were assessed in random fields away from the cover slip edges, and all experiments were done in triplicates from three different ascidians for a total count of 900 sperm cells. Sperm activation was determined by the percentage of sperm undergoing MTL. Sperm cells were characterized and counted as activated or unactivated, based on the shape and location of the mitochondrion on the sperm cell.

Cells were treated with either DAPI (5μL of Prolong Gold antifade reagent with DAPI), MitoTracker Green FM (100nM), rim-1 (300nM), or both agents to determine if rim-1 labeling was artifactual. Prior to the fixation step, cells were incubated with one or both of these agents for 15 min. Cells were mounted with Prolong Gold antifade reagent mixed with DAPI (Invitrogen, Carlsbad, CA) as oppose to glycerol. Fluorescence was observed using a Leica TCS SP2 Confocal Microscope (Bannockburn, IL) at 490nm excitation and 520nm emission and 558nm excitation and 580nm emission for MitoTracker Green FM and rim-1, respectively.

The inhibitory action of PKC-pseudosubstrates (PKC-ps) were tested in an MTL assay. After the sperm cells were allowed to adhere to the cover slip for five min, the negative control was exposed to 6.8 ASW, while the positive controls were exposed to 9.4 ASW or OAG (180 μM), and the treatment was activation by pH 9.4 ASW or OAG in the presence or absence of PKC α -ps (5 μM) or PKC γ -ps (5 μM) for 20 min. PKC-ps was present as a pre-treatment and was present during activation. The sperm cells were then fixed and counted as mentioned above.

Preparation of Cellular Fractions

Dry sperm ($500\text{ }\mu\text{L}$) from three to five ascidians were washed three times in 6.8 ASW by centrifugation at 400g with an IEC centrifuge (Thermo Scientific, Waltham, MA), and sonicated (Fisher Scientific 550 Sonic Dismembrator; Pittsburg, PA) on ice for 5 sec, and allowed to rest for 3 minutes 55 seconds in the presence of the homogenizing buffer. Following twelve sonifications the samples were centrifuged at 600g for 15 min to remove nuclear debris. A second centrifugation at 10,000g for 30 min was performed to isolate the mitochondria. Centrifugation at 10,000g was done three times to completely separate the mitochondria (pellet) from the cytosol (supernatant). This method was used to determine the initial quantity of mitochondria in the homogenate and was only performed before the enzymatic assays were executed.

Enzymatic Assays

Succinate dehydrogenase (SDH) activity was determined in mitochondrial-rich and cytosolic-rich fractions using a spectrophotometric method. The measurement was performed in Tris-HCl buffer (50 mM; pH 8.0) containing NaCN (3 mM), 2,6-dichloroindophenol (50 μM ; DCIP), disodium succinate (10 mM), and an aliquot of the appropriate fraction as described elsewhere (Kis, et al., 2003). The reduction of DCIP by SDH was monitored at 650 nm 9 minutes after the reaction had started in order to exclude endogenous succinate. Readings were taken every 10 sec for 3 minutes after succinate (10 mM) was added. Blanks did not contain succinate. One Unit (IU, International Unit) of SDH will catalyze the conversion of one μmole of succinate to fumarate per min at pH 8.0. SDH activity (IU) = $(\Delta A_{650}/\text{min} \times 200 \times 1000 \times 1)/(21 \times 10 \times 1)$ where 200 μL is the total volume, 1000 is a unit conversion factor, 1 is the dilution factor, 21 is the molar extinction coefficient, 10 μL is the sample volume, and 1 is the path length in centimeters, respectively.

Lactate dehydrogenase (LDH) activity was determined in the various sperm cell fractions using an LDH assay kit (BioAssays, Hayward, CA). An assay mixture was prepared by combining the following kit solutions: MTT (14 μL), NAD (8 μL), PMS (8 μL), and substrate buffer (170 μL ; pH 8.2). LDH activity was determined by combining an aliquot of the appropriate fraction (10 μL) and of the assay mixture (190 μL). Spectrophotometric readings of the sample, water, and calibrator (provided in kit) were taken at 0 and 25 minutes at a wavelength of 565 nm. A water sample reading was taken to represent the minimum amount of activity possible and a calibrator (methylene blue) reading was taken to represent the maximum (200 IU) amount of activity in the reaction. LDH activity was calculated based on the equation provided by BioAssays Systems (Hayward, CA). LDH Activity = $43.68 \times (OD_{525} - OD_{50})/(OD_{CAL} - OD_{H2O}) \times n$ where n is the dilution factor. Unit definition: 1 Unit (IU) of LDH will catalyze the conversion of 1 μmole of lactate to pyruvate per min at pH 8.2 (Babson & Babson, 1973; Coley, Lewandowicz, Sargent, & Verrill, 1997; Karlsen, Norgaard, & Guldbrandsen, 1981).

The PKC assay kit (Upstate, Temecula, CA) is based on an enzyme linked immunosorbent assay (ELISA) that utilizes a synthetic peptide and a monoclonal antibody that recognizes the phosphorylated form of the peptide. The antibody provided was a mouse monoclonal antibody 2B9 against the synthetic phosphopeptide RFARKG[pS]LRQKNV. Component mixture (108 μL) was added to each well of a polystyrene plate and pre-incubated in a water

bath (27° C) for five min. A sample (12 μL) of each fraction prepared was added to each well and mixed thoroughly by pipetting up and down several times. From this reaction mixture, 100 μL was transferred to each PS-peptide coated well (provided in the PKC kit) with a multichannel pipette and incubated in a water bath (27° C) for 15 min. Stop solution (100 μL of 20% H_3PO_4 ; provided in the PKC kit) was added to each well, aspirated, and washed five times with 1X wash solution. Biotinylated antibody 2B9 (100 μL ; provided in the PKC kit) was added to each well and incubated in a water bath (27° C) for 60 min. The wells were washed again five times with 1X wash solution. Substrate solution (100 μL ; provided in the PKC kit) was added to each well and incubated in a water bath (27° C) for five min followed by the addition of stop solution (100 μL). The optical density of each well was read at 490 nm using microplate reader (BioTek Instruments, Winooski, VT). PKC activity was determined by the following equation: $((A_{PKC490}/\text{min} - A_{Blank490}/\text{min}) \times 200 \times 1000 \times 1)/(1.578 \times 12 \times 1)$, where 200 μL is the total volume, 1000 is a unit conversion factor, 1 is the dilution factor, 1.578 mM \cdot cm \cdot 1 is the extinction coefficient, 12 μL is the sample volume, and 1 is the path length in centimeters. One Unit (IU) is the conversion of 1 μmole of o-phenylenediamine to 2,3-diaminophenazine per min at pH 7.0 (Beavo, Bechtel, & Krebs, 1974; Edelman, Blumenthal, & Krebs, 1987; Inagaki, et al., 1990; Inagaki, Watanabe, & Hidaka, 1985).

Statistical Analysis

Fractions were created from three different homogenates and tested for SDH, LDH, and PKC. Statistical analysis was done with a Student t-test for all the enzymatic assays and for the pseudosubstrate experiment.

Results

Succinate Dehydrogenase Assay

SDH activity was used as the indicator of mitochondrial presence in the homogenate and was measured by the reduction of DCIP. Reduction of DCIP in the mitochondrial-rich but not the cytosolic-rich fraction was the

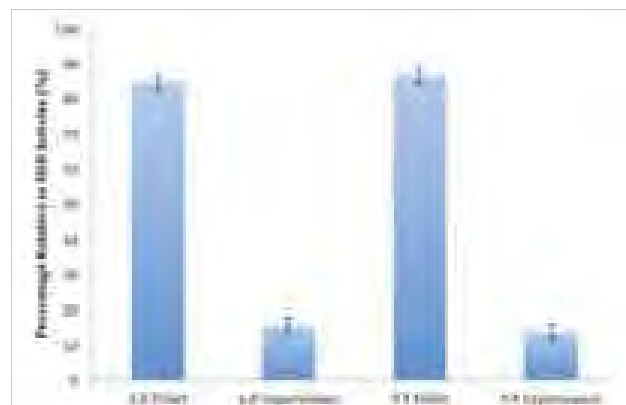


Figure 1: The relative percentage of SDH activity in the various fractions obtained. Both of the pellet fractions contained greater SDH activity (\pm s.d.; $n=3$).

criterion for separation of the two different fractions, and the presence of >80% of SDH activity was used to define a mitochondrial fraction as sufficiently concentrated. The relative activity of SDH was over 85% in the fractions that contained the pellet from both the activated and unactivated sperm cells (Figure 1). There was a significant difference in the unactivated sperm fractions as well as between the activated pellet and supernatant ($P<0.05$). With over 85% of SDH activity in the appropriate fractions, they were considered sufficiently purified fractions with respect to mitochondrial presence and were tested for PKC activity.

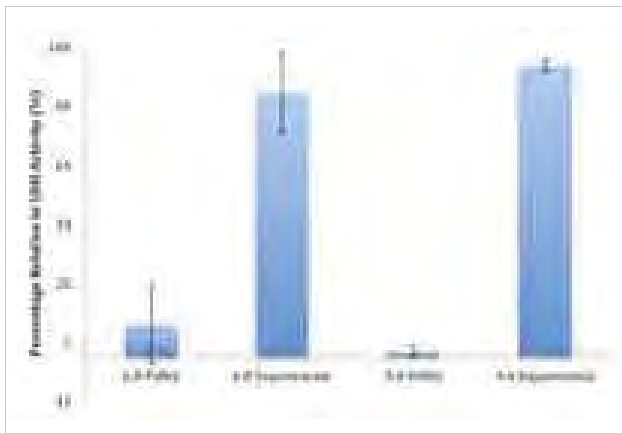


Figure 2: The relative percentage of LDH activity observed in the various fraction obtained. Over 85% of LDH activity was in the supernatant and therefore a pure cytosolic fraction has been achieved ($\bar{x}\pm s.d.$; $n=3$).

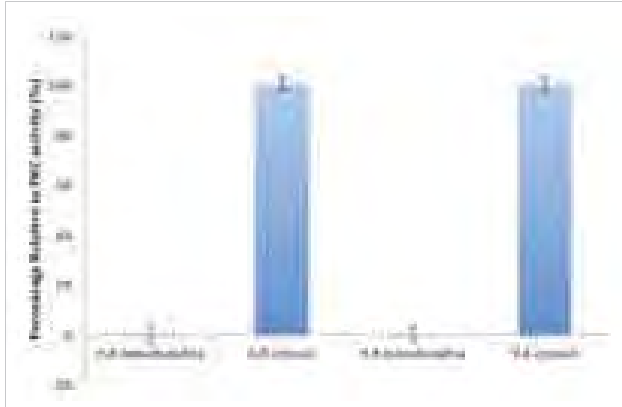


Figure 3: The relative percentage of PKC activity observed in the various fractions obtained. Nearly 100% of PKC activity was in the cytosol. ($\bar{x}\pm s.d.$; $n=3$).

Lactate Dehydrogenase Assay

Because lactate dehydrogenase (LDH) is known to be a cytosolic enzyme, an alternative method to determine a clear separation between the cytosolic and mitochondrial fractions was to measure the conversion of lactate and pyruvate. A clear separation between the fractions would be indicated by higher LDH activity in the supernatant or the cytosolic fraction. LDH assays were conducted on pellet and supernatant fractions obtained using the optimization of the SDH protocol. The percentage relative to LDH activity was significantly ($p<0.05$) higher in the supernatant than pellet in both activated and unactivated fractions with over 85% activity located in the supernatant (Figure 2). This level of activity characterized the supernatant fractions as sufficiently purified for the testing of PKC activity.

Protein Kinase C Activity Assay

PKC activity was determined in the fractions that were sufficiently purified according to the >80% activity criterion, and the fraction that contained the highest PKC activity was considered to be the cellular component with which the enzyme was primarily associated. PKC activity was higher by nearly 100% in the supernatant of both activated and unactivated fractions (Figure 3). There was a significant difference between the supernatant and the pellet in both activated and unactivated fractions ($P<0.05$). Thus, we conclude that the majority of PKC is localized to the cytosol of ascidian sperm cells in both unactivated and activated conditions.

PKC identification

Specific PKC-ps were used to determine the PKC isoforms present in *A. ceratodes* sperm cells. Cells treated with 6.8 ASW and a PKC-ps had a low percent activation (Figure 4). This level of activation was considered the baseline level for unactivated sperm cells. Cells treated with either the activator OAG or pH 9.4 ASW exhibited activation at levels of $75\pm10\%$ and

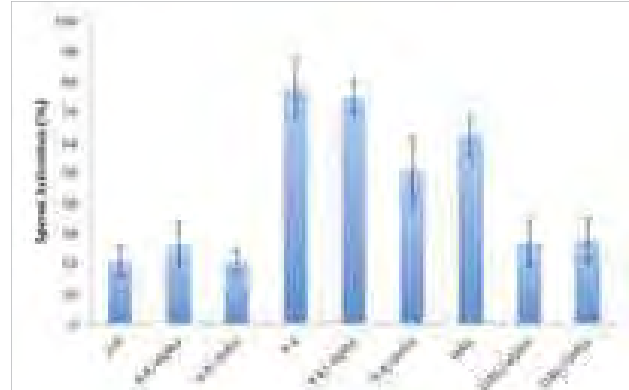
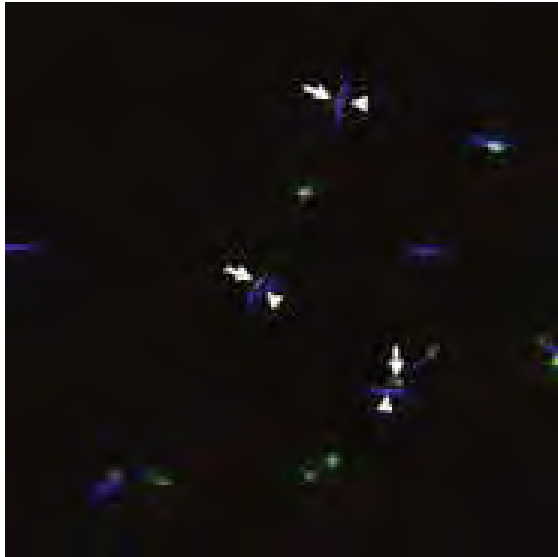


Figure 4: Sperm cell activation percentage when treated with either 6.8 ASW, 9.4 ASW, or OAG in the presence or absence of PKC pseudosubstrate (PKC- α s, PKC- δ s). Cells treated with both a pseudosubstrate and OAG were inhibited to almost control levels. ($\bar{x}\pm s.d.$; $n=900$).



*Figure 5: Fluorescent image of *A. ceratodes* sperm cells treated with 6.8 ASW and labeled with MitoTracker Green FM and DAPI. The arrows indicate mitochondria labeled with MitoTracker Green FM, while the arrowheads point at the nucleus of the sperm cells.*

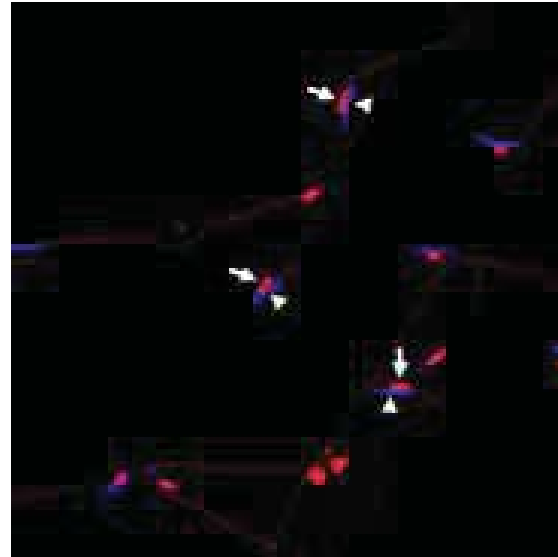


Figure 5b: Fluorescent image of ascidian sperm cells treated with 6.8 ASW and labeled with rim-1 and DAPI. The arrows indicate the distribution of PKC. DNA of the sperm cells was labeled with DAPI and indicated with arrowheads.

62 \pm 7%, respectively (Figure 4). Cells treated with 9.4 ASW in the presence of PKC- α sps were statistically no different from pH 9.4 ASW alone, thus there was no inhibition by the PKC-ps. Unexpectedly, when the cells were treated with 9.4 ASW in the presence of PKC- δ sps, the activation levels dropped down to 50 \pm 11% (Figure 4).

Cells that were treated with the activator OAG in the presence of PKC- δ sps dropped the activation levels down to baseline (i.e., 6.8 ASW) levels ($P<0.05$), hence there was a significant inhibition of activation with PKC- δ sps when compared to OAG-treated sperm cells (Figure 4; $P<0.05$). Similarly, cell treated with PKC- δ sps were also inhibited to 25% activation. We conclude that both PKC- α and PKC- δ subtypes are present in ascidian sperm cells and play a role in sperm activation.

MitoTracker Green FM and Rim-1 Labeling

Ascidian sperm cells were labeled with MitoTracker Green FM, and rim-1 to determine if immunofluorescence agreed with the biochemical tests. DAPI was used to help differentiate nuclear from cytosolic regions. MitoTracker Green FM labeled mitochondria in activated and unactivated sperm cells with minimal background labeling (Figure 5a and 6a). Rim-1 labeling was observed along the tails and on the mitochondrion region

in both activated and unactivated sperm cells (Figure 5b and 6b). In unactivated sperm cells, rim-1 also labeled at the tip of the head (Figure 5b), while that labeling was not observed in activated sperm cells (Figure 6b). MitoTracker Green FM and rim-1 co-localized (as shown by yellow coloration) in the mitochondrion region in both 6.8 ASW- and OAG-treated cells (Figure 5c and 6c).

Discussion

SDH Assay

SDH is a mitochondrial enzyme of the citric acid cycle, which is located in the inner membrane of the mitochondria (Munujos, Coll-Canti, Gonzalez-Sastre, & Gella, 1993). It plays a role in the electron transport chain, energy production, and it also oxidizes succinate to fumarate by transferring electrons straight to ubiquinone (Munujos, et al., 1993). Based on these properties, SDH was used as a biochemical marker to identify mitochondria in a cellular fraction. The fractions obtained by differential centrifugation produced a pellet that contained >80% of the total SDH activity suggesting that mitochondria had been separated from other cellular components. Even so, 20% of the SDH remained in the cytosolic fraction, a result that implied that small mitochondrial vesicles could have remained suspended in the supernatant.

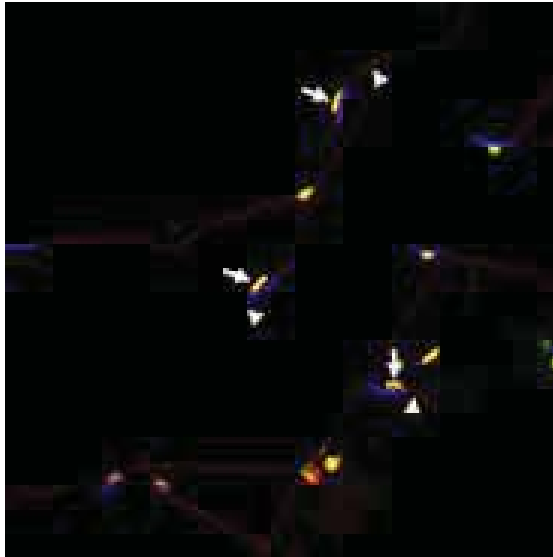


Figure 5c: Merged fluorescent image of unactivated sperm cells labeled with MitoTracker Green FM, rim-1, and DAPI. Arrows indicate co-localization of mitochondria and PKC. Other PKC distributions can be seen along the tail and at the tip of the heads as indicated by arrowheads.

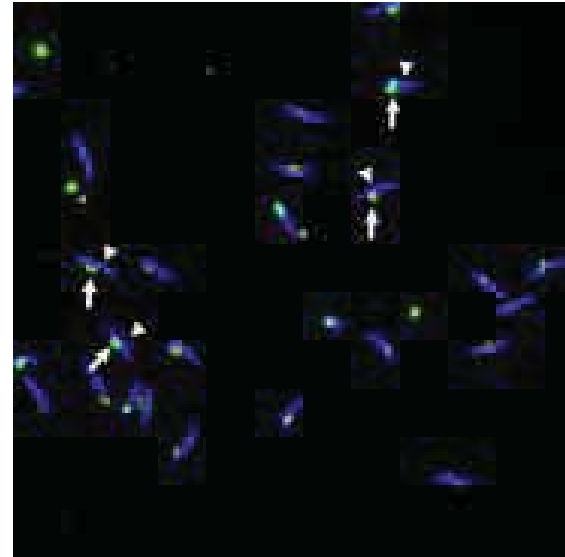


Figure 6a: Fluorescent image of ascidian sperm cells treated with OAG and labeled with DAPI and MitoTracker Green FM. Mitochondria are indicated by arrows and are a circular shape. The nucleus is indicated by an arrowhead.

LDH Assay

LDH is an enzyme that oxidizes lactate to pyruvate during glycolysis (Babson & Babson, 1973). LDH activity is measured by the reduction of nicotine adenine dinucleotide (NAD^+) coupled to the reduction of 3-(4,5-dimethylthiazol-2-yl)-2,5-diphenyltetrazolium bromide (MTT) with phenazine methosulfate (PMS). PMS was used as an intermediate electron carrier so that NADH can be reoxidized to NAD^+ , which is beneficial in order to drive the reaction from lactate to pyruvate (Babson & Babson, 1973; Toyoda, Teramoto, Inui, & Yukawa, 2009). LDH activity was greater in the supernatant fraction of both cells treated with 6.8 ASW and 9.4 ASW. Therefore, most of the cytosolic components were removed from the mitochondrial fraction and remained in the appropriate fraction. Upon achieving the separation of the mitochondrial and cytosolic fractions, they were ready to be tested for PKC activity. This interpretation is consistent with the traditional explanation for the location of inactive PKC (Nishizuka, 1992).

PKC Activity

In many cell models, PKC is located in the cytosol and then relocates to the plasma membrane upon its activation (Nishizuka, 1992). In *A. ceratodes*, PKC is also found in the cytosol of sperm cells treated with 6.8 ASW. In order for *A. ceratodes* to undergo MTL, PKC needs to be activated so that it can translocate to the plasma membrane. When the sperm cells were

treated with 9.4 ASW to trigger sperm activation, PKC activity remained localized in the cytosolic fraction. Even though PKC is localized in the cytosolic fraction in cells treated with 9.4 ASW, it could have translocated to the plasma membrane but only if there were plasma membrane vesicles contaminating the cytosolic fraction. However, because we did not establish a plasma membrane fraction, we can only conclude that PKC is associated with the LDH-rich, cytosolic fraction.

PKC Identification

Previous reports from Lotfizadeh et al. (2001) and Allen et al (1998) indicated that $\text{PKC}\alpha$ and $\text{PKC}\lambda$ are both present in *A. ceratodes* sperm cells. The ps inhibition studies carried out in this study, showed that $\text{PKC}\alpha$ is present, as well as $\text{PKC}\delta$. Lotfizadeh et al. (2001) reported that $\text{PKC}\alpha$ played a minor role in MTL, but the ps studies completed here indicate that MTL is inhibited to control the levels of activation (Figure 4). This finding in turn indicates that $\text{PKC}\alpha$ does not play a minor role in sperm activation, but is a major contributor, like $\text{PKC}\gamma$. Both of these subtypes inhibited MTL and therefore are required, but not necessary, for MTL to occur.

PKC is known to play a role in cellular development and differentiation (Tatone, et al., 2003). In the ascidian *Ciona intestinalis*, $\text{PKC}\alpha$, $\text{PKC}\gamma$, and $\text{PKC}\delta$ are involved in the atypical PKC-Par signaling pathway, which is involved in polarity, cell movements, and involvement of actin filaments during

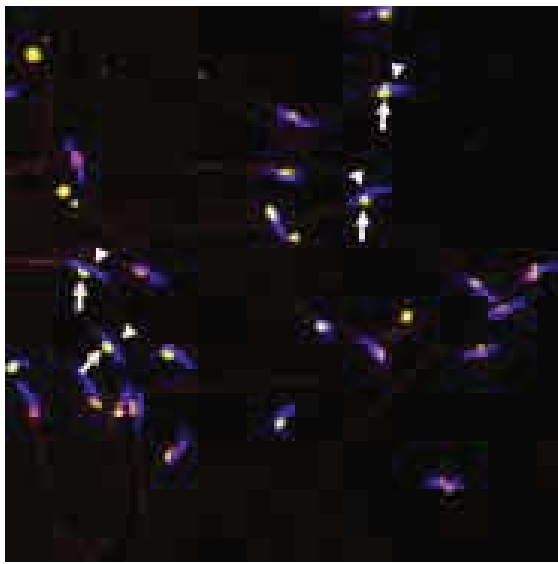


Figure 6b: Fluorescent image of ascidian sperm cells treated with OAG and labeled with rim-1 and DAPI. Rim-1 shows the distribution of PKC, which is indicated by the arrows and can be seen in the mitochondria region and along the tails. The arrowheads point at the nuclei.

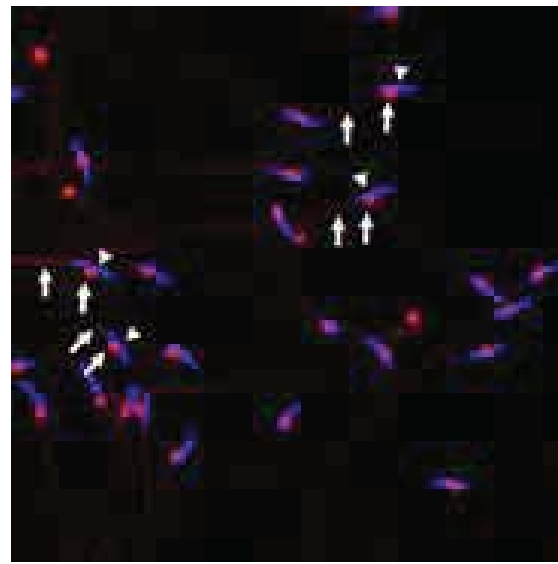


Figure 6c: Merged fluorescent image of activated sperm cells labeled with MitoTracker Green FM, rim-1, and DAPI. Arrows indicate co-localization of mitochondria and PKC. Other PKC distributions can be seen along the tail. Arrowheads point at the nuclei.

ascidian development (Sasakura, Yamada, Takatori, Satou, & Satoh, 2003). Although PKC α , PKC γ , and PKC δ contribute to development of the zygote, their involvement in the atypical PKC-Par signaling pathway suggests that they might be present prior to development. If the atypical PKC-Par signaling pathway is involved in actin filament processes, PKC δ could be triggering MTL via actin polymerization and not myosin activation in ascidian sperm cells.

The integrin signaling pathway is involved in actin polymerization and is mediated via focal adhesion kinase (FAK). Trujillo (unpublished observations) demonstrated that an antibody against the FAK tyrosine-397 that binds Src inhibits MTL. Similar to PKC, Src can be both membrane-associated and localized in the cytosol of cells (Song, et al., 1998). Overexpression of Src can lead to tyrosine phosphorylation of PKC δ (Zang, et al., 1997), but PKC δ can also act as a substrate to Src (Gschwendt, Kielbassa, Kittstein, & Marks, 1994). These findings suggest that PKC δ may be found in the integrin-signaling pathway in our model.

PKC Localization

To elucidate the location of PKC in sperm cells a fluorescent mitochondrial agent, MitoTracker Green FM, was used in addition to rim-1 to determine if there was co-localization. MitoTracker Green FM fluoresces a bright green color when it accumulates in the lipid environment of the mitochondrion. Fluorescent images show rim-1 labeling along the tail and overlaying the mitochondrion region in both activated and unactivated sperm cells (Figure 5c and 6c). Although the rim-1 labeling associated with the mitochondria the biochemical data show that PKC activity is not associated with the mitochondrial fractions. Thus, PKC must

be trapped in cytosolic regions that are closely associated with mitochondria, but is not strongly bound to the surface of the mitochondria.

PKC distribution along the tail was evenly distributed. This distribution of PKC may be required for the transport of the mitochondrion along the tail during MTL. We hypothesize that, in our model, the process required for the movement of the mitochondrion along the tail of the sperm is different than the PKC-dependant actin:myosin process that occurs on the head. Along the tail, intraflagellar transport

(IFT) is the process for movement of organelles (Reese & Haimo, 2000). IFT requires two microtubule-based motors, dynein and kinesin, that can be either enhanced or inhibited by PKC (Reese & Haimo, 2000). Thus, it appears that PKC is involved in the translocation of the mitochondrion in both the head and tail of ascidian sperm cells, but it is not associated with the mitochondrion.

This study has established that: (1) mitochondrial- and cytosolic-rich fractions can easily be obtained by use of differential centrifugation, (2) PKC is associated with the cytosolic fraction which may be closely associated with the mitochondrion but is not bound to it, (3) both PKC α and PKC δ isoforms are present in ascidian sperm, and (4) both PKC α and PKC δ isoforms are involved in MTL.

Acknowledgements

We thank various graduate and undergraduate students in the lab that collected *Ascidia* ceratodes. This work was funded by Cal State Fullerton MARC U*STAR Program 5 T34 GM008612-14 Grant (R.R.), Cal State Fullerton

References

- Babson, A. L., & Babson, S. R. (1973). Kinetic colorimetric measurement of serum lactate dehydrogenase activity. *Clin Chem*, 19(7), 766-769.
- Beavo, J. A., Bechtel, P. J., & Krebs, E. G. (1974). Preparation of homogeneous cyclic AMP-dependent protein kinase(s) and its subunits from rabbit skeletal muscle. *Methods Enzymol*, 38, 299-308.
- Burns, D. J., & Bell, R. M. (1991). Protein kinase C contains two phorbol ester binding domains. *J Biol Chem*, 266(27), 18330-18338.
- Butler, D. M., Allen, K. M., Garrett, F. E., Lauzon, L. L., Lotfizadeh, A., & Koch, R. A. (1999). Release of Ca²⁺ from Intracellular Stores and Entry of Extracellular Ca²⁺ Are Involved in Sea Squirt Sperm Activation. *Developmental Biology*, 215, 453-464.
- Coley, H. M., Lewandowicz, G., Sargent, J. M., & Verrill, M. W. (1997). Chemosensitivity testing of fresh and continuous tumor cell cultures using lactate dehydrogenase. *Anticancer Res*, 17(IA), 231-236.
- Coussens, L., Parker, P. J., Rhee, L., Yang-Feng, T. L., Chen, E., Waterfield, M. D., et al. (1986). Multiple, distinct forms of bovine and human protein kinase C suggest diversity in cellular signaling pathways. *Science*, 233(4766), 859-866.
- Edelman, A. M., Blumenthal, D. K., & Krebs, E. G. (1987). Protein serine/threonine kinases. *Annu Rev Biochem*, 56, 567-613.
- Eichholtz, T., de Bont, D. B., de Widt, J., Liskamp, R. M., & Ploegh, H. L. (1993). A myristoylated pseudosubstrate peptide, a novel protein kinase C inhibitor. *J Biol Chem*, 268(3), 1982-1986.
- Garrett, F. E., Goel, S., Yasul, J., & Koch, R. A. (1999). Liposomes fuse with sperm cells and induce activation by delivery of impermeant agents. *Biochim Biophys Acta*, 1417(1), 77-88.
- Gschwendt, M., Kielbassa, K., Kittstein, W., & Marks, F. (1994). Tyrosine phosphorylation and stimulation of protein kinase C delta from porcine spleen by src in vitro. Dependence on the activated state of protein kinase C delta. *FEBS Lett*, 347(1), 85-89.
- House, C., & Kemp, B. E. (1987). Protein kinase C contains a pseudosubstrate prototype in its regulatory domain. *Science*, 238(4834), 1726-1728.
- Inagaki, M., Gonda, Y., Nishizawa, K., Kitamura, S., Sato, C., Ando, S., et al. (1990). Phosphorylation sites linked to glial filament disassembly in vitro locate in a non-alpha-helical head domain. *J Biol Chem*, 265(8), 4722-4729.
- Inagaki, M., Watanabe, M., & Hidaka, H. (1985). N-(2-Aminoethyl)-5-isoquinolinesulfonamide, a newly synthesized protein kinase inhibitor, functions as a ligand in affinity chromatography. Purification of Ca²⁺-activated, phospholipid-dependent and other protein kinases. *J Biol Chem*, 260(5), 2922-2925.
- Karlsen, R. L., Norgaard, L., & Guldbrandsen, E. B. (1981). A rapid method for the determination of urea stable lactate dehydrogenase on the 'Cobas Bio' centrifugal analyser. *Scand J Clin Lab Invest*, 41(5), 513-516.
- Keenan, C., & Kelleher, D. (1998). Protein Kinase C and the Cytoskeleton. *Cell. Signal.*, 10(4), 225-232.
- Kis, B., Rajapakse, N. C., Snipes, J. A., Nagy, K., Horiguchi, T., & Busija, D. W. (2003). Diazoxide induces delayed pre-conditioning in cultured rat cortical neurons. *J Neurochem*, 87(4), 969-980.
- Koch, R. A., Allen, K. M., & Lotfizadeh, A. (2001). Cell signaling in ascidian sperm: Upstream and downstream of internal calcium release. In Sawada, Yokosawa & C. Lambert (Eds.), *The Biology of Ascidians* (2 ed., pp. 30-35): Elsevier.

References (Continued)

- Lambert, C. (1982). The ascidian sperm reaction. *American Zoologist*, 22, 841-849.
- Lambert, C., & Lambert, G. (1984). The role of actin and myosin in ascidian sperm mitochondrial translocation. *Developmental Biology*, 106, 307-314.
- Lambert, C. C., & Epel, D. (1979). Calcium-mediated mitochondrial movement in ascidian sperm during fertilization. *Developmental Biology*, 69(1), 296-304.
- Lambert, C. C., & Lambert, G. (1981). The ascidian sperm reaction: Ca²⁺ uptake in relation to H⁺ efflux. *Developmental Biology*, 88(2), 312-317.
- Lotfizadeh, A., Allen, K. M., Ghobadi, A., & Koch, R. A. (2001). PKC Plays a Central Role in the Signaling Pathway for Ascidian Sperm Activation. California State University, Fullerton.
- Munujos, P., Coll-Canti, J., Gonzalez-Sastre, F., & Gella, F. J. (1993). Assay of succinate dehydrogenase activity by a colorimetric-continuous method using iodonitrotetrazolium chloride as electron acceptor. *Anal Biochem*, 212(2), 506-509.
- Nishizuka, Y. (1992). Intracellular signaling by hydrolysis of phospholipids and activation of protein kinase C. *Science*, 258(5082), 607-614.
- Reese, E. L., & Haimo, L. T. (2000). Dynein, dy�actin, and kinesin II's interaction with microtubules is regulated during bidirectional organelle transport. *J Cell Biol*, 151(1), 155-166.
- Sasakura, Y., Yamada, L., Takatori, N., Satou, Y., & Satoh, N. (2003). A genomewide survey of developmentally relevant genes in *Ciona intestinalis*. VII. Molecules involved in the regulation of cell polarity and actin dynamics. *Dev Genes Evol*, 213(5-6), 273-283.
- Song, J. S., Swann, P. G., Szallasi, Z., Blank, U., Blumberg, P. M., & Rivera, J. (1998). Tyrosine phosphorylation-dependent and -independent associations of protein kinase C-delta with Src family kinases in the RBL-2H3 mast cell line: regulation of Src family kinase activity by protein kinase C-delta. *Oncogene*, 16(26), 3357-3368.
- Soratorio, J., & Koch, R. A. (2002). Analysis of the role of integrins in sperm activation in the tunicate, *Ascidia ceratodes*. *Molec. Biol.*, 13, L160.
- Tatone, C., Delle Monache, S., Francione, A., Gioia, L., Barboni, B., & Colonna, R. (2003). Ca²⁺-independent protein kinase C signalling in mouse eggs during the early phases of fertilization. *Int J Dev Biol*, 47(5), 327-333.
- Thiam, K., Loing, E., Zoukhri, D., Rommens, C., Hodges, R., Dartt, D., et al. (1999). Direct evidence of cytoplasmic delivery of PKC-alpha, -epsilon and -zeta pseudosubstrate lipopeptides: study of their implication in the induction of apoptosis. *FEBS Lett*, 459(3), 285-290.
- Toyoda, K., Teramoto, H., Inui, M., & Yukawa, H. (2009). Molecular mechanism of SugR-mediated sugar-dependent expression of the *ldhA* gene encoding L-lactate dehydrogenase in *Corynebacterium glutamicum*. *Appl Microbiol Biotechnol*, 83(2), 315-327.
- Zang, Q., Lu, Z., Curto, M., Barile, N., Shalloway, D., & Foster, D. A. (1997). Association between v-Src and protein kinase C delta in v-Src-transformed fibroblasts. *J Biol Chem*, 272(20), 13275-13280.

Influence Of Anthropogenic Noise On Song Structure In *Calypte* Hummingbirds

Department of Biological Science, College of Natural Science and Mathematics, California State University, Fullerton, CA, USA

Sarah English
Advisor: Dr. Anne Houtman

Abstract

Anthropogenic noise (noise pollution) may affect how hummingbirds use song for mate attraction and territory defense. My study focuses on the structure of Anna's Hummingbird (*Calypte anna*) complex song and Costa's Hummingbird (*Calypte costae*) simple song in areas of contrasting noise levels. Recordings were collected in Anza Borrego State Park in Imperial County, CA and at Boyd Deep Canyon Research Station in Riverside County, CA during the Spring of 2007 and 2008. Recordings of *Calypte* hummingbirds found in these areas were analyzed for structural and temporal changes in amplitude, frequency, syllable and bout duration, and complexity, and these measures were compared between natural and high anthropogenic noise levels. It was predicted that Anna's Hummingbirds would sing shorter syllables and longer, less complex bouts and that Costa's Hummingbird would sing longer syllables and shorter bouts. However, it was found that Anna's Hummingbirds sang with a higher peak frequency, slightly louder amplitude, and slightly longer A syllables and Costa's Hummingbirds sang louder amplitude songs in high noise conditions. It was unexpected that *Calypte* hummingbirds would respond to anthropogenic noise in the same way as passerines. Hummingbirds have high metabolic demands and the frequency of the loudest parts of their song is already higher

than the frequency of the loudest parts of anthropogenic noise, so it was not seemingly necessary for them to sing louder or higher frequency. This similar behavior between songbirds and non-songbirds could aid in the understanding of the function of song in all birds that use song for mate attraction and territory defense similar to hummingbirds.

Introduction

Urbanization causes an increase in anthropogenic noise, for example, from traffic, power lines, air conditioners, construction and maintenance, or residential noise. Increasing noise may be a problem for animals that depend on acoustic communication for survival and reproduction.

There are well-documented effects of noise on many animal populations across many species such decreased reproductive success and exposure to predators. Southern California has one of the highest rates of urbanization in the United States and anthropogenic noise may have a significant effect on wildlife as the state's population continues to grow (Wood and Yezerinac, 2006). For example, the Lark Sparrow in California has lower species diversity and decreased breeding density along highways (Slabbeekorn and Ripmeester, 2008). Habitat fragmentation may also increase species' exposure to noise (USDT-FHA, 2006).

Sources of noise can be natural or anthropogenic. Natural noise would include sounds like running water, air passing over vegetation, rain, or other animals vocally communicating. Anthropogenic noises include things like cars, lawn mowers, construction, and other noises from residential areas (Brumm, 2004a, Brumm and Slabbekoorn, 1965).

Hummingbirds may have specific challenges with increasing sources of anthropogenic noise because of metabolic restrictions and the existing characteristics of their song. Anna's Hummingbird BMR is 67% higher than was expected compared to other songbirds, so they don't have as much energy to spare on activities like unnecessary singing and physical activity (Weathers and Stiles, 1988). It has been found that canaries sing more when they are in good body condition and after feeding (Ward et al., 2003). Hummingbirds must spend a considerable amount of time feeding in order to keep their metabolism working properly. They can't spend more energy devoting more time to singing in loud environments because it could decrease their body condition and lead to health and reproduction success problems. Generally, only male hummingbirds sing for the purposes of territory and resource protection or mate attraction, but singing is energetically costly for any songbird. Time spent singing is also less time spent doing other things like feeding and patrolling territory (Ward et al., 2003).

The functions of song have been well documented in passerines, but less is known about the structure and function of song in hummingbirds. Both male Anna's Hummingbirds (*Calypte anna*) and Costa's Hummingbirds (*Calypte costae*) use dive displays unique to each species to attract females (Slabbekoorn and Smith, 2002a), which is another source of precious energy being devoted to reproductive fitness. If competition with noise is high when *Calypte* hummingbirds are trying to sing, then competition among males is increased.

Anna's Hummingbirds and Costa's Hummingbirds males sing in the breeding season from approximately January to July. *Calypte* males hold territories and protect them by perching, singing, chasing, and diving. The frequency of hummingbird song is significantly higher than songbirds and their song is also quieter. It does not have as much volume (which translates into amplitude) as the songs of passerines, which sing within the lower frequency range of most ambient noise. Neighbors can sneak onto a male's territory for food or mating if the protecting male can't hear or see them. In noisy conditions, it is much easier for neighbors to sneak onto other territories and more difficult for each male to hold a territory without intruders.

Anna's Hummingbirds (*Calypete anna*) can be found year-round in southern California, in a broad range of habitats from coastal regions to deserts. They are prevalent in residential and remote wild areas in the region and are well known for visiting and defending artificial feeders. Anna's Hummingbird males exhibit a complex song type consisting of three syllables (Baptista and Schuchmann, 1989; Baptista and Matsui, 1979; Steen and Houtman, 2006) (Figure 1a). These syllables are referred to as A, B, and C. There is a general pattern to male Anna's Hummingbird song: ABCC, though it does vary occasionally depending on the individual, and this entire pattern is often repeated a number of times in a bout. The A syllable

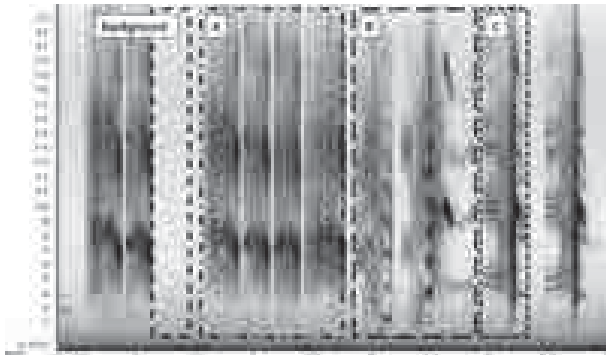


Figure 1a: Spectrogram showing Anna's Hummingbird song with background and individual A, B, and C syllables outlined.

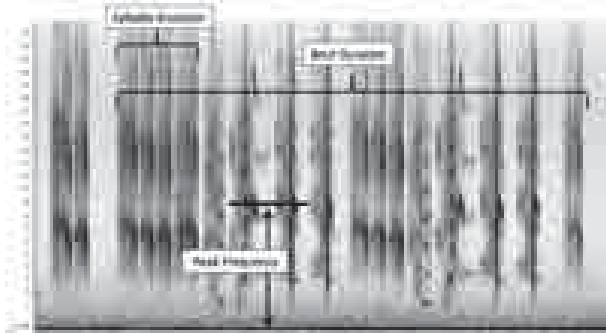


Figure 1b: Spectrogram showing Anna's Hummingbird song with syllable and bout duration defined and an example of peak frequency measurement.

has four elements, the B syllable has two elements, and the C syllable has one element, and each of these elements also varies in duration between individuals based on the frequency of the loudest part of the syllable and the duration of each individual syllable. Males either sing all A songs or more complex songs of mixed A, B, and C syllables. A-only songs are referred to as simple songs, as compared to complex mixed songs.

It is believed that complex songs are more costly to produce than simple song types because muscular function and brain function are of higher demand (Garamszegi et al., 2006). Anna's Hummingbird song generally has a minimum frequency of approximately 2kHz and a maximum frequency of approximately 24kHz, and the loudest part of Anna's Hummingbird song is generally around 11kHz (Steen and Houtman, 2006) (Figure 1b).

Costa's Hummingbird (*Calypete costae*) also prefers southern California desert habitats, and often migrates to higher elevations in the winter, so they are harder to find year-round. They are usually assumed to be less aggressive than Anna's Hummingbird in relation to establishing territories and protecting artificial feeders, but they use the same methods

of perching, singing, chasing, and diving for mate attraction and territory defense. Costa's Hummingbird males exhibit a simple song consisting of only one syllable type that can be repeated any number of times in a bout (Figure 2a). Each syllable is referred to as a song and there are four elements within each song. Costa's Hummingbird song has a minimum frequency of approximately 7kHz and a maximum frequency of approximately 12kHz, and the loudest part of their song is higher than Anna's Hummingbird at 11kHz (Williams and Houtman, 2008) (Figure 2b).

The frequency of anthropogenic noise is generally below 4kHz and is loudest below 2kHz (Wood and Yezernic, 2006; Slabbekoorn, 2004; Brumm and Slater, 2006). The loudest part of hummingbird song is above this 4kHz threshold for both these *Calyppe* species. Studies of passerines (a group of true songbirds) have shown that this group alters the frequency of the loudest part of their song to be above this 4kHz threshold, though the lowest parts of passerine song can be at a low frequency that does interfere with anthropogenic noise. When song interferes with other sources of noise, there is less propagation of the song's sound and there is the potential invasion of territory from other males or less effective attraction of females to the singing bird's territory. Keeping song inside a narrow bandwidth, or frequency range, may increase amplitude of the song and transmission distance of the signal (Slabbekoorn et al., 2002b) and could be something that hummingbirds, which are not true songbirds, may do in a similar noise situation.

Though these changes have been documented in songbirds, hummingbirds are not on the same clade as songbirds, but use song for similar purposes and live in the same environments (Gahr, 2000). Documenting how *Calyppe* hummingbirds change their song in response to the same pressures is one of the major objectives of this study. Song learning evolved independently three times, splitting into groups of songbirds, parrots, and hummingbirds, that all use song for the same basic functions, though the groups are not so closely related. Swifts are most closely related to hummingbirds, and they don't learn or exhibit complex song types (Gahr, 2000; Wood and Yezernic, 2006). Like songbirds, Anna's Hummingbirds learn the syllable types, frequency, rhythm and syntax of their complex songs from parents and neighboring males, meaning that there is easily a geographical population shift of song characteristics.

Slabbekoorn's studies of Great Tits have shown that these songbirds raise the frequency of their song in the presence of ambient noise and sing shorter notes in high ambient noise conditions. This study paired urban and forest birds in many major cities across Europe and found that the urban birds in every pair sang with a higher minimum frequency and a shorter first note. The forest birds also consistently sang more song types and there was no shift in peak frequency or in maximum frequency in either location. It seems that in loud, urban areas, song types that are not likely to be heard by neighbors are dropped (Slabbekoorn and den Boer-Visser, 2006; Brumm, 2006).

Song Sparrows and chaffinches (Brumm and Slater, 2006; Slabbekoorn and Ripmeester, 2008; Patricelli and Blickley, 2006) also sing at higher minimum frequencies in high noise conditions and concentrate more energy in higher frequencies of the song's notes, and the rest of the song was consistent in energy. This suggests that these songbirds choose to sing song types that fit into the current noise conditions (Wood and Yezernic, 2006).

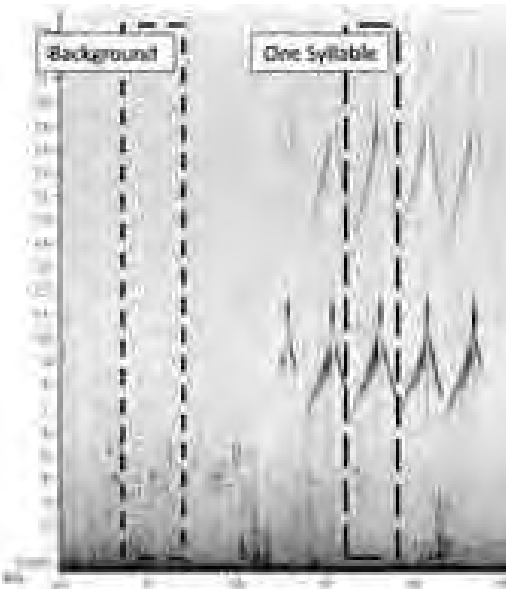


Figure 2a: Spectrogram showing Costa's Hummingbird song with background and a single syllable.

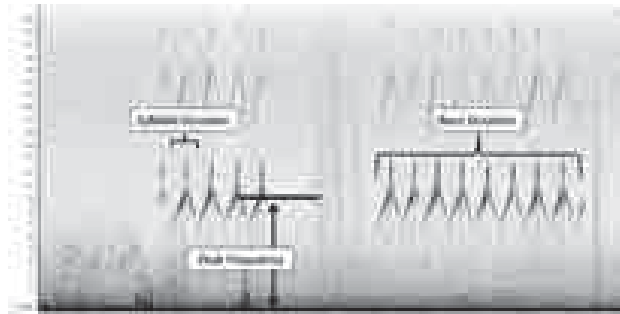


Figure 2b: Spectrogram showing Costa's Hummingbird song with syllable and bout duration defined and an example of peak frequency measurement.

Some birds do not necessarily shift their whole song to a higher minimum frequency. They instead sing less notes with lower frequencies, so overall their song is at a higher average frequency (Patricelli and Blickley, 2006). Zebra finches do regulate the amplitude of their song. They sing louder in response to playback of white noise, but the trade-off of higher amplitude could be a lower song rate (Cynx et al., 1998). House Finches sing at higher frequencies and adjust temporal characteristics of their song in noisy environments (Fernandez-Juricic et al., 2005; Slabbekoorn and Ripmeester, 2008; Patricelli and Blickley, 2006; Brumm and Slabbekoorn, 1995).

It is possible that hummingbirds are unable to alter their song in response to changes in noise levels, in which case anthropogenic noise could have a negative effect on hummingbirds' reproductive success. In order to be successful in a noisy environment, hummingbirds could avoid the noise by altering amplitude, frequency, or timing of their song to be in-between the loudest parts of ambient noise. The latter would not be reasonable in areas with constant noise, but would be advantageous in areas with intermittent noise, for example, next to a roadway. Rush hour traffic could be competing most with birds in the morning and in the late afternoon. If Hummingbirds simply avoided noise by moving their territories, then other population dynamics like male-male interactions would change.

The Lombard effect has been documented in humans and other species like nightingales and the Blue-Throated Hummingbird (Pytte et al., 2002; Slabbekoorn and Ripmeester, 2008). The Lombard effect is a form of short-term regulation where the subject's message gets louder when they are in louder areas (Brumm and Todt, 2002). An example of this is how nightingales increase the amplitude of their song in high noise conditions (Brumm, 2004b; Brumm and Slabbekoorn, 1965). Male nightingales sing louder when around other males, and when in quiet spaces, sing more low frequency notes (Brumm, 2004a).

Species relying on vocal communication could use the Lombard effect to increase transmission distance of the signal, which is called a signal-to-noise ratio. Ambient noise interferes with the signal-to-noise ratio, (Slabbekoorn, 2004) and it has been found that zebra finches and nightingales seem to assess noise conditions and then transmit a signal. This regulation mechanism allows energy to be saved for more complex song, more repetition of one song type (Brumm and Slabbekoorn, 1965), or singing more often (Cynx et al., 1998; Brumm, 2004a; Brumm and Todt, 2002). It is unknown if hummingbirds have this regulation mechanism, but it is possible that they would sing either more often in quiet times, or louder in noisier times.

I predict that peak frequency will not change in high noise conditions in either *Calypte* species because both species have song that is above the frequency of the loudest parts of anthropogenic noise. I also predict no change in average amplitude of either species' song because of hummingbirds' high metabolic rates and strict energy demands. It does not seem that they would have the extra energy to expend in singing louder (Table 1).

I predict that Costa's Hummingbird will sing longer individual songs in the presence of noise in order for the sound to propagate further because the frequency of their song is fairly high relative to most other sounds and they are much quieter than other hummingbirds and songbirds. In contrast, I predict Anna's Hummingbirds will sing shorter individual syllables in the presence of noise because the loudest part of their song is closer to the frequency of anthropogenic noise, and shorter sounds will propagate farther.

I predict that Costa's Hummingbird bout durations will be shorter in high noise conditions because the individual syllables are longer and this limits how much energy can be devoted to song at one time. I expect Anna's Hummingbird song bouts to possibly be longer in noisy areas due to energy distribution. If Anna's Hummingbirds are singing shorter syllables, they can sing for longer amounts of time and at the same time increase or decrease the complexity of their song.

	Summary of Predictions	
	Anna's Hummingbird (<i>Calypte anna</i>)	Costa's Hummingbird (<i>Calypte costae</i>)
Peak Frequency	No Change	No Change
Average Amplitude	No Change	No Change
Duration of syllable/song	Decrease (Shorter)	Increase (Longer)
Duration of bout/song	Increase (Longer)	Decrease (Shorter)
Complexity	Decrease	N/A

Table 1: Summary of predictions for each measured song feature for both *Calypte* species.



Figure 3: Map schematic of locations where hummingbirds were recorded in both 2007 and 2008. The pins are locations where many recordings were taken, most of which were in The Springs at Borrego Golf Course and Palm Canyon Campground at Anza Borrego State Park, and College of the Desert and Boyd Deep Canyon Research Center at Palm Desert.

I predict that Anna's Hummingbird song complexity will decrease in the presence of anthropogenic noise. This means that they will sing more A-only songs and less songs of mixed syllables. I expect more simplicity because of the Lombard effect. Less complex noises travel through air better and will reach neighbors that are farther away.

My measures will focus on individual syllable/song duration and the duration of the entire song bout, as well as average amplitude and peak frequency in both species. I will also measure the complexity of Anna's Hummingbird song. Use of behavioral territory defense cues, such as dive displays will be documented, since hummingbirds could modify the timing of their song when anthropogenic noise levels are highest. Recordings of Anna's Hummingbird and Costa's Hummingbird songs will be analyzed for background noise levels and then correlated with each of these structural song features.

Methods

Location

Multiple species of hummingbirds are residents of southern California habitats, from desert to coastal regions. Anza Borrego State Park in Imperial and San Bernardino Counties and UC Riverside's Boyd Deep Canyon Research Station - Palm Desert in Riverside County, CA (Figure 3) are ideal locations to

study the effects of anthropogenic noise on Anna's Hummingbirds and Costa's Hummingbirds because there are both constant and temporary noises, and there are also areas with no anthropogenic noise pollution. These are also areas in which both species are abundant during the breeding season. Recordings were taken during two breeding seasons - starting January 2007 and January 2008 and ending near June 1, 2007 and 2008.

Recording

Anna's Hummingbirds and Costa's Hummingbirds have slightly different behaviors regarding singing, making it important to observe the birds long enough to find the perch from which they sing the most. As birds were found, their locations were mapped, and GPS coordinates and ambient temperature were recorded. Notes were taken about the perches from which each bird sang. Recording equipment was set up near the perch to record song at a set distance from the perch for recordings with the possibility of an amplitude measurement.

To record song, a unidirectional Sennheiser K6/Me-64 was attached to a studio boom tripod, which could be adjusted to position the end of the microphone as close as possible to the perch without disturbing the bird. The microphone was connected to and powered by a Marantz PMD660 digital recorder. The microphone height and boom angle were adjusted to get within a meter of the perch if possible. The person operating the recorder sat at the bottom of the tripod out of view, so as to not discourage the bird from returning to the perch between song bouts.

Recording was complete when at least two full song bouts were recorded. Notes were taken of observations during singing, including whether the bird was facing the microphone, whether it was interrupted by another noise, whether it was chasing before it sang, and what sources of noise, like cars, were on the recording.

Sound Analysis

We analyzed the song of male Anna's Hummingbirds and Costa's Hummingbirds with Raven Pro 1.3 software, developed by Cornell University, to determine whether they alter song parameters (frequency, amplitude, duration, and complexity) in response to high anthropogenic noise conditions. Every recorded track was split into bouts for analysis. A bout is defined by at least five seconds of silence between each song (Steen and Houtman, 2006). The background noise sampled for each bout was the time from the beginning of the track to immediately before each bout began, up to the five seconds long. Every measurement included was between the frequencies of 2kHz and 24kHz because of restrictions of the microphone and reliability of the sound quality between these two frequencies.

Since all recordings were not taken with the exact same distance from the bird to the microphone, all amplitude measures were standardized to 1 meter. The actual amplitude measures from Raven were in microPascals, and with this transformation were converted to decibels and standardized across recordings so they could be compared. The measures could not be compared before the transformation because amplitude is a measure of loudness that takes into account the effect of propagation and sound degradation. Each measure was converted to decibels using the following

formula: $dB=20\log(RMS)$ where RMS is the average amplitude measure including minimum and maximum amplitude values (Fernandez-Juricic et al., 2005). RMS was reported as μ Pascals in Raven, so the formula $dB=20\mu\text{Pa}$ was also applied to each RMS measure to transform every measure into decibels (Brumm and Slater, 2006). Each decibel measure was then transformed to 1 meter distance with the following formula: $L_{1m}=20\log(d) + L_d$ where the sound level at 1 meter equals 20 multiplied by the log of the distance d in meters plus the sound level recorded at d distance (Brumm, 2004).

Measures of the average amplitude of background noise were split into categories of natural and high levels of anthropogenic noise. The levels were determined by measuring all collected recordings and then splitting the range in half. All bouts whose background average amplitude measured louder than the middle amplitude were considered high noise conditions, and all bouts whose average amplitude measured quieter than the middle amplitude were considered low noise conditions.

Measures of peak frequency, average amplitude (RMS), and duration of bouts and individual syllables were compared across noise conditions. Additionally, Anna's Hummingbird song complexity based on syllable types was measured and compared across noise conditions.

A Mann-Whitney U Test was performed for each feature, comparing natural and high noise conditions with a p-value less than 0.05 indicating significance. The birds were separated by species and breeding season, creating four sets of data.

To determine that five seconds is enough time to measure accurate background noise amplitude, standard noise recordings of only background noise were analyzed for amplitude and correlated with the background amplitudes measured from the song recordings. To get standard noise recordings, 1 minute of ambient noise was recorded in each of the four major directions (North, South, East, West) (Slabbeekoor, 2004) and five seconds of noise was randomly selected out of each recording. These selections were analyzed for RMS amplitude like the song recordings and the values had a positive correlation ($R^2=0.509$).

To determine that my background RMS amplitude measures taken from Raven were accurate to real-time, I took recordings of Anna's Hummingbird and Costa's Hummingbird playbacks and compared them to actual sound pressure levels. I set up the microphone in the same manner that my field recordings were taken, set a speaker 1 meter away, and recorded playback, at the same time reading measures from a sound pressure meter at the same position as the microphone. I analyzed the RMS amplitude from Raven in the same manner as my field recordings and positively correlated them with the RMS amplitude recorded by the sound pressure meter ($R^2=0.507$).

Results

I found that Anna's Hummingbird males from the 2007 season do not change average amplitude, syllable duration, bout duration, or song complexity but do increase peak frequency in high noise conditions (Table 2). Anna's Hummingbird males from the 2008 season do not change duration of B or C syllables, peak frequency, bout duration, or complexity but do sing louder and sing longer A syllables.

	Song Amplitude (dB)	A Syllable Duration (sec)	B Syllable Duration (sec)	C Syllable Duration (sec)	Peak Frequency (kHz)	Bout Duration (sec)	Complexity (value 0.0-1.0)
2007 Anna's	p=0.09 n=19 n=21 n=20 avg=66.33 ±1.71	p=0.14 n=19 n=20 n=19 avg=66.33 ±1.71	p=0.12 n=18 n=19 n=19 avg=67.13 ±0.94	p=0.10 n=18 n=19 n=19 avg=67.09 ±0.93	*p=0.03 n=19 n=19 n=19 avg=67.81 ±0.82	p=0.45 n=19 n=19 n=19 avg=67.12 ±0.82	p=0.25 n=19 n=19 n=19 avg=67.74 ±0.82
2008 Anna's	*p=0.01 n=19 n=20 n=19 n=19 avg=77.08 ±0.89	*p=0.01 n=19 n=19 n=19 avg=77.29 ±0.89	p=0.12 n=18 n=19 n=19 avg=67.81 ±0.82	p=0.16 n=18 n=19 n=19 avg=67.76 ±0.82	p=0.50 n=19 n=19 n=19 avg=67.76 ±0.82	p=0.07 n=19 n=19 n=19 avg=67.26 ±0.82	
	Song Amplitude (dB)	Song Duration (sec)		Peak Frequency (kHz)	Bout Duration (sec)		
2007 Costa's	p=0.24 n=11 n=10 n=10 avg=61.31 ±1.47	p=0.09 n=11 n=10 n=10 avg=44.74 ±1.80		p=0.42 n=11 n=10 n=10 avg=10.04 ±0.71	p=0.26 n=10 n=10 n=10 avg=9.44 ±0.71		
2008 Costa's	*p=0.001 n=19 n=17 n=19 n=19 avg=62.37 ±1.71	*p=0.09 n=19 n=17 n=19 avg=42.08 ±0.89		p=0.18 n=19 n=17 n=19 avg=9.33 ±0.81	p=0.36 n=19 n=17 n=19 avg=9.52 ±1.82		

Table 2: Summary of Mann-Whitney U-Test p-values and significance for each feature test of background against high noise conditions with average value for all conditions \pm standard error.

* = significant difference ($p < 0.05$)

Costa's Hummingbird males from the 2007 season do not change average amplitude, peak frequency, or bout duration. They do seem to sing longer songs but without a significant p-value ($p=0.07$). Costa's Hummingbirds from the 2008 season do not change song duration, peak frequency, or bout duration but also do sing louder songs.

Background RMS amplitudes were measured between 56 decibels and 89 decibels with an average of approximately 65 decibels in the 2007 season and between 52 decibels and 83 decibels with an average of approximately 70 decibels in the 2008 season. Some studies suggest that natural noise conditions are background noise levels of 48-62 decibels (Pytte, et al., 2002). In 1997, California published data that suggests that most species are disturbed in some way as background noise levels reach 60 decibels (TransSafety, Inc., 1997). As investigation into noise pollution continues, the standard level of noise that disturbs animals becomes clearer.

Discussion

Anna's Hummingbirds and Costa's Hummingbirds have much higher metabolic rates than passerines. Their metabolic processes are pushed to the extreme and they must operate at their maximum metabolic rate throughout the entire day. Their small size and high metabolism demand constant feeding and could limit the amount of energy they have to devote to song and dive displays.

Passerines have the potential to sing louder and expend energy in order to be heard, but not being able to sing louder may force hummingbirds to find other ways to be heard by neighbors and defend their resources.

Anna's Hummingbirds do respond to high anthropogenic noise conditions in the same way as passerines. This result was unexpected for many reasons. First, it was not believed that hummingbirds had any necessity to sing higher pitched songs. Anna's Hummingbird song is fairly close to the loudest parts of anthropogenic noise, so moving it farther away may mean that sound propagates farther. They may also be saving energy by singing higher in pitch because they don't have to sing louder or longer to be heard.

Costa's Hummingbirds also respond to high noise conditions in some of the same ways as passerines. In the 2007 season, they sang longer songs, which allows the sound to propagate farther. They sang louder songs in the 2008 season, which was not expected because of the already high frequency and metabolic restrictions. Also, Costa's Hummingbird song in general is not as loud as Anna's Hummingbird or passerine song in natural noise conditions.

Not being heard by neighbors means that males are less likely to be able to hold distinctive territories. In high noise conditions, males cannot maximize their territory size (Brumm, 2004b; Brumm and Slabbekoorn, 1965) and are likely to be involved in more male-male interactions because of male intrusion (Slabbekoorn and den Boer-Visser, 2006). Some of the

major factors that urban birds, or birds in high noise conditions, face that could potentially have an impact on song characteristics and song propagation are light, heat, chemical exposure, non-native vegetation, and changes in diet (Slabbekoorn and Ripmeester, 2008).

It has been speculated that the amplitude of ambient noise that disturbs songbirds' breeding biology is 60dB (James, 2006; TransSafety, Inc, 1997). A California construction project anticipated traffic diversions to temporarily increase background noise in a particular area by 3-4 decibels. This area was home to the endangered Least Bell's Vireo and because 60 decibels of noise is slowly becoming a standard level of disturbing noise, the project took other measures to decrease the noise in the detour area so as not to disturb the birds (TransSafety, Inc, 1997).

The possible consequence of raising the frequency of song too far is a reduction in mating success per male (Slabbekoorn, 2004). By raising frequency, they are seemingly heard by farther neighbors, but females must be able to hear the higher frequency song in order for males to have successful matings. Females still have to be able to hear chick calls and dive displays (Brumm and Slabbekoorn, 1965), which are in the range of 6-8kHz. This may interfere with some background anthropogenic noise, and males that sing at higher frequencies may be perceived as less aggressive (Patricelli and Blickley, 2006).

It is unknown exactly what frequencies hummingbirds hear and respond to. It is quite obvious that they hear in the 4-10kHz range, but whether they can hear above 24kHz, which is the highest frequency response of a studio-quality microphone is also unknown. Another possible factor is how low in frequency hummingbirds can hear. This is also unknown and if song changes in high noise conditions for territory defense, then ambient noise could be less of a factor in changing song features. Just like humans, there are limits to what frequencies hummingbirds can hear and if some of the human-created noise in the low frequencies is not heard, then they may not be affected as significantly as if they could hear a wide range of frequencies (Pytte, 2002).

Speciation is possible if females discriminate against certain song types or characteristics (Patricelli and Blickley, 2006; Brumm and Slabbekoorn, 1965). This would in turn create reproductive isolation and decrease reproductive fitness of any single male, and would also increase male-male interactions. There would eventually be a population-level shift of song characteristics if juveniles hear song differently in high noise conditions because the noise would block and decrease the quality of learning song (Wood and Yezerinac, 2006; Slabbekoorn and Ripmeester, 2008). The effectiveness of young-age learning and genetic factors may also leave an impact on how much potential a bird has to use a regulation mechanism to make song characteristics favorable in high noise conditions (Brumm, 2006) and how aggressive a bird is in a male-male interaction (Brumm, 2004a). Male songbirds are more aggressive and more successful at holding a territory against a male with similar song (Slabbekoorn and Smith, 2002a).

There is a trade-off in singing louder. Higher amplitude of song could alert predators in the area, which if were done by juveniles that are not able to escape, would decrease the size of the population itself (Cynx et al., 1998; Slabbekoorn and Ripmeester, 2008). Singing louder could also mean that the song rate decreases (Fernandez-Juricic et al., 2005; Patricelli and Blickley, 2006). Song rate and other song characteristics could be perceived by females as an indication of male quality, which would in turn increase or decrease the chances of the male being reproductively successful (Oberweger and Goller, 2001; Brumm, 2004a).

It was shown that particularly high amounts of singing decreased nightingales' body mass. Nightingales had to rest to avoid syringeal exhaustion (Thomas, 2002; Patricelli and Blickley, 2006). Besides a trade-off with amplitude, there is also a trade-off between fighting fatigue from singing and transmitting a signal that is likely to be heard by neighbors (Brumm and Slater, 2006). The degree of beak opening has been shown to positively correlate with frequency and other vocal tract movements do change song characteristics in songbirds (Hoesel et al., 2000). If singing loudly wasn't costly, the function of bird song may have been drastically different (Brumm, 2004a). Singing is not only costly in birds. For example, frogs and insects that sang regularly used 5-30 times the amount of oxygen as their resting respiratory rate (Thomas, 2002).

It has also been previously found that chaffinches sing longer bouts of the same song type, suggesting that repetition increases the chances that the signal will be received by neighbors, and singing one song type promotes fatigue. Switching song types after a long bout of one type creates a balance between fatigue and signal transmission success (Brumm and Slater, 2006). These and the above-mentioned pressures on song characteristics leave the possibility of speciation in urban areas where background noise is high (Slabbekoorn and den Boer-Visser, 2006).

Finding unexpected responses to anthropogenic noise in *Calypte* hummingbirds has profound effects on how we understand the function of song in this group. The similarities to passerines, though they are not the most closely related group to hummingbirds gives even more significance to the function of song in birds. Avoiding encroachment on birds' territories in terms of noise can have lasting effects on population dynamics, though there is encouragement in the possible plasticity of a population's song structure in response to noise.

Acknowledgements

I thank the SCERP program (UMEB DBI #0602922) and Drs. Bill Hoesel, Darren Sandquist, Danielle Zacherl and Sean Walker. Dr. Anne Houtman was my wonderful mentor. CSUF Biology Department, Undergraduate-Faculty Award, CSUF Associated Students and NSF provided funds. Fellow lab and cohort members provided help in the field.

References

- Baptista, L. F., and M. Matsui. Feb. 1979. The source of the dive-noise of the Anna's hummingbird. *The Condor* 81(1):87-89.
- Baptista, L. F., and K. L. Schuchmann. 1989. Song learning in the Anna hummingbird (*Calypte anna*). *Ethology* 84:15-26.
- Brumm, H., and H. Slabbekoorn. 1965. Acoustic communication in noise. *Advances in the Study of Behavior*, ed. D. S. Lehrman, R. A. Hinde, E. Shaw 35:151-209.
- Brumm, H., and D. Todt. 2002. Noise-dependent song amplitude regulation in a territorial songbird. *Animal Behaviour* 63:891-897.
- Brumm, H. Feb. 2004a. Causes and consequences of song amplitude adjustment in a territorial bird: a case study in nightingales. *Annals of the Brazilian Academy of Sciences* 76(2):289-295.
- Brumm, H. 2004b. The impact of environmental noise on song amplitude in a territorial bird. *Journal of Animal Ecology* 73:434-440.
- Brumm, H. Dec. 2006. Animal communication: city birds have changed their tune. *Current Biology* 16(23):R1003-R1004.
- Brumm, H., and P. J. B. Slater. 2006. Ambient noise, motor fatigue, and serial redundancy in chaffinch song. *Behav Ecol Sociobiol* 60:475-481.
- Cynx, J., R. Lewis, B. Tavel, and T. Hanson. 1998. Amplitude regulation of vocalizations in noise by a songbird, *Taeniopygia guttata*. *Animal Behavior* 56:107-113.
- Fernandez-Juricic, E. et al. Dec. 2005. Microhabitat selection and singing behavior patterns of male house finches (*Carpodacus mexicanus*) in urban parks in a heavily urbanized landscape in the western U.S. *Urban Habitats* 3:1(49-69).
- Gahr, M. 2000. Neural song control system of hummingbirds: comparison to swifts, vocal learning (Songbirds) and nonlearning (Suboscines) passerines, and vocal learning (Budgerigars) and nonlearning (Dove, Owl, Gull, Quail, Chicken) nonpasserines. *The Journal of Comparative Neurology* 426:182-196.
- Garamszegi, L., M. Zsolt, J. Moller, A. Pape. 2006. Avian song complexity is associated with high field metabolic rate. *Evolutionary Ecology Research* 8:75-90.
- Hoese, W., J. Podos, N. C. Boetticher, S. Nowicki. 2000. Vocal tract function in birdsong production: experimental manipulation of beak movements. *The Journal of Experimental Biology* 203:1845-1855.
- James, R. A. 2006. California innovation with highway noise and bird issues. <http://72.14.253.104.search?q=cache:onahjriwbUj:repositories.cdlib.org/cgi>
- Oberweger, K., and F. Goller. 2001. The metabolic cost of birdsong production. *The Journal of Experimental Biology* 204:3379-3388.
- Patricelli, G. L., and J. L. Blickley. 2006. Avian communication in urban noise: causes and consequences of vocal adjustment. *The Auk* 123(3):639-649.
- Pytte, C. L., K. M. Rusch, M. S. Ficken. Oct. 2002. Regulation of vocal amplitude by the Blue-Throated hummingbird, *Lampornis clemenciae*. *Animal Behavior* 66:703-710.
- Slabbekoorn, H., and T. B. Smith. 2002a. Bird song, ecology, and speciation. *Phil. Trans. R. Soc. Lond. B* 357:493-503.
- Slabbekoorn, H., J. Ellers, T. B. Smith. 2002b. Birdsong and sound transmission: the benefits of reverberations. *The Condor* 104(3):564-573.
- Slabbekoorn, H. Dec. 2004. Habitat-dependent ambient noise: consistent spectral profiles in two african forest types. *Journal of Acoustical Society of America* 116(6):3727-3733.
- Slabbekoorn, H., and A. den Boer-Visser. Dec. 2006. Cities change the songs of birds. *Current Biology* 16:2326-2331.
- Slabbekoorn, H., and E. A. P. Ripmeester. 2008. Birdsong and anthropogenic noise: implications and applications for conservation. *Molecular Ecology* 17:72-83.
- Steen, L., and A. M. Houtman. 2006. The song of the male Anna's hummingbird, *Calypte anna*, in southern California. Poster Presentation at Animal Behavior Society 43rd Annual Meeting Snowbird, Utah, 12-16.
- Thomas, R. J. 2002. The costs of singing in nightingales. *Animal Behavior* 63:959-966.
- TransSafety, Inc. 1997. California study addresses issues of roadway noise control for the benefit of endangered songbirds. *Road Engineering Journal*, <http://www.usroads.com/journals/p/rej/9710/re971003.htm>.
- U.S. Department of Transportation Federal Highway Administration. 2006. Synthesis of noise effects on wildlife populations. <http://www.fhwa.dot.gov/environment/noise/effects/preface.htm>.
- Ward, S., J. R. Speakman., P. J. B. Slater. 2003. The energy cost of song in the canary, *Serinus canaria*. *Animal Behavior* 66:893-902.
- Weathers, W. W., and G. F. Stiles. 1988. Energetics and water balance in free-living tropical hummingbirds. *The Condor* 91:324-331.
- Williams, B. R., and A. M. Houtman. 2008. Song of Costa's hummingbird *Calypte costae*. *The Auk* 125(3):663-669.
- Wood, W. E., and S. M. Yezerinac. 2006. Song sparrow (*Melospiza melodia*) song varies with urban noise. *The Auk* 123(3):650-659.

Remarks on De Sitter Spacetime: Geometry in the Theory of Relativity

Department of Mathematics, College of Natural Science and Mathematics, California State University, Fullerton, CA, USA

Peter Ho
Advisor: Dr. Bogdan D. Suceava

Abstract

Einstein's theory of relativity plays an important role in the development of modern mathematics and physics. De Sitter spacetime is perhaps the simplest curved spacetime possible. Our goal here is to present the geometry of De Sitter spacetime following James J. Callahan's *The Geometry of Spacetime: An Introduction to Special and General Relativity*. We solve the problems proposed in this text in section 5.3, where De Sitter spacetime is presented.

"With this most valiant piece of chalk I might project upon the blackboard four world axes. Since merely one chalky axis, as it is, consists of molecules all a-thrill, and moreover is taking part in the earth's travels in the universe, it already affords us ample scope for abstraction; that somewhat greater abstraction associated with the number four is for the mathematician no infliction." - H. Minkowski in "Space and Time," 1908

Introduction

De Sitter spacetime is a well-studied topic in mathematics and an important building block to understanding Einstein's solution to special and general relativity. In essence, it is a mathematical structure with unique features that model the shape of the universe in Einstein's equations. A simple curved surface incorporates time and space to show geometric results in ordinary three dimensions. The purpose of our note is to develop a basic understanding of De Sitter spacetime. Moreover, the development of De Sitter spacetime requires an understanding of Minkowski spacetime, which combines the concept of space and time in four dimensions instead of three dimensions. Also, we aim to understand De Sitter spacetime by applying vector calculus of curvilinear coordinate systems and parametrization. We will visualize hyperbolic solutions that are useful in explaining our geometric results. Lastly, we solve the problems proposed in section 5.3 of James J. Callahan's *The Geometry of Spacetime: An Introduction to Special and General Relativity* (2000), where De Sitter spacetime is presented.

Minkowski Spacetime

In his classical work, Minkowski combined space and time in his vision of geometry to model Einstein's theory of relativity. The idea of spacetime provides the framework towards developing the mathematical background and physical implications that come as a result of applying geometry in three dimensions. Minkowski discovered spacetime by taking the ordinary Euclidean three dimensional coordinate system and associating a new component that is considered to be time. The development of spacetime was a revolutionary idea used to formulate Einstein's equations in the theory of relativity. Minkowski's vision of spacetime is apparent throughout the theory of relativity in his 1908 paper "Space and Time" (Minkowski, 1952), where he presents his idea with geometric interpretations that are identified by measuring distances and defining a velocity limit that is in the spacetime continuum.

To begin, we consider looking into spacetime by taking the ordinary three dimensional coordinate system

$$\mathbb{R}^3 = \{(x, y, z) | x, y, z \in \mathbb{R}\},$$

which satisfies the viewpoint of ordinary three dimensional space. Minkowski spacetime is essentially understood by associating a time component t which brings us to a four dimensional space so that

$$\mathbb{R}^4 = \{(x, y, z, t) | x, y, z, t \in \mathbb{R}\},$$

where \mathbb{R}^4 or \mathbb{M} is denoted as the representation of Minkowski spacetime (Agnew, 2010).

Furthermore, the geometric implications of De Sitter spacetime are inherited from Minkowski geometry (Callahan, 2000). The structure of De Sitter spacetime becomes apparent by applying Minkowski's construct of measuring lengths, distances, and the velocity limit. To visualize Minkowski spacetime, we may consider a positive value for c and the point $(0, 0, 0, 0)$ for the origin O so that

$$f(x, y, z, t) = c^2 t^2 - x^2 - y^2 - z^2 = 0 \quad (1)$$

is the equation of a circular cone about the origin O . We apply the graph of the level surface that is a hyperboloid of two sheets given by equation (1). The hyperboloid is an important geometric representation that allows for significant interpretation in Minkowski spacetime. Since the graph exists from above and below the x -axis, we can consider the level surface by the equation

$$f(x, y, z, t) = c^2 t^2 - x^2 - y^2 - z^2 = 1, \quad (2)$$

which represents one sheet of the hyperboloid that lies in the half space above for $t > 0$ and the other sheet that lies below for $t < 0$. From the hyperboloid, we can examine the geometry by measuring lengths, distances, and angles on this level surface given by equation (2). Also, from the result, the asymptote of the hyperboloid takes the value and slope of $c = 1$, which represents the velocity limit. In Minkowski spacetime, no observer may go beyond the speed limit c . Graphically, the pair of intersecting lines with slope $c = 1$ can be visualized geometrically in our interpretation called the light cone. To an observer who appears to be traveling near the speed of light, the geometric result will have a slope that can be approximated close to 1 but is bounded by the asymptote.

Geometry on Surfaces and Planes

The approach to De Sitter spacetime stems from the concept of understanding Minkowski spacetime and the application of geometry on surfaces and tangent planes. Curve distance measurement results from applying geometry on surfaces and planes. Using methods from vector calculus

we can define a level surface that maps from two dimensions to three dimensions, a process known as parametrization. This application of parametrization produces results of tangent vectors that span a plane to measure angles and curvature along a curved surface. Meanwhile, calculus methods are applied to put these concepts together to model the shape of the De Sitter spacetime, which will be formulated as a curved surface. In essence, the De Sitter spacetime is described by analyzing the intrinsic geometry of a surface to a plane (Callahan, 2000).

Fundamentally, we begin by parametrizing to find curvature, lengths, and angles on a surface. We first take the approach of defining a surface of ordinary Euclidean space followed by an example in examining the geometric features of vectors on a plane and on a surface.

We consider an ordinary Euclidean plane with parameters of the curvilinear coordinate system $(q^1, q^2) \in \mathbb{R}^2$. Then for some constants k^1 and k^2 , we let the parameters $q^1 = k^1 = \text{constant}$, where every q^1 sweeps out a set of vertical lines in the plane. Hence, $q^2 = k^2 = \text{constant}$ sweeps out a set of horizontal lines in the plane. When composed with $q^1 = k^1$, vertical and horizontal lines produce an image of a grid or tiles that span the entire plane.¹

By taking the curvilinear coordinate system of (q^1, q^2) , we define a map

$$V : \mathbb{R}^2 \rightarrow \mathbb{R}^3 : (q^1, q^2) \rightarrow [x(q^1, q^2), y(q^1, q^2), z(q^1, q^2)] \quad (3)$$

so that the image of V maps the plane in \mathbb{R}^2 onto a surface in \mathbb{R}^3 . By taking the plane of (q^1, q^2) coordinates, we can visualize a surface with coordinate lines and points corresponding to (q^1, q^2) in \mathbb{R}^3 . Parametrization allows us to perform methods of calculus on a new domain that has familiar features.

We look particularly at a feature by determining a set of vectors, which allow us to find distances and angles by taking a tangent plane to the surface where some features are found. For instance, in \mathbb{R}^2 the (q^1, q^2) coordinate lines appear to be orthogonal, but when mapped into \mathbb{R}^3 , the lines may not necessarily imply the same orthogonality. Since V is a vector valued function, testing for orthogonality of coordinate curves can be done by evaluating tangent vectors at a point on the surface. The tangent vectors are considered to be basis vectors that span the tangent plane to the surface. Performing differential calculus on the surface will produce tangent vectors with the respected direction corresponding to the (q^1, q^2) coordinate lines (Callahan, 2000). We consider the following basis vectors $V_1, V_2 \in \mathbb{R}^2$ so that

$$V_1 = V'(q^1, k^2) = \frac{\partial V}{\partial q^1} \quad \text{and} \quad V_2 = V'(k^1, q^2) = \frac{\partial V}{\partial q^2}$$

The value of V_1 is determined as the tangent to the coordinate curve q^1 and V_2 as the tangent to the coordinate curve q^2 . The tangents at each point on the surface will allow for computations of lengths, distances, angles, and curvature on a surface. To see more in detail, the following example presents some features of geometry on a surface.

Example

We are interested in determining the orthogonality of the coordinate lines of the hyperboloid in Euclidean space². So we consider the hyperboloid in ordinary Euclidean space and assume that the given basis is the standard $\{\hat{i}, \hat{j}, \hat{k}\}$ set. To begin, we define the parametrization of the surface by the map

$$X : \mathbb{R}^2 \rightarrow \mathbb{R}^3 : x(q^1, q^2) \rightarrow [x(q^1, q^2), y(q^1, q^2), z(q^1, q^2)],$$

¹Note that superscripts do not infer exponents but infer coordinate curves to ordinary two dimensional Euclidean plane. Superscripts are the standard notation in vector and tensor calculus. They originate from the work "Méthodes de calcul différentiel absolu et leurs applications" by Tullio Levi-Civita and Gregorio Ricci-Curbastro, who continued the earlier work of Bernhard Riemann and Elwin Bruno Christoffel during the 19th century.

²This example is the solution to an exercise problem. See Reference [1], Exercise 2.(a) p.240.

so that the equation of the map X is given by

$$x(q^1, q^2) = (\sinh(q^1), \cosh(q^1) \cos(q^2), \cosh(q^1) \sin(q^2)),$$

where $\infty < q^1 < \infty$ and $-\pi \leq q^2 \leq \pi$. Then the basis vectors are given by

$$\begin{aligned} x_1 &= \frac{\partial x}{\partial q^1}(q^1, q^2) = [\cosh(q^1), \sinh(q^1) \cos(q^2), \sinh(q^1) \sin(q^2)] \\ x_2 &= \frac{\partial x}{\partial q^2}(q^1, q^2) = [0, -\cosh(q^1) \sin(q^2), \cosh(q^1) \cos(q^2)] \end{aligned}$$

and taking the cross product yields

$$\begin{aligned} x_1 \times x_2 &= [\sinh(q^1) \cosh(q^1) \cos^2(q^2) + \cosh(q^1) \sinh(q^1) \sin^2(q^2)]\hat{i} \\ &\quad - [\cosh^2(q^1) \cos(q^2) - 0]\hat{j} + [-\cosh^2(q^1) - 0]\hat{k} \\ &= [\sinh(q^1) \cosh(q^1)]\hat{i} - [\cosh^2(q^1) \cos(q^2)]\hat{j} - [\cosh^2(q^1)]\hat{k} \end{aligned}$$

Given our basis vectors, we can construct a metric tensor g_{ij} so that

$$g_{ij} = \begin{bmatrix} g_{11} & g_{12} \\ g_{21} & g_{22} \end{bmatrix} \text{ where } g \text{ is orthogonal when } g_{ij} = \delta_{ij} = \begin{cases} 1 & \text{if } i \neq j \\ 0 & \text{if } i = j \end{cases}$$

Computing the metric tensor components,

$$\begin{aligned} g_{11} &= x_1 \cdot x_1 \\ &= \cosh^2(q^1) + \sinh^2(q^1) \cos^2(q^2) + \sinh^2(q^1) \sin^2(q^2) \\ &= \cosh^2(q^1) + \sinh^2(q^1) = \cosh(2q^1), \\ g_{12} &= x_1 \cdot x_2 = g_{21} \\ &= 0 - \sinh(q^1) \cosh(q^1) \cos(q^2) \sin(q^2) + \sinh(q^1) \cosh(q^1) \sin(q^2) \cos(q^2) = 0, \\ g_{22} &= x_2 \cdot x_2 \\ &= 0 + \cosh^2(q^1) \sin^2(q^2) + \cos^2(q^1) \cos^2(q^2) = \cosh^2(q^1), \end{aligned}$$

then the resultant metric tensor is given by

$$g_{ij} = \begin{bmatrix} g_{11} & g_{12} \\ g_{21} & g_{22} \end{bmatrix} = \begin{bmatrix} \cosh(2q^1) & 0 \\ 0 & \cosh^2(q^1) \end{bmatrix} \text{ and } \sqrt{g_{ij}} = \begin{bmatrix} \sqrt{\cosh(2q^1)} & 0 \\ 0 & \cosh(q^1) \end{bmatrix}$$

Thus, computing the metric tensor of the basis vectors x_1 and x_2 shows orthogonality.

Parametrization of De Sitter Spacetime

The application of Minkowski spacetime raises the opportunity to visualize De Sitter spacetime by associating a time t component in a geometric representation of ordinary Euclidean space. In analogy to Minkowski spacetime, De Sitter spacetime is confined to a level surface that is modeled by a hyperboloid of one sheet. The simple hyperboloid is the structure applied to model De Sitter spacetime, a curved surface that consists of two spaces $t > 0$ and $t < 0$ centered about the origin O . Furthermore, an important feature to De Sitter spacetime is the application of Minkowski spacetime. We take a two dimensional slice through the origin of the hyperboloid of one sheet and examine its features. The image that traces on this two-dimensional piece represents hyperbolas of two sheets in Minkowski spacetime. On the slice, the asymptotes of the hyperbolas represent the velocity limit, or the speed of light c . Similar to Minkowski spacetime, an observer may approach speeds close to light, but exceeding the velocity limit is not allowed in De Sitter spacetime. Another unique feature of De Sitter spacetime is that time spans infinitely far into the future and into the past (Callahan, 2000).

We begin analyzing the concept of De Sitter space first by parametrizing the equation of the surface. We let the plane be defined by the coordinate parameters (q^1, q^2) , and we consider the map

$$\mathbb{X} : \mathbb{R}^2 \rightarrow \mathbb{R}^3 : (q^1, q^2) \rightarrow [x(q^1, q^2), y(q^1, q^2), z(q^1, q^2)]$$

Since De Sitter spacetime is modeled as a hyperboloid of one sheet, parametrization here is similar to that in the previous example given. That is we consider the given parametrization by letting q^1 denote time and q^2 denote position in space so that

$$\mathbb{X}(q^1, q^2) = (\sinh(q^1), \cosh(q^2) \cos(q^2), \cosh(q^1) \sin(q^2)), \quad (4)$$

where $-\infty < q^1 < \infty$ and $-\pi \leq q^2 \leq \pi$. Then determining the basis vectors yields

$$\mathbb{X}_1 = \frac{\partial \mathbb{X}}{\partial q^1} = (\cosh(q^1), \sinh(q^1) \cos(q^2), \sinh(q^1) \sin(q^2)) \quad (5)$$

$$\mathbb{X}_2 = \frac{\partial \mathbb{X}}{\partial q^2} = (0, -\cosh(q^1) \sin(q^2), \cosh(q^1) \cos(q^2)) \quad (6)$$

From the basis vectors, we construct geometric features through the metric tensor given by computing its dot products so that

$$g_{11} = \mathbb{X}_1 \cdot \mathbb{X}_1 = (\cosh^2(q^1) - \sinh^2(q^1) \cos^2(q^2) - \sinh^2(q^1) \sin^2(q^2)) = 1,$$

$$\begin{aligned} g_{12} &= \mathbb{X}_1 \cdot \mathbb{X}_2 = g_{21} \\ &= (\sinh(q^1) \cosh(q^1) \cos(q^2) \sin(q^2) - \sinh(q^1) \cosh(q^1) \cos(q^2) \sin(q^2)) = 0, \end{aligned}$$

$$g_{22} = \mathbb{X}_2 \cdot \mathbb{X}_2 = 0 - \cosh^2(q^1) \sin^2(q^2) - \cosh^2(q^1) \cos^2(q^2) = -\cosh^2(q^1),$$

where the matrix representation is given by

$$g_{ij} = \begin{bmatrix} 1 & 0 \\ 0 & -\cosh^2(q^1) \end{bmatrix}$$

The metric tensor has a non-zero diagonal implying that the coordinate curves (q^1, q^2) are orthogonal. The components of the metric tensor can be represented by \mathbb{X}_1 as the time-like vector and \mathbb{X}_2 as the space-like vector, where both are orthogonal to one another. Time and space point in independent directions of each other, but one of the physical consequences of relativity is that time and space are dependent on each other.

Proper Time

Further investigation into spacetime leads to the establishment of a proper time τ , which will be fundamental for describing the time-like feature in De Sitter spacetime. Proper time holds the property of outlining the worldcurve in which an observer or photon may be found tracing its path. Defining proper time is analogous to defining arclength in Euclidean space. The arclength along a curve C can be determined by

$$dS = \sqrt{dx^2 + dy^2 + dz^2}$$

In comparison, proper time is measuring the arclength along a curve within the interval of two events A and B so that in differential form

$$d\tau = \sqrt{(dt)^2 - (dx)^2 - (dy)^2 - (dz)^2}$$

The integral, in consideration to the time-like vector q^1 , can be computed for $A \leq q \leq B$. Then the proper time τ is

$$\tau(q) = \int_B^A \sqrt{\left(\frac{dt}{dq}\right)^2 - \left(\frac{dx}{dq}\right)^2 - \left(\frac{dy}{dq}\right)^2 - \left(\frac{dz}{dq}\right)^2} dq = \int_0^{q^1} \|\mathbb{X}_1\| dq$$

The proper time τ will be useful in interpreting the behavior of De Sitter spacetime such as in the event of increasing time. Proper time will be applied in the domain of De Sitter spacetime.

De Sitter Spacetime

The simplicity of De Sitter spacetime allows us to parametrize a model that fits accordingly to Einstein's formulation of relativity. It allows us to place emphasis on several geometric features such as lengths, angles, and distances. An important feature of discovering the metric on the hyperboloid is the feature of the velocity limit in Einstein's formulation. That is, the speed of light is the speed limit of the universe, where no observer or photon may travel faster than $c = 1$. In comparison to Minkowski spacetime, we see that the light cone binds De Sitter spacetime to a finite space.

From our previous result, we use the given metric tensor by

$$g_{ij} = \begin{bmatrix} 1 & 0 \\ 0 & -\cosh^2(q^1) \end{bmatrix}$$

The basis vector \mathbb{X}_1 is considered to be time-like along the set of $q^2 = \text{constant}$ coordinate lines, and \mathbb{X}_2 is considered to be space-like along the set of $q^1 = \text{constant}$ coordinate lines. The worldcurve of X can be written as a linear combination of \mathbb{X}_1 and \mathbb{X}_2 so that

$$X(q^1, q^2) = [q^1, q^2] \begin{bmatrix} 1 & 0 \\ 0 & -\cosh^2(q^1) \end{bmatrix} \begin{bmatrix} 1 \\ \pm \operatorname{sech}(q^1) \end{bmatrix} = \underbrace{q^1}_{\text{timelike}} \mp \underbrace{q^2 \cosh(\tau)}_{\text{spacelike}}$$

To determine the velocity limit in De Sitter spacetime, the speed limit $c = 1$ can be determined by analyzing the velocity of an observer. By taking the ratio of the space-like vector to the time-like vector components,

$$c = \frac{\pm \operatorname{sech}(\tau) \|\mathbb{X}_2\|}{\|\mathbb{X}_1\|} = \frac{\pm \operatorname{sech}(\tau) \cosh(\tau)}{1} = \pm 1,$$

and the velocity limit to be no greater than 1. The speed of light is the speed limit of the universe, where no observer can travel faster than c . In comparison to Minkowski spacetime, the speed of light $c = 1$ is the slope of a straight line in two dimensions. Embedded into three dimensions is a set of straight lines that, if rotated about the hyperboloid, draws a ruled surface since there is symmetry about the axis of t . Since the value of c contains the slopes $c = \pm 1$, the slopes produce pairs of intersecting lines that represent a vector field. As τ increases, the angles between the space-like and time-like vectors decrease to 0, where space and time meet.

De Sitter spacetime is then represented by

$$-Q(\mathbb{X}) = x^2 + y^2 + z^2 + w^2 - t^2 = 1$$

To an observer, De Sitter spacetime has no boundary but appears to be finite with time expanding infinitely far into the future and also into the past directions. Observers traveling about De Sitter spacetime may travel in a direction that ends at the starting point, which explains why the universe is finite.

Solutions to Exercise Problems

The solution sets presented here are solutions to exercise problems proposed in section 5.3 (page 240-241) of James J. Callahan's *The Geometry of Spacetime: An Introduction to Special and General Relativity*, where De Sitter spacetime is presented. The solution to problem 2.a is used as an example stated above, where we computed the parametrization for a hyperboloid in Euclidean space. The solutions can be computed directly using methods of differential and vector calculus to arrive at desired solutions.

1. (a) For the parametrization of \mathbb{X} of de Sitter spacetime, that we use, show that $\mathbb{X}_1 \times \mathbb{X}_2 = \cosh(q^1)\mathbb{X}$

Solution: We let the parametrization of De Sitter space time be given by equation (4). By showing that $\mathbb{X}_1 \times \mathbb{X}_2 = \cosh(q^1)\mathbb{X}$, we make the following claim:

Claim: $\mathbb{X}_1 \times \mathbb{X}_2 = \cosh(q^1)\mathbb{X}$

Reason: Assume the given basis is the standard $\{\hat{i}, \hat{j}, \hat{k}\}$ set and assume the basis vectors are given by

$$\begin{aligned} \mathbb{X}_1 &= \frac{\partial \mathbb{X}}{\partial q^1} = (\cosh(q^1), \sinh(q^1) \cos(q^2), \sinh(q^1) \sin(q^2)) \\ \mathbb{X}_2 &= \frac{\partial \mathbb{X}}{\partial q^2} = (0, -\cosh(q^1) \sin(q^2), \cosh(q^1) \cos(q^2)) \end{aligned}$$

Then $\mathbb{X}_1 \times \mathbb{X}_2 = \begin{vmatrix} \hat{i} & \hat{j} & \hat{k} \\ \cosh(q^1) & \sinh(q^1) \cos(q^2) & \sinh(q^1) \sin(q^2) \\ 0 & -\cosh(q^1) \sin(q^2) & \cosh(q^1) \cos(q^2) \end{vmatrix}$

$$\begin{aligned}
&= [\sinh(q^1) \cos(q^2) \cos(q^1) \cos(q^2) + \sinh(q^1) \sin(q^2) \cosh(q^1) \sin(q^2)]\hat{i} \\
&\quad - [\cosh(q^1) \cosh(q^2) \cos(q^2)]\hat{j} + [-\cosh(q^1) \cosh(q^1) \sinh(q^2)]\hat{k} \\
&= [\sinh(q^1) \cos(q^1) \cos^2(q^2) + \sinh(q^1) \cosh(q^1) \sin^2(q^2)]\hat{i} \\
&\quad - [\cosh^2(q^1) \cos(q^2)]\hat{j} - [\cosh^2(q^1) \sin(q^2)]\hat{k} \\
&= [\sinh(q^1) \cosh(q^1)]\hat{i} - [\cosh^2(q^1) \cos(q^2)]\hat{j} - [\cosh^2(q^1) \sin(q^2)]\hat{k} \\
&= \cosh(q^1)\{\[\sinh(q^1)]\hat{i} - [\cosh(q^1) \cos(q^2)]\hat{j} - [\cosh(q^1) \sin(q^2)]\hat{k}\} \\
&= \cosh(q^1)\mathbb{X}
\end{aligned}$$

Thus, the parametrization of De Sitter spacetime is given by (5), which implies that $\mathbb{X}_1 \times \mathbb{X}_2 = \cosh(q^1)\mathbb{X}$. \square

1. (b) Show that $(\mathbb{X}_1 \times \mathbb{X}_2) \perp \mathbb{X}_1$ and $(\mathbb{X} \times \mathbb{X}_2) \perp \mathbb{X}_2$, in the sense of the Minkowski norm.

Solution: Let the parametrization of De Sitter space time be given by (5) so that in the Minkowski norm we make the claim by showing that $(\mathbb{X}_1 \times \mathbb{X}_2) \perp \mathbb{X}_1$ and $(\mathbb{X}_1 \times \mathbb{X}_2) \perp \mathbb{X}_2$.

Claim: $(\mathbb{X}_1 \times \mathbb{X}_2) \perp \mathbb{X}_1$

Reason: Assume the given basis is the standard $\{\hat{i}, \hat{j}, \hat{k}\}$ set. To show orthogonality, we need to show that $(\mathbb{X}_1 \times \mathbb{X}_2) \cdot \mathbb{X}_1 = 0$. Since $(\mathbb{X}_1 \times \mathbb{X}_2) = \cosh(q^1)\mathbb{X}$, this implies

$$\begin{aligned}
(\mathbb{X}_1 \times \mathbb{X}_2) \cdot \mathbb{X}_1 &= \cosh(q^1)\mathbb{X} \cdot \mathbb{X}_1 \\
&= \cosh(q^1)\mathbb{X} \cdot [\cosh(q^1)\hat{i} + \sinh(q^1) \cos(q^2)\hat{j} + \sinh(q^1) \sin(q^2)\hat{k}] \\
&= [\sinh(q^1) \cosh(q^1)\hat{i} - \cosh^2(q^1) \cos(q^2)\hat{j} - \cosh^2(q^1) \sin(q^2)\hat{k}] \\
&\quad \cdot [\cosh(q^1)\hat{i} + \sinh(q^1) \cos(q^2)\hat{j} + \sinh(q^1) \sin(q^2)\hat{k}] \\
&= [\sinh(q^1) \cosh^2(q^1) - \cosh^2(q^1) \sinh(q^1) \cos^2(q^2) - \cosh^2(q^1) \sinh(q^1) \sin^2(q^2)] \\
&= \{\sinh(q^1) \cosh^2(q^1) - \cosh^2(q^1) \sinh(q^1)[\cos^2(q^2) + \sin^2(q^2)]\} \\
&= \cosh^2(q^1) \sinh(q^1) - \cosh^2(q^1) \sinh(q^1) \\
&= 0
\end{aligned}$$

Thus, $(\mathbb{X}_1 \times \mathbb{X}_2) \cdot \mathbb{X}_1 = 0$ implies $(\mathbb{X}_1 \times \mathbb{X}_2) \perp \mathbb{X}_1$. \square

Claim: $(\mathbb{X}_1 \times \mathbb{X}_2) \perp \mathbb{X}_2$

Reason: Assume the given basis is the standard $\{\hat{i}, \hat{j}, \hat{k}\}$ set. To show orthogonality, we need to show that $(\mathbb{X}_1 \times \mathbb{X}_2) \cdot \mathbb{X}_2 = 0$.

Since $(\mathbb{X}_1 \times \mathbb{X}_2) = \cosh(q^1)\mathbb{X}$, this implies

$$\begin{aligned}
 (\mathbb{X}_1 \times \mathbb{X}_2) \cdot \mathbb{X}_2 &= \cosh(q^1)\mathbb{X} \cdot \mathbb{X}_2 \\
 &= \cosh(q^1)\mathbb{X} \cdot [-\cosh(q^1)\sin(q^2)\hat{i} + \cosh(q^1)\cos(q^2)\hat{k}] \\
 &= [\sinh(q^1)\cos(q^1)\hat{i} - \cosh^2(q^1)\cos(q^2)\hat{j} - (\cosh^2(q^1)\sin(q^2)\hat{k}] \\
 &\quad \cdot [0\hat{i} - \cosh(q^1)\sin(q^1)\hat{j} + \cosh(q^1)\cos(q^2)\hat{k}] \\
 &= 0 + \cosh^3(q^1)\cos(q^2)\sin(q^2) - \cosh^3(q^1)\cos(q^2)\sin(q^2) \\
 &= 0
 \end{aligned}$$

Thus, $(\mathbb{X}_1 \times \mathbb{X}_2) \cdot \mathbb{X}_2 = 0$ implies $(\mathbb{X}_1 \times \mathbb{X}_2) \perp \mathbb{X}_1$. □

1. (c) Show that $\|\mathbb{X}_1 \times \mathbb{X}_2\| = \sqrt{-g} = \cosh(q^1)$, the area magnification factor.

Solution: We let the parametrization of De Sitter space time \mathbb{X} be given by (5) and its basis vectors \mathbb{X}_1 and \mathbb{X}_2 be given by (6) and (7) respectively. For the area magnification factor, we make the following claim that $\|\mathbb{X}_1 \times \mathbb{X}_2\| = \sqrt{-g} = \cosh(q^1)$.

Claim: $\|\mathbb{X}_1 \times \mathbb{X}_2\| = \sqrt{-g} = \cosh(q^1)$

Reason: Assume the given basis is the standard $\{\hat{i}, \hat{j}, \hat{k}\}$ set. Given that

$$\begin{aligned}
 \text{Since } \mathbb{X}_1 \times \mathbb{X}_2 &= \cosh(q^1)\mathbb{X} \\
 &= [\sinh(q^1)\cosh(q^1)]\hat{i} - [\cosh^2(q^1)\cos(q^2)]\hat{j} - [\cosh^2(q^1)\sin(q^2)]\hat{k}
 \end{aligned}$$

this implies

$$\begin{aligned}
 \|\mathbb{X}_1 \times \mathbb{X}_2\| &= \|\cosh(q^1)\mathbb{X}\| \\
 &= \{\[\sinh(q^1)\cosh(q^1)]^2 + [-\cosh^2(q^1)\cos(q^2)]^2 + [-\cosh^2(q^1)\sin(q^2)]^2\}^{1/2} \\
 &= \{\[\sinh^2(q^1)\cosh^2(q^1)] + [\cosh^4(q^1)\cos^2(q^2)] + [\cosh^4(q^1)\sin^2(q^2)]\}^{1/2} \\
 &= \{\sinh^2(q^1)\cosh^2(q^1) + \cosh^4(q^1)[\cos^2(q^2)] + \sin^2(q^2)\}^{1/2} \\
 &= \{\sinh^2(q^1)\cosh^2(q^1) + \cosh^4(q^1)\}^{1/2} \\
 &= \{\cosh^2(q^1)[\sinh^2(q^1) + \cosh^2(q^1)]\}^{1/2} \\
 &= \{\cosh^2(q^1)[\cosh(2q^1)]\}^{1/2} \\
 &= \cosh(q^1)\sqrt{\cosh(2q^1)}
 \end{aligned}$$

Since $g = -\cosh^2(q^1)$, this implies $\sqrt{-g} = \cosh(q^1)$.

Thus, $\|\mathbb{X}_1 \times \mathbb{X}_2\| = \sqrt{-g} = \cosh(q^1)$. □

2. Consider the hyperboloid

$$\mathbf{x}(q^1, q^2) = (\sinh(q^1), \cosh(q^1)\cos(q^2), \cosh(q^1)\sin(q^2)),$$

as being an embedding in Euclidean space instead of Minkowski space, and calculate $x_1, x_2, x_1 \times x_2, g_{ij}$, and \sqrt{g} . Are the coordinate lines still orthogonal?

Solution: We are interested in determining the orthogonality of the coordinate lines of the hyperboloid in Euclidean space, so we consider the hyperboloid in ordinary Euclidean space and assume the given basis is the standard $\{\hat{i}, \hat{j}, \hat{k}\}$ set. To begin, we define the parametrization of the surface by

$$x(q^1, q^2) = (\sinh(q^1), \cosh(q^1) \cos(q^2), \cosh(q^1) \sin(q^2)),$$

where $\infty < q^1 < \infty$ and $-\pi \leq q^2 \leq \pi$. Then the basis vectors are given by

$$\begin{aligned} x_1 &= \frac{\partial x}{\partial q^1}(q^1, q^2) = [\cosh(q^1), \sinh(q^1) \cos(q^2), \sinh(q^1) \sin(q^2)] \\ x_2 &= \frac{\partial x}{\partial q^2}(q^1, q^2) = [0, -\cosh(q^1) \sin(q^2), \cosh(q^1) \cos(q^2)] \end{aligned}$$

and taking the cross product yields

$$\begin{aligned} x_1 \times x_2 &= [\sinh(q^1) \cosh(q^1) \cos^2(q^2) + \cosh(q^1) \sinh(q^1) \sin^2(q^2)]\hat{i} \\ &\quad - [\cosh^2(q^1) \cos(q^2) - 0]\hat{j} + [-\cosh^2(q^1) - 0]\hat{k} \\ &= [\sinh(q^1) \cosh(q^1)]\hat{i} - [\cosh^2(q^1) \cos(q^2)]\hat{j} - [\cosh^2(q^1)]\hat{k} \end{aligned}$$

Given our basis vectors, we can construct a metric tensor g_{ij} so that

$$g_{ij} = \begin{bmatrix} g_{11} & g_{12} \\ g_{21} & g_{22} \end{bmatrix} \text{ where } g \text{ is orthogonal when } g_{ij} = \delta_{ij} = \begin{cases} 1 & \text{if } i \neq j \\ 0 & \text{if } i = j \end{cases}$$

Computing the metric tensor components,

$$\begin{aligned} g_{11} &= x_1 \cdot x_1 \\ &= \cosh^2(q^1) + \sinh^2(q^1) \cos^2(q^2) + \sinh^2(q^1) \sin^2(q^2) \\ &= \cosh^2(q^1) + \sinh^2(q^1) \\ &= \cosh(2q^1), \\ g_{12} &= x_1 \cdot x_2 = g_{21} \\ &= 0 - \sinh(q^1) \cosh(q^1) \cos(q^2) \sin(q^2) + \sinh(q^1) \cosh(q^1) \sin(q^2) \cos(q^2) \\ &= 0, \\ g_{22} &= x_2 \cdot x_2 \\ &= 0 + \cosh^2(q^1) \sin^2(q^2) + \cos^2(q^1) \cos^2(q^2) \\ &= \cosh^2(q^1), \end{aligned}$$

then the resultant metric tensor is given by

$$g_{ij} = \begin{bmatrix} g_{11} & g_{12} \\ g_{21} & g_{22} \end{bmatrix} = \begin{bmatrix} \cosh(2q^1) & 0 \\ 0 & \cosh^2(q^1) \end{bmatrix} \text{ and } \sqrt{g_{ij}} = \begin{bmatrix} \sqrt{\cosh(2q^1)} & 0 \\ 0 & \cosh(q^1) \end{bmatrix}$$

Note that this problem was presented previously as an example in order to show orthogonality of a tangent surface. \square

3. Prove that $\cos(\pm A \mp \pi/2) = \sin(A)$ and $\sin(\pm A \mp \pi/2) = \cos(A)$

Proof:

Since A is the angle $-\pi/2 \leq A \leq \pi/2$, we have

$$\cos(A - \pi/2) = \sin(A) \quad \text{and} \quad \cos(-A + \pi/2) = \sin(A)$$

It follows that $\cos(\pm A \mp \pi/2) = \sin(A)$.

Then for the second portion A is the angle $-\pi/2 \leq A \leq \pi/2$, we have

$$\sin(A - \pi/2) = \cos(A) \quad \text{and} \quad \sin(-A + \pi/2) = \cos(A)$$

It follows that $\sin(\pm A \mp \pi/2) = \pm \cos(A)$. \square

Acknowledgements

Many thanks to Dr. B. Suceavă for giving me this opportunity to explore different possibilities in mathematics. Also thanks to Dr. A. Agnew for allowing me to use his notes as reference.

References

- Agnew, A. F. (2010) Lecture Notes: Quantum Field Theory, California State University, Fullerton.
- Callahan, J. J. (2000) Geometry of Spacetime: An Introduction to Special and General Relativity, Springer-Verlag, New York.
- Coxeter, H. S. M. A Geometrical Background For De Sitter's World, Am. Math. Mon., 50 (1943) No. 4, pp. 217-228.
- Minkowski, H. (1952) The Principle of Relativity: A Collection of Original Papers on the Special and General Theory of Relativity, Dover, New York. 75.

Economical generating sets for the symmetric and alternating groups consisting of cycles of a fixed length

Josh Maglione
Advisor: Dr. Scott Annin

Department of Mathematics, College of Natural Science and Mathematics, California State University, Fullerton, CA, USA

Abstract

The symmetric group S_n and the alternating group A_n are groups of permutations on the set $\{0, 1, 2, \dots, n-1\}$ whose elements can be represented as products of disjoint cycles (the representation is unique up to the order of the cycles). In this paper, we show that whenever $n \geq k \geq 3$, the collection of all k -cycles generates S_n if k is even, and generates A_n if k is odd. Furthermore, we algorithmically construct generating sets for these groups of smallest possible size consisting exclusively of k -cycles, thereby strengthening results in (Ben-Shimol, 2007).

Introduction

The concept of a generating set for a mathematical structure is extraordinarily important across a broad spectrum of mathematics, particularly in algebra. It arises front and center in core undergraduate mathematics material in both linear and abstract algebra (e.g. (Dummit, Foote, 2004), (Goode, Annin, 2007), (Hungerford, 1996)), and it has been the subject of many research investigations (e.g. (Annin, 1997), (Babai et al., 1990), (Ben-Shimol, 2007), (Heath et al., 2009), (Nekkoei, Jabari, 2003), (Stong, Suceava, 2003)). In the context of a group G , for example, a common goal is to find a subset $S \subseteq G$ such that S generates G , often written as $G = \langle S \rangle$. The present article, largely motivated by the question posed in (Stong, Suceava, 2003), extends the list of known generating sets for the symmetric group S_n and the alternating group A_n (and strengthens the main result in (Ben-Shimol, 2007)) by considering the collection $C_{n,k}$ of all cycles in S_n of a fixed length k (i.e. all k -cycles), where, of course, $k \leq n$. As we shall see, if k is odd, then we can construct a subset S of $C_{n,k}$ such that $A_n = \langle S \rangle$, and if k is even, then we can do the same for S_n . In both cases, we do this in such a way that the subset S constructed has the smallest possible size. The results we prove rely on the following well known result that highlights what is perhaps the best known generating set for A_n .

Theorem 0.1 The alternating group A_n is generated by $C_{n,3}$.

This theorem is useful in proving that A_n is simple whenever $n \geq 5$ (e.g. (Dummit, Foote, 2004), (Hungerford, 1996)).

Preliminary Results

We begin with some basic notations and terminology. For a given set X , let S_X (resp. A_X) denote the group of all permutations (resp. even permutations) of X . In case $X = \{0, 1, 2, \dots, n - 1\}$, we denote this group by S_n (resp. A_n). For each positive integer n , let \mathbb{Z}_n denote the group of integers modulo n . If k is a positive integer with $n \geq k$, a k -cycle $\sigma \in S_n$ that can be written in the form $\sigma = (a_0, a_1, a_2, \dots, a_{k-1})$ such that $a_i \in \mathbb{Z}_n$ for all $i = 0, 1, 2, \dots, k - 1$ and $a_i = a_0 + i$ in \mathbb{Z}_n for all $i = 0, 1, 2, \dots, k - 1$ will be called a step k -cycle, or simply step cycle, and we write $\sigma = h_k(a_0)$. We will refer to $a_0, a_1, a_2, \dots, a_{k-1}$ as the elements of $h_k(a_0)$. Note that in the case $n > k$, the choice of a_0 is unique for each step k -cycle. We will sometimes refer to a pair of step cycles $h_k(a)$ and $h_k(a+1)$ as consecutive step cycles. Finally, let $H_{n,k} \subseteq C_{n,k}$ denote the set of all step cycles of length k in S_n . Observe that $|H_{n,n}| = 1$ for all n , and for $n > k$, we have $|H_{n,k}| = n$.

Our first main goal is to show, for positive integers k and n with $n > k \geq 3$, that $H_{n,k}$ generates A_n if k is odd, and $H_{n,k}$ generates S_n if k is even. The first step towards this end is Lemma 0.3 below, but before we proceed, we remind the reader of an important fact regarding the computation of conjugate elements in S_n that will be used freely throughout this paper (see, e.g. (Dummit, Foote, 2004), (Hungerford, 1996)).

Proposition 0.2 Let $\sigma, \tau \in S_n$. For each cycle $(a_0, a_1, a_2, \dots, a_r)$ in the disjoint cycle representation of σ , the element $\tau\sigma\tau^{-1}$ contains the cycle $(\tau(a_0), \tau(a_1), \tau(a_2), \dots, \tau(a_r))$ in its disjoint cycle representation, where $\tau(a_i)$ denotes the image of a_i under the permutation τ . In particular, the elements σ and $\tau\sigma\tau^{-1}$ have the same structure when expressed (uniquely up to order) as a product of disjoint cycles.

Lemma 0.3 Let n be an integer with $n \geq 3$. Then $C_{n,3} \subseteq \langle H_{n,3} \rangle$.

Proof: We proceed by induction on n , with the case $n = 3$ being obvious. Now assume that $C_{n,3} \subseteq \langle H_{n,3} \rangle$. We claim that $C_{n+1,3} \subseteq \langle H_{n+1,3} \rangle$. The first step is to show that

$$\langle H_{n,3} \rangle \subseteq \langle H_{n+1,3} \rangle. \quad (1)$$

Note that the only elements of $H_{n,3}$ not belonging to $H_{n+1,3}$ are $(n-2, n-1, 0)$ and $(n-1, 0, 1)$, and these can be generated by elements of $H_{n+1,3}$ as follows:

$$(n-2, n-1, 0) = (n, 0, 1)(n-2, n-1, n)(n, 0, 1)^{-1} \quad \text{and} \quad (n-1, 0, 1) = (n, 0, 1)(n-1, n, 0)(n, 0, 1)^{-1}.$$

This establishes (1). Now consider $(a, b, c) \in C_{n+1,3}$. If $0 \leq a, b, c \leq n-1$, then already we have

$$(a, b, c) \in C_{n,3} \subseteq \langle H_{n,3} \rangle \subseteq \langle H_{n+1,3} \rangle,$$

as needed. Therefore, we may assume without loss of generality that $c = n$. Observe that

$$(a, b, n) = (a, n-2, n-1)(n-2, n-1, n)^2(a, b, n-2),$$

and all cycles on the right-hand side belong to $C_{n,3} \cup H_{n+1,3} \subseteq \langle H_{n+1,3} \rangle$. Thus, $(a, b, n) \in \langle H_{n+1,3} \rangle$. Therefore, all cycles $(a, b, c) \in C_{n+1,3}$ belong to $\langle H_{n+1,3} \rangle$, as needed. \blacksquare

Proposition 0.4 Let n and k be positive integers with $n > k \geq 2$. Then, $H_{n,3} \subseteq \langle H_{n,k} \rangle$.

Proof: For all $a \in \mathbb{Z}_n$,

$$h_k(a+2)^2 h_k(a) h_k(a+1)^{-1} h_k(a+2)^{-2} = \begin{cases} h_3(a) & \text{if } n > k+1, \\ h_3(a+1) & \text{if } n = k+1, \end{cases}$$

from which the result immediately follows. \blacksquare

Corollary 0.5 Let n and k be positive integers with $n > k \geq 2$. If k is odd, then $\langle H_{n,k} \rangle = A_n$, and if k is even, then $\langle H_{n,k} \rangle = S_n$.

Proof: Observe from Lemma 0.3 and Proposition 0.4 that $C_{n,3} \subseteq \langle H_{n,k} \rangle$. Hence, by Theorem 0.1, $A_n \subseteq \langle H_{n,k} \rangle$. If k is odd, then $\langle H_{n,k} \rangle \subseteq A_n$ and we conclude that $A_n = \langle H_{n,k} \rangle$. On the other hand, if k is even, then $A_n \subsetneq \langle H_{n,k} \rangle$ (since $H_{n,k}$ contains an odd permutation), so $\langle H_{n,k} \rangle = S_n$. \blacksquare

The aim of the remainder of this article is to shrink the size of the generating set $H_{n,k}$ for A_n (or S_n , if k is even) in Corollary 0.5. In what follows, we adopt the notation that

$$\alpha := h_k(0) \quad \text{and} \quad \beta := h_k(k).$$

Corollary 0.6 Suppose $k \geq 2$ and $n = k+1$. If k is odd, we have $\langle \alpha, \beta \rangle = A_n$, and if k is even, we have $\langle \alpha, \beta \rangle = S_n$.

Proof: From the fact that $h_3(k-1) = \beta\alpha^{-1} \in \langle \alpha, \beta \rangle$, we can apply Proposition 0.2 to deduce that

$$\begin{aligned} h_3(k) &= \alpha h_3(k-1)^{-1} \alpha^{-1} \in \langle \alpha, \beta \rangle, \\ h_3(r) &= \beta^{r+1} h_3(k) \beta^{-(r+1)} \in \langle \alpha, \beta \rangle \quad \text{for } 0 \leq r \leq k-4, \\ h_3(k-3) &= \alpha h_3(k-4) \alpha^{-1} \in \langle \alpha, \beta \rangle, \\ h_3(k-2) &= \beta h_3(k-3)^{-1} \beta^{-1} \in \langle \alpha, \beta \rangle, \end{aligned}$$

so we have shown that $H_{n,3} \subseteq \langle \alpha, \beta \rangle$. Therefore, by Theorem 0.1 and Lemma 0.3, we have that $A_n \subseteq \langle \alpha, \beta \rangle$. If k is even, we deduce that $A_n \subsetneq \langle \alpha, \beta \rangle$. Thus, in both cases, the proof is complete. \blacksquare

A consequence of Corollary 0.6 is that if k is odd (resp. even), two consecutive step cycles $h_k(a)$ and $h_k(a+1)$ generate A_X (resp. S_X), where $X = \{a, a+1, a+2, \dots, a+k\}$ and $a+i \in \mathbb{Z}_n$ for all $i = 0, 1, 2, \dots, k$.

Proposition 0.7 Let n and k be positive integers with $7 \leq k+2 \leq n \leq 2k-2$. We have $\langle \alpha, \beta \rangle = S_n$ if k is even and $\langle \alpha, \beta \rangle = A_n$ if k is odd.

Proof: We have

$$[\alpha, \beta] := \alpha\beta\alpha^{-1}\beta^{-1} = (0, 1)(2k-n, k).$$

Therefore, by Proposition 0.2, we obtain

$$\gamma := \alpha^{-2}[\alpha, \beta]\alpha^2 = (k-2, k-1)(2k-n-2, k).$$

Define

$$\mu := \beta^{n-k-4}(\beta^2\gamma\beta^2\gamma\beta^{-4})\beta^{-(n-k-4)} = \beta^{n-k-4}(k, k+2, k+4)\beta^{-(n-k-4)} = (n-4, n-2, 0).$$

Direct calculation verifies that we have

$$h_3(0) = \begin{cases} \alpha^2\beta^2\alpha^{-2}[\alpha, \mu^{-1}]\alpha^2\beta^{-2}\alpha^{-2} & \text{if } n \geq k+4 \\ \alpha^2\beta\alpha^{-2}[\mu^{-1}, \alpha^{-1}]\alpha^2\beta^{-1}\alpha^{-2} & \text{if } n = k+3 \\ \beta^2\alpha^{-3}\beta\mu^{-1}\beta^{-1}\alpha\mu\alpha^2\beta^{-2} & \text{if } n = k+2. \end{cases}$$

Conjugation by α^a for $a = 0, 1, 2, \dots, k-3$ shows that $h_3(a) \in \langle \alpha, \beta \rangle$ for $a = 0, 1, 2, \dots, k-3$. On the other hand, observe that

$$h_3(n-1) = \begin{cases} \beta^{-1}h_3(0)\beta & \text{if } n < 2k+2. \\ \beta\alpha^{-2}\beta^{-2}h_3(0)\beta^2\alpha^2\beta^{-1} & \text{if } n = 2k+2 \end{cases}$$

Then, conjugating by β^{-a} for each $a = 0, 1, 2, \dots, n-k-1$ shows that $h_3(a) \in \langle \alpha, \beta \rangle$ for each $a = k, k+1, \dots, n-1$. Furthermore,

$$h_3(k-2) = \beta^{-(n-k)}\alpha h_3(k-3)\alpha^{-1}\beta^{n-k} \quad \text{and} \quad h_3(k-1) = \alpha^{n-k}\beta^{-1}h_3(k)\beta\alpha^{-(n-k)}.$$

Thus, $h_3(a) \in \langle \alpha, \beta \rangle$ for all $a = 0, 1, 2, \dots, n-1$, so that $H_{n,3} \subseteq \langle \alpha, \beta \rangle$, and thus by Corollary 0.5, $A_n \subseteq \langle \alpha, \beta \rangle$. Therefore, the conclusion of the proposition follows. \blacksquare

Main Results

The main result of this paper is as follows:

Theorem 0.8 Let n and k be positive integers with $n \geq k \geq 3$ and $n \neq 3$. If k is odd (resp. even), then the minimum number of k -cycles needed to generate A_n (resp. S_n) is

$$\max \left\{ 2, \left\lceil \frac{n-1}{k-1} \right\rceil \right\}.$$

Notice that Proposition 0.7 immediately implies this result in the case when $2 \leq k < n \leq 2k-2$. To establish Theorem 0.8 more generally, we need some additional preliminary steps. We first establish a lower bound on the size of any generating set of A_n (resp. S_n) consisting exclusively of k -cycles.

Lemma 0.9 Let n and k be positive integers with $n \geq k \geq 2$, and let $S \subseteq C_{n,k}$ with $A_n \subseteq \langle S \rangle$. Then,

$$|S| \geq \left\lceil \frac{n-1}{k-1} \right\rceil.$$

Proof: Consider the graph G whose vertices are $V := \{0, 1, 2, \dots, n-1\}$ and whose edge set E is defined by the condition that $\{a, b\} \in E$ if and only if there exists $\sigma \in \langle S \rangle$ such that $\sigma(a) = b$. Of course, if $\sigma \in S$, then the k elements of σ belong to the same connected component of G . From this, it is easy to see that the number of connected components of G is at least $n - |S|(k-1)$. Since $A_n \subseteq \langle S \rangle$, the graph G must be connected; hence, G has one connected component. We conclude that

$$|S| \geq \left\lceil \frac{n-1}{k-1} \right\rceil,$$

as required. ■

Our next goal is to establish Theorem 0.8 in the special case $n = k^j$ for some $j \geq 2$. This will be done by induction on j . In the case $j = 2$, we have $\left\lceil \frac{k^2 - 1}{k - 1} \right\rceil = k + 1$, so we need to construct a generating set L for A_{k^2} (resp. S_{k^2}) with $|L| = k + 1$ consisting of k -cycles (no smaller collection of k -cycles can generate A_{k^2} (resp. S_{k^2}) according to Lemma 0.9). To this end, let

$$\tau_0 = (0, k, 2k, \dots, (k-1)k)$$

and set

$$L := \{h_k(0), h_k(k), h_k(2k), \dots, h_k((k-1)k), \tau_0\}. \quad (2)$$

We have $|L| = k + 1$. To show that $\langle L \rangle = A_{k^2}$ (resp. $\langle L \rangle = S_{k^2}$), it suffices by Corollary 0.5 to prove that $H_{k^2, k} \subseteq \langle L \rangle$. It will be useful to set up the notation:

$$\begin{aligned} \tau_i &:= \left[h_k((k-1)k) h_k((k-2)k) \cdots h_k(0) \right]^i \tau_0 \left[h_k((k-1)k) h_k((k-2)k) \cdots h_k(0) \right]^{-i} \\ &= (i, i+k, i+2k, \dots, i+(k-1)k) \end{aligned}$$

for $i = 0, 1, \dots, k-1$. By construction, observe that $\{\tau_0, \tau_1, \dots, \tau_{k-1}\} \subseteq \langle L \rangle$. Next, we will show using induction on a that

$$h_k(a) \in \langle L \rangle \quad \text{for all } a = 0, 1, 2, \dots, k^2 - 1.$$

We are given in (2) that $h_k(0) \in \langle L \rangle$, and if $h_k(a-1) \in \langle L \rangle$, then, using the notation $[a] := a \bmod k$, we have

$$h_k(a) = \tau_{[a-1]} h_k(a-1) \tau_{[a-1]}^{-1} \in \langle L \rangle$$

for all $a = 0, 1, 2, \dots, k^2 - 1$. The claim follows by induction on a . Thus, $H_{k^2, k} \subseteq \langle L \rangle$ as claimed, and the case $n = k^2$ is complete. To carry out the inductive step on j , we proceed as follows. Note that

$$\left\lceil \frac{n-1}{k-1} \right\rceil = \left\lceil \frac{k^j - 1}{k-1} \right\rceil = \frac{k^j - 1}{k-1},$$

so we will inductively manufacture a generating set L for A_{k^j} (resp. S_{k^j}) consisting of $\frac{k^j - 1}{k-1}$ k -cycles. To this end, let us define

$$X_i := \{ik^{j-1}, ik^{j-1} + 1, \dots, (i+1)k^{j-1} - 1\} \quad \text{for } i = 0, 1, \dots, k-1.$$

Observe that the sets X_i form a partition of the set $\{0, 1, 2, \dots, k^j - 1\}$. We can consider the group A_{X_i} (resp. S_{X_i}) on the elements of X_i . Since $|X_i| = k^{j-1}$, by the induction hypothesis, there exists a minimal generating set, L_i , for A_{X_i} (resp. S_{X_i}) for each $i = 0, 1, \dots, k-1$, with

$$|L_i| = \frac{k^{j-1} - 1}{k-1}.$$

Define

$$L := L_0 \cup L_1 \cup \dots \cup L_{k-1} \cup \{(0, k^{j-1}, 2k^{j-1}, \dots, (k-1)k^{j-1})\}$$

and observe that

$$|L| = k \left(\frac{k^{j-1} - 1}{k - 1} \right) + 1 = \frac{k^j - 1}{k - 1}.$$

Thus, by Lemma 0.9, L has the smallest possible size for a generating set of A_{k^j} (resp. S_{k^j}). It remains only to show that L is indeed such a generating set.

Our strategy is to show that $H_{k^j, k} \subseteq \langle L \rangle$ and use Corollary 0.5. Since L_i generates A_{X_i} (resp. S_{X_i}), all step cycles of length k whose elements lie within X_i for some i have been generated. Therefore, it is easy to see that the only step cycles of length k not inductively generated within A_{X_i} (resp. S_{X_i}) for some i are the following:

$$h_k(rk^{j-1} - k + s) \quad \text{for } r = 1, 2, \dots, k, \quad s = 1, 2, \dots, k - 1. \quad (3)$$

To show that these cycles do indeed belong to $\langle L \rangle$, note that for all $i = 0, 1, 2, \dots, k - 1$, and for all $\ell = 0, 1, 2, \dots, k^{j-1} - 1$ we can find $\sigma_{i,\ell} \in L_i$ such that

$$\sigma_{i,\ell}(ik^{j-1}) = \ell + ik^{j-1}.$$

Now define

$$\begin{aligned} \mu_{(\ell_0, \ell_1, \dots, \ell_{k-1})} &:= [\sigma_{k-1, \ell_{k-1}} \dots \sigma_{1, \ell_1} \sigma_{0, \ell_0}] (0, k^{j-1}, 2k^{j-1}, \dots, (k-1)k^{j-1}) [\sigma_{k-1, \ell_{k-1}} \dots \sigma_{1, \ell_1} \sigma_{0, \ell_0}]^{-1} \\ &= (\ell_0, \ell_1 + k^{j-1}, \ell_2 + 2k^{j-1}, \dots, \ell_{k-1} + (k-1)k^{j-1}) \in \langle L \rangle. \end{aligned}$$

For each $r = 1, 2, 3, \dots, k$ and $s = 1, 2, \dots, k - 1$, we can find an element $\mu_{(\ell_0, \ell_1, \dots, \ell_{k-1})}^{(r,s)}$, written simply as $\mu^{(r,s)}$, such that

$$\mu^{(r,s)}(rk^{j-1} - k + s - 1) = rk^{j-1} + s - 1 \pmod{k^j}.$$

Then,

$$[\mu^{(r,s)}] h_k(rk^{j-1} - k + s - 1) [\mu^{(r,s)}]^{-1} = h_k(rk^{j-1} - k + s). \quad (4)$$

Using (4), we can perform mathematical induction on s to verify that all cycles in (3) belong to $\langle L \rangle$. Therefore, $H_{k^j, k} \subseteq \langle L \rangle$. Thus, by Corollary 0.5, $\langle L \rangle = A_{k^j}$ (resp. $\langle L \rangle = S_{k^j}$), as claimed.

The above inductive argument establishes the following important special case of Theorem 0.8.

Lemma 0.10 Let k and j be positive integers with $k \geq 3$ and $j \geq 2$. If k is odd (resp. even), then the minimum number of k -cycles needed to generate A_{k^j} (resp. S_{k^j}) is $\frac{k^j - 1}{k - 1}$.

Example 0.11 Let us find an economical generating set consisting of 5-cycles for the group A_{125} .

Note that $n = 125$, $k = 5$ and $j = 3$. According to Lemma 0.10, the smallest possible generating set for A_{125} consisting of 5-cycles contains $\frac{124}{4} = 31$ cyclic generators. Proceeding inductively as in the proof of Lemma 0.10, we use Equation (2) to form a generating set $L = L_0$ for A_{X_0} , where $X_0 = \{0, 1, 2, \dots, 24\}$, as follows:

$$L_0 := \{h_5(0), h_5(5), h_5(10), h_5(15), h_5(20), (0, 5, 10, 15, 20)\}.$$

Similarly, if we define

$$X_1 := \{25, 26, \dots, 49\}, \quad X_2 := \{50, 51, \dots, 74\}, \quad X_3 := \{75, 76, \dots, 99\}, \quad X_4 := \{100, 101, \dots, 124\},$$

then we can construct generating sets L_1, L_2, L_3 , and L_4 for $A_{X_1}, A_{X_2}, A_{X_3}$, and A_{X_4} , respectively. Finally, we set

$$L := L_0 \cup L_1 \cup L_2 \cup L_3 \cup L_4 \cup \{(0, 25, 50, 75, 100)\}.$$

Since $|L_i| = 6$ for each $i = 0, 1, 2, 3, 4$, we have $|L| = 31$, and thus by Lemma 0.10, L minimally generates A_{125} , as needed. \blacksquare

Now we turn our attention to Theorem 0.8 in the case of an arbitrary integer $n \geq k \geq 3$.

Notation 0.12 Let n and k be positive integers with $n \geq k$. Let m be the largest positive integer such that $k^m \leq n$. Then, there exist unique integers $a_0, a_1, a_2, \dots, a_m$ with $0 \leq a_r \leq k - 1$ ($r = 0, 1, \dots, m$) and $a_m \neq 0$, such that

$$n = a_m k^m + a_{m-1} k^{m-1} + \cdots + a_1 k + a_0.$$

Further, let $b := \sum_{i=0}^m a_i$.

Lemma 0.13 With the notation as above, we have

$$\left\lceil \frac{n-1}{k-1} \right\rceil = a_1 \left(\frac{k-1}{k-1} \right) + a_2 \left(\frac{k^2-1}{k-1} \right) + \cdots + a_m \left(\frac{k^m-1}{k-1} \right) + \left\lceil \frac{b-1}{k-1} \right\rceil.$$

Proof: Let n and k be positive integers with $k \leq n$. Then, there exists an integer r with $0 \leq r \leq k - 2$, such that

$$\left\lceil \frac{b-1}{k-1} \right\rceil = \frac{b-1+r}{k-1}.$$

Then,

$$\begin{aligned} & a_1 \left(\frac{k-1}{k-1} \right) + a_2 \left(\frac{k^2-1}{k-1} \right) + \cdots + a_m \left(\frac{k^m-1}{k-1} \right) + \frac{b-1+r}{k-1} \\ &= \frac{(a_0 + a_1 k + a_2 k^2 + \cdots + a_m k^m) - (a_0 + a_1 + a_2 + \cdots + a_m) + b-1+r}{k-1} \\ &= \frac{n-1+r}{k-1} = \left\lceil \frac{n-1}{k-1} \right\rceil, \end{aligned}$$

as required. \blacksquare

Now we are ready to prove Theorem 0.8.

Proof of Theorem 0.8: Let n and k be positive integers with $n \geq k \geq 3$ and $n \neq 3$. Assume k is odd. We have three cases.

Case 1: $k = n$. In this case, let

$$S := \{h_n(0), (0, 1, 2, \dots, n-3, n-1, n-2)\}.$$

Observe that for all $a = 0, 1, 2, \dots, n-1$,

$$h_3(a) = h_n(0)^{a+2} [(0, 1, 2, \dots, n-3, n-1, n-2)h_n(0)^{-1}]h_n(0)^{-(a+2)} \in \langle S \rangle.$$

Hence, $H_{n,3} \subseteq \langle S \rangle$. Therefore, by Corollary 0.5, if k is odd, we have $A_n = \langle S \rangle$, and if k is even, we have $S_n = \langle S \rangle$. Since A_n and S_n are not cyclic for $n > 3$, no generating set smaller than S can be found.

Case 2: $k+1 \leq n \leq 2k-2$. For $n = k+1$, this follows from Corollary 0.6. Otherwise, $k+2 \leq n \leq 2k-2$. If $k = 4$ and $n = 6$, note that $\langle (0123), (4051) \rangle = S_6$ by direct verification. Thus, assume $k \geq 5$ and use Proposition 0.7.

Case 3: $2k-1 \leq n$. We use Notation 0.12, and in addition, for $j = 0, 1, 2, \dots, m$, let

$$\theta_j := a_m k^m + a_{m-1} k^{m-1} + \dots + a_{j+1} k^{j+1}.$$

Note that $\theta_m = 0$ and $\theta_0 = n - a_0$. Then, for $i = 0, 1, 2, \dots, a_j - 1$, let

$$X_{i,j} := \{\theta_j + ik^j, \theta_j + ik^j + 1, \theta_j + ik^j + 2, \dots, \theta_j + ik^j + k^j - 1\}.$$

It is easy to see that the sets $X_{i,j}$ form a partition of $\{0, 1, 2, \dots, n-1\}$. The number of sets $X_{i,j}$ is b , and for all $j = 0, 1, 2, \dots, m$ and $i = 0, 1, 2, \dots, a_j - 1$, we have $|X_{i,j}| = k^j$. So, by Lemma 0.10, we can generate each group $A_{X_{i,j}}$ (resp. $S_{X_{i,j}}$) for $j = 2, 3, 4, \dots, m$, with as few as

$$\frac{k^j - 1}{k - 1}$$

k -cycles. For each $j = 2, 3, 4, \dots, m$, there are a_j sets $X_{i,j}$. Using Lemma 0.10 to find generators for each of the groups $A_{X_{i,j}}$ with j fixed, and then summing over j , we can generate all of the groups $A_{X_{i,j}}$ (resp. $S_{X_{i,j}}$) for $j = 2, 3, 4, \dots, m$ collectively with

$$\sum_{j=2}^m a_j \frac{k^j - 1}{k - 1}$$

generators. Let T_0 denote the collection of all of these generators of the groups $A_{X_{i,j}}$ (resp. $S_{X_{i,j}}$) for all $j = 2, 3, 4, \dots, m$ and $i = 0, 1, 2, \dots, a_j - 1$, as constructed in Lemma 0.10. Two elements of $\{0, 1, 2, \dots, n-1\}$ belonging to different sets $X_{i,j}$ lie in different orbits under the action of the group $\langle T_0 \rangle$. Thus, T_0 is a generating set for A_n (resp. S_n) if and only if $b = 1$; that is, if and only if $a_m = 1$ and $a_r = 0$, for all $r < m$, which means precisely that $n = k^m$. This in turn requires that $m \geq 2$ since $n > k$. Thus, in this case, Lemma 0.10 already finishes the proof. Therefore, we may assume that $b > 1$. We will construct additional cycles to generate the remaining elements of A_n (resp. S_n). To this end, in what follows let

$$T_1 := \{h_k(\theta_1 + pk) : p = 0, 1, 2, \dots, a_1 - 1\}.$$

We begin with the following Lemma.

Lemma 0.14 Using the notation already established, for $i \geq 0$ and $j \geq 1$ and $x, y \in X_{i,j}$, there exists $\sigma \in \langle T_0 \cup T_1 \rangle$ such that

$$\sigma(x) = y,$$

where σ fixes all elements outside of $X_{i,j}$.

Proof: In the case $j > 1$, we can clearly find $\sigma \in A_{X_{i,j}} \subseteq \langle T_0 \rangle \subseteq \langle T_0 \cup T_1 \rangle$ such that $\sigma(x) = y$, as required. On the other hand, if $j = 1$, then $|X_{i,j}| = k$ and by construction of T_1 , there is a unique step cycle $\tau \in T_1$ (of length k) that permutes all members of $X_{i,j}$ (and no elements outside of $X_{i,j}$). In particular, for some integer r , $\tau^r(x) = y$, and $\tau^r \in \langle T_0 \cup T_1 \rangle$, as needed. ■

For each $j = 0, 1, 2, \dots, m$ and $i = 0, 1, 2, \dots, a_j - 1$, let $c_{i,j}$ denote the smallest member of $X_{i,j}$. Therefore,

$$c_{i,j} = \theta_j + ik^j.$$

Relabel these numbers in increasing order: $0 = c_1 < c_2 < \dots < c_b$. Since $n > k$, note that $c_2 \geq k$. Now, use the Division Algorithm to find integers r and t with $0 \leq r < k - 1$, such that

$$b - 1 = t(k - 1) + r.$$

For all $p = 0, 1, 2, \dots, t - 1$, let σ_p be the k -cycle defined by

$$\sigma_p = (c_1, c_{pk-(p-2)}, c_{pk-(p-3)}, \dots, c_{pk-(p-k)}), \quad (5)$$

and if $r \neq 0$, let

$$\sigma_t = (c_1, c_{tk-t+2}, c_{tk-t+3}, \dots, c_b, 1, 2, 3, \dots, k - r - 1),$$

which is also a k -cycle. Then, define

$$T_2 := \begin{cases} \{\sigma_0, \sigma_1, \sigma_2, \sigma_3, \dots, \sigma_t\}, & \text{if } r \neq 0 \\ \{\sigma_0, \sigma_1, \sigma_2, \dots, \sigma_{t-1}\}, & \text{if } r = 0 \end{cases}$$

and

$$T := T_0 \cup T_1 \cup T_2.$$

We claim that T generates A_n (resp. S_n). To show this, it suffices by Corollary 0.5 to show all step k -cycles are generated by T . The elements of any step k -cycle $h_k(a)$ in A_n (resp. S_n) that is not a member of $\langle T_0 \cup T_1 \rangle$ must intersect non-trivially with more than one of the sets $X_{i,j}$. Such step cycles must contain the element $\theta_j + ik^j + k^j - 1$ for some $j = 0, 1, 2, \dots, m$ and for some $i = 0, 1, 2, \dots, a_j - 1$, since any step cycle not contained in a single set $X_{i,j}$ must contain the largest member of some set $X_{i,j}$. Therefore, we may assume

$$\theta_j + ik^j + k^j - k + 1 \leq a \leq \theta_j + ik^j + k^j - 1.$$

Hence, $\theta_j + ik^j + k^j - 1 = a + s - 1$, for some $s = 1, 2, 3, \dots, k$. Hence, for fixed $j = 0, 1, \dots, m$ and $i = 0, 1, \dots, a_j - 1$, the set of step k -cycles that it is now sufficient to show are generated by T is

$$\{h_k(\theta_j + ik^j + k^j - s) : s = 1, 2, \dots, k\} = \{h_k(\theta_j + ik^j + k^j - k + s - 1) : s = 1, 2, \dots, k\},$$

where the equality of these sets is seen by replacing s by $k - s + 1$. We now demonstrate that the step cycles, viewed in terms of the expressions in the sets on the right, are generated by T . We proceed in 2 cases.

Case 1: $n - 1 \notin h_k(\theta_j + ik^j + k^j - k + s - 1)$.

Note that $j \neq 0$ in this case, because any step k -cycle of the form

$$h_k(\theta_j + ik^j + k^j - k + s - 1) \quad (6)$$

with $j = 0$ must contain the element $n - 1$. Thus, $j \geq 1$, so when $s = 1$, the elements in the step k -cycle in (6) belong to a single set $X_{i,j}$. Thus, for $s = 1$,

$$h_k(\theta_j + ik^j + k^j - k + s - 1) \in \langle T_0 \cup T_1 \rangle \subseteq \langle T \rangle.$$

We will now prove inductively on s that if the step k -cycle in (6) belongs to $\langle T \rangle$, then so does $h_k(\theta_j + ik^j + k^j - k + s)$. Lemma 0.15 accomplishes this.

Lemma 0.15 Using the notation already established, there exists $\rho \in \langle T \rangle$ such that

$$\rho h_k(\theta_j + ik^j + k^j - k + s - 1) \rho^{-1} = h_k(\theta_j + ik^j + k^j - k + s). \quad (7)$$

The proof of Lemma 0.15 is postponed to the end of the paper so as not to distract our attention from the main objective.

Case 2: $n - 1 \in h_k(\theta_j + ik^j + k^j - k + s - 1)$.

It suffices to show that for each $u \in \{0, 1, \dots, k - 1\}$, we have $h_k(n - k + u) \in \langle T \rangle$. Note that for $u = 0$, $h_k(n - k) \in \langle T \rangle$ by the inductive argument in Case 1, since $n - 1 \notin h_k(n - k - 1)$. Note that our earlier works shows that all cycles of the form $h_k(v)$ for $v = u, u + 1, \dots, n - 2k + u$ have been shown to belong to $\langle T \rangle$. We can use a product of these elements to construct an element $\gamma \in \langle T \rangle$ such that γ maps $n - k + u$ to u and fixes all elements in the set

$$\{0, 1, \dots, u - 1, n - k + u + 1, \dots, n - 2, n - 1\}.$$

Therefore,

$$\gamma h_k(n - k + u) \gamma^{-1} = h_k(n - k + u + 1).$$

From this calculation, a straightforward induction argument on u becomes apparent.

Therefore, from Case 1 and Case 2 and the earlier analysis, we have $H_{n,k} \subseteq \langle T \rangle$. Thus, by Corollary 0.5, if k is odd, $A_n = \langle T \rangle$, and if k is even, $S_n = \langle T \rangle$. We need to verify that T has minimal size among generating sets for A_n (resp. S_n) consisting of k -cycles. Note that

$$|T| = |T_0| + |T_1| + |T_2| = \sum_{j=2}^m a_j \frac{k^j - 1}{k - 1} + a_1 + |T_2|.$$

To determine $|T_2|$, note that if $r = 0$, $|T_2| = t = \frac{b-1}{k-1} = \left\lceil \frac{b-1}{k-1} \right\rceil$. Otherwise, if $r > 0$, then $|T_2| = t+1 = \left\lceil \frac{b-1}{k-1} \right\rceil$. In either case,

$$|T_2| = \left\lceil \frac{b-1}{k-1} \right\rceil.$$

Hence, by Lemma 0.13,

$$|T| = \sum_{j=2}^m a_j \frac{k^j - 1}{k - 1} + a_1 + |T_2| = \sum_{j=1}^m a_j \frac{k^j - 1}{k - 1} + \left\lceil \frac{b-1}{k-1} \right\rceil = \left\lceil \frac{n-1}{k-1} \right\rceil.$$

Hence, by Lemma 0.9, T has minimal size among generating sets for A_n (resp. S_n) consisting of cycles of length k . ■

Example 0.16 Let us find an economical generating set consisting of only 5-cycles for A_{274} .

Note that $n = 274$, $k = 5$, $a_0 = 4$, $a_1 = 4$, $a_2 = 0$ and $a_3 = 2$. From Theorem 0.8, the fewest number of 5-cycles needed to generate A_{274} is $\lceil \frac{274-1}{5-1} \rceil = 69$. We proceed in the same fashion as in Theorem 0.8. First, note that θ_i for each $i = 0, 1, 2, 3$, we have $\theta_0 = 270$, $\theta_1 = 250$, $\theta_2 = 250$, and $\theta_3 = 0$. Thus,

$$\begin{array}{lll} X_{0,3} = \{0, 1, \dots, 124\} & X_{0,1} = \{250, 251, \dots, 254\} & X_{0,0} = \{270\} \\ X_{1,3} = \{125, 126, \dots, 249\} & X_{1,1} = \{255, 256, \dots, 259\} & X_{1,0} = \{271\} \\ & X_{2,1} = \{260, 261, \dots, 264\} & X_{2,0} = \{272\} \\ & X_{3,1} = \{265, 266, \dots, 269\} & X_{3,0} = \{273\} \end{array}$$

It follows that $c_1 = 0$, $c_2 = 125$, $c_3 = 250$, $c_4 = 255$, $c_5 = 260$, $c_6 = 265$, $c_7 = 270$, $c_8 = 271$, $c_9 = 272$, and $c_{10} = 273$. From Lemma 3.3, we can generate $A_{X_{0,3}}$ with 31 generators. Let L_1 be the set of generators in Example 0.11. Similarly, let L_2 be the set of generators for $A_{X_{1,3}}$. Thus, define $T_0 := L_1 \cup L_2$. Note from Example 0.11, $|L_1| = |L_2| = 31$. Then, define

$$T_1 := \{h_5(250), h_5(255), h_5(260), h_5(265)\},$$

and let

$$T_2 := \{(0, 125, 250, 255, 260), (0, 265, 270, 271, 272), (0, 273, 1, 2, 3)\}.$$

Let $T = T_0 \cup T_1 \cup T_2$. Since $|T_1| = 4$ and $|T_2| = 3$, then $|T| = 31 + 31 + 4 + 3 = 69$. Therefore, by Theorem 0.8, T minimally generates A_{274} . ■

Proof of Lemma 0.15:

We remind the reader that Lemma 0.15 is introduced under the assumption that

$$n - 1 \notin h_k(\theta_j + ik^j + k^j - k + s - 1), \quad (8)$$

which implies that $j \geq 1$ as explained above the statement of Lemma 0.15. To facilitate this discussion, we set

$$\omega := \theta_j + ik^j + k^j - k + t \quad \text{for each } t = 0, 1, 2, \dots, 2k - 3.$$

It will also be helping to label the (unique) set containing the element $\theta_j + ik^j + k^j$ as $Y_{i,j}$. We will construct $\rho \in \langle T \rangle$ such that

$$\rho(\omega) = \omega + 1, \quad \text{for each } t = 0, 1, 2, \dots, 2k - 3,$$

where $\omega \leq n - 2$, from which (7) follows from Proposition 0.2. Define

$$\tau_0 := h_k(\theta_j + ik^j + k^j - k).$$

Note that $\tau_0 \in \langle T_0 \cup T_1 \rangle$ since $|X_{i,j}| = k^j \geq k$. Write $c_{i,j} = \theta_j + ik^j = c_\lambda$ for some $\lambda = 1, 2, \dots, b$. We claim that $\lambda < b$. To see this, note that $\theta_j + ik^j + k^j - 1 \in h_k(\theta_j + ik^j + k^j - k + s - 1)$. If $\lambda = b$, then

$$n - 1 = \theta_j + ik^j + k^j - 1 \in h_k(\theta_j + ik^j + k^j - k + s - 1),$$

which contradicts (8). Thus,

$$c_\lambda = \theta_j + ik^j < \theta_j + ik^j + k^j \leq c_b.$$

Thus, $\lambda < b$. Next, define

$$\sigma := \begin{cases} \sigma_t \sigma_{t-1} \cdots \sigma_1 \sigma_0 &= (c_1, c_2, c_3, \dots, c_b, 1, 2, 3, \dots, k-r-1) & \text{if } r \neq 0 \\ \sigma_{t-1} \sigma_{t-2} \cdots \sigma_1 \sigma_0 &= (c_1, c_2, c_3, \dots, c_b) & \text{if } r = 0 \end{cases},$$

where $\sigma_i \in T_2$ is defined in (5).

Let us first assume that $j \geq 2$. In this case, there exists $\mu \in A_{X_{i,j}}$ such that

$$\mu(\theta_j + ik^j + k^j - k) = c_\lambda,$$

where μ fixes all other elements of τ_0 .

Case A: $n - a_0 \notin h_k(\theta_j + ik^j + k^j - k + s)$.

Define

$$\tau_1 := h_k(\theta_j + ik^j + k^j).$$

Since $n - a_0 \notin h_k(\theta_j + ik^j + k^j - k + s)$, $h_k(\theta_j + ik^j + k^j - k + s)$ intersects none of the singleton sets $X_{i',j'}$, which are $\{n - a_0\}, \{n - a_0 + 1\}, \dots, \{n - 1\}$. In particular, since $\theta_j + ik^j + k^j \in h_k(\theta_j + ik^j + k^j - k + s)$, we know that $\theta_j + ik^j + k^j$ does not lie in a singleton set $X_{i',j'}$, for any values of i' and j' . Hence, $|Y_{i,j}| \geq k$. Thus, $\tau_1 \in \langle T_0 \cup T_1 \rangle$. Define

$$\rho := \sigma \mu \tau_1 \tau_0 \in \langle T \rangle.$$

Subcase A1: $0 \leq t \leq k - 2$.

Then,

$$\theta_j + ik^j + k^j - k + 1 \leq \omega + 1 \leq \theta_j + ik^j + k^j - 1.$$

Thus, applying ρ to ω results in the following calculation¹:

$$\omega \xrightarrow{\tau_0} \omega + 1 \xrightarrow{\tau_1} \omega + 1 \xrightarrow{\mu} \omega + 1 \xrightarrow{\sigma} \omega + 1,$$

where the first three arrows are clear and $\omega + 1 \in X_{i,j} \setminus \{c_\lambda\}$ hence fixed by σ . Thus, $\rho(\omega) = \omega + 1$.

Subcase A2: $t = k - 1$.

Note that $\omega = \theta_j + ik^j + k^j - 1$. In this case, we apply ρ to ω to obtain:

$$\omega \xrightarrow{\tau_0} \omega - t \xrightarrow{\tau_1} \omega - t \xrightarrow{\mu} c_\lambda \xrightarrow{\sigma} c_{\lambda+1} = \theta_j + ik^j + k^j = \omega + 1,$$

where we have used the facts that $\lambda < b$ and τ_1 fixes $\omega - t$ since $\omega - t \notin \tau_1$ by virtue of the fact that $n \geq 2k - 1$ since $j \geq 2$.

Subcase A3: $k \leq t \leq 2k - 3$.

Note that

$$\theta_j + ik^j + k^j + 1 \leq \omega + 1 \leq \theta_j + ik^j + k^j + k - 2,$$

¹In the diagrams appearing below, the notation $a \xrightarrow{\sigma} b$ is used to indicate that the permutation σ maps the element a to the element b .

thus $\omega + 1$ belongs to $Y_{i,j}$, which is a set of size $\geq k$ since $n - a_0 \notin h_k(\theta_j + ik^j + k^j - k + s)$. Therefore, since $\omega + 1 \neq \theta_j + ik^j + k^j$, σ fixes $\omega + 1$. Therefore, applying ρ to ω yields the following diagram:

$$\omega \xrightarrow{\tau_0} \omega \xrightarrow{\tau_1} \omega + 1 \xrightarrow{\mu} \omega + 1 \xrightarrow{\sigma} \omega + 1.$$

Note that μ fixes $\omega + 1$ since $\omega + 1 \notin X_{i,j}$.

Case B: $n - a_0 \in h_k(\theta_j + ik^j + k^j - k + s)$.

Define

$$\rho := \sigma\mu\tau_0 \in \langle T \rangle.$$

Subcase B1: $0 \leq t \leq k - 2$.

As in Subcase A1, we apply ρ to ω to obtain:

$$\omega \xrightarrow{\tau_0} \omega + 1 \xrightarrow{\mu} \omega + 1 \xrightarrow{\sigma} \omega + 1.$$

Subcase B2: $t = k - 1$.

As in Subcase A2, we apply ρ to ω to obtain:

$$\omega \xrightarrow{\tau_0} \omega - t \xrightarrow{\mu} c_\lambda \xrightarrow{\sigma} c_{\lambda+1} = \theta_j + ik^j + k^j = \omega + 1.$$

Subcase B3: $k \leq t \leq 2k - 3$.

Since $h_k(\theta_j + ik^j + k^j - k + s)$ contains the element $n - a_0$, the set $Y_{i,j}$ must be a singleton. That is, $Y_{i,j} = \{\theta_j + ik^j + k^j\}$. Since $\theta_j + ik^j + k^j \leq \omega \leq n - 2$, $\{\omega\} = X_{i',j'}$, for some i' and j' . Thus, $\omega = c_\alpha$ for some $\alpha = \lambda + 1, \lambda + 2, \dots, b - 1$. (Note $\alpha < b$ since $\omega \leq n - 2$.) Hence, $\sigma(\omega) = c_{\alpha+1} = c_\alpha + 1 = \omega + 1$. So we have the following diagram:

$$\omega \xrightarrow{\tau_0} \omega \xrightarrow{\mu} \omega \xrightarrow{\sigma} \omega + 1.$$

Once more, μ fixes ω since $\omega \notin X_{i,j}$ (see Subcase A3).

The above Cases A and B applied only when $j \geq 2$. We must now present a parallel discussion for the case $j = 1$. In Cases C and D below, we operate under the assumption that $j = 1$.

Case C: $n - a_0 \notin h_k(\theta_j + ik^j + k^j - k + s)$.

As in Case A, define $\tau_1 := h_k(\theta_j + ik^j + k^j) \in \langle T_0 \cup T_1 \rangle$, and define

$$\rho := \sigma\tau_1\tau_0 \in \langle T \rangle.$$

Subcase C1: $0 \leq t \leq k - 2$.

A similar argument from Subcase A1 can be used to show that applying ρ to ω yields:

$$\omega \xrightarrow{\tau_0} \omega + 1 \xrightarrow{\tau_1} \omega + 1 \xrightarrow{\sigma} \omega + 1,$$

as needed.

Subcase C2: $t = k - 1$.

Applying ρ to ω yields:

$$\omega \xrightarrow{\tau_0} \omega - t = c_\lambda \xrightarrow{\tau_1} c_\lambda \xrightarrow{\sigma} c_{\lambda+1} = \omega + 1,$$

as required.

Subcase C3: $k \leq t \leq 2k - 3$.

A similar argument from Subcase A3 can be used to show that ρ applied to ω yields:

$$\omega \xrightarrow{\tau_0} \omega \xrightarrow{\tau_1} \omega + 1 \xrightarrow{\sigma} \omega + 1.$$

Finally, if $j = 1$, we consider:

Case D: $n - a_0 \in h_k(\theta_j + ik^j + k^j - k + s)$.

Define

$$\rho := \sigma\tau_0 \in \langle T \rangle.$$

Subcase D1: $0 \leq t \leq k - 2$.

A similar argument from Subcase A1 can be used to show that applying ρ to ω yields:

$$\omega \xrightarrow{\tau_0} \omega + 1 \xrightarrow{\sigma} \omega + 1,$$

as needed.

Subcase D2: $t = k - 1$.

It is clear that $\tau_0(\omega) = \omega - t$. Since $j = 1$, $|X_{i,j}| = k$, and hence, $\omega - t = c_\lambda$. Since $\lambda < b$, $\sigma(c_\lambda) = c_{\lambda+1}$. Thus, applying ρ to ω yields:

$$\omega \xrightarrow{\tau_0} \omega - t = c_\lambda \xrightarrow{\sigma} c_{\lambda+1} = \omega + 1.$$

Subcase D3: $k \leq t \leq 2k - 3$.

The arrow diagram

$$\omega \xrightarrow{\tau_0} \omega \xrightarrow{\sigma} \omega + 1$$

is justified via the same reasoning used in Subcase B3. This concludes the discussion on the case where $j = 1$, and thus, completes the proof.

Acknowledgments

I would like to thank the CSUF Mathematics Department for supporting my research endeavor. I also extend my gratitude to the editors and reviewers of the manuscript for their comments and suggestions.

References

- Annin, S. Hierarchy of efficient generators of the symmetric inverse monoid, Semigroup Forum, 54:3 (1997), 327-355.
- Babai, L., et. al., On the diameter of finite groups, 31st Annual Symposium on Foundations of Computer Science, Vol. I, II (St. Louis, MO, 1990), 857-865, IEEE Comput. Soc. Press, Los Alamitos, CA, 1990.
- Ben-Shimol, O. The minimal number of cyclic generators of the symmetric and alternating groups, Comm. Algebra, 35:10 (2007), 3034-3037.
- Dummit, D., Foote, R. Abstract Algebra, 3rd ed., John Wiley & Sons, Inc., Hoboken, NJ, 932 (2004).
- Goode, S., Annin, S. Differential Equations and Linear Algebra, 3rd ed., Prentice Hall, Upper Saddle River, NJ, 804 (2007).
- Heath, D., Isaacs, I.M., Kiltinen, J., Sklar J. Symmetric and alternating groups generated by a full cycle and another element, Amer. Math Monthly, 116 (2009), 447-451.
- Hungerford, T. Abstract Algebra: An Introduction, 2nd ed., Brooks Cole, Florence, KY, (1996)
- Nekkoei, R., Jabari, A. Generating alternating groups, Algebras Groups Geom. 20 (2003), 435-442.
- Stong, R., Suceava, B. The Fewest 3-cycles to Generate an Even Permutation, Amer. Math Monthly, 110:2 (2003), 162.

Rindler Temperature Result and Distributional Modes

Department of Mathematics, College of Natural Science and Mathematics, California State University, Fullerton, CA, USA

Joshua Strong
Advisor: Dr. Alfonso Agnew

Abstract

The Rindler wedge is a space-time that corresponds to constantly accelerating observers in Minkowski space-time. When we compare the Rindler and Minkowski quantum vacuum states, we find that the Minkowski vacuum contains a thermal distribution of particles at temperature $a/2\pi$, relative to the accelerated observers. According to Agnew and Dray, (Agnew & Dray, 2001) we can use a new mode decomposition, based on the "distributional modes," to define a quantum field in any globally hyperbolic space-time. Therefore, it is of interest to determine the extent to which standard results can be derived in the new formalism. As a first step in this direction, we compute the distributional mode version of the Bogolubov relation that leads to the aforementioned thermal particle spectrum.

Background

In this paper, we will consider two-dimensional Minkowski, and Rindler space-times. Two-dimensional Minkowski space-time, \mathbb{M} , may be coordinatized by time, t , and space, x , such that the inner product on vector components is given by,

$$\vec{v}_1 \cdot \vec{v}_2 = -t_1 t_2 + x_1 x_2, \quad (1)$$

$$\text{where, } \vec{v}_1 = \langle t_1, x_1 \rangle \text{ and } \vec{v}_2 = \langle t_2, x_2 \rangle. \quad (2)$$

The two dimensional Rindler wedge is an open submanifold of Minkowski space-time which is globally hyperbolic. It corresponds to the wedge $x < |t|$ in \mathbb{M} . 2D Rindler space-time may be coordinatized by time, τ , and space, ρ , with an inner product of the same form. In Minkowski space-time, constant τ values are represented as lines and constant ρ values are represented as hyperbolas that are symmetric about the x -axis and have asymptotes $x = t$ and $x = -t$. Constant ρ values represent observers moving at constant acceleration $\frac{a}{e^{\rho}}$. We define Rindler coordinates in terms of Minkowski coordinates by,

$$\tau = \frac{1}{a} \tanh^{-1} \left(\frac{t}{x} \right) \quad \text{and} \quad (3)$$

$$\rho = \frac{1}{2a} \ln [a^2 (x^2 - t^2)], \quad (4)$$

where $a > 0$ is constant.

We will also note the initial data surface $t = \tau = 0$ slice of the Rindler wedge, and note that this corresponds to $x = \frac{e^{a\rho}}{a} > 0$. On these space-times, we consider the scalar quantum field generated by the Klein-Gordon equation:

$$(\square + m^2)\phi = 0, \quad \text{where} \quad (5)$$

$$\square = \partial^\mu \partial_\mu = (\eta^{\mu\nu} \partial_\nu) \partial_\mu = -\frac{\partial^2}{\partial t^2} + \frac{\partial^2}{\partial x^2}, \quad m > 0. \quad (6)$$

If we consider Rindler observers in the presence of the Minkowski quantum vacuum, one can show (Birrell & Davies, 1982) that the Rindler observers will detect not a vacuum, but rather a thermal distribution of particles. This is the Unruh effect. Here, we will derive the distributional mode equivalent of the Bogolubov relation that leads to the Unruh conclusion. In this paper, we will denote Minkowski modes with a superscript I and Rindler modes with a superscript II.

The plane wave modes $\{U_k^I, \bar{U}_k^I\}$, that are typically used to derive the Unruh effect are solutions to the Klein-Gordon equation and are defined by,

$$U_k^I = \frac{1}{\sqrt{4\pi\omega_k}} e^{-i\omega_k t + ikx} \quad \text{and} \quad (7)$$

$$\bar{U}_k^I = \frac{1}{\sqrt{4\pi\omega_k}} e^{i\omega_k t - ikx}, \quad (8)$$

$$\text{where } \omega_k = \sqrt{k^2 + m^2} \quad \text{and} \quad k \in \mathbb{R}. \quad (9)$$

In order to derive the Unruh effect, one must compute the Bogolubov coefficients, using the Klein-Gordon inner product. The Klein-Gordon inner product is defined by,

$$(\phi, \psi)_{KG} := -i \int_{\Sigma} \psi \frac{\partial}{\partial t} \bar{\phi} - \bar{\phi} \frac{\partial}{\partial t} \psi d\Sigma, \quad (10)$$

where Σ is an arbitrary smooth space-like hypersurface, which can be taken to be $t = \tau = 0$. It also has the property of being Hermitian symmetric:

$$(\phi, \psi)_{KG} = \overline{(\psi, \phi)}_{KG} = -(\bar{\psi}, \bar{\phi})_{KG}. \quad (11)$$

Agnew and Dray (2001) pointed out that the Bogolubov coefficients

$$\alpha_{lk} = (U_l^{II}, U_k^I)_{KG} \quad \text{and} \quad (12)$$

$$\beta_{lk} = -(U_l^{II}, \bar{U}_k^I)_{KG}, \quad (13)$$

satisfy the key Bogolubov relation

$$|\alpha_{lk}|^2 = e^{\frac{2l\pi}{a}} |\beta_{lk}|, \quad (14)$$

which is the property from which the Unruh effect follows.

Calculation of the Distributional Mode Form of the Bogolubov Relation

The following result is a first step towards deriving a version of the Unruh effect in terms of distributional modes, rather than plane wave modes. We define the distributional modes by

$$\Theta_z^I(t, x) = \frac{1}{2}[\theta(x - z + t) - \theta(x - z - t)], \quad (15)$$

$$\Delta_z^I(t, x) = \frac{1}{2}[\delta(x - z + t) + \delta(x - z - t)], \quad (16)$$

$$\Theta_y^{II}(\tau, \rho) = \frac{1}{2}[\theta(\rho - y + \tau) - \theta(\rho - y - \tau)], \quad \text{and} \quad (17)$$

$$\Delta_y^{II}(\tau, \rho) = \frac{1}{2}[\delta(\rho - y + \tau) + \delta(\rho - y - \tau)], \quad (18)$$

where δ is the Dirac delta function and θ is the Heaviside step function. We note that the Dirac delta function has the properties

$$\int_x \delta(x) dx = 1 \quad \text{and} \quad (19)$$

$$\int_x f(x)\delta(x) dx = f(0). \quad (20)$$

We will also make use of the Fourier transform, which can be represented by

$$\mathcal{F}(f) = \frac{1}{\sqrt{2\pi}} \int_x f(x)e^{-ikx} dx. \quad (21)$$

We now calculate a few Klein-Gordon inner products of distributional modes. We note that the integral (10) does not depend on the choice of Σ . Thus, we will choose to integrate over $t = \tau = 0$. We also note that the distributional modes are indexed by position, whereas the plane wave modes are indexed by momentum. And since the distributional modes are real valued, we have

$$\Theta_z^I = \overline{\Theta}_z^I, \quad (22)$$

$$\Theta_y^{II} = \overline{\Theta}_y^{II}, \quad (23)$$

$$\Delta_z^I = \overline{\Delta}_z^I, \quad \text{and} \quad (24)$$

$$\Delta_y^{II} = \overline{\Delta}_y^{II}. \quad (25)$$

Firstly, we calculate $(\Theta_y^{II}, \Delta_z^I)_{KG}$.

$$(\Theta_y^{II}, \Delta_z^I)_{KG} = -i \int_{\Sigma} \Delta_z^I \frac{\partial}{\partial t} \Theta_y^{II} - \Theta_y^{II} \frac{\partial}{\partial t} \Delta_z^I d\Sigma \quad (26)$$

$$= -i \int_{\Sigma} \frac{1}{2} [\delta(x - z + t) + \delta(x - z - t)] \frac{\partial}{\partial t} \left(\frac{1}{2} [\delta(\rho - y + \tau) + \delta(\rho - y - \tau)] \right) \\ - \frac{1}{2} [\theta(\rho - z + \tau) - \theta(\rho - z - \tau)] \frac{1}{2} [\delta'(x - z + t) - \delta'(x - z - t)] d\Sigma \quad (27)$$

$$\begin{aligned}
&= -i \int_{\Sigma} \frac{1}{2} [\delta(x - z + t) + \delta(x - z - t)] \\
&\quad \cdot \frac{1}{2} [\delta \left(\frac{1}{2a} \ln[a^2(x^2 - t^2)] - y + \tanh^{-1} \left(\frac{t}{x} \right) \right) \left(\frac{-t + x}{a(x^2 - t^2)} \right) \\
&\quad - \delta \left(\frac{1}{2a} \ln[a^2(x^2 - t^2)] - y - \tanh^{-1} \left(\frac{t}{x} \right) \right) \left(\frac{-t - x}{a(x^2 - t^2)} \right)] \\
&\quad - \frac{1}{2} [\theta \left(\frac{1}{2a} \ln[a^2(x^2 - t^2)] - z + \tanh^{-1} \left(\frac{t}{x} \right) \right) - \theta \left(\frac{1}{2a} \ln[a^2(x^2 - t^2)] - z - \tanh^{-1} \left(\frac{t}{x} \right) \right)] \\
&\quad \cdot \frac{1}{2} [\delta'(x - z + t) - \delta'(x - z - t)] d\Sigma. \tag{28}
\end{aligned}$$

Setting $t = 0$, we get

$$(\Theta_y^{II}, \Delta_z^I)_{KG} = -i \int_{x>0} \delta(x - z) \frac{1}{ax} \delta \left(\frac{1}{a} \ln(ax) - y \right) - (0) \delta(x - z) dx \tag{29}$$

$$= -\frac{i}{a} \int_{x>0} \frac{1}{x} \delta(x - z) \delta \left(\frac{1}{a} \ln(ax) - y \right) dx. \tag{30}$$

To see what the distribution represents, set

$$D(z, y) = \int_{x>0} \frac{1}{x} \delta(x - z) \delta \left(\frac{1}{a} \ln(ax) - y \right) dx, \tag{31}$$

and act on a test function, $f(z)$. Then

$$D(z, y)[f(z)] = \int_z f(z) \int_{x>0} \frac{1}{x} \delta(x - z) \delta \left(\frac{1}{a} \ln(ax) - y \right) dx dz \tag{32}$$

$$= \int_{x>0} \frac{1}{x} \delta \left(\frac{1}{a} \ln(ax) - y \right) \int_z f(z) \delta(x - z) dz dx \tag{33}$$

$$= \int_{x>0} \frac{f(x)}{x} \delta \left(\frac{1}{a} \ln(ax) - y \right) dx \tag{34}$$

$$= \frac{f(e^{\frac{ay}{a}})}{\frac{e^{ay}}{a}} \tag{35}$$

$$= \frac{a}{e^{ay}} f \left(e^{\frac{ay}{a}} \right). \tag{36}$$

Also,

$$\frac{a}{e^{ay}} \int_z \delta \left(\frac{e^{ay}}{a} - z \right) f(z) dz = \frac{a}{e^{ay}} f \left(e^{\frac{ay}{a}} \right). \tag{37}$$

Therefore, we can say that

$$D(z, y) = \frac{a}{e^{ay}} \delta \left(\frac{e^{ay}}{a} - z \right), \tag{38}$$

and substituting back into (30) we get

$$(\Theta_y^{II}, \Delta_z^I)_{KG} = -\frac{i}{e^{ay}} \delta \left(\frac{e^{ay}}{a} - z \right). \quad (39)$$

Similar calculations show that

$$(\Delta_y^{II}, \Theta_z^I)_{KG} = i\delta \left(\frac{e^{ay}}{a} - z \right), \quad (40)$$

$$(\Theta_y^{II}, \Theta_z^I)_{KG} = 0, \quad \text{and} \quad (41)$$

$$(\Delta_y^{II}, \Delta_z^I)_{KG} = 0. \quad (42)$$

We now calculate a few Klein-Gordon inner products of distributional modes and plane wave modes.

Firstly, we calculate $(\Theta_z^I, U_k^I)_{KG}$.

$$(\Theta_z^I, U_k^I)_{KG} = -i \int_{\Sigma} U_k^I \frac{\partial}{\partial t} \Theta_z^I - \Theta_z^I \frac{\partial}{\partial t} U_k^I d\Sigma \quad (43)$$

$$\begin{aligned} &= -i \int_{\Sigma} \frac{1}{\sqrt{4\pi\omega_k}} e^{-i\omega_k t + ikx} \frac{1}{2} [\delta(x - z + t) + \delta(x - z - t)] \\ &\quad - \frac{1}{2} [\theta(x - z + t) - \theta(x - z - t)] \frac{-i\omega_k}{\sqrt{4\pi\omega_k}} e^{-i\omega_k t + ikx} d\Sigma. \end{aligned} \quad (44)$$

Setting $t = 0$, we get

$$(\Theta_z^I, U_k^I)_{KG} = -i \int_{x>0} \frac{1}{\sqrt{4\pi\omega_k}} e^{ikx} \delta(x - z) dx \quad (45)$$

$$= \frac{-i}{\sqrt{2\omega_k}} \frac{1}{2\pi} \int_{x>0} e^{ikx} \delta(x - z) dz \quad (46)$$

$$= \frac{-i}{\sqrt{2\omega_k}} \mathcal{F}^{-1}(\delta(x - z)) \quad (47)$$

$$= \frac{-i}{\sqrt{2\omega_k}} \frac{e^{ikz}}{\sqrt{2\pi}} \quad (48)$$

$$= \frac{-ie^{ikz}}{2\sqrt{\pi\omega_k}}. \quad (49)$$

Now we calculate $(\Delta_z^I, U_k^I)_{KG}$.

$$(\Delta_z^I, U_k^I)_{KG} = -i \int_{\Sigma} U_k^I \frac{\partial}{\partial t} \Delta_z^I - \Delta_z^I \frac{\partial}{\partial t} U_k^I d\Sigma \quad (50)$$

$$\begin{aligned} &= -i \int_{\Sigma} \frac{1}{\sqrt{4\pi\omega_k}} e^{-i\omega_k t + ikx} \frac{1}{2} [\delta'(x - z + t) - \delta'(x - z - t)] \\ &\quad - \frac{1}{2} [\delta(x - z + t) + \delta(x - z - t)] \frac{-i\omega_k}{\sqrt{4\pi\omega_k}} e^{-i\omega_k t + ikx} d\Sigma. \end{aligned} \quad (51)$$

Setting $t = 0$, we get

$$(\Delta_z^I, U_k^I)_{KG} = -i \int_{x>0} \frac{i\omega_k}{\sqrt{4\pi\omega_k}} e^{ikx} \delta(x-z) dx \quad (52)$$

$$= \sqrt{\frac{\omega_k}{2}} \frac{1}{2\pi} \int_{x>0} e^{ikx} \delta(x-z) dz \quad (53)$$

$$= \sqrt{\frac{\omega_k}{2}} \mathcal{F}^{-1}(\delta(x-z)) \quad (54)$$

$$= \sqrt{\frac{\omega_k}{2}} \frac{e^{ikz}}{\sqrt{2\pi}} \quad (55)$$

$$= \frac{1}{2} \sqrt{\frac{\omega_k}{2}} e^{ikz}. \quad (56)$$

Similar calculations for $(\Theta_y^{II}, U_l^{II})_{KG}$ and $(\Theta_y^{II}, U_l^{II})_{KG}$, left in terms of Rindler variables, yields

$$(\Theta_y^{II}, U_l^{II})_{KG} = \frac{-ie^{ily}}{2\sqrt{\pi\nu_l}} \quad \text{and} \quad (57)$$

$$(\Delta_y^{II}, U_l^{II})_{KG} = \frac{1}{2} \sqrt{\frac{\nu_l}{2}} e^{ily}. \quad (58)$$

We can expand the plane wave modes in terms of distributional modes by

$$U_k^I = \int_z P_{kz} \Theta_z^I + Q_{kz} \Delta_z^I dz \quad \text{and} \quad (59)$$

$$U_k^{II} = \int_y M_{ly} \Theta_y^{II} + N_{ly} \Delta_z^{II} dy. \quad (60)$$

Then from (12), we get

$$\alpha_{lk} = (U_l^{II}, U_k^I)_{KG} \quad (61)$$

$$= (\int_y M_{ly} \Theta_y^{II} + N_{ly} \Delta_z^{II} dy, \int_z P_{kz} \Theta_z^I + Q_{kz} \Delta_z^I dz)_{KG} \quad (62)$$

$$= \int_y \int_z (M_{ly} \Theta_y^{II} + N_{ly} \Delta_z^{II}, P_{kz} \Theta_z^I + Q_{kz} \Delta_z^I)_{KG} dz dy \quad (63)$$

$$= \int_y \int_z (M_{ly} \Theta_y^{II}, P_{kz} \Theta_z^I)_{KG} + (M_{ly} \Theta_y^{II}, Q_{kz} \Delta_z^I)_{KG} \\ + (N_{ly} \Delta_z^{II}, P_{kz} \Theta_z^I)_{KG} + (N_{ly} \Delta_z^{II}, Q_{kz} \Delta_z^I)_{KG} dz dy \quad (64)$$

$$= \int_y \int_z M_{ly} P_{kz} (\Theta_y^{II}, \Theta_z^I)_{KG} + M_{ly} Q_{kz} (\Theta_y^{II}, \Delta_z^I)_{KG} \\ + N_{ly} P_{kz} (\Delta_z^{II}, \Theta_z^I)_{KG} + N_{ly} Q_{kz} (\Delta_z^{II}, \Delta_z^I)_{KG} dz dy. \quad (65)$$

Since

$$(\Delta_y^{II}, \Delta_z^I)_{KG} = 0 = (\Theta_y^{II}, \Theta_z^I)_{KG}, \quad (66)$$

then we can say that

$$\alpha_{lk} = \int_y \int_z M_{ly} Q_{kz} (\Theta_y^{II}, \Delta_z^I)_{KG} + N_{ly} P_{kz} (\Delta_z^{II}, \Theta_z^I)_{KG} dz dy. \quad (67)$$

And from (13), we get

$$-\beta_{lk} = (U_l^{II}, \bar{U}_k^I)_{KG} \quad (68)$$

$$= \left(\int_y M_{ly} \Theta_y^{II} + N_{ly} \Delta_z^{II} dy, \int_z \bar{P}_{kz} \Theta_z^I + \bar{Q}_{kz} \Delta_z^I dz \right)_{KG} \quad (69)$$

$$= \int_y \int_z (M_{ly} \Theta_y^{II} + N_{ly} \Delta_z^{II}, \bar{P}_{kz} \Theta_z^I + \bar{Q}_{kz} \Delta_z^I)_{KG} dz dy \quad (70)$$

$$= \int_y \int_z (M_{ly} \Theta_y^{II}, \bar{P}_{kz} \Theta_z^I)_{KG} + (M_{ly} \Theta_y^{II}, \bar{Q}_{kz} \Delta_z^I)_{KG} \\ + (N_{ly} \Delta_z^{II}, \bar{P}_{kz} \Theta_z^I)_{KG} + (N_{ly} \Delta_z^{II}, \bar{Q}_{kz} \Delta_z^I)_{KG} dz dy \quad (71)$$

$$= \int_y \int_z M_{ly} \bar{P}_{kz} (\Theta_y^{II}, \Theta_z^I)_{KG} + M_{ly} \bar{Q}_{kz} (\Theta_y^{II}, \Delta_z^I)_{KG} \\ + N_{ly} \bar{P}_{kz} (\Delta_z^{II}, \Theta_z^I)_{KG} + N_{ly} \bar{Q}_{kz} (\Delta_z^{II}, \Delta_z^I)_{KG} dz dy. \quad (72)$$

Thus,

$$-\beta_{lk} = \int_y \int_z M_{ly} \bar{Q}_{kz} (\Theta_y^{II}, \Delta_z^I)_{KG} + N_{ly} \bar{P}_{kz} (\Delta_z^{II}, \Theta_z^I)_{KG} dz dy. \quad (73)$$

We now calculate the variables P_{kz} , Q_{kz} , M_{ly} , and N_{ly} . In order to do so, we take inner products with U_k^I and U_l^{II} on the left and with Θ_z^I , Δ_z^I , Θ_z^{II} , and Δ_y^{II} on the right. Then we can say that

$$(\Theta_{\tilde{z}}^I, U_k^I)_{KG} = (\Theta_{\tilde{z}}^I, \int_z P_{kz} \Theta_z^I + Q_{kz} \Delta_z^I dz)_{KG} \quad (74)$$

$$= \int_z P_{kz} (\Theta_{\tilde{z}}^I, \Theta_z^I)_{KG} + Q_{kz} (\Theta_{\tilde{z}}^I, \Delta_z^I)_{KG} dz \quad (75)$$

$$= \int_z Q_{kz} (\Theta_z^I, \Delta_z^I)_{KG} dz \quad (76)$$

$$= -i \int_z Q_{kz} \delta(z - \tilde{z})_{KG} dz \quad (77)$$

$$= -i Q_{k\tilde{z}}. \quad (78)$$

Thus

$$-iQ_{kz} = (\Theta_z^I, U_k^I)_{KG} \quad (79)$$

which implies that

$$Q_{kz} = \frac{e^{ikz}}{2\sqrt{\pi\omega_k}}. \quad (80)$$

Also,

$$(\Delta_{\tilde{z}}^I, U_k^I)_{KG} = (\Delta_{\tilde{z}}^I, \int_z P_{kz}\Theta_z^I + Q_{kz}\Delta_z^I dz)_{KG} \quad (81)$$

$$= \int_z P_{kz}(\Theta_{\tilde{z}}^I, \Delta_z^I)_{KG} + Q_{kz}(\Delta_z^I, \Delta_z^I)_{KG} dz \quad (82)$$

$$= \int_z P_{kz}(\Theta_z^I, \Delta_z^I)_{KG} dz \quad (83)$$

$$= i \int_z P_{kz}\delta(z - \tilde{z})_{KG} dz \quad (84)$$

$$= iP_{k\tilde{z}}. \quad (85)$$

Thus

$$iP_{kz} = (\Delta_z^I, U_k^I)_{KG} \quad (86)$$

which implies that

$$P_{kz} = \frac{-i}{2} \sqrt{\frac{\omega_k}{\pi}} e^{ikz}. \quad (87)$$

Similar calculations for M_{ly} and N_{ly} , yields

$$M_{ly} = \frac{-i}{2} \sqrt{\frac{\nu_l}{\pi}} e^{ily} \quad \text{and} \quad (88)$$

$$N_{ly} = \frac{e^{ily}}{2\sqrt{\pi\nu_l}}. \quad (89)$$

Note that we leave M_{ly} and N_{ly} in terms of their Rindler variables.

Now assuming that $\alpha_{lk} = e^{\frac{l\pi}{a}} \bar{\beta}_{lk}$, we can say that

$$\begin{aligned} & \int_y \int_z M_{ly} Q_{kz}(\Theta_y^{II}, \Delta_z^I)_{KG} + N_{ly} P_{kz}(\Delta_z^{II}, \Theta_z^I)_{KG} dz dy \\ &= -e^{\frac{l\pi}{a}} \int_y \int_z \overline{M}_{ly} Q_{kz}(\Theta_y^{II}, \Delta_z^I)_{KG} + \overline{N}_{ly} P_{kz}(\Delta_z^{II}, \Theta_z^I)_{KG} dz dy, \end{aligned} \quad (90)$$

$$\begin{aligned}
& \int_y \int_z M_{ly} Q_{kz}(\Theta_y^{II}, \Delta_z^I)_{KG} dz dy + \int_y \int_z N_{ly} P_{kz}(\Delta_z^{II}, \Theta_z^I)_{KG} dz dy \\
= & -e^{\frac{l\pi}{a}} \int_y \int_z \overline{M}_{ly} Q_{kz}(\Theta_y^{II}, \Delta_z^I)_{KG} dz dy - e^{\frac{l\pi}{a}} \int_y \int_z \overline{N}_{ly} P_{kz}(\Delta_z^{II}, \Theta_z^I)_{KG} dz dy,
\end{aligned} \tag{91}$$

$$\begin{aligned}
& \int_y \int_z M_{ly} Q_{kz}(\Theta_y^{II}, \Delta_z^I)_{KG} dz dy + e^{\frac{l\pi}{a}} \int_y \int_z \overline{M}_{ly} Q_{kz}(\Theta_y^{II}, \Delta_z^I)_{KG} dz dy \\
= & -e^{\frac{l\pi}{a}} \int_y \int_z \overline{N}_{ly} P_{kz}(\Delta_z^{II}, \Theta_z^I)_{KG} dz dy - \int_y \int_z N_{ly} P_{kz}(\Delta_z^{II}, \Theta_z^I)_{KG} dz dy,
\end{aligned} \tag{92}$$

$$\begin{aligned}
& \int_y \int_z Q_{kz}(\Theta_y^{II}, \Delta_z^I)_{KG} (M_{ly} + e^{\frac{l\pi}{a}} \overline{M}_{ly}) dz dy \\
= & - \int_y \int_z P_{kz}(\Delta_z^{II}, \Theta_z^I)_{KG} (N_{ly} + e^{\frac{l\pi}{a}} \overline{N}_{ly}) dz dy,
\end{aligned} \tag{93}$$

$$\begin{aligned}
& \int_y \int_z \frac{e^{ikz}}{2\sqrt{\pi\omega_k}} (\Theta_y^{II}, \Delta_z^I)_{KG} \left(\frac{-i}{2} \sqrt{\frac{\nu_l}{\pi}} e^{ily} + e^{\frac{l\pi}{a}} \frac{i}{2} \sqrt{\frac{\nu_l}{\pi}} e^{-ily} \right) dz dy \\
= & - \int_y \int_z \frac{-i}{2} \sqrt{\frac{\omega_k}{\pi}} e^{ikz} (\Delta_z^{II}, \Theta_z^I)_{KG} \left(\frac{e^{ily}}{2\sqrt{\pi\nu_l}} + e^{\frac{l\pi}{a}} \frac{e^{-ily}}{2\sqrt{\pi\nu_l}} \right) dz dy,
\end{aligned} \tag{94}$$

$$\begin{aligned}
\sqrt{\frac{\nu_l}{\omega_k}} \int_y \int_z e^{ikz} (\Theta_y^{II}, \Delta_z^I)_{KG} \left(e^{ily} - e^{\frac{l\pi}{a}} e^{-ily} \right) dz dy &= -\sqrt{\frac{\omega_k}{\nu_l}} \int_y \int_z e^{ikz} (\Delta_z^{II}, \Theta_z^I)_{KG} \left(e^{ily} + e^{\frac{l\pi}{a}} e^{-ily} \right) dz dy, \\
\int_y \int_z e^{ikz} (\Theta_y^{II}, \Delta_z^I)_{KG} \left(e^{ily} - e^{\frac{l\pi}{a}} e^{-ily} \right) dz dy &= -\frac{\omega_k}{\nu_l} \int_y \int_z e^{ikz} (\Delta_z^{II}, \Theta_z^I)_{KG} \left(e^{ily} + e^{\frac{l\pi}{a}} e^{-ily} \right) dz dy,
\end{aligned}$$

and lastly

$$\int_y \mathcal{F}^{-1}[(\Theta_y^{II}, \Delta_z^I)_{KG}] \left(e^{ily} - e^{\frac{l\pi}{a}} e^{-ily} \right) dy = -\frac{\omega_k}{\nu_l} \int_y \mathcal{F}^{-1}[(\Delta_z^{II}, \Theta_z^I)_{KG}] \left(e^{ily} + e^{\frac{l\pi}{a}} e^{-ily} \right) dy,$$

where \mathcal{F}^{-1} denotes the inverse Fourier transform.

Conclusion

The two dimensional Rindler wedge is a globally hyperbolic submanifold of Minkowski space-time. When considering the vacuum states in Minkowski space-time, one finds that the Minkowski vacuum contains particles relative to accelerating observers in Rindler space-time. We can use plane wave modes to derive the Bogolubov relation that leads to this property, which is called the Unruh effect. Moreover, if we express this relation in terms of their distributional mode equivalence, we find a new representation of this property that is based on real valued distributional modes, rather than complex valued plane wave modes. In order to derive this relation, we expanded the plane wave modes in terms of the distributional modes. This lead us to a distributional mode representation of the plane wave mode Bogolubov relation, which we showed

to be

$$\int_y \mathcal{F}^{-1}[(\Theta_y^{II}, \Delta_z^I)_{KG}] \left(e^{ily} - e^{\frac{l\pi}{\alpha}} e^{-ily} \right) dy = -\frac{\omega_k}{\nu_l} \int_y \mathcal{F}^{-1}[(\Delta_z^{II}, \Theta_z^I)_{KG}] \left(e^{ily} + e^{\frac{l\pi}{\alpha}} e^{-ily} \right) dy.$$

And from this result, we may be able to find further representations of the aforementioned relation, from which the Unruh effect follows.

Acknowledgements

I would like to thank Dr. Alfonso Agnew for all his help and direction in putting this paper together.

References

- Agnew, A. F. & Dray, T. (2001) Distributional Modes for Scalar Field Quantization, General Relativity and Gravitation, Vol. 33, No. 3, 429-453
Birrell, N. D. & Davies, P.C.W. (1982) Quantum Fields in Curved Space, Cambridge University Press, Cambridge.

The Sayre-Reitsma Direct Proof of the Steiner-Lehmus Theorem

Department of Mathematics, College of Natural Science and Mathematics, California State University, Fullerton, CA, USA

Jonathan Sayre and Jeremy Reitsma
Advisor: Dr. Martin Bonsangue

Abstract

In 1840, D. C. L. Lehmus put forth a theorem, 'Any triangle with two angle bisectors of equal lengths is isosceles' which became known as the Steiner-Lehmus Theorem after noted geometrist, Jakob Steiner, authored a proof. His proof was done by using the contrapositive form of the theorem and many noted mathematicians since have stated that the theorem could not be proven directly. The Sayre-Reitsma Direct Proof of the Steiner-Lehmus Theorem presented in this article not only lays out a pedigree of 'directness' but also tackles the proof in a very straightforward (and unique) method.

Introduction

In 1840, D. C. L. Lehmus put forth a theorem: Any triangle with two angle bisectors of equal lengths is isosceles. This became known as the Steiner-Lehmus Theorem after noted geometer Jakob Steiner authored a proof (Coxeter et al., 1967). As students of mathematics focused on becoming teachers, the converse of this theorem was presented to us in a class geared toward future high school geometry teachers: 'Any isosceles triangle has equal angle bisectors.' When asked to prove this statement we were quite smug in our abilities to whip out a proof. To put our egos in check, the professor then asked us to prove the original theorem. Our text, Advanced Euclidean Geometry by Alfred S. Posamentier (2002), stated, that "the proof of this theorem is regarded as one of the most difficult in elementary geometry" (p. 88).

The professor asked if we would present the rest of the class one of the four proofs offered in the text. It is at this time that we notice that three of the four proofs were done in the contrapositive manner. In other words, the proofs were done on the statement, "If the triangles is not isosceles, then the angle bisectors are not congruent." All three end in a contradiction, thus making the original statement true. The one proof that did not rely on the contrapositive and contradiction involved a non-trivial construction (which we will present shortly). For the presentation, we did further research to discover that the theorem had not seemed to be proven directly. Although the word 'direct' opened a whole new line of investigation, a burning curiosity of why this problem was impossible had already been lit.

This problem has a distinguished lineage of problems and solutions linked to it. Euclid of Alexandria (circa 300 BC) gave an early proof of the law of cosines based on the Pythagorean Theorem. Daniel Christian Ludolph Lehmus wrote books and papers on mathematics and was one of the contributors of Crelle's Journal since its first issue in 1826. Jakob Steiner was a Swiss mathematician and considered to be 'the greatest geometer since the time of Euclid' (O'Connor et al., 2009). Steiner's mathematical work was mainly confined to geometry. This he treated synthetically, to the total exclusion of analysis, which he hated, and is said to have considered it a disgrace to synthetic geometry if equal or higher results were obtained by analytical geometry methods. In addition, Matthew Stewart was a Scottish mathematician known for, amongst other things, what is now known as Stewart's theorem which relates measurements on a triangle to an additional line through a vertex.

Several noted mathematicians claimed that a 'direct proof' was impossible. James Joseph Sylvester was born in London in 1814, and made fundamental contributions to matrix theory, invariant theory, number theory, partition theory and combinatorics. Sylvester argued that a direct proof would be impossible but his "impossibility proof" wasn't rigorous enough to deter others (Chow, 2004). In addition, John Horton Conway is a prolific mathematician active in the theory of finite groups, knot theory, number theory, combinatorial game theory and coding theory. He claims that because an 'equality-chasing' proof does not hold over an arbitrary field or include negative numbers, then it isn't valid (Chow, 2004).

To get a better perspective of a 'direct proof' of the theorem, we present two non-direct proofs from the textbook mentioned above, a construction proof and an indirect proof.

Construction Proof

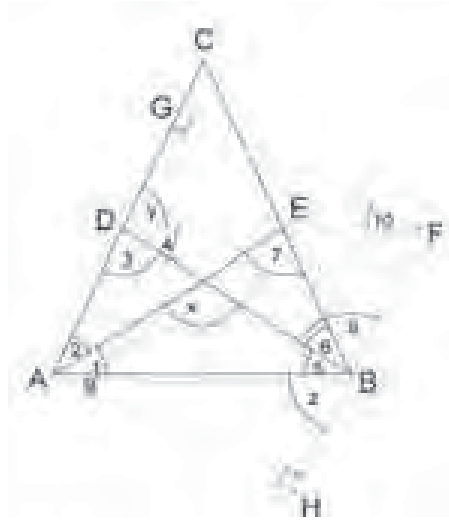


Figure 1

Draw $\angle DBF \cong \angle AEB$ so that $\overline{BF} \cong \overline{BE}$. Then draw $\overline{DF} \perp \overline{AC}$ and $\overline{AH} \perp \overline{FB}$ at H (Figure 1). Because by hypothesis $\overline{AE} \cong \overline{DB}$, $\overline{FB} \cong \overline{EB}$, and $\angle 8 \cong \angle 7$, we have $\Delta AEB \cong \Delta DBF$. Thus, $\overline{DF} \cong \overline{AB}$ and $m\angle 1 \cong m\angle 4$. It follows that

$$m\angle 4 + m\angle 3 = m\angle 8 + m\angle 5$$

so that

$$m\angle z = m\angle y.$$

Now $\Delta FDG \cong \Delta ABH$ (by SAA), $DG = BH$, $FG = AH$. $\Delta AFG = \Delta AFG$ (by HL), and $AG = FH$. Therefore, quadrilateral GFHA is a parallelogram. Also, $m\angle 9 = m\angle 10$ (from ΔABH and ΔFDG). Thus,

$$\begin{aligned} m\angle DAB &= m\angle DFB \text{ and} \\ m\angle DFB &= m\angle EBA. \end{aligned}$$

Therefore, $m\angle DAB = m\angle EBA$ and ΔABC is isosceles.

QED

Indirect Proof

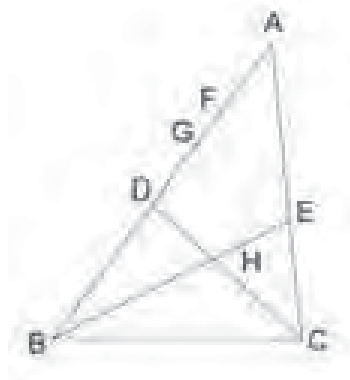


Figure 2

In $\triangle ABC$ (see Figure 2), the bisectors of angles ABC and ACB have equal lengths (i.e., $BE = DC$). Assume that $m\angle ABC < m\angle ACB$. We then draw $m\angle FCD$ congruent to $\angle ABE$. Note that we may take point F between vertices B and A without loss of generality. In $\triangle FBC$, $FB > PC$. Choose a point G so that $BG \cong FC$. Then draw $GH \parallel FC$. Now $\angle BGH = \angle BFC$ and $\triangle BGH \cong \triangle CFD$ (ASA). It follows that $BH = DC$. Because $BH < BE$, this contradicts the hypothesis that the lengths of the angle bisectors DC and BE are equal. A similar argument will show that it is impossible to have $m\angle ABC < m\angle ACB$. It then follows that $m\angle ABC = m\angle ACB$ and that $\triangle ABC$ is isosceles.

QED

Problem and Solution

The search for a direct proof on the internet yielded an interesting observation. Jim Loy's website puts it this way (Loy, 2004):

"Here is a clue about what the difficulty is. I drew a triangle and bisected the two base angles. I kept the base and one angle bisector (upper left to lower right) at constant lengths. As I changed the far right angle, I traced the path of the [larger point], and got the curve shown. Certainly this curve is of fourth degree or higher. What this means is that if you have the length of the base and the length of one angle bisector and the size of the angle that it bisects, then you will have great difficulty calculating the length of the other angle bisector. So, a straightforward attempt at a proof, using equations giving the lengths of the angle bisectors, may be very difficult to find, as the equations may be of fourth degree or higher."

The solution presented here is based upon Stewart's Theorem: Let a , b , and c be the lengths of the sides of a triangle. Let d be the length of a cevian (connecting segment) to the side of length a . If the cevian divides a into two segments of length m and n , then

$$b^2m + c^2n = a(d^2 + mn).$$

Indeed, our proof begins with the equivalent of a fourth degree equation. However, combined with Stewart's Theorem, we did find a direct way to prove the Steiner-Lehmus Theorem.

The Sayre-Reitsma Direct Proof

We are given $\triangle ABC$ with angle bisectors at vertices A and B such that the length of the bisectors are equal that is, $AE = BD$.

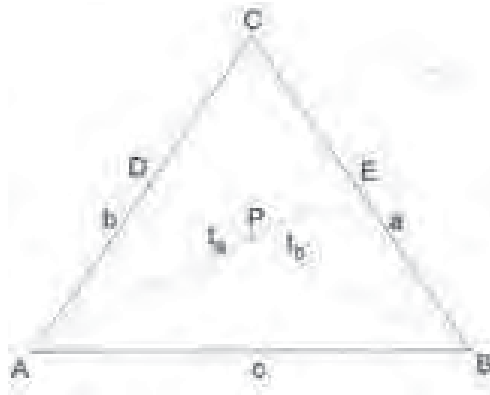


Figure 3

In Figure 3, we have $m\angle CAD = m\angle DAB$, $m\angle CBE = m\angle EBA$, and $t_a = t_b$. We need to show that the triangle is isosceles, that is, that $\overline{AC} = \overline{BC}$.

From Stewart's Theorem (Johnson, 2007):

$$t_a = \frac{2\sqrt{bcs(s-a)}}{(b+c)}$$

where s is the semiperimeter, $(a+b+c)/2$, of the triangle. Thus, it follows that for the length of the internal bisector of angle B (t_b),

$$t_b = \frac{2\sqrt{acs(s-b)}}{(a+c)}.$$

But since $t_a = t_b$ we have,

$$\frac{2\sqrt{bcs(s-a)}}{(b+c)} = \frac{2\sqrt{acs(s-b)}}{(a+c)}.$$

Dividing by 2 and squaring both sides, we get

$$\frac{bcs(s-a)}{(b+c)^2} = \frac{acs(s-b)}{(a+c)^2}.$$

Cross multiplying yields

$$bcs(s-a)(a+c)^2 = acs(s-b)(b+c)^2$$

so that

$$b(s-a)(a+c)^2 = a(s-b)(b+c)^2.$$

Expanding both sides gives this string of equations:

$$\begin{aligned} b(s-a)(a+c)^2 &= a(s-b)(b+c)^2 \\ (bs-ba)(a^2+2ac+c^2) &= (as-ab)(b^2+2bc+c^2) \\ a^2bs + 2abcs + bc^2s - a^3b - 2a^2bc - abc^2 &= ab^2s + 2abcs + asc^2 - ab^3 - 2ab^2c - abc^2 \\ a^2bs + bc^2s - a^3b - 2a^2bc + (2abcs - abc^2) &= (2abcs - abc^2) + ab^2s + asc^2 - ab^3 - 2ab^2c \\ a^2bs + bc^2s - a^3b - 2a^2bc &= ab^2s + asc^2 - ab^3 - 2ab^2c \end{aligned}$$

Since $s = \frac{a+b+c}{2}$, we have

$$a^2b\left(\frac{a+b+c}{2}\right) + bc^2\left(\frac{a+b+c}{2}\right) - a^3b - 2a^2bc = ab^2\left(\frac{a+b+c}{2}\right) + ac^2\left(\frac{a+b+c}{2}\right) - ab^3 - 2ab^2c$$

or

$$\frac{a^3b + a^2b^2 + a^2bc + abc^2 + b^2c^2 + bc^3 - 2a^3b - 4a^2bc}{2} = \frac{b^3a + a^2b^2 + ab^2c + abc^2 + a^2c^2 + ac^3 - 2ab^3 - 4ab^2c}{2}.$$

Thus, we have the set of equations:

$$\begin{aligned} a^3b + [a^2b^2] + a^2bc + [abc^2] + b^2c^2 + bc^3 - 2a^3b - 4a^2bc &= b^3a + [a^2b^2] + ab^2c + [abc^2] + a^2c^2 + ac^3 - 2ab^3 - 4ab^2c \\ [a^3b] + a^2bc + b^2c^2 + bc^3 - [2a^3b] - 4a^2bc &= [b^3a] + ab^2c + a^2c^2 + ac^3 - [2ab^3] - 4ab^2c \\ [a^2bc] + b^2c^2 + bc^3 - a^3b - [4a^2bc] &= [ab^2c] + a^2c^2 + ac^3 - ab^3 - [4ab^2c] \\ b^2c^2 + bc^3 - a^3b - 3a^2bc &= a^2c^2 + ac^3 - ab^3 - 3ab^2c \end{aligned}$$

Moving all the terms to one side and factoring gives the following:

$$\begin{aligned}
& b^2c^2 + bc^3 - a^3b - 3a^2bc - (a^2c^2 + ac^3 - ab^3 - 3ab^2c) = 0 \\
& b^2c^2 + bc^3 - a^3b - 3a^2bc - a^2c^2 - ac^3 + ab^3 + 3ab^2c = 0 \\
& 3ab^2c - 3a^2bc + b^2c^2 - a^2c^2 + bc^3 - ac^3 + ab^3 - a^3b = 0 \\
& (3abc)(b-a) + c^2(b^2 - a^2) + c^3(b-a) + ab(b^2 - a^2) = 0 \\
& (3abc)(b-a) + c^2(b-a)(b+a) + c^3(b-a) + ab(b-a)(b+a) = 0 \\
& (b-a)[(3abc) + c^2(b+a) + c^3 + ab(b+a)] = 0
\end{aligned}$$

For

$$(b-a)[(3abc) + c^2(b+a) + c^3 + ab(b+a)] = 0.$$

to be true, either

$$[(3abc) + c^2(b+a) + c^3 + ab(b+a)] = 0$$

or

$$(b-a) = 0$$

must be true. Since a , b , and c are all sides of a triangle, then they must have positive values. Thus,

$$[(3abc) + c^2(b+a) + c^3 + ab(b+a)] > 0.$$

Hence,

$$(b-a) = 0.$$

or

$$b = a.$$

Therefore the triangle is isosceles.

QED

References

- Chow, Timothy Y. (2004) [FOM] Alleged impossibility of "direct" proof of Steiner-Lehmus theorem, retrieved from <http://www.cs.nyu.edu/pipermail/fom/2004-August/008394.html>
- Coxeter, H. S. M. and Greitzer, S. L. (1967) Chapter 1.5 The Steiner-Lehmus theorem, Pg. 14 in Geometry Revisited, vol. 19, The Mathematical Association of America, Washington D.C.
- Johnson, Roger A., 2007 (orig. 1929) p. 70. in Advanced Euclidean Geometry, Dover Publ., retrieved from <http://en.wikipedia.org/wiki/Bisection>
- Loy, Jim (1999) Proof, Jim Loy's Mathematics Page, retrieved from <http://www.jimloy.com/geometry/iso0.htm>
- O'Connor, J J and Robertson E F (2009) Jakob Steiner, The MacTutor History of Mathematics, retrieved from <http://www-history.mcs.st-andrews.ac.uk/Biographies/Steiner.html>
- Posamentier, Alfred S. (2002) Chapter 5 More Triangle Properties, Pg. 88 in Advanced Euclidean Geometry, Steven Rasmussen, Key College Publishing, New York

Statistical Modeling of the Fat Fraction in Magnetic Resonance Imaging (MRI)

Anne M. Calder, Eden A. Ellis, Li-Hsuan Huang, and Kevin Park
Advisor: Dr. Angel R. Pineda

Department of Mathematics, College of Natural Science and Mathematics, California State University, Fullerton, CA, USA

Abstract

Our project studies the quantification of the uncertainty in fat-fraction estimates using Magnetic Resonance Imaging (MRI). The fat fraction is $\frac{|F|}{|F| + |W|}$, where F is the fat signal and W is the water signal obtained using MRI. The fat and water signal magnitudes have a Rician distribution. However, the fat fraction has an unknown distribution. One medical application of the fat fraction is to diagnose Non-Alcoholic Fatty Liver Disease (NAFLD). Knowing the fat-fraction probability distribution will provide us with a better understanding of the uncertainty of fat-fraction estimates used for the diagnosis of liver disease. Our current research focuses on finding the analytic distribution of the fat fraction and numerical simulation using Monte Carlo methods. In the analytic approach, for simplicity, we explored the fat fraction where the fat and water magnitudes follow a normal distribution because the normal distribution approximates a Rician distribution for large signal-to-noise ratio (SNR). In the numerical approach, we applied Monte Carlo methods to optimize the fat-fraction estimation, studied the distribution and compared analytic with numerical results.

Introduction

Motivation

In many developed countries, especially the United States, the percentage of the population that is obese is on the rise. A recent study, by the Organization for Economic Cooperation and Development (OECD), looked at this epidemic, and estimates that by the year 2020, 75% of Americans will be obese. There are many health problems associated with obesity, in particular, non-alcoholic fatty liver disease (NAFLD), which affects 30% of adults and 10% of children in the United States. NAFLD can lead to cirrhosis, hepatocellular carcinoma (HCC), and ultimately liver failure. The current standard for diagnosing NAFLD is through a liver biopsy, an invasive procedure that samples a piece of tissue from the liver. However, a biopsy has its limitations, as there is the assumption that the tissue sample that tests 1/50,000th of the liver is representative of the entire liver. With each sample there is high variability, and as a result, the biopsy can give an inaccurate measurement (Reeder et al., 2009).

In addition to its limitations, a biopsy is painful and expensive, and so there is interest in using a non-invasive method in its place. Two methods of particular interest are Magnetic Resonance Imaging (MRI) and Magnetic Resonance Spectroscopy (MRS). MRI uses strong magnetic fields and radio frequency fields to manipulate the magnetization of some atoms in the body, this is read by a scanner which is recorded into an image. An MRI scan provides a good contrast of different tissues in the body, as well as water and fat. Adjusting the parameters, or settings, on the scanner can provide different levels of contrast. A study by Reeder (Reeder et al., 2009) has shown promise in using both MRI and MRS as a non-invasive method for quantifying fatty liver disease. The way the fat content of a tissue is quantified is through the fat fraction. The current focus of our research is the quantification of fat fraction associated with MRI.

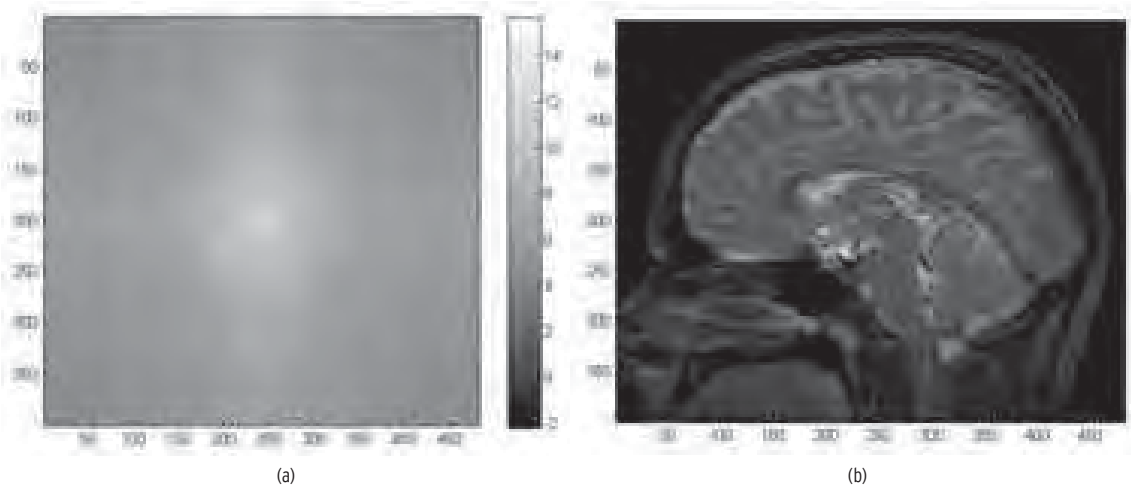


Figure 1: (a) water signal given by the MRI and (b) the magnitude of the inverse Fourier transformation of the data, which is the image used by a radiologist.

Fat Fraction

We are defining the fat fraction to be $\eta = \frac{|F|}{|F| + |W|}$, where F and W are the fat and water signals picked up by the MRI scan. A signal ($X = a + bi$) taken from an MRI scan (Figure 1) is complex, and taking the magnitude of the signal allows us to analyze the intensity of the pixel the signal represents. The real and imaginary components of a signal follow a normal distribution, while the magnitude of the signal follows a Rician distribution (Gudbjartsson, 1995), hence, $|F|$ and $|W|$ are the magnitudes of the fat and water signals, and follow a Rician distribution. However, when the Signal-to-Noise Ratio (SNR), or mean to standard deviation ratio, is sufficiently large (i.e., $\frac{\mu}{\sigma} > 3$), the fat and water magnitudes are well approximated by a normal distribution (Gudbjartsson, 1995).

It is difficult to analyze the fat fraction, because its distribution is unknown. Our goal is to determine an analytical expression for the distribution of the fat fraction and verify it with numerical simulations using Monte Carlo methods. Along with the search for an analytic expression, we will use Monte Carlo methods to optimize acquisition of the MRI based on the full distribution of the fat fraction.

Methods

Analytical

We simplified the fat fraction by assuming the SNR was sufficiently high such that the fat and water magnitudes follow a standard normal distribution. We let $X = |F|$ and $Y = |W|$. If $X, Y \sim N(0, 1)$, then we try to find the distribution of $U = \frac{X}{X + Y}$. To find the fat-fraction distribution we did a bivariate transformation (DeGroot, 2002) by letting $U = \frac{X}{X + Y}$ and $V = X + Y$. After obtaining the joint distribution we determined the marginal distribution of U . Thus we obtain the distribution of the fat fraction.

Numerical

It is difficult to find an analytic expression for the distribution of the fat fraction when the fat and water magnitudes follow a Rician distribution. Numerical simulations provided us with intuitive ideas and allowed us to explore different properties of the fat fraction. We utilized Graphical User Interfaces (GUIs) to: (1) visualize the Monte Carlo simulations used to verify analytical results, and (2) as an aid in optimization. Our first GUI, used to verify analytic results, allows the user to control the sample size¹ and the means and variances for the fat and water components. Along with plotting normalized (where the area of the distribution = 1), histograms for the fat and water components, the GUI plots a histogram for the fat fraction overlaid with the actual fat fraction. The actual fat fraction $\left(\frac{\mu_F}{\mu_F + \mu_W}\right)$ cannot be determined in clinical settings. However, since we controlled the parameters we were able to use the GUI to determine how closely our analytical expression estimated the actual fat fraction.

We considered the accuracy of our fat fraction estimate by computing the mean square error (MSE). The MSE is the average of the square of the error, given by

$$\text{MSE} = \frac{1}{n} \sum_{i=0}^n (y - \hat{y}_i)^2$$

where y is the actual fat fraction and \hat{y} is obtained from simulation, and n is the total number of simulated samples.²

To optimize the variance, we chose the relationship between the variances to be $\sigma_F^2 + \sigma_W^2 = 1$. While this is not the actual relationship between the variances, it is a simplified approach that can give us an idea of how we can change the parameters to obtain a more accurate fat-fraction estimate by minimizing the MSE (Bice). Our second GUI allows the user to input values for the means of the fat and water, and based on the chosen relationship, explores the effect different values for the variances of fat and water have on the MSE. We want to find the values of the variances that result in the lowest MSE, because they would tell us what values to put on the MRI scanner to obtain the best estimate of the fat fraction.

¹The number of samples used by the Monte Carlo simulation was 10,000.

²When MSE = 0 the estimator of the fat fraction (\hat{y}) predicts the actual value (y) fat fraction perfectly.

Results

Analytical

Assuming the magnitudes of the fat ($|F|$) and water ($|W|$) follow a standard normal distribution in the fat fraction, we derived the probability density of the fat fraction to be:

$$f_U(u) = \frac{1}{\pi(2u^2 - 2u + 1)} \text{ for } u > 0, \quad (1)$$

which is a Cauchy distribution $\left(f(x; x_0; \gamma) = \frac{1}{\pi} \left[\frac{\gamma}{(x - x_0)^2 + \gamma^2} \right]\right)$ with parameters $x_0 = \frac{1}{2}$ and $\gamma = \frac{1}{2}$.

This analytic result was validated using simulations as shown in Figure 2.

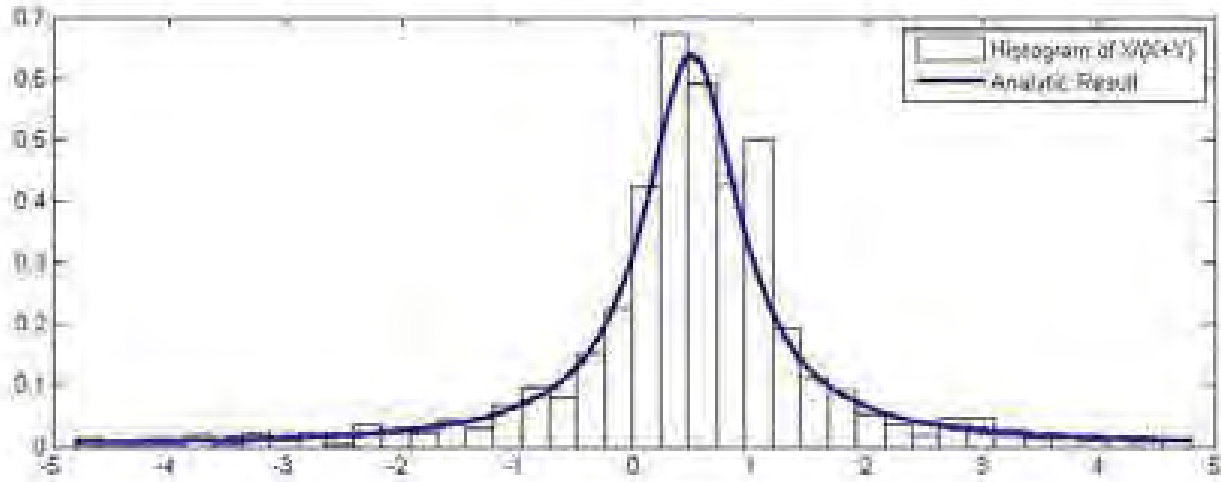


Figure 2: Our analytical result of the fat fraction with standard normal components (Eqn. 1) verified with Monte Carlo simulations. Note that in this simplified model for the fat fraction the range is $(-\infty, \infty)$ not $[0,1]$.

Numerical

Our results were obtained through a combination of analytical results and use of the Monte Carlo simulations. Aside from verifying the analytical results, our goal was to optimize the variances of the fat and water components. We chose the relationship between the variances to always be $\sigma_F^2 + \sigma_W^2 = 1$ and looked at a couple of different cases.

Case 1: Equal Means

When the means of the fat and the water are set to be equal to each other, the results with the lowest MSE are obtained when the variances of the fat and water are relatively equal, at about 0.5 (Figure 3). Using Monte Carlo simulations, we verified these results, and were able to understand the behavior of the fat fraction distribution with equal means and variances (Figure 5).

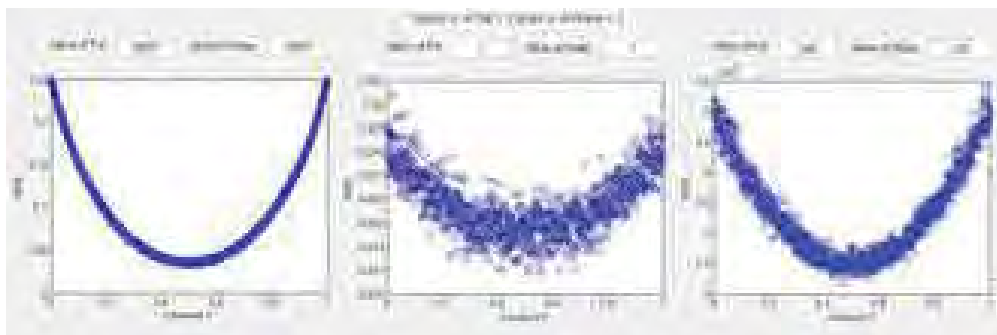


Figure 3: For values of the mean of fat equal to the mean of water, the lowest MSE is obtained when the variances are approximately equal.

Case 2: One Mean a Tenth of the Other

When the mean of one component is set to be one-tenth of the mean of the other, the results with the lowest MSE are obtained when the variance of the component with the smaller mean (i.e., the fat variance) is minimized (Figure 4). This is an important result because in clinical settings it is common for the mean of the fat to be one-tenth of the mean of the water.

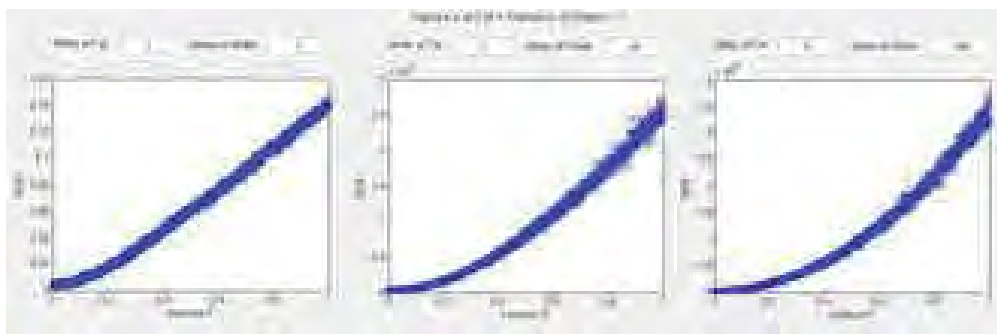


Figure 4: When the mean of the fat is one-tenth of the mean of the water, the fat component must have a very low variance in order to obtain the lowest MSE.

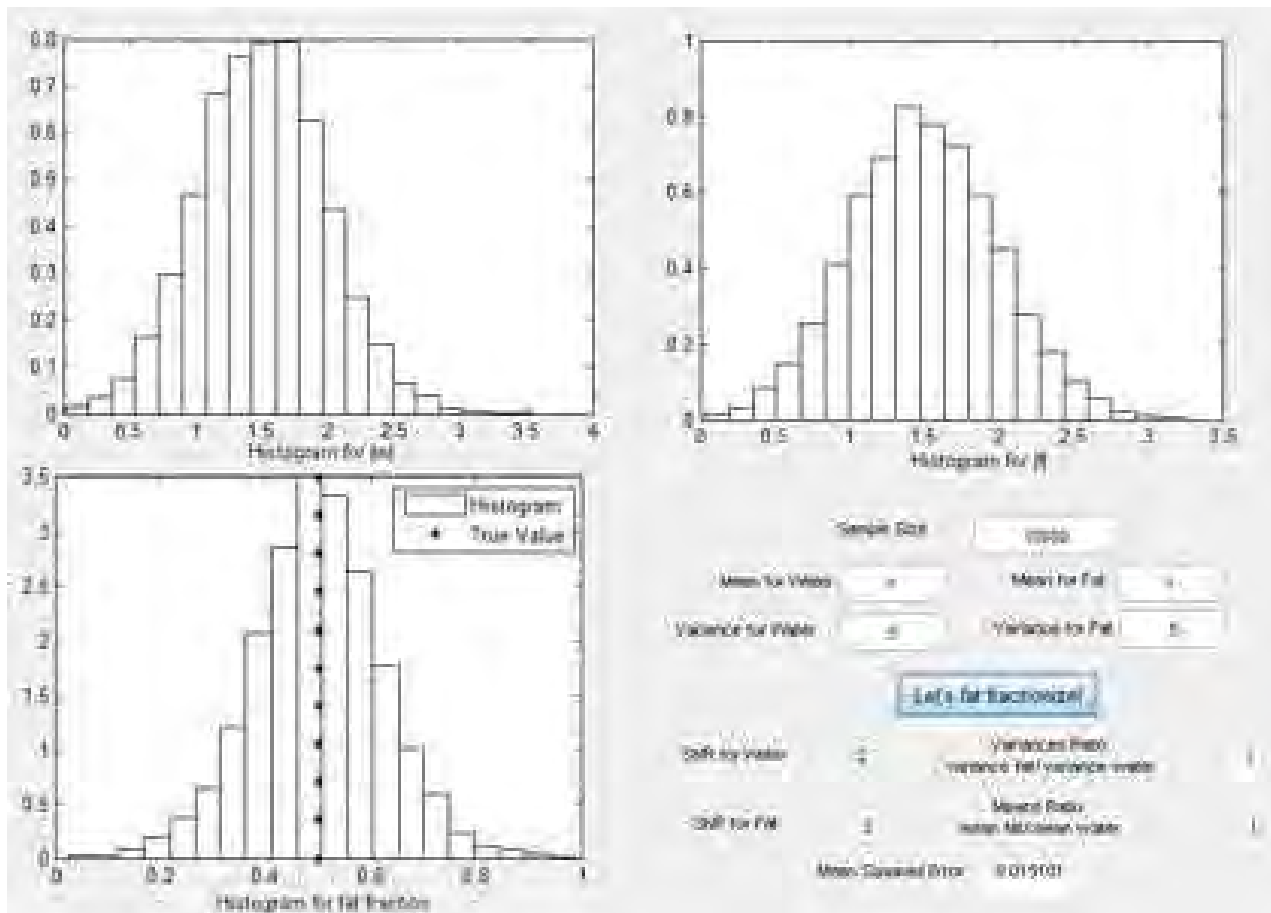


Figure 5: Corresponding to MSE optimization, the means and variances of the fat and water are equal. Notice the fat fraction is estimated with high accuracy ($MSE = 0.015001$). The actual fat fraction is overlaid over the histogram of the fat fraction and is close to the estimated mean.

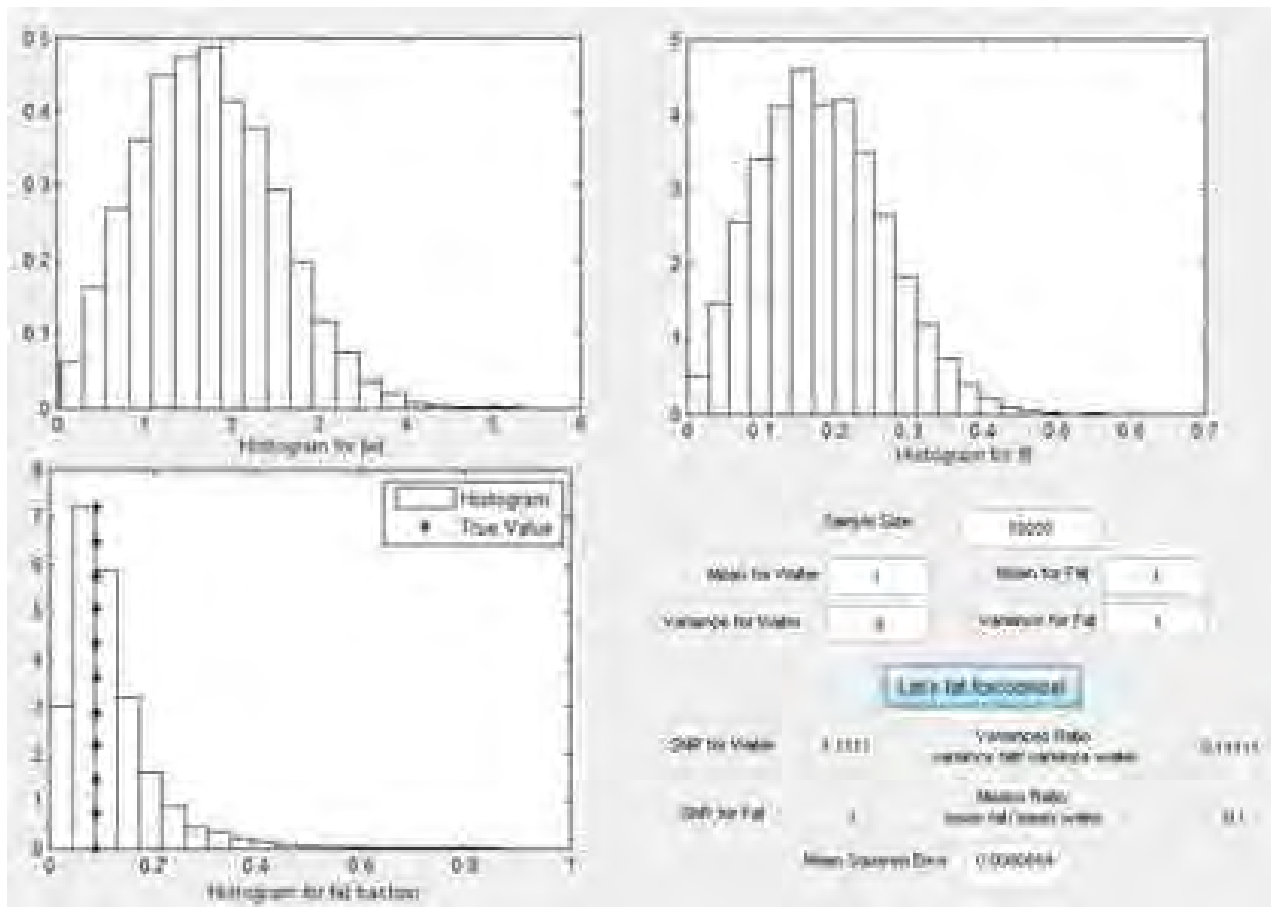


Figure 6: When the mean of fat is one-tenth of the mean of water, and the variance for the fat is low, while the variance of the water is high, the fat fraction is estimated with high accuracy ($MSE = 0.0080854$). The actual fat fraction is overlaid over the histogram of the fat fraction and is close to the estimated mean.

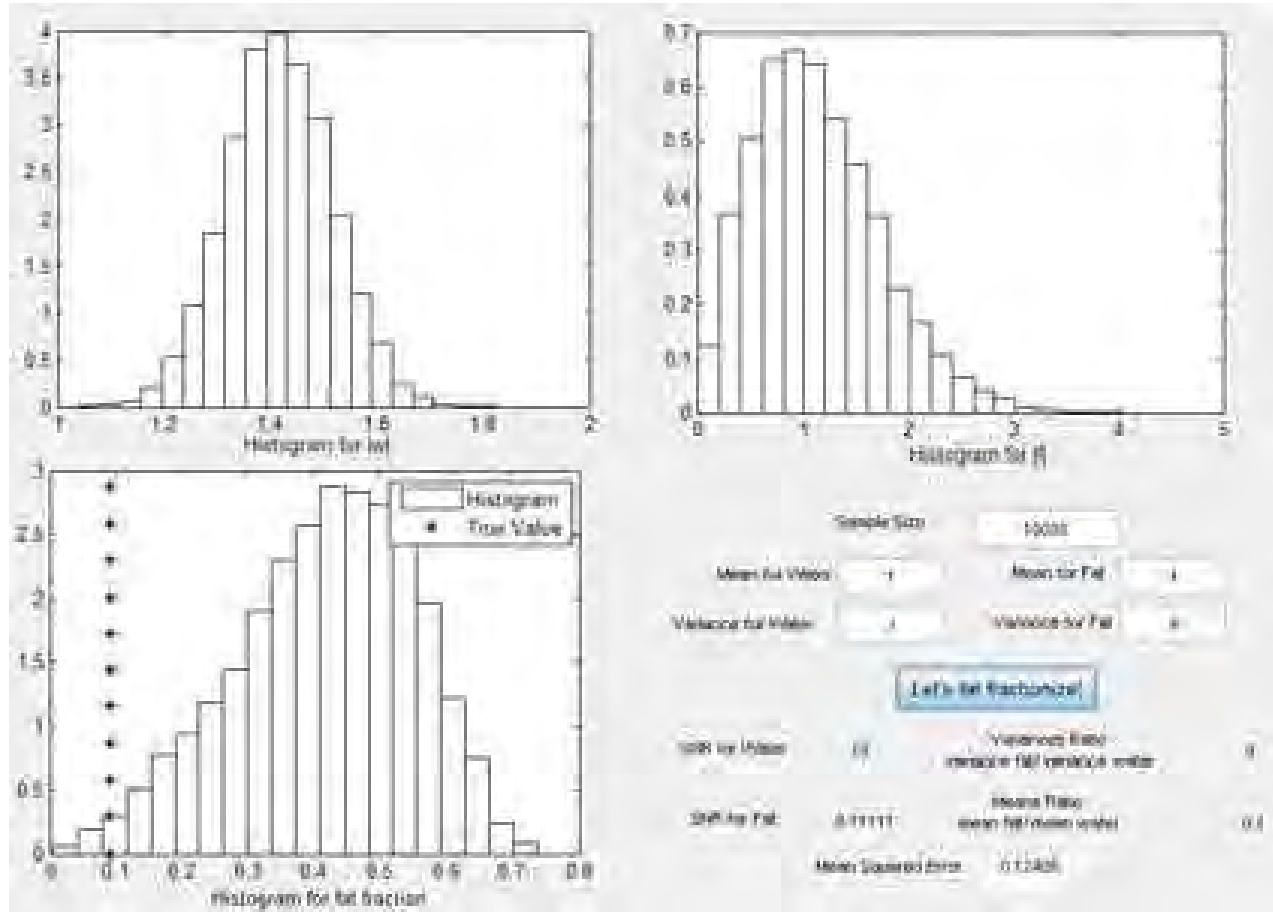


Figure 7: When the mean of fat is one-tenth of the mean of water, and the variance for the fat is high, while the variance for the water is low, the fat fraction is estimated with low accuracy ($\text{MSE} = 0.12406$). The actual fat fraction is overlaid over the histogram of the fat fraction and is far from the estimated mean.

Discussion

Fat-Fraction Expression

We were able to derive an expression for the fat fraction assuming the magnitudes of the fat and water followed a standard normal distribution. This is significant, as it is a step towards finding an expression where the magnitudes of the components follow a normal distribution, specifically with non-zero means and different variances of each component. This distribution would be applicable for large SNR.

Monte Carlo Simulations

Our simulations have given us insight to the relationship between the means and variances of the fat and water components, and how they effect the accuracy of our fat-fraction estimate. We know that depending on the values of the fat and water means, the variances should be changed according to our MSE optimization. For our chosen relationship between the variances, this requires a trade off. It may be necessary to increase the noise in one variable in order to obtain a more accurate fat-fraction estimation.

In Figure 6, we set the mean of the fat to be one-tenth of the mean of the water, and the variances to correspond with the results of our MSE optimization. The fat fraction histogram appears to follow a Rician distribution, and the actual fat fraction is very close to the mean of our simulation. This can be seen numerically as the MSE is very low at .0080854. As optimizing the MSE is a goal of our project, this is the type of result we would like to see.

In Figure 7, we keep the parameters for mean of the fat to be one-tenth of the mean of the water, but change the variances to go against our MSE optimization results. The importance in this case is that the actual fat fraction varies significantly from our simulated fat fraction. With these parameters, it does not appear that our fat fraction simulation estimates the actual fat fraction very well. This is further verified numerically, since the MSE is larger at 0.12406.

As our fat-fraction simulations represents the current industry standard in estimating the fat fraction, this result is very alarming. This shows that the current estimations for fat fraction used for diagnosis of disease can, under certain circumstances, be extremely off³.

Our results show that our estimated value for the fat fraction does not consistently predict the actual fat fraction with accuracy⁴. Since our simulations were run in the same way the fat fraction is currently estimated, it is apparent that the current industry standard for estimating the fat fraction at low SNR requires a new approach that yields a more accurate fat-fraction estimate.

Future Work

As our research continues, we have plans for both the analytic and numerical aspects of the project. Analytically, we will work towards finding an expression for the distribution of the fat fraction, where the water and fat magnitudes follow a general normal distribution, as opposed to a standard normal. Numerically, we will explore more relationships between the variances of the fat and water components in an attempt to understand their effect on the fat-fraction estimate. We hope to gain sufficient understanding to enable us to explore a more clinically accurate model. Finally, we will use the theory of maximum likelihood estimation to determine whether there is a better estimator for the fat fraction⁵.

³Results are exact mirror images when we switch means and have the mean of water be one-tenth of the mean of the fat.

⁴This error is represented by the MSE in each figure.

⁵Recall our current estimator is $\eta = \frac{|F|}{|F| + |W|}$.

Acknowledgments

We would like to thank the Mathematical Association of America Travel Grant (MAA), the National Science Foundation (NSF), grant DMS-03664 through a mini grant from the Center for Undergraduate Research in Mathematics (CURM) and the Louis Stokes Alliance for Minority Participation (LSAMP) for financial support. We also would like to especially thank our advisor, Dr. Angel R. Pineda, for his support and guidance in our research.

References

- Bice, E. Cramer-Rao Bounds for Chemical Species Decomposition in MRI in the Presence of R_2^* , in preparation.
- DeGroot, M. and Schervish, M. (2002) Probability and Statistics, 3rd ed. Addison-Wesley.
- Gudbjartsson, H. and Patz, Samuel. (1995) The Rician Distribution of Noisy MRI Data. Magnetic Resonance in Medicine.34:910-914.
- Reeder S., Robson P., Yu H., Shimakawa A., Hines C., McKenzie H., Brittain J. (2009) Quantification of Hepatic Steatosis With MRI: The Effects of Accurate Fat Spectral Modeling. Journal of Magnetic Resonance Imaging. 29:1332-1339.

A Comparative Study of Divergence Metrics in the Analysis of Neuronal Data

Mikhail Y. Popov, David Rock, and Victor Ying
Advisor: Dr. Sam Behseta

Department of Mathematics, College of Natural Science and Mathematics, California State University, Fullerton, CA, USA

Abstract

In this research, we investigate the application of a series of multidimensional distance-based measurements in order to calibrate the divergence of neuronal intensity functions under two experimental conditions. We consider four measures of divergence, namely Kullback-Leibler, Hellinger, χ^2 , and total variation. With the aid of a Bayesian curve-fitting technology coupled with simulation, we demonstrate that total variation attains considerably smaller mean squared errors than Kullback-Leibler, Hellinger, and Chi-Squared distances. We propose using total variation as the preferred method of measuring divergence, specifically when the spiking activities of the neuron are significantly different in the two experimental conditions.

Introduction

An efficient strategy in calibrating the distance between data obtained from two conditions of a scientific experiment is to employ a divergence metric. Such a metric must generate the lowest possible error, yet retain sensitivity needed for selecting differences between the two conditions. The primary objective of this work is to investigate the efficiency of a class of established divergence metrics for the purpose of measuring different patterns of neuronal firing activities between two modes of an experiment. Using the Mean Squared Error (MSE) as a criterion of comparison, we provide a practical guideline for selecting a subset of metrics whose applications can reveal the differential patterns of spiking activities along with their statistical significance. We consider four commonly utilized metrics: the Hellinger distance, total variation distance, χ^2 -divergence, and the Kullback-Leibler divergence. We create an algorithmic translation for each metric in order to facilitate the computational features of our calculations.

The motivation for this work stems from analysis of neuronal data generated during a study involving a group of motor cortex neurons of a Macaque monkey performing a sequential task (Matsuzaka et al., 2007). The monkey was trained to press a target within 800 ms of appearance on a touch-sensitive screen. Five illuminating targets were placed horizontally. The study operated under two experimental modes. As described by Behseta and Chenouri (2001), the random mode entailed a pseudo-random illumination of targets, while the repeating mode consisted of a predetermined sequence, such as the triplet of targets 2-3-4. The neuronal firing patterns under the individual modes lend them to be a prime environment for our concern of comparing divergence metrics.

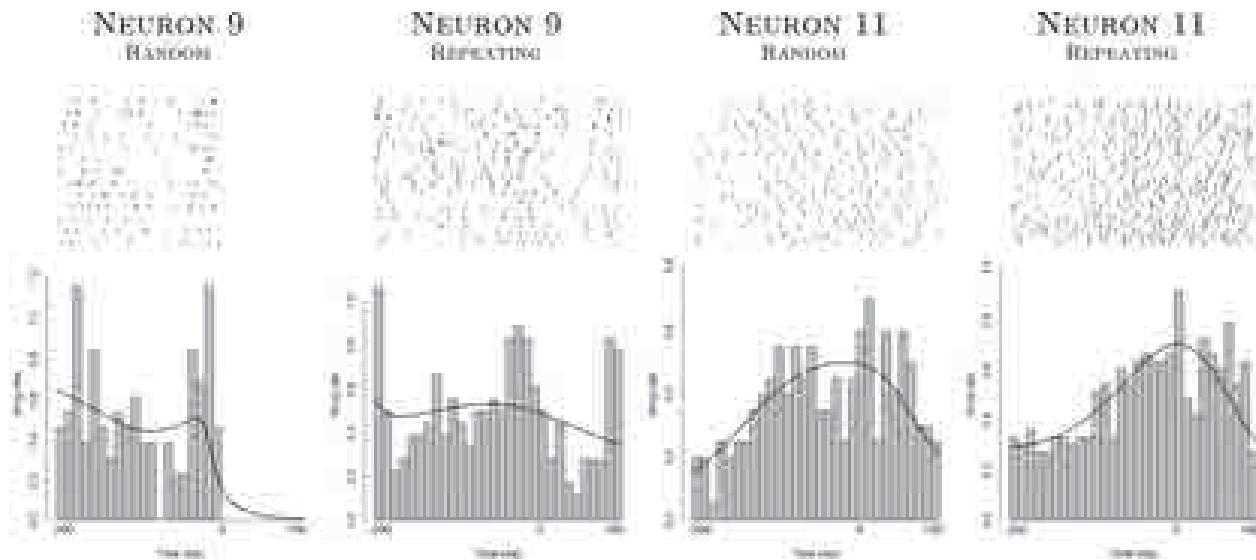


Figure 1: Raster plots and neuronal firing intensity rates with overlaid BARS-fitted curves for neurons 9 and 11. In the raster plots, tick-marks signify spikes; the horizontal axis represents time and the rows are individual trials. In the barplots below the raster plots, each bar represents the number of neuronal firings in a single 10 ms time bin across all trials and adjusted by the number of trials within the experimental mode. Note that we can consider neuron 9 to be an example of a "differential" neuron (behaves differently between the two experimental modes) and neuron 11 to be an example of a "non-differential" neuron (behaves similarly between the two experimental modes).

It is beneficial to review the underlying neurological theory behind this experiment. Two components of the neuron, the axon and dendrite, communicate through a process which releases an electric current. The point in time at which the electrical pulse occurs is referred to as a neuronal firing. Prior to the firing, there is a build up of chemicals between the axon and dendrite called an action potential. Once the levels of chemicals surpass a specific threshold, the firing occurs. Immediately following the firing, a momentary period of time allows for the axon and dendrite to rest and recover (Gazzaniga et al., 1998). When recorded, the firings appear as spikes. A sequence of such neuronal activity is called a spike train. Mathematically, one can model a spiking occurrence with a point process (Kass et al., 2005). Consequently, by modeling individual spikes with a Bernoulli distribution, it becomes possible to capture the stochastic features of the sum of a group of spiking events with a Poisson distribution.

In this work, we utilize a graphical tool called Peristimulus Time Histograms (PSTH) as an exploratory method of capturing the firing patterns. PSTH are commonly used in statistical applications to neuroscience, as they facilitate a visual realization of an accumulation of spike trains.

In Figure 1, we demonstrate the spiking activities of two neurons recorded in both conditions of the experiment for multiple trials. Each trial is defined as a time period related to the appearance of triplets of targets. In each trial, the time period of our interest ranging from 200 ms prior to the moment when the monkey struck the target, until 100 ms after. The top part in Figure 1 is called a raster-plot, the bottom part is called a PSTH. In the raster-plot, each tick mark is a spike time and each row of tick marks represents a trial. Spikes last for about a millisecond, so if we bin the experimental time into bins of size 10 ms and pool spike occurrences over all trials within each bin, we can create a PSTH. We considered 15 neurons under two experimental conditions; thus, we had a total 30 PSTH, a PSTH for random and a PSTH for repeating for each

of the 15 neurons of interest. The main objective in this paper is to study metrics of divergence suitable for measuring distance between the PSTH for mode 1 versus its counterpart in mode 2.

In order to fit a continuous curve to the PSTH, we use a technique called Bayesian Adaptive Regression Splines or BARS (DiMatteo et al., 2001). This fully Bayesian process employs a reversible jump Markov Chain Monte Carlo (MCMC) to sample from a posterior distribution of curves to approximate placement of splines to smooth a discrete data set. We fit BARS to firing intensity rates, by dividing each pool of spikes by the total number of trials per mode to obtain firing intensity rates. Next, BARS is fitted to the intensity rates (adjusted PSTH). Throughout the remainder of this paper, curves obtained through BARS are taken as the objects of our statistical inference.

Methods

Notation

As mentioned before, we work with an experimental window of 300 ms. We partition our experimental window into 30 bins of size 10 ms each. We fit BARS to histograms of intensity rates in both modes and thus create two curves, one for each experimental mode, that may be represented as two vectors of size 30. We devise the following notation of expressing these two vectors: $\hat{u}^1 = (f^1(t_1), \dots, f^1(t_{30}))$ and $\hat{u}^2 = (f^2(t_1), \dots, f^2(t_{30}))$ where superscript 1 refers to random mode and superscript 2 refers to repeating mode and t_i represents the i -th time bin for $i = 1, \dots, 30$ (Puente, 2010).

We standardize our curves obtained through fitting BARS to neuronal PSTH by dividing each component of the vectors \hat{u}^1 and \hat{u}^2 by the sum of their components. Let $|\hat{u}^1| = \sum_{i=1}^{30} f^1(t_i)$ and $|\hat{u}^2| = \sum_{i=1}^{30} f^2(t_i)$. This lets us define the vectors:

$$\hat{r}^1 = \left(\frac{f^1(t_1)}{|\hat{u}^1|}, \dots, \frac{f^1(t_{30})}{|\hat{u}^1|} \right) \quad (1)$$

$$\hat{r}^2 = \left(\frac{f^2(t_1)}{|\hat{u}^2|}, \dots, \frac{f^2(t_{30})}{|\hat{u}^2|} \right) \quad (2)$$

For $i = 1, \dots, 30$, we can work with the i -th component of each vector:

$$\hat{r}_i^1 = \frac{f^1(t_i)}{|\hat{u}^1|} \quad (3)$$

$$\hat{r}_i^2 = \frac{f^2(t_i)}{|\hat{u}^2|} \quad (4)$$

Since $\sum_{i=1}^{30} \hat{r}_i^1 = 1$ and $\sum_{i=1}^{30} \hat{r}_i^2 = 1$; $\hat{r}_i^1 \geq 0$ and $\hat{r}_i^2 \geq 0 \forall i \in \{1, \dots, 30\}$, \hat{r}^1 and \hat{r}^2 are probability mass functions.

Divergence Metrics

Let (χ, A) be a measurable space and let P and Q be two probability measures on (χ, A) . Suppose that v is a σ -finite measure on (χ, A) satisfying $P \ll v$ and $Q \ll v$. Define $p = dP/dv, q = dQ/dv$. That is, p and q are probability density functions. Let $\theta^K, \theta^H, \theta^V, \theta^{\chi^2}$ denote the statistics derived from comparing the curves \hat{r}^1 and \hat{r}^2 using one of the Kullback-Leibler (K), Hellinger Distance (H), total variation (V), and χ^2 Divergence metrics, respectively.

Table 1: Divergence and Distance Metrics

Metric	Theoretical Definition	Empirical Translation
Kullback-Leibler Divergence	$K = \begin{cases} \int \log\left(\frac{dP}{dQ}\right) dP, & \text{if } P \ll Q, \\ +\infty, & \text{otherwise.} \end{cases}$	$\theta^K(\hat{r}^1, \hat{r}^2) = \sum_{i=1}^{30} \log\left(\frac{\hat{r}_i^1}{\hat{r}_i^2}\right) \hat{r}_i^1$
Hellinger Distance	$H = \left(\int [\sqrt{dP} - \sqrt{dQ}]^2 \right)^{\frac{1}{2}}$	$\theta^H(\hat{r}^1, \hat{r}^2) = \left(\sum_{i=1}^{30} [\sqrt{\hat{r}_i^1} - \sqrt{\hat{r}_i^2}]^2 \right)^{\frac{1}{2}}$
Total Variation Distance	$V = \sup_{\alpha \in A} \int_{\alpha} dP - dQ $	$\theta^V(\hat{r}^1, \hat{r}^2) = \max \{ \hat{r}_1^1 - \hat{r}_1^2 , \dots, \hat{r}_{30}^1 - \hat{r}_{30}^2 \}$
χ^2 Divergence	$\chi^2 = \begin{cases} \int \frac{(dP - dQ)^2}{dQ}, & \text{if } P \ll Q, \\ +\infty, & \text{otherwise.} \end{cases}$	$\theta^{\chi^2}(\hat{r}^1, \hat{r}^2) = \sum_{i=1}^{30} \frac{(\hat{r}_i^1 - \hat{r}_i^2)^2}{\hat{r}_i^2}$

Table 1 lists the theoretical definitions of the four metrics as well as empirical formulas suitable for the calculation of divergence. The empirical formulas are obtained based on the assumption that \hat{r}^1 and \hat{r}^2 are probability mass functions. There is an established relationship between metrics (see p. 90, Lemma 2.7 in Tsybakov, 2009) and it is defined as follows:

$$0 \leq V(P, Q) \leq H(P, Q) \leq \sqrt{K(P, Q)} \leq \sqrt{\chi^2(P, Q)} \quad (5)$$

Each metric will approach 0 when $P \sim Q$. Using the empirical translations in Table 1, we verified Eq. 5 for all neurons studied.

Permutation Tests

General Approach

To assess the significance of the empirical version of divergence metrics, we describe a resampling (permutation) algorithm to be used on the neuronal data. Let tr^1 denote the number of trials in the random mode and tr^2 represent the number of trials in the repeating mode for a single neuron. Hence, $tr^{tot} = tr^1 + tr^2$ is the total number of trials in both modes. We begin by introducing the following sets:

1. The set of firing times for experimental mode 1 (the random mode) for the j -th trial where $j = 1, \dots, tr^1$

$$T_j^1 := \{t : -200 \leq t \leq 100, t \text{ is a time (ms) during which a neuron spike occurred}\},$$

2. The set of firing times for experimental mode 2 (the repeating mode) for the k -th trial where $k = 1, \dots, tr^2$

$$T_k^2 := \{t : -200 \leq t \leq 100, t \text{ is a time (ms) during which a neuron spike occurred}\},$$

3. The set of all trials under experimental mode 1 (random mode) where each trial is a set of firing times

$$T^1 := \{T_j^1 : j \in 1, \dots, tr^1\},$$

4. The set of all trials under experimental mode 2 (repeating mode) where each trial is a set of firing times

$$T^2 := \{T_k^2 : k \in 1, \dots, tr^2\},$$

5. The set of all trials under both experimental modes $T := T^1 \cup T^2$.

Next, we randomly sample tr^1 many trials from T without replacement to create a new T^1 which may include some trials from the original T^1 and some trials from the original T^2 . We use the remaining tr^2 many trials in T to construct a new T^2 . We repeat this process B many times such that B is a large number. Suppose that P_i represents the i -th permutation where $i = 1, \dots, B$ so the i -th iteration of the permutation process yields two sets of trials: $T_{P_i}^1$ and $T_{P_i}^2$, which enables us to create two new PSTHs: one for $T_{P_i}^1$ and one for $T_{P_i}^2$ which results in the two following firing intensity rate vectors:

1. $F_i^1 = \{\frac{c_1}{tr^1}, \dots, \frac{c_{30}}{tr^1}\}$ where each c_b is the count of spikes across all trials for time bin $b = 1, \dots, 30$ in the random mode.
2. $F_i^2 = \{\frac{c_1}{tr^2}, \dots, \frac{c_{30}}{tr^2}\}$ where each c_b is the count of spikes across all trials for time bin $b = 1, \dots, 30$ in the repeating mode.

We then define two new vectors of size 30, $\hat{u}_{P_i}^1$ and $\hat{u}_{P_i}^2$, by fitting BARS to the firing intensity rates F_i^1 and F_i^2 . Finally, we transform these two vectors into probability mass functions to create $\hat{r}_{P_i}^1$ and $\hat{r}_{P_i}^2$, for $i = 1, \dots, B$. This will allow us to calculate the empirical translation of each metric given in Table 1 per permutation iteration, resulting in a permutation-based distribution for each metric.

Using this general approach, we will launch two sets of analyses: a global firing analysis to calibrate the difference between the two intensity rates over the entire experimental window, and a local analysis to distinguish different patterns of intensities at certain time bins.

Global Analysis

We begin by detecting significant distances over the entire experimental window of 300 ms. Comparison of the two original curves \hat{u}^1 and \hat{u}^2 requires standardizing them into \hat{r}^1 and \hat{r}^2 and obtaining the statistic $\hat{\theta}_{\text{obs}}^m$ for each metric $m = \{K, H, V, \chi^2\}$. When $\hat{r}^1 \approx \hat{r}^2$, $\hat{\theta}^m \rightarrow 0$, for every metric m . We devise the following hypothesis testing procedure:

$$\begin{cases} H_0 : \theta^m = 0 \\ H_a : \theta^m > 0 \end{cases}$$

Through computing $\hat{\theta}_{P_i}^m$ for each i -th permutation P_i for each metric $m = \{K, H, V, \chi^2\}$, we derive a distribution of $\hat{\theta}^m$ for large B . Then, we calculate the resampling p-value p for each metric m using the following formula:

$$p^m = \frac{\text{number of } \hat{\theta}_{P_i}^m \geq \hat{\theta}_{\text{obs}}^m}{B} \quad (6)$$

That is, the proportion of resampled metrics that are as or more extreme than the observed metric. A small value of p may be taken as a sign of rejecting the null hypothesis.

Local Analysis

In the second stage of the analysis, we consider a hypothesis testing procedure for each of the 30 time bins for each of the 15 neurons. Recall that we have B permutations of intensity rates and each one referred to as P_i where $i = 1, \dots, B$. We also have 30 time bins of 10ms referred to as t_k where $k = 1, \dots, 30$. Furthermore, we have probability mass functions evaluated at each bin given by vectors \hat{r}^1 (Eq. 1) and \hat{r}^2 (Eq. 2). We introduce a metric for local analysis inspired by the Kullback-Leibler divergence. We refer to this metric as the Log-Ratio metric (LR metric).

$$\hat{\theta}^{LR(t_k)} = \log \frac{\hat{r}_{t_k}^1}{\hat{r}_{t_k}^2} \quad (7)$$

To formalize, we calculate a $\hat{\theta}_{\text{obs}}^{LR(t_k)}$ for t_1, \dots, t_{30} from the original \hat{r}^1 and \hat{r}^2 . Also we obtain $\hat{\theta}_{P_i}^{LR(t_k)}$ for all t_k and for P_1, \dots, P_B . For the time bin t_k when the neuron behaves similarly in both experimental modes, we have that $\hat{r}_{t_k}^1 \approx \hat{r}_{t_k}^2$, so their ratio is approximately 1. Hence $\hat{\theta}^{LR(t_k)} \rightarrow 0$. We can test the hypothesis for any time bin t_k that the neuron behaves similarly in both experimental modes:

$$\begin{cases} H_0 : \hat{\theta}^{LR(t_k)} = 0 \\ H_a : \hat{\theta}^{LR(t_k)} \neq 0 \end{cases}$$

Using permutation, we obtain a p-value for the local test. We can represent the local p-values as:

$$p^{LR(t_k)} = \begin{cases} \frac{\text{number of } \hat{\theta}_{P_i}^{LR(t_k)} \geq \hat{\theta}_{\text{obs}}^{LR(t_k)}}{B}, & \hat{\theta}_{\text{obs}}^{LR(t_k)} \geq 0, \\ \frac{\text{number of } \hat{\theta}_{P_i}^{LR(t_k)} \leq \hat{\theta}_{\text{obs}}^{LR(t_k)}}{B}, & \hat{\theta}_{\text{obs}}^{LR(t_k)} < 0, \end{cases}$$

Mean Square Error for the Comparative Study

Figure 2 depicts an algorithm for simulation of neuronal spike trains based on real data. Following the process described in the figure, we have two new curves $\hat{u}_{S_i}^1$ and $\hat{u}_{S_i}^2$, where S_i is the i -th simulation of a neuron and $i = 1, \dots, G$; for some large G . We standardize these two curves as in Equations 1 and 2 to obtain a $\hat{r}_{S_i}^1$ and $\hat{r}_{S_i}^2$. We compute $\hat{\theta}_{S_i}^m$ for each i -th simulation S_i and each metric $m = \{K, H, V, \chi^2\}$. Then, we use these metrics derived from the simulations to calculate the metric mean $\bar{x}_{\hat{\theta}^m}$ and the metric variance $s_{\hat{\theta}^m}^2$. Consequently, we calculate the bias using $\hat{\theta}_{\text{obs}}^m$. Finally, we can calculate the mean square error (MSE) for each metric m :

$$\begin{aligned} \text{MSE}(\hat{\theta}^m) &= \text{Var}(\hat{\theta}^m) + (\text{Bias}(\hat{\theta}^m, \theta^m))^2 \\ \text{MSE}(\hat{\theta}^m) &= \text{Var}(\hat{\theta}^m) + (\text{E}(\hat{\theta}^m) - \theta^m)^2 \\ \Rightarrow \widehat{\text{MSE}}(\hat{\theta}^m) &= s_{\hat{\theta}^m}^2 + (\bar{x}_{\hat{\theta}^m} - \hat{\theta}_{\text{obs}}^m)^2 \end{aligned}$$

NEURONAL SPIKING SIMULATION

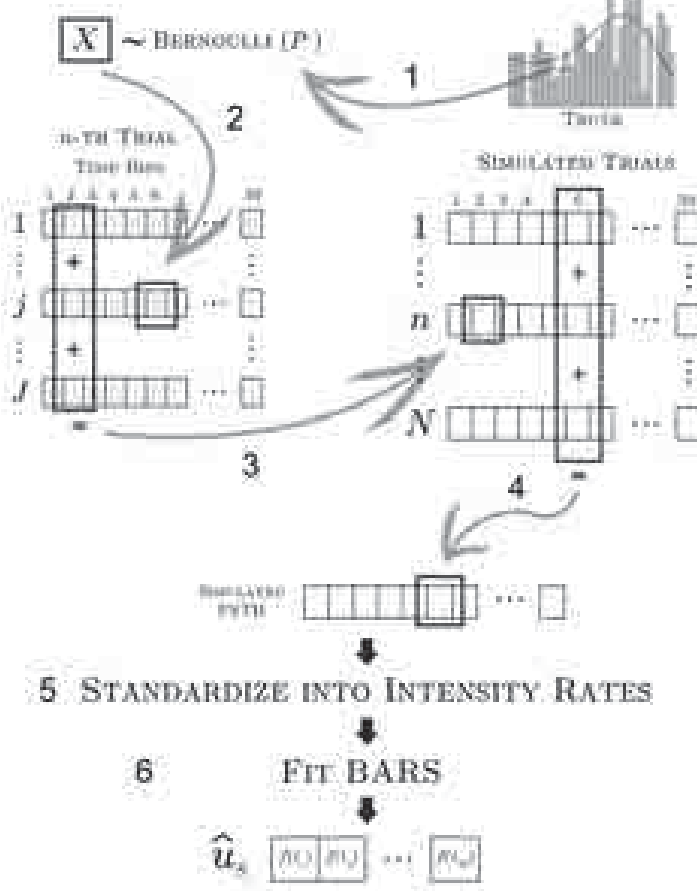


Figure 2: This is a diagram of the simulation of a neuron under one of the two experimental modes. We consider a random variable X that lasts for 1 ms of time. Our simulation process consists of the following steps: (1) X is 1 when there is a spike and X is 0 when there is no spike. X is a Bernoulli trial with success probability of P where $P = \lambda \hat{u}_k$ in which \hat{u}_k is the firing intensity rate curve at the k -th bin, λ is a constant between 0 and 1 that makes \hat{u}_k smaller. (2) We assign that X to the k -th bin (column) of the j -th row inside a $J \times 30$ matrix. We populate the matrix with ones and zeroes (spikes and no spikes). (3) For each k -th bin (column), we sum across the rows to obtain the k -th bin (column) value for the n -th trial for $n = 1, \dots, N$. (4) For each k -th bin (column) we sum across all trials (rows) to create the k -th bin (column) of a simulated PSTH. We then (5) divide by the number of trials N as we did before with the original data and then (6) fit a curve to the simulated intensity rates with BARS to obtain \hat{u}_{S_i} .

Results

Global Analysis

We calculated the p-value for every studied neuron and for every metric. The summary of our results is presented in Figure 3. Two trends are evident in Figure 3. First, there was an overall agreement between the four measures. That is, when a difference between experimental modes was declared significant by one measure, it was generally declared significant by the other measures as well. Similarly, when the difference was declared insignificant by one measure it was generally also declared insignificant by the others.

Despite the overall agreement between measures, the total variation distance appears to have been less sensitive than the other measures. That is, the total variation metric was unable to detect differences that were picked up by the others. For example, in the case of neuron 2 (see Figure 3 and Table 2), a difference was detected at the $\alpha=0.05$ level by the χ^2 , Kullback-Leibler, and Hellinger measures but not by the total variation distance. Similarly, at the $\alpha=0.01$ level, neurons 2 and 9 were also declared differential by every metric except the total variation distance.

Local Analysis

For local analysis, each of a neuron's 30 bins was examined individually. A permutation test using the proposed LR metric method was performed and a p-value was calculated for each bin. General results are presented in Figures 4 and 5. A summary of these results is presented below.

A few things should be noted in Figure 4. Time periods associated with the beginning and the end of the experimental window were generally declared differential. Second, every neuron exhibited an increase in p-value sometime between bins 10 and 20, corresponding to the window of time starting 110 ms before and ending at the touch of the button. This leads to similarity between the neuronal firing patterns in the two experimental modes. In every neuron, at least one bin was declared differential at the $\alpha=0.01$ level. Finally, in almost every studied neuron, a majority of the bins were declared differential at the $\alpha=0.01$ level.

Neuron 5 is an example where all four metrics agreed. As shown in Figure 5, a majority of the bins were differential according to the LR metric at both the $\alpha = 0.05$ and $\alpha = 0.01$ levels. At the $\alpha=0.05$ level, 29 out of 30 bins were differential, whereas at the $\alpha = 0.01$ level 28 out of 30 were differential.

Neuron 11, on the other hand, is an example of a non-differential case, as confirmed by all four metrics. As seen in Figure 5, only a minority of the bins were declared differential by our LR metric. This was true at both the $\alpha=0.05$ and $\alpha=0.01$ levels. At the $\alpha=0.05$ level, 13 out of 30 bins were differential, whereas at the $\alpha=0.01$ level that number dropped to 6 out of 30 bins.

Metric Comparison

The results of our metric comparison are given below. For a graphical presentation of the results, see Figure 6. For a tabular presentation, see Table 3. The total variation distance performed best. Both the average and standard deviation of its MSE were the lowest. Also, in every studied neuron, it was the metric with the lowest MSE. It was followed in performance by the Hellinger and Kullback-Leibler metrics. The average and standard deviation of the MSEs from the Hellinger metric came in second while the the Kullback-Leibler metric came in third. The Hellinger metric yielded an MSE lower than the Kullback-Leibler's in 8 out of the 15 studied neurons. Performing worst of the group was the χ^2 metric. Both the average and standard deviation of the χ^2 metric's MSE were, unquestionably, the highest since in each studied neurons, it was the metric with the highest MSE. Based on these results, we recommend using the total variation distance.

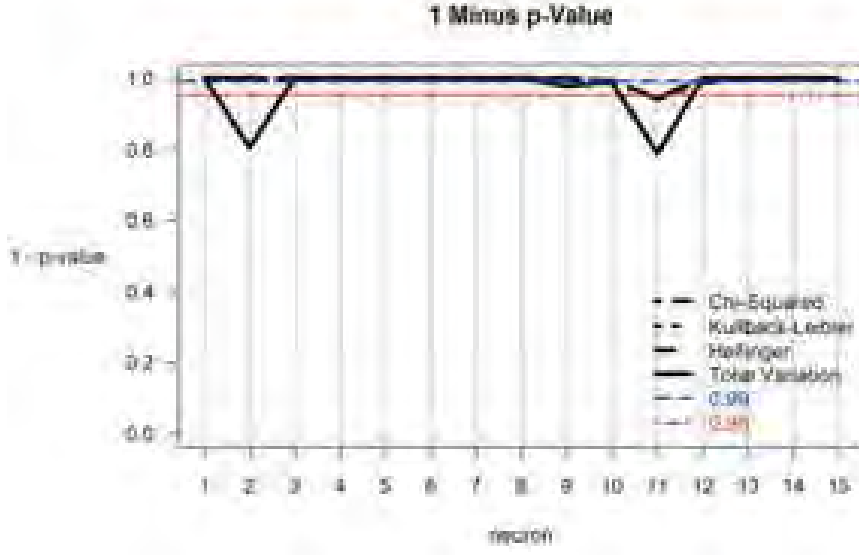


Figure 3: Global analysis for the 15 studied neurons. The upper and lower dashed lines correspond to cutoff points $\alpha=0.01$ and $\alpha=0.05$, respectively. There is an overall agreement among measures. At the $\alpha=0.05$ level, there is agreement among all four metrics in the case of every neuron except neuron 2. In the case of neuron 2, the total variation distance was unable to detect the difference identified by the other measures. At the $\alpha=0.01$ level, there is agreement among all four metrics in the case of every neuron except neurons 2 and 9. In both cases, it is again the total variation distance that was unable to detect the differences identified by the others. For a closer look at the p-values for neurons 2, 5, 9, and 11, see Table 2.

	Kullback-Leibler	Hellinger	χ^2	Total Variation
Neuron 2	0.000	0.000	0.000	0.143
Neuron 5	0.000	0.000	0.000	0.000
Neuron 9	0.000	0.000	0.000	0.027
Neuron 11	0.113	0.114	0.110	0.280

Table 2: A comparison of resampling p-values for four specific neurons. In the case of neuron 2, the total variation distance was unable to detect the differences picked up by the other three measures at either the $\alpha=0.05$ or $\alpha=0.01$ levels. In the case of neurons 5 and 11, there is agreement among all four measures at the $\alpha=0.01$ level. In the case of neuron 9, there is agreement at the $\alpha=0.05$ level, but not at the $\alpha=0.01$. At the $\alpha=0.01$ level, it is again the total variation distance that was unable to detect a difference picked up by the other metrics.

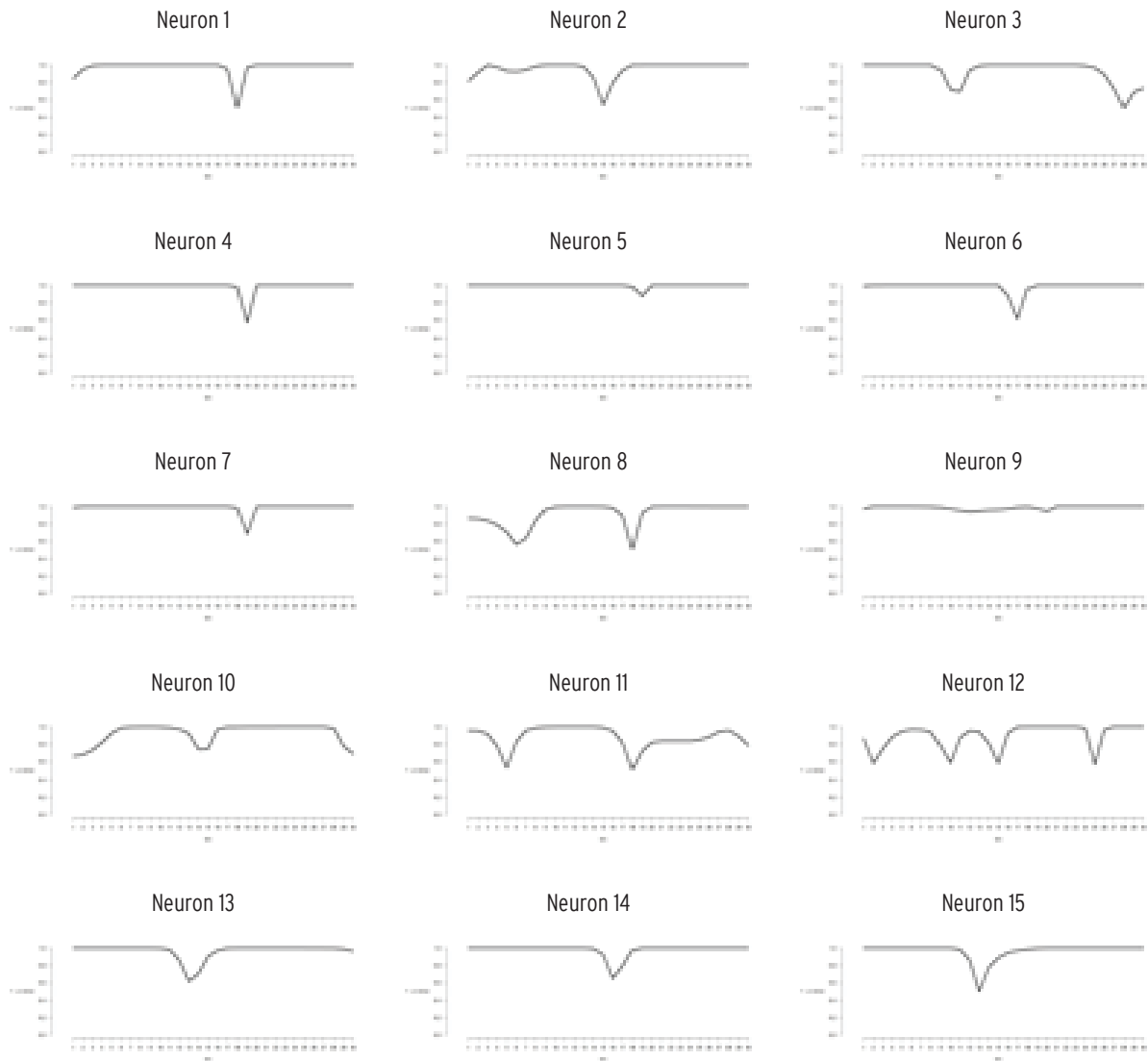
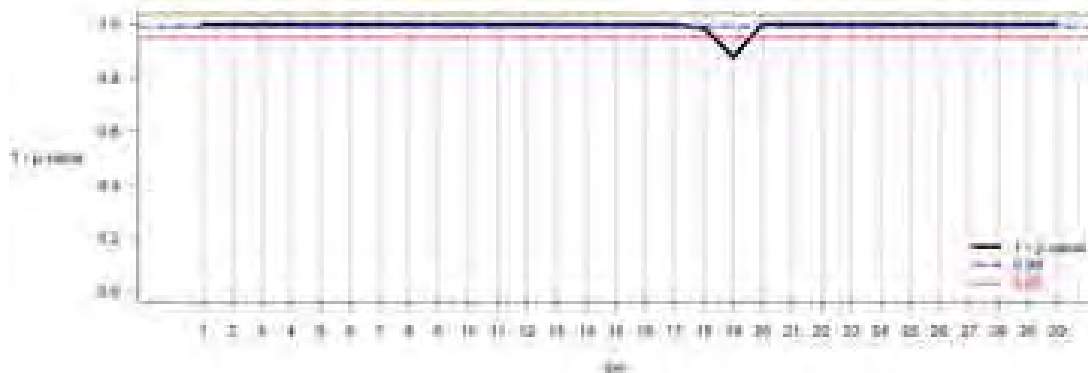


Figure 4: Local analysis of 15 motor neurons. The y-axis is 1 minus p-value of the LR metric. The x-axis is the bin number. A higher value in the y-axis indicates more statistical significance between repeating and random modes. A common feature between most of the neurons is a decrease in 1 minus p-value between bins 10 and 20.

Neuron 5 (differential)



Neuron 11 (non-differential)

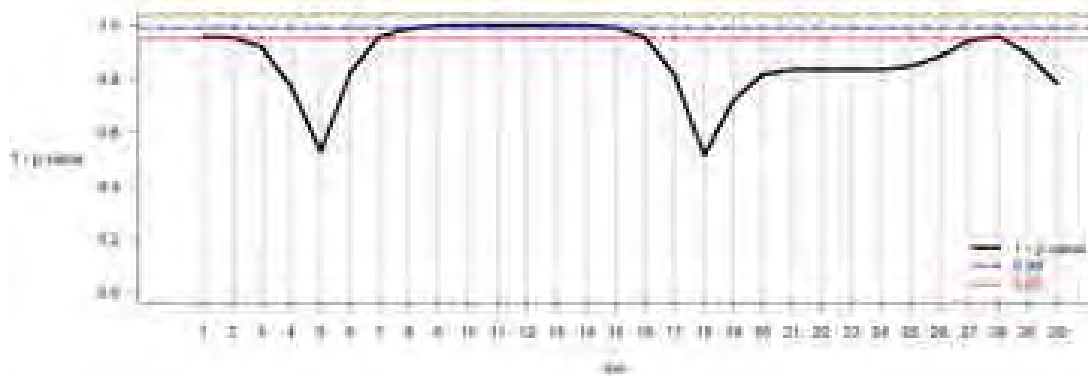


Figure 5: Plots of 1 minus p-value for neurons 5 and 11. The solid line indicates the value of 1 minus the p-value for each bin. The lower dashed horizontal line indicates the cutoff point corresponding to an α -level of 0.05 and the upper dashed horizontal line indicates the cutoff point for an α -level of 0.01. In the case of neuron 5 (a differential neuron), the majority of bins were differential according to the LR metric at both the $\alpha=0.05$ and $\alpha=0.01$ levels. Specifically, bins 1 through 18 and 20 through 30 were declared differential at the $\alpha=0.05$ level. At the $\alpha=0.01$ level, bins 1 through 17 and 20 through 30 were differential. For neuron 11 (a non-differential neuron) only a small subset of the bins were differential. That is, 13 out of 30 bins were differential according to the LR metric—bins 1, 2, 7 through 15, 27, and 28. At the $\alpha=0.01$ level, that number drops to 6 out of 30.

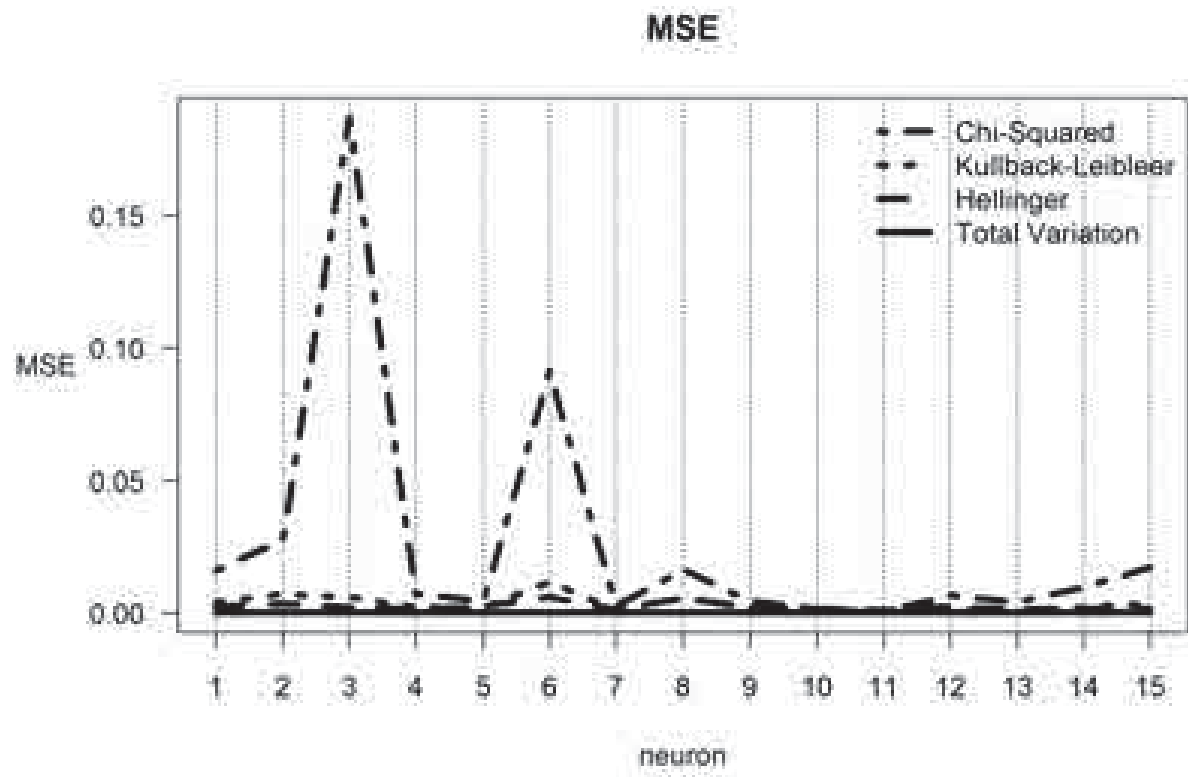


Figure 6: Plot of MSE for each metric. The y-axis represents the mean squared error. The x-axis represents the neuron number. For most of the neurons, the χ^2 metric yields a higher MSE than any other metric.

	χ^2	Kullback-Leibler	Hellinger	Total Variation			
Neuron 1	1.615e-02	>	4.176e-03	>	2.331e-03	>	1.741e-05
Neuron 2	2.793e-02	>	7.107e-03	>	3.429e-03	>	6.005e-05
Neuron 3	1.875e-01	>	6.082e-03	>	2.215e-03	>	6.070e-05
Neuron 4	7.403e-03	>	2.190e-03	>	1.543e-03	>	9.823e-06
Neuron 5	4.299e-03	>	2.069e-03	<	2.729e-03	>	1.910e-05
Neuron 6	9.124e-02	>	1.194e-02	>	5.988e-03	>	7.014e-05
Neuron 7	2.730e-03	>	1.103e-03	<	1.336e-03	>	7.764e-06
Neuron 8	1.649e-02	>	5.721e-03	>	5.638e-03	>	9.717e-05
Neuron 9	4.662e-03	>	1.988e-03	<	2.280e-03	>	3.779e-05
Neuron 10	1.497e-03	>	4.004e-04	<	1.472e-03	>	4.445e-05
Neuron 11	3.260e-04	>	8.600e-05	<	8.460e-04	>	1.355e-05
Neuron 12	6.778e-03	>	9.108e-04	<	2.343e-03	>	9.938e-05
Neuron 13	4.044e-03	>	6.894e-04	<	1.458e-03	>	6.338e-05
Neuron 14	9.654e-03	>	2.177e-03	>	1.508e-03	>	9.076e-05
Neuron 15	1.733e-02	>	3.521e-03	>	1.616e-03	>	3.330e-04
Mean	2.654e-02	>	3.344e-03	>	2.449e-03	>	6.829e-05
Standard Deviation	4.986e-02	>	3.222e-03	>	1.512e-03	>	7.977e-05

Table 3: From the above table, it is clear that the total variation distance performed best and the χ^2 divergence performed worst in terms of MSE. The similar performance of the Kullback-Leibler and Hellinger metrics is evident as well—the Hellinger distance outperformed the Kullback-Leibler divergence in only about half of the studied (8 out of 15) neurons.

Discussion

We investigated global and local firing discrepancies using the methodology proposed in Section 2. We noted that the total variation distance performed better than the other metrics. It is also worth noting that our analysis was limited to simulation-based approaches. We shall leave the more rigorous and theoretical study of comparing the efficiency of distance-based metrics to a future study. The main advantages of our devised methods are: 1) they can be easily implemented using familiar software such as R, 2) due to the nonparametric nature of our permutation tests, they can be used without the fear of violating too many restrictive statistical assumptions.

Acknowledgements

We would like to give a special thanks to Dr. Sam Behseta for introducing us to undergraduate research and statistics in neuroscience; for being a great professor, a wonderful advisor, and a good friend on this journey.

References

- Behseta, S. and Chenouri, S. (2011) Comparison of two populations of curves with an application in neuronal data analysis. To appear in Statistics in Medicine.
- DiMatteo, I., Genovese, C.R., and Kass, R.E. (2001) Bayesian Curve-Fitting with Free-Knot Splines. *Biometrika*. 88 (4): 1055-1071.
- Efron, B. (1982) The Jackknife, the Bootstrap, and Other Resampling Plans. Society for Industrial and Applied Mathematics, Philadelphia.
- Gazzaniga, M.S., Ivry, R.B., and Mangun (1998) Cognitive Neuroscience: The Biology of the Mind. W.W. Norton & Company, New York.
- Kass, R.E., Ventura, V., and Brown, E.N. (2005) Statistical issues in the analysis of neuronal data. *Journal of Neurophysiology*, 94: 8-25.
- Matsuzaka, Y., Picard N., and Strich, P. L. (2007) Skill representation in the Primary Motor Cortex after long-term practice. *Journal of Neurophysiology*, 97: 1819-1832.
- Puente, S. (2010) A re-sampling approach for the comparison of two random curves with an application in neuronal data analysis. *Dimensions*, 12: 80-86.
- R Development Core Team (2009). R: A language and environment for statistical computing. R Foundation for Statistical Computing, Vienna, Austria. URL <http://www.R-project.org>.
- Tsybakov, A. (2009) Introduction to Nonparametric Estimation. Springer, Berlin.

Biographies Authors



Angela Perez, a geological science major, has worked under the direction of Dr. Brady Rhodes for three years. During this time, her studies have taken her all over the world including Thailand, where her research takes place. She will graduate from California State University, Fullerton in 2011 with a B.S. degree and is planning to continue her education in the future.



Anne Calder is a senior majoring in Applied Mathematics at California State University Fullerton. Along with her studies, Anne is a member of a research team directed by Dr. Pineda studying the Statistical Modeling of the Fat Fraction in MRI. This research is being funded by the Center for Undergraduate Research (CURM). Anne is currently applying to graduate programs with the goal to get a Master's degree in Applied Mathematics.

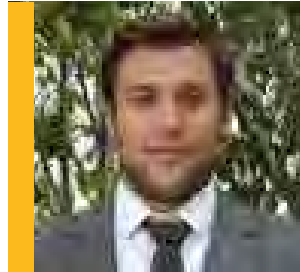


Bryan White works with faculty mentor Paul Stapp. He is interested in evolutionary biology, phylogenetics and bioinformatics, and has recently finished an independent research project to test the effects of illumination levels on the foraging behavior of nocturnal rodents in the Mojave Desert. He presented a poster on the effects of predation risk on foraging behavior of desert rodents at the Society for the Advancement of Chicanos and Native Americans in Science (SACNAS) conference in Dallas, Texas in 2009 and in 2010.

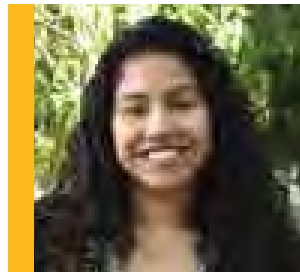


Crystal Castellanos is a geology major currently finishing her undergraduate research project studying a package of metamorphic rocks called the Kings Sequence in the west-central Sierra Nevada mountains under the supervision of Dr. Diane Clemens-Knott. Her participation in the Louis Stokes Alliances for Minority Participation Program partially funded the use of analytical instruments such as a scanning electron microscope, an electron microprobe, and an X-ray fluorescence unit. This data assisted in the identification of minerals and of the pre-metamorphic type of sediment. Crystal presented her research at the 2010 Geological Society of America Cordilleran Section Meeting. Part of her undergraduate experience includes a variety of leadership positions, including serving as the first President of the student chapter of SACNAS. Crystal has aspirations of pursuing a master's degree in geological science and becoming a professional geologist.

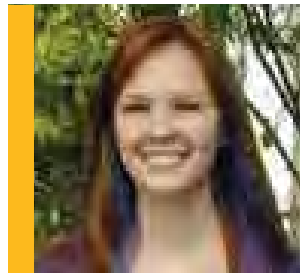
David Rock is a graduating senior majoring in Mathematics with a concentration in Probability and Statistics along with a cognate in Economics. He will be attending graduate school in the fall and hopes to continue research in Statistics. This is his first published work and he would like to thank his advisor, Dr. Sam Behseta, for his guidance and his research team for their collaborative effort. Along with Mathematics and Statistics, David's interests include sports, especially rugby and cycling. He has served as the CSUF Rugby treasurer for the past two years.



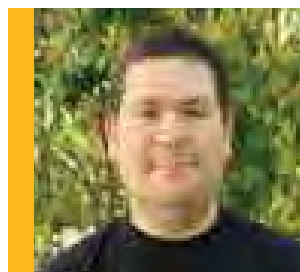
Denise Soto is currently working on her B.S in Biology with a concentration in cell and developmental biology. She volunteers at the Marine Mammal Center and helps rehabilitate pinnipeds. She is also a volunteer at Found Animals, a non-profit organization where she works with felines, providing them with a healthy and safe environment. Denise is interested in the field of veterinary medicine and is currently the pre-vet chair for the Student Health Professions Association.



Eden Ellis was born and raised in Southern California. She is now in her third year at CSUF pursuing a degree in Mathematics with a concentration in Probability and Statistics. She is currently working with Dr. Angel R. Pineda and three other undergraduates on the Statistical Modeling of the Fat Fraction in Magnetic Resonance Imaging (MRI). Eden is thankful for the opportunities she has had at CSUF and would especially like to thank Dr. Pineda for believing in her, Kevin, Anne and Li for making this project so fun, and the President's Scholars program for their continued support.



Eric Peralta completed his B.S. in biological science in Summer 2008. From 2006-2008, Eric was in the Southern California Ecosystems Research Program studying sexual selection in insects and presented his research at the Southern California Academy of Sciences meeting in 2008. He is currently a graduate student at Cal State Fullerton in the laboratory of Dr. Sean Walker investigating sperm competition and sexual conflict in house crickets.



Biographies Authors (continued)



Josh Maglione is a senior at Cal State Fullerton, where he will graduate with BA in Math in May 2011. For the past few years, he worked with Dr. Scott Annin researching generating sets for the alternating and symmetric groups. He has attended various mathematical conventions, where he presented his research to several audiences. His research has garnered attention from the math community, winning him multiple awards nationally and within the university, including the Special Recognition for Undergraduate Research Scholarship from CSUF and Outstanding Poster Award from the 2009 Joint Mathematics Meeting. Once he graduates from CSUF, Josh will go on to pursue his Ph.D. in mathematics in hopes of returning to the classroom as a university professor.



Joshua Strong is a mathematics student at California State University, Fullerton. After attending Citrus College, in Glendora, he decided to pursue mathematics at CSUF. He is currently working on research, under the advisement of Dr. Alfonso Agnew, in the field of mathematical physics. He plans to graduate in the spring of 2011 and then pursue a Ph.D. in pure math.



Karolis Raudys is originally from Kaunas, Lithuania. He moved to the United States when he was eight years of age and has spent the majority of his time in the states living in Southern California. He is majoring in Biology with a minor in Chemistry and will be graduating in the Spring of 2011. He has spent a total of 3 years working in Dr. Sandquist's physiological plant ecology lab and will continue to always have an interest in the ecological aspects of Biology. However, he plans to apply to medical school immediately following graduation to pursue a career in medicine- the source of his true passion for life and the sciences.



Kevin Park is a Mathematics major, with a focus in Applied Mathematics. From 2009 he had the opportunity to work with Dr. Angel R. Pineda in the field of medical imaging where he presented his work on Noise Analysis of Accelerated Magnetic Resonance Imaging (MRI) at the Joint Mathematics Meeting 2010 in San Francisco. In the summer of 2010, he had participated in a Research Experience for Undergraduates at Worcester Polytechnic Institute (WPI) in Worcester, MA. At WPI he worked on an industrial project the Mathematical Modeling of Cobbling Instabilities in Steel Rod Fabrication. Additionally, he had the chance to attend the Graduate Student Mathematical Modeling Camp at Rensselaer Polytechnic Institute in Troy, NY. As of now, he continues to work with Dr. Pineda, and other undergraduates from CSUF. The focus of their project is the Statistical Modeling of the Fat Fraction in MRI funded by the Center for Undergraduate Research in Mathematics. He plans to attend graduate school and continue studying the applications of mathematics. Notably, he would like thank Dr. Pineda for his mentorship and his infinite patience.

Leslie Herington will be completing her Bachelor's of Science in Biological Science in the Spring of 2011. During her undergraduate studies, she was a member of the Vertebrate Ecology and Conservation lab with Dr. Paul Stapp. She presented a poster at Southern California Academy of Sciences (SCAS) in 2010 and participated in the National Science Foundation's Research Experience for Undergraduates program at Colorado State University in Fort Collins, Colorado. She will be presenting this project at the American Society of Mammalogists annual meeting in Portland, Oregon this summer.



Li-Hsuan Huang is a senior majoring in applied mathematics and accounting at California State University, Fullerton. He is currently working with Dr. Pineda and three research members on the Statistical Modeling of the Fat Fraction using MRI. In summer 2010, Li-Hsuan had an opportunity to participate in a Research Experience for Undergraduates (REU) program at California State University, Channel Islands, where he embarked on a research project on Two-dimensional Shape Modeling with other four students. As Li-Hsuan is wrapping up his last semester, he is considering an applied mathematics Ph.D. and wants to teach in a college or university one day in the future.



Rolando Ruiz completed his Bachelor's of Science in Biological Science in the spring of 2010 and is currently working at Tufts University as a Post-baccalaureate student. During his undergraduate studies, he was part of the Minority Access to Research Careers (MARC) where he conducted research in the laboratory of Dr. Koch. He presented his work at various conferences including SACNAS National Conference, CSUPERB, and at the NSM ICC symposium. He lead various genetics workshops through NSM for Young Black Scholars Day and John's Hopkins Kids in Science day at CSUF. In the fall, Ruiz plans to enter a graduate program in the biomedical sciences.



Sarah English graduated from CSUF with her Bachelor's degree in Biological Science in the Spring of 2008 and completed her undergraduate thesis in the Spring of 2009. Her degree concentration was Biodiversity, Ecology, and Conservation and she also graduated with a Chemistry minor. She was accepted into the 2006 cohort of the Southern California Ecosystems Research (SCERP) program, led by Drs. Bill Hoese and Darren Sandquist. She has a special interest in studying the interactions between humans and animals and their environment and conservation for the future. Sarah's work as an undergraduate in Dr. Anne Houtman's lab studied the effects of human noise pollution on the song structure and behavior of two southern California hummingbird species. While at CSUF, she was the recipient of the Emeriti Memorial Scholarship and the Rachel Carson Scholarship in Conservation Biology. She is currently a general education elementary substitute teacher and is working in a Master's program in Environmental Engineering at National University in San Diego.



Biographies Authors (continued)



Victor Ying is a probability & statistics major at California State University, Fullerton. He has a broad interest in both theoretical and applied statistics. His current research, under the advisement of Dr. Sam Behseta and in collaboration with Mikhail Popov and David Rock, is on an application of statistics in neuroscience. He plans to enter a graduate program in the fall.



Steven Schill will graduate with his bachelor's degree of science in chemistry and a minor in mathematics in the fall of 2011. He is completing his second year with the Howard Hughes Medical Institute Research Scholars Program at CSUF, and is also a member of the University Honors Program. Steven currently serves as President of the CSUF Chemistry and Biochemistry Club, and is a member of the National Society of Collegiate Scholars as well as the Golden Key International Honor Society. After completing his degree with honors in three and a half years, Steven plans to attend graduate school to obtain his Ph.D. in physical/analytical chemistry. Steven would like to thank Dr. Richard Deming and Dr. Narongpan Chunram for their success in coordinating research activities through Chiang Mai Rajabhat University in Chiang Mai, Thailand, as well as Dr. Maria Linder and the HHMI Program for the gracious support and many opportunities afforded to him thus far. He would also like to thank his CSUF research mentor, Dr. Paula Hudson, for her endless support and encouragement through his undergraduate research career and education while at CSUF.



Peter Ho is a senior majoring in mathematics and physics at California State University Fullerton. He is involved with Math Club as an Interclub council representative, and with students taking math courses as a Supplemental Instruction Leader. Also, he plans on attending graduate school after graduation and eventually teaching students the joy of finding things out.

Jonathan Sayre is an undergraduate working on his degree in mathematics. His article focuses on an interesting problem that arises in the 10th grade Geometry curriculum. He will graduate in the Spring of 2012 and will enter the credential program at California State University, Fullerton. He will then pursue a Masters in Education to complete his training to be a high school math teacher. Jonathan is a returning student after a successful career as a field technician for computerized engraving machines. He is the father of three children and looks forward to being an inspirational high school math and science teacher.

Jeremy Reitsma is a senior at Cal. State Fullerton majoring in mathematics with an emphasis on teaching. The focus of this article is on a problem that arises in tenth grade geometry curriculum. He was born and raised on a dairy farm in Ontario, California, and found a love for mathematics in his high school calculus class. That was when he knew that he wanted to dedicate my professional life to the discovery of mathematics, and to be able to pass that love on to others by teaching. He hopes to finish my degree in the fall of 2011 and go on the credential program here at Cal. State Fullerton with the ultimate goal of becoming a high school teacher.

Michael Prior is a senior geology major who will graduate cum laude with a Bachelors of Science in May 2011. Michael conducted fieldwork in southern Alaska for his undergraduate thesis, where he studied the structural and tectonic evolution of the Chugach Mountains. Traveling throughout the western U.S. while growing up, and a love of outdoors activities such as camping, hiking, and fishing gave Michael the desire to study the processes that shape the Earth. While at CSUF Michael has been awarded the Outstanding Geology Major award and presented research at professional conferences. After graduation Michael plans to pursue a M.S. and PhD in geological sciences.

Michelle Gevedon will graduate from CSUF with a B.S. in geology in May 2011. Michelle's love of the natural world drew her to pursue an education in the geosciences. She has served as a camp director and counselor at the YMCA, teaching students the joys of the outdoors and how to be responsible stewards of the planet. While going to school Michelle served a Peer Transfer Advisor for the STEM Transfer Students Services Office at CSUF, and taught in K-12 programs promoting science education. Michelle plans to pursue a Ph.D. in geology and hopes to investigate the varied processes that create and exhume metamorphic rocks.

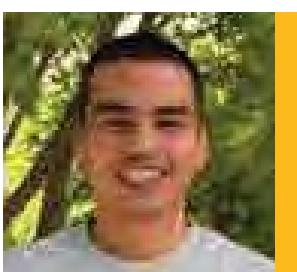
Biographies Editors



Amber Shah (Executive Editor) is currently an undergraduate studying biology at California State University, Fullerton. She intends to graduate having achieved a Bachelor's of Science concentrating in Molecular Biology and Biotechnology. She is a part of the University Honors Program and is intrigued by its many diverse disciplines. In addition, Amber has worked in Dr. Sacco's lab as a volunteer and wishes to further her understanding in genetics and molecular biology. In addition, Amber is interested in pediatrics. After graduating from Cal State Fullerton, she will pursue medical school and fulfill her many aspirations within the medical field.



Erin Driver (Geology) is a second-year geological sciences master's student with an emphasis in biogeochemistry. She received her B.S in environmental systems with an emphasis in earth science, and minors in chemistry and environmental studies from the University of California at San Diego in 2006. Her research interests focus on the influence of chemical heterogeneity on microbial activity and distribution in aqueous sediments; she is advised by Dr. Tara Kneeshaw. Erin is currently a part-time faculty member at California State University Fullerton and a research assistant at the Southern California Coastal Water Research Project.



Ernesto Casillas (Biology) is an undergraduate Biological Science major at CSUF. Currently he is a research scholar in the Southern California Ecosystems Research Program, an NSF-funded undergraduate training program. He is working on a thesis that studies the metal loads in tissues of the marine gastropod *Kelletia kelletii* in the lab of Dr. Danielle Zacherl. After he graduates, Ernesto plans on pursuing a career as a biomedical scientist.



Julie Yang (Chemistry/Biochemistry) is a second year graduate student at California State University, Fullerton. She obtained a Bachelors of Science at California State University, Los Angeles. Julie is currently working in Dr. Chandra Srinivasan's and Dr. Nikolas Nikolaidis research labs in characterizing the metalloprotein cutC found in *C. elegans*. She is also working on a proteomics project with Dr. Srinivasan and Dr. Julian Whitelegge (UCLA collaborator) to elucidate the antioxidant like effects of manganese. In the fall 2011, she will be attending Cedars Sinai doctoral program in biomedical sciences and translational medicine.

Mikhail Popov (Mathematics) is a modern Renaissance man. He plans to graduate in 2012 with a degree in Mathematics (specifically Probability and Statistics) and then enter a graduate program (most likely machine learning). This is his first published work as a researcher and editor. Along with math, he loves hiking, illustration, programming, graphic design, video game design / development / analysis / criticism, obtaining new knowledge, and being verbose & clever. He would like to thank Dr. Sam Behseta for his guidance along the Sisyphean journey known as college education.



Brian Bouskill (Cover Designer) A graduate student at California State University, Fullerton in the MFA program. Graduated from CSUF in 1982 and has worked as a Graphic Designer, Art Director, and Photographic Retoucher and has returned to school in order to teach Graphic Design.



Carolyn Luu (Layout Editor) is an undergraduate Graphic Design Student at California State University, Fullerton expecting to graduate in Spring 2012 with a BFA in Graphic Design. Once obtaining her BFA she would like to return to school and get a MFA in Graphic Design to teach. Her work has also appeared in magazines such as 944 Magazine.

